

MR-only Radiotherapy of prostate cancer

Matteo Maspero

MR-only Radiotherapy of prostate cancer
PhD Thesis, Utrecht University, The Netherlands

Cover *An irradiation with Stijl*

© Matteo Maspero, Utrecht, 2018. All rights reserved. No part of this thesis may be reproduced, stored in a retrieval system or transmitted in any other form or by any means, without written permission from the author. The copyrights of published articles have been transferred to the respective journals.

© IOP Publishing Ltd for Chapter 2, 3 and 4.

Printed in Almere, The Netherlands in March 2018.

ISBN 978-90-393-6953-1

Colophon The work in this thesis has been carried out under the auspices of the “Graduate Programme Medical Imaging” (ImagO) as part of the “Graduate School of Life Sciences”, and the Faculty of Medicine/University Medical Center Utrecht within the Utrecht University. The research was conducted at the Radiotherapy Department in collaboration with the Image Sciences Institute and the Center for Image Sciences in the University Medical Center Utrecht.

This thesis was accomplished with financial support from ZonMw Innovative Medical Devices Initiative (IMDI) Programme project 1040030 (2014-2018).

Financial support for publication of this thesis was kindly provided by Computerized Imaging Reference Systems, Inc., Elekta AB and Philips Healthcare.

MR-only Radiotherapy of prostate cancer

Radiotherapie van prostaatkanker op basis van MRI

(met een samenvatting in het Nederlands)

Radioterapia della prostata con sola risonanza magnetica

(con un riassunto in lingua italiana)

Proefschrift

ter verkrijging van de graad van doctor aan de Universiteit Utrecht op gezag van de rector magnificus, prof. dr. G.J van der Zwaan, ingevolge het besluit van het college voor promoties in het openbaar te verdedigen op donderdag 26 april 2018 des middags te 12.45 uur

door

Matteo Maspero

geboren op 24 mei 1989 te Como, Italië

Promotoren: Prof. dr. ir. J.J.W Lagendijk
Prof. dr. ir. M.A. Viergever
Copromotoren: Dr. ir. C.A.T. van den Berg
Dr. ir. P.R. Seevinck

Concern for man and his fate must always form the chief interest of all technical endeavors. Never forget this in the midst of your diagrams and equations.

Albert Einstein

*...fatti non foste a viver come bruti,
ma per seguir virtute e canoscenza.*

Dante Alighieri
Canto XXIV, Inferno

To the upcoming generation: Pietro, Luca, Giovanni, Daniele; my nephews.

Forewords

If I have seen further, it is by standing on the shoulders of giants.

Isaac Newton

Dear Reader,

First of all thank you very much for indulging in this thesis presenting the work of the last (almost) four years at the Radiotherapy department of UMC Utrecht. I hope you will enjoy the following (couple of) pages, and on the contrary, please, do not hesitate to contact me: your comments will undoubtedly be highly appreciated.

The goal of this Forewords is to shortly guide you through the content of this thesis. So, let's start from the very beginning.

The **cover** sketches a daily fraction of external beam radiotherapy¹ for a prostate patient. It was designed as a homage to the *de Stijl* movement, which was founded exactly one hundred years ago. You are probably recognising some similarities with one of Piet Mondriaan's series of painting, the "Boogie Woogie". Yes, you are right! The version called "Victory", which is exhibited at *het Gemeentemuseum Den Haag*, triggered my interest to further investigate on the *de Stijl*. Also, *het Gemeentemuseum Den Haag* is the first museum that I ever visited in the Netherlands, so I thought that it would have been nice to pay homage to the place where so much started for my personal development. Let's further consider that in 2017 the *de Stijl* became 100 years old, so no better excuse to join the celebrations!

I hope that the content of this thesis could demonstrate at least a tiny bit of that amazing **synthetic** skill possessed by Piet & friends.

After this first artistic *excursus*, unfortunately, the thesis would move into a less "coloured" matter.

The first chapter presents in Section 1.1 and 1.2 a condensed general introduction to the complex radiotherapy world. Here, I tried to accommodate the curiosity and needs of a general audience moving the first steps in a possibly unfamiliar environment. Unfortunately, not all the necessary information for the full comprehension of the subjects that were touched upon in this thesis has been presented. In particular, what it is mostly missing is an explanation of imaging techniques, and especially of magnetic resonance imaging (MRI), which is the undiscussed (intriguing) protagonist of this thesis. For this reason, you will not find any explanation of terms like echo time (TE), relaxation time (TR), flip angle (FA) or T₁ and T₂ weighting. However, do not worry about this, at least you know from the very beginning which are the acronyms of such terms, and this is all you may need to know for now. My apologies if your curiosity remains mostly unsatisfied with such a choice. But, dear Reader, you never know what the future will unveil: maybe there will be an occasion to write some more lines on imaging modalities with a particular focus on MRI. Time will tell, let's see. . .

¹If you have not exactly clear what "external beam radiotherapy" means, please have a look at Section 1.1.

In case you feel like mastering the “complex radiotherapy world”, please do not hesitate to skip Section 1.1 and 1.2 and get ready to dive into the practical realm of “MRI-only radiotherapy”.

The central chapters of the thesis (chapters from 2 to 5) will present work based on articles that are published (Chapter 2, 3 and 4), or under revision (Chapter 5). The last part of the thesis (Chapter 6) aims at placing the contribution offered in this thesis within a “bigger picture”. Summaries in Dutch and Italian are also included in Chapter 7.

This thesis could not be made without the contribution of many, and to correctly highlight such contributions, a separated chapter has been dedicated in the Addendum (Part V).

But I am sure that I have already bored you enough, dear Reader, through this Forewords, so please do not indulge further and good luck with the upcoming lines, keeping in mind that. . .

*Tu m' hai con disiderio il cor disposto
sí al venir con le parole tue,
ch'i son tornato nel primo proposto.
Or va, ch'un sol volere è d'ambidue . . . ”
Così li disti; e poi che mosso fue,
intraì per lo cammino alto e silvestro.*

**Dante Alighieri,
Canto II, Inferno**

Matteo Maspero
December, 2017
Utrecht, The Netherlands

Contents

Colophon	ii
Title page	i
Forewords	v
Table of Contents	vi
1 Introduction and Objectives	1
1.1 General introduction to radiotherapy	1
1.2 The clinical radiotherapy pathway	3
1.2.1 Patient simulation	4
1.2.2 Irradiation plan	5
1.2.3 Position verification and irradiation	5
1.3 Radiotherapy for prostate cancer patients	6
1.3.1 Magnetic resonance imaging in radiotherapy	7
1.3.2 MRI-based treatment planning & its challenges	9
1.4 Objectives and Outline	13
I Dose Calculation	15
2 Synthetic CT for photon radiotherapy	17
2.1 Introduction	19
2.2 Materials and Methods	21
2.2.1 Patient data collection	21
2.2.2 Image processing for sCT generation	23
2.2.3 Treatment planning	25
2.2.4 Evaluation of inter-scan differences	26
2.2.5 Dosimetric comparison	26
2.3 Results	28
2.3.1 Evaluation of inter-scan differences	28
2.3.2 Dosimetric comparison	28
2.4 Discussion	30
2.5 Conclusion	32
2.6 Appendix: CT-based sCT similarity	32
2.7 Supplementary material: Gamma analysis	35
3 Synthetic CT for proton radiotherapy	37
3.1 Introduction	39
3.2 Materials and Methods	41
3.2.1 Patient data collection	41
3.2.2 sCT generation	42
3.2.3 Treatment planning	44

3.2.4	sCT evaluation	45
3.3	Results	46
3.3.1	Image evaluation	46
3.3.2	Proton range comparison	46
3.3.3	Dosimetric comparison	49
3.4	Discussion	50
3.5	Conclusion	53

II Patient Positioning 55

4	Automatic gold fiducial marker localisation	57
4.1	Introduction	59
4.2	Materials and Methods	61
4.2.1	Patient data collection	61
4.2.2	Clinical fiducial marker localisation	62
4.2.3	MR-based fiducial marker localisation	63
4.2.4	Evaluation	64
4.3	Results	67
4.3.1	Detection rates	67
4.3.2	Geometric accuracy and precision	68
4.3.3	Outliers of MR-based FM localisation	70
4.3.4	Impact on patient alignment	71
4.4	Discussion	72
4.5	Conclusion	75
4.6	Appendix: Performances of MR-based automatic FM localisation	76
5	Manual gold fiducial marker localisation	79
5.1	Introduction	81
5.2	Materials and Methods	82
5.2.1	Patient preparation and selection	82
5.2.2	MR-based fiducial marker localisation	83
5.2.3	Statistical analysis	85
5.3	Results	86
5.3.1	Single FM locations	87
5.3.2	Center of mass locations	89
5.3.3	Spatial accuracy	90
5.4	Discussion	90
5.5	Conclusion	93
5.6	Supplementary Material	94
5.6.1	Instructions provided to the clinical observers	94
5.6.2	Annotations on the FM localisation	94
5.6.3	Single patient investigation	96

III Discussion and Summaries	99
6 Discussion	101
6.1 MR-based dose calculations	101
6.2 MR-based set-up corrections	104
6.3 Practical considerations: a clinical perspective	108
6.3.1 MR protocol optimisation: an example from Utrecht	108
6.3.2 MR-only delineations for OARs	109
6.4 Future perspectives	110
6.4.1 . . . beyond prostate treatments	110
6.4.2 MR-only for MRI-guided radiotherapy	111
6.5 Conclusion	112
7 Summaries	115
Samenvatting	115
Riassunto	117
IV Index	121
Bibliography	123
List of Figures	143
List of Tables	145
List of Abbreviations	147
Units and Symbols	148
V Addendum	151
List of Publications	153
Acknowledgements	157
About the author	163

Introduction and Objectives

1

Nothing in life is to be feared, it is only to be understood. Now is the time to understand more, so that we may fear less.

Marie Curie

1.1 GENERAL INTRODUCTION TO RADIOTHERAPY

Radiotherapy, also called radiation therapy, is one of the treatments in use to cure cancer (curative therapy), alleviate patients' pain (palliative treatment), reduce the risk of cancer recursion (adjuvant radiotherapy) or strengthen the effectiveness of other treatments, e.g. chemotherapy (chemoradiation) or surgery (neoadjuvant therapy) [Gunderson & Tepper 2016]. Also, radiotherapy is a local, or locoregional, approach.

Within the scope of a curative therapy, there is a chance of treating cancer using a locoregional approach as radiotherapy as long as the disease is localised to its site of origin or has spread to the regional lymph nodes only. Cancer cells, however, may not be confined locally or regionally [Wan *et al.* 2013]. In this scenario, local therapies are not sufficient, and the treatment of cancer requires a systemic approach involving chemotherapy, hormonal therapy or targeted therapy [IAEA *et al.* 2017].

Overall, 50-65% of all cancer patients undergo radiotherapy during the course of their disease, either as a single modality or in combination with other treatment modalities [IAEA & Izewska 2008]. This shows the crucial role of radiotherapy in the treatment of cancer.

By definition, radiotherapy involves the use of ionising radiation. The mechanism by which radiotherapy is effective in the treatment of cancer is described in more detail elsewhere [Joiner & van der. Kogel 2009], but, in short, ionising radiation in sufficient doses has a cell-killing effect. This effect, however, is not specific to damage only cancerous cells and spare healthy cells. Therefore, strategies to enlarge the therapeutic effect were proposed, either by physically enhancing target conformity and dose level or by increasing the radiation sensitivity of the cancer cells relative to the normal cells [IAEA *et al.* 2017]. To optimise the therapeutic effect, developments in radiotherapy have been motivated by the need to reduce treatment uncertainties such that a curative radiation dose may be delivered to a malignant tumour, while decreasing the dose received by healthy tissues [Jaffray 2012]. In this sense, one of the main requirements of a radiotherapy treatment is the spatial accurate tumour localisation.

Three techniques are generally employed to deliver ionising radiation to patients:

- Teletherapy (therapy delivered from “tele” = distance) or external beam radiotherapy - where a radiation beam is directed to a patient, e.g. passing through the skin. Teletherapy, if used alone, is by definition a non-invasive technique;
- Brachytherapy (therapy delivered from “brakhus” = not far off) - where a radioactive source is placed near or in a tumour. Brachytherapy is considered an invasive technique;
- Systemic or radioisotope therapy - where radioactive material is injected or orally administered to a patient, and the targeting of a tumour relies on patient’s metabolism or physiology. To effectively perform such treatment, prior knowledge of the patients’ metabolism or physiology is required.

This thesis will focus on external beam radiotherapy and, for simplicity, in the remainder of this thesis, when referring to “radiotherapy”, external beam radiotherapy will be intended¹. For radiotherapy, different types of radiation can be used: photons and electrons are the most used in-hospital form of radiation [Rosenblatt *et al.* 2013], however, heavier particles like protons, neutrons, helium, carbon-ions, etc. are also delivered to patients [Durante & Loeffler 2010, Jermann 2015, Schulz-Ertner & Tsujii 2007]. The biological effect of each radiation type depends on their ionisation power: photons and electrons produce comparable density of ionisation in particle tracks resulting in similar biological effects, while protons and more massive particles have a higher density of ionisation resulting in a more significant effect [Joiner & van der. Kogel 2009]. This leads to differences in the spatial distribution of the deposited energy and different penetrative power depending on the energy of particles. An example of such difference in the spatial distributions is presented in Figure 1.1 showing percent dose-depth profiles of electron, photon and proton beams.

To reach deep tumours limiting the dose delivered to the skin, high energy photons are chosen because of their penetrating power. As shown in Figure 1.1, the depth of the maximum dose increases with increasing beam energy.

However, how can the radiation be generated with an energy suitable to reach deep-seated tumours? Photon-based radiotherapy is produced exploiting the radiation naturally emitted when specific radioactive materials decay such as Radium-226, Cesium-137 and Cobalt-60, or exploiting the “bremsstrahlung” radiation that is produced with particle accelerators. The second option is the most popular and linear accelerators (linacs) are usually employed in the radiotherapy departments, creating beams of pulsed photons in the energetic range of 4-25 MV [IAEA *et al.* 2017]. Proton or heavier particle irradiation can be produced by circular accelerators (cyclotrons), synchrotrons or cyclo-synchrotrons. These devices employ strong magnetic fields and radio-frequency (RF) electromagnetic waves to accelerate a given particle to a specific energy. Such equipment is considerably more expensive than standard radiotherapy equipment, both in capital costs and in maintenance and servicing costs, thus precluding a widespread use

¹For the reader interest in brachytherapy, two recent and explicative contributions are suggested [Tanderup *et al.* 2014, Zaorsky *et al.* 2017]. In particular, Zaorsky *et al.* focused on prostate treatments.

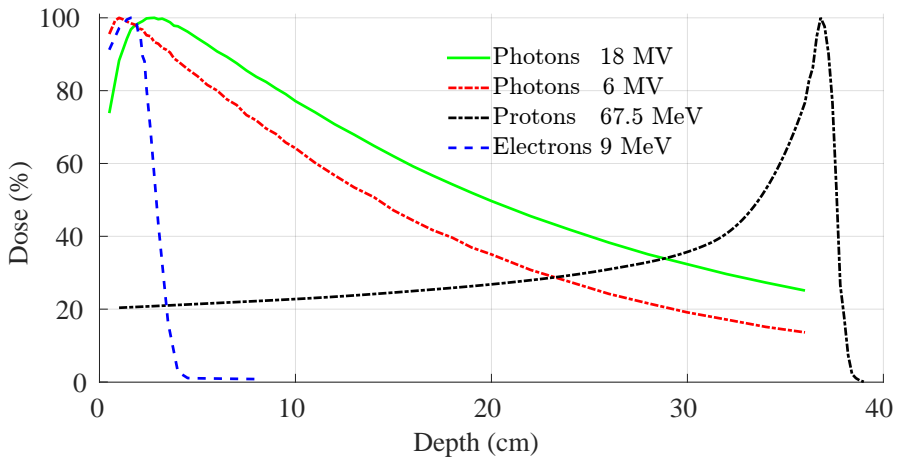


Figure 1.1 **Percent Dose depth profile** for three different type of radiations: (blue) a 9 MeV electron beam, (green) an 18 MV photon beam, (red) a 6 MV photon beam and (black) a 67.5 MeV proton beams. All data were experimentally acquired: the proton profile was extrapolated from Table 2 in [Faddegon *et al.* 2015], while photon and electron profiles were acquired in 2011 to characterise a linear accelerator clinically used at the “Ospedale Sant’Anna” (San Fermo della Battaglia, Como, Italy).

in radiotherapy departments [IAEA & Podgorsak 2005]. The use of heavy particles is, however, advantageous given the obtainable dose deposition distribution. Besides, in the last decade, the cost of the equipment is decreasing, making such technologies increasingly used [Newhauser & Zhang 2015].

1.2 THE CLINICAL RADIOTHERAPY PATHWAY

Nowadays, cancer patients who have access to the healthcare system are treated by a surgeon, a radiation oncologist, a medical oncologist or, preferably [Patkar *et al.* 2011], a multidisciplinary team. When radiotherapy is the treatment of choice for a given patient, the radiation oncologist, who works in close collaboration with the other members of the radiotherapy team, is the doctor responsible for prescribing, planning, monitoring and following the patient throughout and after the course of treatment.

Within the radiotherapy process itself, a multidisciplinary team comprising of a radiation oncologist, a medical physicist and radiotherapy technicians (RTTs) and in some countries a dosimetrist, is necessary. Each member of the team is responsible for different aspects of the entire radiotherapy process. After the cancer stage [Brierley *et al.* 2017] is known, and the appropriate treatment is determined, a series of interlinked steps follow to accommodate the decision to treat. Figure 1.2 shows a schematic overview of the possible steps involved in the therapy when radiotherapy is the treatment of choice². The radiation oncologist imple-

²The schematic does not include treatments others than radiotherapy. Please, note that the clinical pathway may be much more complex in the real cases and it may also not always be streamlined as depicted in Figure 1.1. An interesting perspective to such pathway is presented in [Gupta & Narayan 2012].



Figure 1.2 Flowchart illustrating an ideal patient treatment during which external beam radiotherapy is the treatment of choice. The patient treatment represented starts with diagnosis and ends with treatment delivery. Note that in reality the radiotherapy treatment can be used for adjuvant/palliative purposes and in such cases, the patients will undergo other treatments, e.g. chemotherapy or surgery. The shaded background refers to the sub-processes that are considered part of radiotherapy treatment planning.

ments the treatment directive. This directive includes the dose prescription for the target volumes as well as the dose limitations for healthy tissues. From this moment, the process of treatment planning, a preparatory phase leading to the actual treatment delivery, is initiated. During the treatment planning, the most effective modality and beam arrangement, or combinations thereof, for irradiating the target are established resulting in an individualised treatment for each patient [IAEA *et al.* 2017]. The following subsections describe the steps involved in treatment planning in more details.

1.2.1 Patient simulation

POSITIONING & IMMOBILISATION One of the paradigms accepted in modern radiotherapy is that delivering the total dose to a tumour in several irradiation sessions provides a more effective way of delivering radiation than in a single session [Verellen *et al.* 2008]. Such a practice is called “dose fractionation” and is based on the different radiobiological characteristics of a tumour and normal tissues [Baskar *et al.* 2012]. In particular, a dose of about 2 Gy per fraction is generally delivered trying to maximise cancerous cell impairment and minimise radiation-induced side effects in healthy tissues [Mitchell 2013, Kim & Tannock 2005]. Different tumour sites, however, showed different radiosensitivity. Therefore, according to how (radio)sensitive is a specific tumour type, different fractionation regimens are defined [The Royal College of Radiologists 2016]. The introduction of fractionation schemes required strategies to ensure reproducible patient positioning throughout the whole treatment. With this concern, immobilisation devices (such as thermoplastic masks, knee supports, vacuum cushions) have been introduced. Skin marks are also drawn during simulation such that RTTs have clear reference points to guide the pre-irradiation patient positioning [Verellen *et al.* 2007].

IMAGING & DELINEATION The second step consists of localising the target and identifying surrounding high-risk structures, such that the radiation can be focused on the target volume and high-risk healthy structures are avoided as much as

possible. Target and risk volume definition can be achieved by palpation or visualisation using planar X-ray radiography, or from imaging procedures like ultrasound, computed tomography (CT), magnetic resonance imaging (MRI) and positron emission tomography. Images produced with photons (e.g. CT) provide a measure of the beam attenuation in the patient body expressed in CT numbers or hounsfield unit (HU) [Knöös *et al.* 1986, Constantinou *et al.* 1992]. This information is of primary importance because, with the use of calibration curves or phantoms, HU can directly provide a measure of the electron density of the tissue. The electron density is the quantity on which the physical interaction of photons and electrons in the patient can be predicted and simulated yielding a three-dimensional (3D) radiation dose distribution in the body. The other imaging modalities assist in the localisation and determination of the extent of the disease, mainly because they provide better soft tissue contrast (MRI) or additional physiological or metabolic information (positron emission tomography) [IAEA *et al.* 2017].

To standardise the definition of the target, the International Commission on Radiation Units and Measurements has proposed to name gross tumour volume the visible part of a tumour [ICRU 2010]. To account for possible microscopic tumour spread, the gross tumour volume needs to be expanded, creating the clinical target volume (CTV). Finally, to account for all geometric inaccuracies and uncertainties, such as patient setup errors, delineations inaccuracies and tumour position, an additional margin is added to the CTV, creating the so-called planning target volume (PTV). The radiation oncologist manually delineates the gross tumour volume and margin recipes define the expansion according to the site treated. In addition, the surrounding organs at risk (OARs) are delineated by the physician or specialised RTTs.

1.2.2 Irradiation plan

A radiation treatment plan is then generated by optimising the placement of the treatment fields to obtain a radiation dose that meets predefined sets of prescriptions and constraints for the target and OARs.

This optimisation is generally performed in the treatment planning system. A treatment planning system is a software capable of generating 3D dose distributions according to the 3D patient model acquired during simulation, the dose prescriptions and constraints defined and the machine chosen for the irradiation. Medical physicists or dosimetrists are responsible for generating the plan. Before delivery, the plan requires being controlled and accepted by the radiation oncologist.

1.2.3 Position verification and irradiation

The last step of the preparation process is conducted just before irradiation when RTTs carefully position the patient such that the relative location of the target with respect to the linac may correspond to the location defined in the irradiation plan. To verify and improve target localisation and pre-irradiation patient set-up, pathways have been designed consisting of a series of consecutive imaging tasks

known as image-guided radiotherapy (IGRT). The imaging techniques involved in IGRT can range from planar imaging to fluoroscopy to cone-beam CT or optically detecting body surface and can follow procedures as simple as using a single set-up image or as complex as intra-fractional tumour tracking [Verellen *et al.* 2007]. Moreover, the number and moment of imaging steps for position verification can be varied. In this sense, set-up position verification for IGRT can be grossly classified as “offline” or “online”. The offline approach monitors the position of the patient during a limited number of fractions and adapts the safety margins and treatment plan. Offline approaches are designed to correct for inter-fractional positioning errors. The online approach requires continuous quantification and correction of the target position. Online set-up correction schemes can be designed to account for intra-fraction positioning errors. In principle, online correction can achieve ideal alignment of planned and irradiated anatomy assuming that body deformation did not take place. Nevertheless, the use of online position verification schemes can result in longer fraction time (considering the patient preparation during the total time of a fraction) and increased radiation burden to the patient [Verellen *et al.* 2008].

During IGRT, an assumption is usually made: positioning errors can be corrected only with rigid transformations via table shifts and, if available, rotations. Unfortunately, such rigid body corrections are sometimes a simplification of the needed corrections since non-rigid motion may occur for the target structures. In these cases, replanning may be necessary. Even if it may be a simplified correction, it has been demonstrated that in most body sites, IGRT reduces the set-up error and irradiated volume of healthy tissue adjacent to the target. [Dawson & Jaffray 2007].

1.3 RADIOTHERAPY FOR PROSTATE CANCER PATIENTS

In Western countries, prostate cancer is one of the most commonly diagnosed cancer in men. To place the situation into perspective, more than 20% of the 840 thousand new cases of cancer registered in 2016 in the United States of America³ were prostate cancer cases [Siegel *et al.* 2016]. Several possibilities are available for primary treatment, of which prostatectomy is the most elected option [Cooperberg *et al.* 2010]. However, a recent study showed that the outcome of prostatectomy against radiotherapy did not substantially differ [Grimm *et al.* 2012], making the analysis of the side-effects decisive for an evidence-based choice of the treatment. In this sense, radiotherapy becomes a favourable option [Zelevsky *et al.* 2008]. Intensity-modulated radiotherapy (IMRT), with or without IGRT, is considered being the gold standard according to the guidelines recently released by the European Association of Urology, the European Society of Radiotherapy and Oncology and the Society of Geriatric Oncology [Mottet *et al.* 2017]. In classical IMRT treatments, a dose between 64 and 72 Gy is generally prescribed, but dose-escalated IMRT regimens with a prescription of 74-78 Gy delivered in 2 Gy/fraction also results in effective treatments [Kalbasi *et al.* 2015]. However, this has not translated into an overall survival advantage for all the patient risk-groups

³The male population of the States in 2016 was about 324 million people according to www.census.gov/popclock



Figure 1.3 Comparison of axial CT (left), 2D T2 weighted fast spin echo MRI (centre) and 3D balanced fat-suppressed gradient-echo MRI sequence (centre and right) images used in UMC Utrecht for treatment planning. In the MR image, the internal structure of the prostate is readily apparent, while on CT bones and the intraprostatic fiducial marker are clearly visible.

when compared to lower doses [The Royal College of Radiologists 2016]. Based on biological modelling, hypofractionated regimes have also been proposed. For example, a fractionation regime delivering 60 Gy in 20 fractions was demonstrated being non-inferior to 74 Gy in 37 fractions [Dearnaley *et al.* 2016]. In addition, thanks to the theoretical advantages in dose deposition, also proton therapy has been adopted. However, preliminary results seem to favour IMRT over proton therapy in terms of treatment-related side-effects [Kim *et al.* 2011, Goldin *et al.* 2012].

The accuracy of dose delivery in radiotherapy is limited by multiple factors: organ delineation, set-up error and inter-/intra-fraction organ motion [Kupelian & Meyer 2011]. In this sense, IGRT plays a fundamental role in ensuring the delivery of an accurate treatment [Verellen *et al.* 2007] aiming at compensating inter- and intra-fractional variations occurring over the course of the treatment [Tree *et al.* 2012, McPartlin *et al.* 2016]. In particular, use of cone beam CT images or prostate surrogates, e.g. fiducial markers (FMs) is suggested [The Royal College of Radiologists 2016] for positioning verification to minimise inter-fraction motion [Zelefsky *et al.* 2012, Singh *et al.* 2013].

1.3.1 Magnetic resonance imaging in radiotherapy

Advances in imaging techniques in the last decades impacted radiotherapy treatment strategies enormously [Verellen *et al.* 2008]. CT is considered the primary modality in radiotherapy, being able to provide a patient model for treatment planning. Nevertheless, we can observe that MRI is increasingly used in radiotherapy planning, especially for delineation, owing to its superior soft-tissue contrast compared with CT [Metcalf *et al.* 2013, Ménard & van der Heide 2014, Schmidt & Payne 2015].

Since the prostate is a gland constituted of soft tissue, the advantage of using MRI for radiotherapy is recognised [Dirix *et al.* 2014]. As a direct example, Figure 1.3 illustrates the difference between CT and MR images of the prostate. In the CT scan, the boundaries of the prostate are hard to identify, whereas in the MR image not only the prostate boundary but also the internal structure of peripheral zone and the central gland are easily observed. This is of primary importance for

radiotherapy since it facilitates target delineation that has been considered as “the weakest link in radiotherapy accuracy” [Njeh 2008], or as the “major source of error in prostate external beam radiation treatment” [Rasch *et al.* 1999]. Owing to the better tissue contrast, MRI was able to reduce the target volume by about 30% compared to CT and reduce inter-observer variability [Rasch *et al.* 1999, Roach *et al.* 1996, Villeirs *et al.* 2005] preserving clinical outcomes [Sander *et al.* 2014]. In addition, MRI offers access to diverse tissue contrast when recurring to different MR sequences, as presented in Figure 1.3. Moreover, imaging, e.g. perfusion, diffusion or functional MRI, has also been introduced. The use of multiple functional and quantitative MRI techniques, known as multiparametric-MRI, has shown promising results in diagnosis, delineation, risk stratification and staging of clinically significant prostate cancer [Thompson *et al.* 2013]. In particular, for prostate cancer treatment, MR-simulations including T2-weighted, diffusion and perfusion imaging were recommended [Barentsz *et al.* 2012] offering a precise definition of tumours and the prostate itself [Sefrova *et al.* 2012, McLaughlin *et al.* 2005]. Such a precise definition has also opened up opportunities for focal treatment of prostate cancer [Sciarra *et al.* 2011, Hegde *et al.* 2013] or the additional possibility of targeting a boost dose to this region [Pouliot *et al.* 2004, Riches *et al.* 2014] when one or more of the dominant intraprostatic lesions are seen.

MRI uses non-ionising radio waves, unlike CT which uses ionising radiation. In this sense, MRI can be of particular benefit for paediatric populations in which radiation dose needs to be carefully controlled. Also, MRI is favourable in cases where repeated scanning can be of help during treatment both to ensure that the treatment plan is revised to follow radiation-induced tissue changes and monitor early response [Schmidt & Payne 2015]. For an effective integration of MRI into the planning process, MR images are registered to CT images such that the delineations can be transferred from MRI to CT [Khoo & Joon 2006]. A schematic overview of an integrated CT/MRI pathway is presented in Figure 1.4.

Unfortunately, image registration potentially causes systematic spatial uncertainties and introduces errors during radiotherapy treatment planning since CT and MR are acquired at a different moment and potentially affected by set-up differences [Nyholm *et al.* 2009].

To minimise the uncertainties and errors coming from possible set-up differences, the so-called “MR-simulators” have been developed. From a historical perspective, MR scanners were initially designed to accommodate **diagnostic** needs. For such a scope, the standard size of the bore of MR scanners was 60 cm. When assuming a **therapeutic** perspective for radiotherapy treatments, such bore size does not facilitate scanning the patient in treatment position. In addition, diagnostic MRI beds were equipped with soft padding, sometimes concave, to ensure patient comfort over the duration of an MRI examination. Such a configuration is not necessarily compatible with positions used during irradiations since they are typically flat [Schmidt & Payne 2015].

Recently, after the first investigation performed by a Japanese group as early as 1993 [Okamoto *et al.* 1993, Mizowaki *et al.* 1996], the MR vendors responded to the radiotherapy demand producing wide bores (70 cm) MRI-simulators [Devic 2012, Metcalfe *et al.* 2013], which can be equipped of flat table tops [Mcjury *et al.* 2011]. The scanners have also been equipped with coil support to avoid compression of

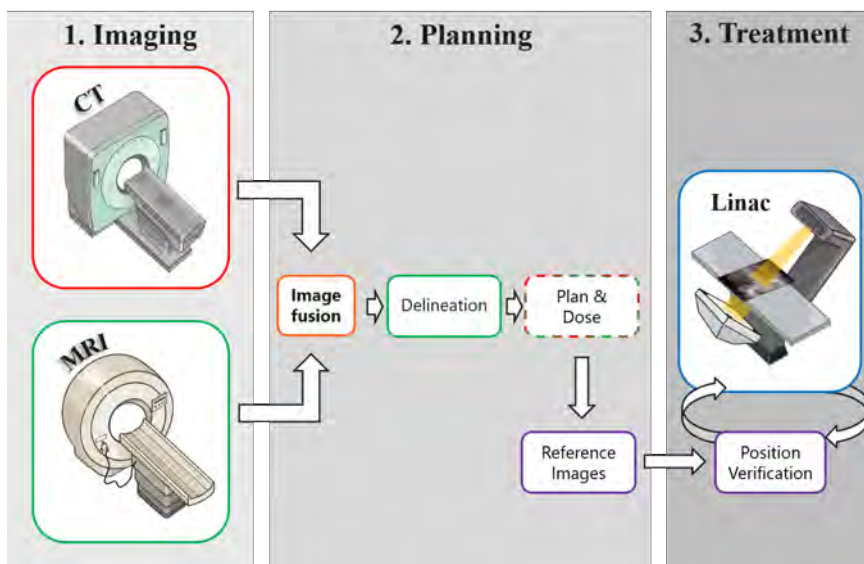


Figure 1.4 Schematic overview of a radiotherapy pathway for prostate cancer treatments showing the integration of CT and MR imaging. CT and MR images are acquired and registered such that delineation can be performed on them. Dose calculation relies on CT images since they provide electron density information. Moreover, CT images produce the reference position used during irradiation.

patient contours and with laser systems to facilitate the RTTs during the patient positioning [Low 2017 (Chapter MRI Guided Radiotherapy)].

1.3.2 MRI-based treatment planning & its challenges

The use of MR-simulators has ameliorated consistency of patient positioning between CT and MR imaging sessions. However, using an MR-simulator cannot ensure lack of inter-scan differences between the two imaging sessions.

To remove potential inter-scan differences “MR-only radiotherapy” has been proposed [Ramsey & Oliver 1998, Beavis *et al.* 1998, Khoo *et al.* 1997, Lee *et al.* 2003]. In MR-only radiotherapy, sole MR images are used for delineation and dose planning. To facilitate the understanding of an MR-only pathway, a schematic representation of an MR-only treatment is presented in Figure 1.5. With MR-only radiotherapy, inter-modality image registration can be avoided, potentially reducing systematic errors [Nyholm *et al.* 2009]. In addition, MR-only radiotherapy offers practical and logistical advantages: the radiotherapy pathway can be simplified reducing the overall treatment cost [Devic 2012] and workload [Karlsson *et al.* 2009]. Moreover, patient exposure to ionising radiation can be lowered, which is particularly important when several re-plans have to be made or in specific patient groups, such as children [Schmidt & Payne 2015].

MR-only is also of interest considering the advent of MRI-guided radiotherapy (MRIgRT) systems [Lagendijk *et al.* 2014]. With MRIgRT, MRI and linacs or radioactive sources have been integrated [Raaymakers *et al.* 2004, Dempsey *et al.* 2005, Fallone *et al.* 2009, Karlsson *et al.* 2009, Raaymakers *et al.* 2017] such that MR

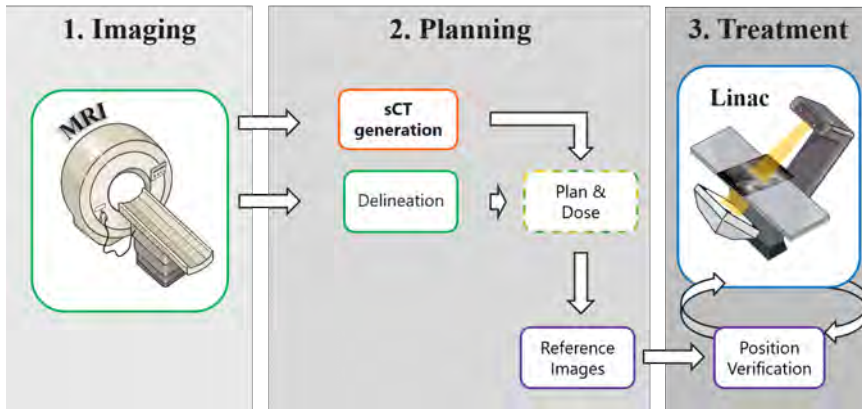


Figure 1.5 Schematic overview of an MR-only radiotherapy pathway. MRI is the primary imaging modality and it is used for delineation and generating synthetic CT (sCT) images, which enable MR-based dose calculations. MRI-based images can be then used as a reference for position verification purposes.

images can be used for patient set-up correction based on soft tissues monitoring and adapting to tumour movements between radiation fractions (inter-fraction motion) or during irradiation (intra-fraction motion).

The introduction of an MR-only radiotherapy pathway raises a series of challenges, which are presented in the following paragraphs.

MR-BASED DOSE CALCULATIONS Voxel intensity of MR images depends on proton density tissue and the nuclear magnetic relaxation [McRobbie *et al.* 2006, Brown *et al.* 2014]. No physically justifiable correlation has been reported between the nuclear magnetic tissue properties and the radiological properties that are necessary to model radiation attenuation in a human being. This means that dose calculations cannot be performed directly on MR images. From 1997 onwards [Khoo *et al.* 1997, Beavis *et al.* 1998, Ramsey & Oliver 1998], researchers started to investigate whether this lack of physical relationship may be otherwise overcome. Methods have been developed aiming to generate the so-called “synthetic CT”, “substitute CT” or “pseudo CT” images⁴ that should enable accurate MR-based dose calculations. In this thesis, the term synthetic CT (sCT) will be used to avoid confusion between acronyms of pseudo-CT and planning CT and adhering to the convention adopted by the European Society for Radiation Oncology. As pointed out in a recent review on the topic [Edmund & Nyholm 2017], more than fifty methods have been proposed up to November 2015. Following and extending the classification of sCT generation methods proposed by Edmund & Nyholm, sCT generation methods can be classified into four classes:

- **Atlas-based** approaches focus on aligning through registration the MR images of a single patient to the corresponding CT images in an atlas;

⁴No agreement among in the nomenclature has been reached in literature. However, the name “synthetic CT” has been chosen for this thesis. Note that the chapters of the thesis were revised to adhere to such a choice, even if in the original version pseudo-CT was chosen.

- **Voxel-based** approaches primarily use information about voxel intensities in the MR images to assign HU or electron densities;
- **Bulk assignment** approaches, where the sCT images are generated after segmentation of MR images in tissue classes and assignment of synthetic-HU to the classes;
- **Hybrid** approaches combine categories of the voxel-, atlas-, or bulk assignment-based methods.

To offer an overview of the MR-based dose calculation evaluated up to now (December 2017) for the treatment of prostate cases, Table 1.1 has been compiled complementing the list of methods along with the performance metrics presented by Edmund & Nyholm [Edmund & Nyholm 2017]. For prostate radiotherapy, sCT generation generally enables dose calculation with a deviation of maximum Table 1.1 Overview of sCT generation approaches for prostate radiotherapy, along with their performances in terms of percent dose difference (DD), mean absolute error (MAE) and gamma pass rate on gamma 2%,2mm (if not differently specified). For each approach, the classification class, type of radiation involved - photon (γ) or proton (p) -, the number of patients included in the study and the associated reference have been specified.

Approach	Radiation	Pt	Performance metrics			Reference
			DD [%]	MAE [HU]	$\gamma_{2\%,2mm}$ [%]	
bulk	γ	5	<2			[Lee <i>et al.</i> 2003]
bulk	γ	15	<2.5			[Chen <i>et al.</i> 2004]
bulk	γ	10	<1			[Eilertsen <i>et al.</i> 2008]
bulk	γ	10	<1			[Jonsson <i>et al.</i> 2010]
bulk	γ	39	1.3			[Lambert <i>et al.</i> 2011]
bulk	γ	21	<2			[Korsholm <i>et al.</i> 2014]
bulk	γ	10	<1			[Doemer <i>et al.</i> 2015]
atlas	γ	37	1.5			[Dowling <i>et al.</i> 2012]
atlas	γ	39	0.3	40.5	100	[Dowling <i>et al.</i> 2015]
atlas	γ	15	<0.7	50	97.1	[Guerreiro <i>et al.</i> 2017]
hybrid	γ	39	0.3	108	99.6/94.2 ^a	[Ghose <i>et al.</i> 2017]
voxel	γ	15	<1		97 ^a	[Kim <i>et al.</i> 2015]
voxel	γ	10	0.4	54	99/97 ^a	[Andreasen <i>et al.</i> 2016]
voxel	γ	10	<0.8		>99/93 ^a	[Korhonen <i>et al.</i> 2014]
voxel	γ	15	0.2		>99	[Korhonen <i>et al.</i> 014b]
voxel	p	10	0.6	42	98.6/95 ^a	[Koivula <i>et al.</i> 2016]
voxel	γ	35	0.3-2	135	93 ^a	[Koivula <i>et al.</i> 2017]
Vendors' solutions						
hybrid	γ	10	0.4	36.5	99.9 ^b	[Siverson <i>et al.</i> 2015]
hybrid	γ	170	0.3		99.1	[Persson <i>et al.</i> 2017]
bulk ^c	γ	25	<0.6			[Tyagi <i>et al.</i> 2016]
bulk ^c	γ	5	0.7		100/99.1 ^a	[Kempainen <i>et al.</i> 2017]
bulk ^c	γ	29			99.8/97.3 ^a	[Christiansen <i>et al.</i> 2017]

^a $\gamma_{1\%,1mm}$; ^b $\gamma_{2\%,1mm}$; ^cBulk assignment using a model for bone segmentation.

2% when compared to CT-based dose calculations (see Table 1.1). Some methods were so promising that they have been adopted in the clinical practice. For example, in 2014, the Helsinki hospital started treating prostate cancer patients with an MR-only radiotherapy pathway for the first time. To generate sCT images, an in-house approach was developed by Korhonen and coworkers [Korhonen *et al.* 2016]. Since 2016, vendors can provide certified solutions that may enable MR-based dose calculations⁵ for the sole prostate cancer radiotherapy. The arrival of certified solutions facilitated the spread of an MR-only pathway [Persson *et al.* 2017, Tyagi *et al.* 2017]. However, an institution interested in introducing an MR-only planning solution into the clinic still needs to perform an internal assessment to ensure the dosimetric accuracy of the treatment [Korsholm *et al.* 2014, Schmidt & Payne 2015] in its pathway.

MRI GEOMETRIC INACCURACY MR images may be compromised by geometric distortions caused by the system (system-related distortions) and the patient (patient-induced distortions) [Jezzard 2000, Fransson *et al.* 2001, Walker *et al.* 2014]. This may impact accuracy of MR-based dose calculation as well as the spatial accuracy of MR-based delineations. To correct for system-related distortions, modern scanners are equipped with state-of-art gradient systems, where geometric inhomogeneities have been minimised [Devic 2012]. The scanners are also equipped with software for further correcting the images [Schmidt & Payne 2015]. Displacements after the corrections reach a maximum of 2-3 mm on the outer edges of the scan volume [Wang *et al.* 2004]. Considering that system-related distortions increase with the distance to the isocentre of the magnet of the scanner, distortions may be even lower in the proximity of a target structure, when it is correctly positioned in the scanner. Patient-induced distortions can be larger than residual system distortions after using vendor supplied 3D correction. They may be mitigated by careful choice of scan parameters, e.g. high bandwidth and low slice thickness, ensuring the spatial geometric accuracy of MR images used for delineation or sCT generation [Devic 2012, Stanescu *et al.* 2012]. In particular, it has been shown that proper choice of scan parameters can result in dose errors below 0.5% [Adjeiwaah *et al.* 2017].

DELINEATIONS ON MR IMAGES In hybrid CT/MRI simulation pathways, MR images are used to perform target delineations [Dirix *et al.* 2014]. In an MR-only pathway, MR images should also be used for OARs delineations. Given the superb soft tissue contrast of MR images, it is possible to hypothesise that MRI enables OARs delineation. However, the field of view (FOV) acquired for diagnostic purposes is generally too small to include all the OARs. This implies that institutes should revise their MR protocols to meet the needs of radiotherapy [Schmidt & Payne 2015]. Revising MR protocols can be challenging because there is no clear consensus about which MR sequences should be used for such a scope, and no guidelines are available to facilitate delineations of the OARs. Moreover, given the fact that system-related geometric distortion scales with the distance to the

⁵Royal Philips (The Netherlands) developed the so-called MR for calculating attenuation (MRCAT) announcing its European Conformity (CE) and approval from the Food and Drug Administration (FDA) on 2016-03-21 goo.gl/jtyX8H, while Spectronic Medical AB (Sweden) announced that their solution called MriPlanner received a CE mark approval and a FDA k510 was on 2016-06-16 <https://goo.gl/cY5Zrn>.

scanner isocentre, OARs may be distorted in case attention is not dedicated to the geometric fidelity of the MR sequences.

MRI AS THE REFERENCE FOR SET-UP CORRECTIONS In an MR-only pathway, MR or sCT images are used to calculate patient set-up corrections. MR or sCT images may be designed according to the IGRT techniques adopted [Das *et al.* 2014, Nabavizadeh *et al.* 2016]. IGRT for prostate cancer can be performed based on the location of the prostate itself (usually using cone beam CT), anatomical landmarks, or prostate surrogates, e.g. intraprostatic gold FMs and implanted electromagnetic transponders [Bujold *et al.* 2012, Ng *et al.* 2014, Zaorsky *et al.* 2017]. Most of the MR-only oriented investigations so far have focused on the MR-based generation of digitally reconstructed radiographs for bone alignment [Chen *et al.* 2004, Dowling *et al.* 2012, Korhonen *et al.* 2014, Kim *et al.* 2015, Tyagi *et al.* 2016]. However, it has been shown that bone-based landmarks represent an unreliable surrogate of the true prostate position due to the motion of the prostate with respect to the pelvic bones [Schallenkamp *et al.* 2005], demanding larger PTV margin recipes with respect to FM-based alignment [Beard *et al.* 1996, van Herk *et al.* 1995, Greer *et al.* 2008]. Therefore, MR-based localisation of gold FM is crucial for accurate position verification of prostate IGRT.

1.4 OBJECTIVES AND OUTLINE

This thesis aims at investigating strategies to achieve accurate MRI-based prostate radiotherapy to facilitate future clinical implementation of an MR-only pathway within the University Medical Center Utrecht. The thesis is composed of two parts both comprehending two chapters.

Part I, comprising of Chapter 2 and 3, focuses on the evaluation of the dosimetric accuracy obtainable during MR-based planning studies. Embracing the clinical perspective, the accuracy of MR-based dose calculation has been investigated using a commercially available solution for sCT generation called MRCAT (Philips Healthcare, The Netherlands).

Chapter 2 deals with MR-based dose calculation for photon radiotherapy. The feasibility of MR-based photon radiotherapy was assessed proposing an approach to disentangle and quantify factors that possibly confound dose comparison studies that assess CT and MR-based dose calculations.

Chapter 3 investigates whether the commercially available sCT generation solution adopted at the University Medical Center Utrecht enables MR-based dose calculation also for proton prostate radiotherapy. A retrospective study is presented assessing sCT-based dose calculations in terms of dose difference, gamma pass rates and proton range difference against CT-based dose planning.

Part II, comprising of Chapter 4 and 5, assesses whether accurate IGRT is feasible when patient setup correction relies solely on MRI as a reference imaging modality. At the University Medical Center Utrecht, intraprostatic gold FMs are currently employed. Therefore, this part focuses on MR-based FM localisation.

In **Chapter 4** a new method to perform automatic localisation of the FMs on MR images is presented. The method requires the use of a priori information, like the MRI sequence and the size/shape of the used FMs. A simulation is performed to generate a template of the marker to be used with a generic voxelwise

template matching technique. A criterion is proposed to select possible FM candidates among voxels showing correlations between the template and MR images. The localisation performances of the methods are evaluated in terms of spatial accuracy, precision and in terms of missed localisations.

Chapter 5 investigates manual localisation performances when FM localisation cannot be performed with the aid of CT images and without the aid of an automatic method. Such a scenario is generally considered as reliable for localisation of the markers. To test this hypothesis, an inter-observer study was designed and conducted among RTTs investigating the use of different MR sequences. The results for the different scenarios are reported in terms of precision, accuracy and agreement among observers.

Finally, the most relevant findings of this work are summarised in **Chapter 6** as well as the contributions of this work are discussed. The perspective of a clinic interested in introducing an MR-only radiotherapy pathway is adopted through the discussion. To conclude, possible future perspectives are examined.

Part I

Dose Calculation

Synthetic CT for photon radiotherapy

2

This chapter is based on:

Maspero, M., Seevinck, P. R., Schubert, G., Hoesl, M. A. U., van Asselen, B., Viergever, M. A., Lagendijk, J. J. W., Meijer, G. J., & van den Berg, C. A. T. (2017). **Quantification of confounding factors in MRI-based dose calculations as applied to prostate IMRT.** *Phys. Med. Biol.*, 62(3), 948-965 <http://dx.doi.org/10.1088/1361-6560/aa4fe7> [Maspero *et al.* 2017].

Abstract

Background Magnetic resonance (MR)-only radiotherapy treatment planning requires synthetic CT (sCT) images to enable MR-based dose calculations. To verify the accuracy of MR-based dose calculations, institutions interested in introducing MR-only planning needs to compare sCT-based and computed tomography (CT)-based dose calculations. However, interpreting such comparison studies may be challenging, since potential differences arise from a range of confounding factors which are not necessarily specific to MR-only planning. Therefore, the aim of this study is to identify and quantify the contribution of factors confounding dosimetric accuracy estimation in comparison studies between CT and sCT. The following factors were distinguished: set-up and positioning differences between imaging sessions, MR-related geometric inaccuracy, sCT generation, use of specific calibration curves to convert sCT into electron density information, and registration errors.

Methods The study comprised fourteen prostate cancer patients who underwent CT/MR-based treatment planning. To enable sCT generation, a commercial solution called MR for calculating attenuation (MRCAT) (Philips Healthcare, Vantaa, Finland) was adopted. Intensity-modulated radiotherapy (IMRT) plans were calculated on CT (gold standard) and sCT images. Dose difference maps in a high dose region (clinical target volume (CTV)) and in the body volume were evaluated, and the contribution to dose errors of possible confounding factors was individually quantified.

Results We found that the largest confounding factor leading to dose difference was the use of different calibration curves to convert sCT and CT into electron density (0.7%). The second largest factor was the stratification of sCT images into a fixed number of tissue classes (0.16%). Inter-scan differences due to patient repositioning, MR-related geometric inaccuracy, and registration errors did not significantly contribute to dose differences (0.01%).

Conclusion The proposed approach successfully identified and quantified the factors confounding accurate MR-based dose calculation in the prostate. This study will be valuable for institutions interested in introducing MR-only dose planning in their clinical practice.

Keywords: **magnetic resonance, radiotherapy planning, dosimetry, mr-only treatment planning, intensity modulated radiotherapy, quality assurance**

2.1 INTRODUCTION

In (external beam) radiotherapy, computed tomography (CT) is the primary imaging modality for treatment planning [Chernak *et al.* 1975, Pereira *et al.* 2014], since it enables precise calculation of dose distributions [Seco & Evans 2006, Skrzyski *et al.* 2010, Brock & Dawson 2014], and provides reference images allowing for pre-treatment positioning [Van den Berge *et al.* 2000].

In the last few decades, magnetic resonance imaging (MRI) has found its way into the radiotherapy workflow as it provides superior soft tissue contrast with respect to CT [Debois *et al.* 1999, Dirix *et al.* 2014], thus enabling more accurate delineation of target regions and critical structures [Roach *et al.* 1996, Rasch *et al.* 1999, Villeirs *et al.* 2005].

To benefit from the advantages offered by both imaging modalities, magnetic resonance (MR) images are nowadays fused to CT images to transfer target and organ at risk contours [Khoo *et al.* 1997, Schmidt & Payne 2015, Paulson *et al.* 2015]. However, image fusion potentially causes systematic spatial uncertainties and introduces errors during radiotherapy treatment planning [Nyholm *et al.* 2009, Karlsson *et al.* 2009]. To minimise these uncertainties and errors, an MR-only based workflow has been proposed [Fraass *et al.* 1987, Lee *et al.* 2003, Nyholm & Jonsson 2014], aiming at prevention of inter-modality registration errors [Nyholm *et al.* 2009]. Furthermore, an MR-only based workflow will result in practical and logistical advantages: it can simplify the workflow and reduce the overall treatment cost [Devic 2012] and workload [Karlsson *et al.* 2009], and it can decrease exposure to ionising radiation, which is particularly important when several replans have to be made [Kapanen *et al.* 2013].

Additionally, based on the growing importance of the exclusive use of MRI in radiotherapy [Raaymakers *et al.* 2004, Dempsey *et al.* 2005, Fallone *et al.* 2009, Karlsson *et al.* 2009], we foresee that MR-based dose calculations will also be of increasing importance to radiotherapy.

The main obstacle regarding the introduction of MR-only radiotherapy is the lack of tissue attenuation information, which is required for accurate dose calculations [Nyholm *et al.* 2009, Jonsson *et al.* 2010]. To estimate tissue attenuation properties from MRI, several methods have been proposed in the last few decades [Lee *et al.* 2003, Chen *et al.* 2004, Schmidt & Payne 2015, Prior *et al.* 2016]. More recently, MRI vendors have launched solutions as well [Schadewaldt *et al.* 2014, Siverson *et al.* 2015]. The proposed methods can be categorised into three classes [Prior *et al.* 2016]: (1) atlas-based, (2) voxel-based or (3) bulk assignment-based techniques. Along with these techniques, several names have been used all referring to MR-based tissue attenuation maps, e.g. synthetic-CT [Kim *et al.* 2015, Siverson *et al.* 2015], pseudo-CT [Dowling *et al.* 2012, Korhonen *et al.* 2014], and substitute-CT [Johansson *et al.* 2012]. For clarity, without differentiating among generation techniques, the term synthetic CT (sCT) will be used to refer to the tissue attenuation equivalent images, and “synthetic-HU” to indicate the assigned hounsfield unit (HU) values.

An institution interested in introducing an MR-only planning solution into the clinic will face the challenge of determining the accuracy of the MR-based dose planning with respect to the gold standard CT planning [Korsholm *et al.* 2014,

Schmidt & Payne 2015]. Based on the quantitative outcome of a comparison study an institute should decide whether the MR-based planning accuracy is acceptable. Very likely, such a comparison study may result in observed dose differences [Lee *et al.* 2003, Chen *et al.* 2004, Dowling *et al.* 2012, Johansson *et al.* 2012, Korhonen *et al.* 2014, Kim *et al.* 2015, Schadevaldt *et al.* 2014, Siversson *et al.* 2015, Prior *et al.* 2016]. To understand and gauge the potential impact of these differences, and thus, possibly facilitate institutions to reduce them (reducing in this way overall treatment inaccuracies), it is important to understand their origin. Differences may have origin other than the adopted sCT generation technique [Siversson *et al.* 2015, Sun *et al.* 2015]. In particular, considering the treatment planning workflow, such differences originate from the following processes: image acquisition, image processing for sCT generation, and dose calculations. In each individual process we hypothesise that at least one among the following four confounding factors will contribute to the observed dose differences between plan generated using CT and sCT:

- (1) **Set-up & positioning differences.** During image acquisition the patient is repositioned between CT and MR imaging sessions. To minimise possible positioning differences between imaging sessions, the use of a flat table top [Mcjury *et al.* 2011], coil supports [Kapanen *et al.* 2013, Sun *et al.* 2014], and positioning devices such as lasers [Schmidt & Payne 2015] at MR scanner (and also CT scanner) are generally used. We refer to this set-up configuration as “MR simulator”. However, even if an MR simulator is employed, differences in patient positioning, and possible set-up errors may occur [van Herk *et al.* 1995].
- (2) **MR-related geometric inaccuracy.** MR image acquisition may be compromised by geometric distortions caused by the system and/or patient [Fransson *et al.* 2001, Walker *et al.* 2014]. Modern scanners are equipped with solutions [Schmidt & Payne 2015] that limit system-related displacements to 2-3 mm on the outer edges of a clinically relevant volume of approximately 25x25x25 cm³ [Wang *et al.* 2004]. Patient-related distortion may be mitigated by careful choice of scan parameters, e.g. bandwidth and slice thickness, ensuring spatial geometric accuracy of MR images [Stanescu *et al.* 2012]. Nonetheless, residual distortions may still be among the potential factors that confound the accuracy of sCT-based dose calculations.
- (3) **Synthetic-CT generation.** This factor solely originates from the sCT generation method used. All the sCT generation techniques (atlas-based, voxel-based or bulk assignment-based) assign HU voxel values that may differ with respect to the corresponding voxel on CT (assuming spatial relationship), thus contributing to observed dose differences.
- (4) **Electron density conversion.** To enable dose calculations, electron density information is derived from tissue attenuation equivalent data (CT or sCT). In particular, for radiotherapy planning, each CT scanner is calibrated such that HU can be converted into electron density by using a calibration curve derived from literature [Knöös *et al.* 1986, IAEA 2008], or by using a one-to-one relationship obtained from a phantom made of tissue equivalent mate-

rials [Constantinou *et al.* 1992]. The use of different phantoms (usually the phantoms differ in the high HU region due to the use of slightly different bone-like materials) to calibrate CT scanners can result in dose differences up to 1% [Thomas 1999]. If a sCT generation method assigns HU, it may implicitly assume also a certain calibration curve for electron density conversion [Lee *et al.* 2003, Jonsson *et al.* 2010, Lambert *et al.* 2011]. The assumed conversion curve may differ from the one clinically adopted for CT images, thus contributing to observed dose differences.

Moreover, when comparing the output of dose calculations, another factor could contribute to observed dose differences:

- (5) **Registration errors.** During dose comparisons it may be necessary to align the spatial coordinates of CT and sCT. When registrations are performed, registration errors may play a role in differences between doses calculated on CT and sCT [Roberson *et al.* 2005, Nyholm *et al.* 2009].

Factors (1), (2) and (5) together with internal motion may result in *inter-scan differences* between imaging sessions in the case that one session is performed at an MR scanner.

This work aims to quantify the possible contributions of *inter-scan differences* (as combination of 1, 2 and 5), *synthetic-CT generation* (3), and *electron density conversion* (4) to dose differences between CT- and sCT-based dose calculations. The effects of the different factors were isolated by the specific design of the approach: CT-based sCT images were generated to circumvent the presence of inter-scan differences, as these differences are independent of the synthetic-HU values assigned by the sCT generation method. This study will focus on the pelvic area, with particular attention to prostate radiotherapy treatments.

2.2 MATERIALS AND METHODS

We conducted a study using data from prostate cancer patients undergoing external beam radiotherapy to compare CT/MR-based and MR-only based dose calculations. The study is divided into five parts. First, we acquired CT and MR images (Section 2.2.1). Second, we generated a series of CT- and MR-based sCT images which allows disentanglement of the confounding factors hypothesised in Section 2.1 (Section 2.2.2). Third, we performed dose planning on sCT images (Section 2.2.3). Fourth, we evaluated the body contour differences between the CT-based and MR-based sCT images (Sections 2.2.4). Finally, we quantified the impact of possible confounding factors on dose calculations (Sections 2.2.5).

2.2.1 Patient data collection

In the first part of the study we collected data of fourteen prostate cancer patients (57.7-80.2 yr old) who underwent standard treatment planning between November and December 2015. As part of the treatment planning, gold fiducial markers (HA2 Medizintechnik GmbH, Germany) were transperineally implanted for position verification purposes one week before acquisition of planning images. The

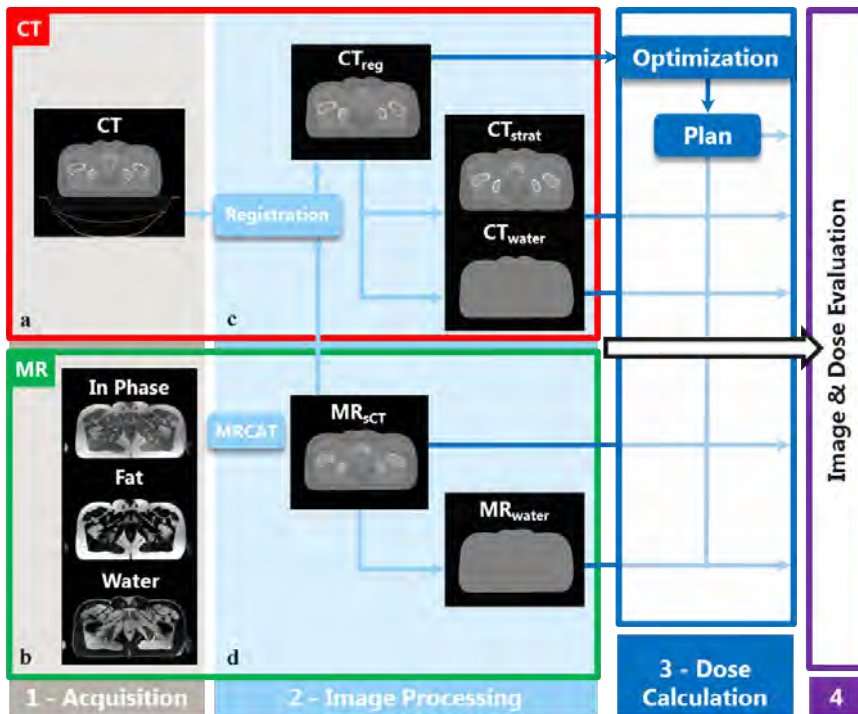


Figure 2.1 **Schematic of the study.** After patient data collection [1] on CT (a) and MR(b), via image processing [2] three CT-based sCT datasets (c), and two MR-based sCT datasets (d) were produced. CT-based sCT generation (c) was performed after image registration and couch removal (CT_{reg}) to obtain a dataset similar to MR_{sCT} (CT_{strat}) and a homogeneous water density dataset (CT_{water}). MR-based sCT images (d) were generated using the MRCAT method (MR_{sCT}), and, from its body contour, a homogeneous water density dataset (MR_{water}) was created. Planning and dose calculations [3] followed the sCT generation, and finally image and dose evaluation [4] was performed to disentangle and quantify possible confounding factors.

data collection was conducted following the local statutory requirements, and in accordance with the local medical ethical guidelines.

Image acquisition

The patients underwent a CT scan (Brilliance CT Big Bore Oncology, Philips Healthcare, Best, The Netherlands - Figure 2.1a) and a 3 T MR scan (Ingenia - 70 cm wide bore, Philips Healthcare, Best, The Netherlands - Figure 2.1b) as part of clinical treatment planning. CT scans were performed with the following imaging parameters: 120 kV, exposure time = 923 ms, tube current between 121 and 183 mA, in-plane matrix of 512×512 pixels, and 3 mm slice thickness. The resolution was variable depending on the field of view (FOV) used. The typical size of the FOV was $500 \times 500 \times 300 \text{ mm}^3$, which corresponds to an in-plane resolution of $0.98 \times 0.98 \text{ mm}^2$.

MR scans were carried out 1-2 hours after CT scans. To simulate treatment positioning, the patients were marked with three skin tattoos at the CT scanner, and the position of the tattoos was used to reposition the patient at the MR scanner. To facilitate patient positioning, the MR scanner was equipped with an external laser positioning device (Dorado 3, LAP GmbH Laser Applikationen, Lueneburg, Germany), an in-house-built flat table top. Also, liquid fiducial markers (PinPoint ref 128, Beekley Medical, Bristol, CT, USA) aided the operator at the MR scanner during patient positioning. Patients were scanned using anterior and posterior coils (dS Torso and Posterior coils, Philips Healthcare, Best, The Netherlands). To avoid compression of patients, two in-house-built coil bridges supported the anterior coil.

To generate MR-based sCT images, a two echoes three-dimensional (3D) Cartesian radio-frequency (RF) spoiled gradient-recalled echo (SPGR) sequence was added to the standard MR exam. In particular, two images were acquired with the following imaging parameters: echo times = 1.21/2.53 ms, repetition time = 3.93 ms, flip angle = 10° , FOV = $477 \times 477 \times 300$ mm³, acquisition matrix = $248 \times 281 \times 120$, reconstructed matrix = $480 \times 480 \times 120$, bandwidth = 1083 Hz, and acquisition time of 2 min 13 s. A Dixon [Dixon 1984] reconstruction [Eggers *et al.* 2011] was performed to obtain in-phase, fat, and water images (Figure 2.1b).

2.2.2 Image processing for sCT generation

In the second part of the study, we generated five image datasets (Figure 2.1c,d) comprising two sCT datasets based on MR images (Figure 2.1c), one registered CT, and two MRI datasets based on CT data (Figure 2.1d), for all fourteen patients. Each sCT dataset was generated with a specific goal, as described below.

To enable MR-only dose planning, we generated sCT using a vendor solution tailored to prostate patients which is called MRCAT (prototype rev. 257, Philips Healthcare, Vantaa, Finland). MRCAT is a bulk assignment sCT generation method based on sequential intensity- and model-based segmentation techniques [Schadewaldt *et al.* 2014]. In particular, MRCAT segments images from a dedicated MR sequence (see Section 2.2.1) into five classes, and assigns to each class the synthetic-HU specified in Table 2.1. MRCAT uses a constrained shape model to estimate body contour and to segment bone structures. Within the bone structures two classes are assigned: spongy and compact bone. Similarly, soft tissue structures are assigned either fat or muscle. MRCAT does not recognise gold fiducial markers implanted in the patients, and classifies them as soft tissue. Furthermore, MRCAT produces images with no air compartments within the body contour. As MRCAT converts synthetic-HU in electron density using a vendor specific curve, MRCAT can be considered an electron density map generation method. The term MR_{sCT} (Figure 2.1d) was used to refer to the dataset produced by MRCAT.

To align the spatial coordinates of the CT with the MR, and to minimise positioning errors, the CT was rigidly registered and resampled to the MR_{sCT}. We considered MR_{sCT} as a fixed image to prevent changes of the synthetic-HU values during the resampling. A multi-resolution registration with a mutual information metric was performed in Elastix [Klein *et al.* 2010, Klein *et al.* 2009]. The parameter

file used has been stored on <http://elastix.bigr.nl/wiki/>.

To enable planning, the delineations used in the clinical plan were propagated to the registered CT, and the clinical target volume (CTV) was propagated to MR_{sCT} . To further minimise differences between CT and MR, the couch in the CT images was removed by assigning the value -968 HU outside body contour. Body contour detection was performed using an intensity threshold of -200 HU. We refer to the resulting dataset as CT_{reg} .

To quantify *set-up & positioning differences*, *MR-related geometric inaccuracy*, and *registration errors* (referred to as *inter-scan differences*), homogeneous water density CT- and MR-based sCT were generated. In particular, the entire body volume of CT_{reg} and MR_{sCT} were considered being water-equivalent (synthetic-HU = 0) after thresholding the images at -200 HU. We refer to these datasets as CT_{water} and MR_{water} , respectively. For clarity, the only difference between both datasets is the body outline.

To quantify the *synthetic-CT generation* factor, we aimed to circumvent *inter-scan differences* by producing CT-based sCT similar to MR_{sCT} . More specifically, we stratified the registered CT by assigning the same synthetic-HU values as employed in MRCAT to the different tissue classes. First, the voxels of CT_{reg} were separated into five classes according to the ranges shown in Table 2.1. These ranges were chosen by adjusting the values proposed by [Helle *et al.* 2014]. Second, since MR_{sCT} has no air in the body region, air pockets within the body outline were classified as fat. Third, since no soft tissue is present within bone regions of MR_{sCT} , all voxels that were labelled as soft tissue and surrounded by spongy or compact bone regions were reclassified as spongy bone. To do so, a morphological closing filter was used. As a final step, the lack of gold fiducial marker on MR_{sCT} was emulated: the voxels in the CTV classified as bone were reclassified as muscle. We use the term CT_{strat} to refer to this dataset. In 2.6, we show that CT_{strat} can be used to quantify the contribution of the *synthetic-CT generation* confounding factor.

Before planning, CTV delineations were propagated to CT-based sCT. CT (a) and MR (b) images of one of the patients, together with the five corresponding datasets (c,d) are shown in Figure 2.1.

The code used to generate CT_{reg} , CT_{strat} , and CT_{water} has been made publicly available at <https://matteomaspero.github.io/pseudo-CT-generation/>.

Table 2.1 The synthetic-HU assigned to the five tissue classes of MR_{sCT} , together with the ranges used during the stratification of CT_{reg} (i.e. the CT_{strat} generation).

Classes	synthetic-HU [HU]	Range
		stratification [HU]
<i>Outside Air</i>	-968	$(-\infty; -200]$
<i>Fat</i>	-86	$(-200; 28.5]$
<i>Muscle</i>	42	$(-28.5; 100]$
<i>Spongy Bone</i>	198	$(100; 575]$
<i>Compact Bone</i>	949	$(575; \infty)$

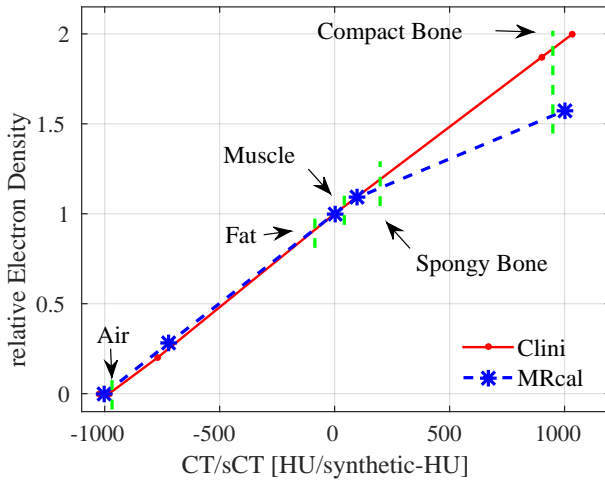


Figure 2.2 **Calibration curves used to convert CT or sCT in relative electron density.** The (red) straight curve, called *Clini*, is used in our institute and based on the Catphan (The Phantom Laboratory, Greenwich, New York, USA) phantom, while the (blue) dashed curve, called *MRcal*, has been provided along with the MRCAT method and based on literature [ICRU 1989, ICRU 1992]. The (green) vertical dashed line corresponds to the synthetic-HU used in the MRCAT method, as presented in 2.1.

2.2.3 Treatment planning

In the third part of the study, intensity-modulated radiotherapy (IMRT) plans, using 5 beams of 10 MV, were generated for each patient using a Monte Carlo-based treatment planning system (Monaco v5.10.00, Elekta AB, Stockholm, Sweden). The plan isocentre was the centre of gravity of the CTV. The beam angles were fixed: 40° , 100° , 180° , 260° , and 320° (considering 0° the anterior direction and rotating clockwise). The prescribed mean dose to the entire prostate gland was 77 Gy. Plan optimisation was carried out on CT_{reg} to fulfil clinical requirements (described by Lips *et al.* 2008). Dose calculations were performed on a 3 mm^3 grid and 1% statistical uncertainty per control point.

To eliminate the dose differences that could arise during separated optimisation procedures, the plans were recalculated on each sCT dataset keeping the planning parameters, i.e. beam energies, angles, photon fluency, and monitor units unchanged.

The vendor of MRCAT provided a calibration curve to convert synthetic-HU into electron density adapted from literature [ICRU 1989, ICRU 1992]. We refer to this calibration curve as *MRcal*. In our institution, a different calibration curve is currently used, which is a curve obtained with a Catphan phantom (The Phantom Laboratory, Greenwich, New York, USA) for CT scanner calibration. We refer to this curve as *Clini*. To investigate the impact of these different calibration curves on dose calculations (referred to as the *electron density conversion factor*), dose calculations using both calibration curves were carried out. Figure 2.2 depicts both the *MRcal* and *Clini* curve.

2.2.4 Evaluation of inter-scan differences

In the fourth part of our study, we investigated inter-scan differences due to possible *set-up & positioning differences*, *MR-related geometric inaccuracy*, and *registration errors*. More specifically, we took into consideration body contour differences of MR and CT. The body contour may be affected by set-up errors and patient repositioning that occurs during different imaging sessions. Additionally, the body contour is the anatomical region expected to be maximally influenced by MR geometric distortion, considering that distortion radially increases from the scan isocentre [Baldwin *et al.* 2007]. For these reasons, we considered the beam depth difference between MR_{sCT} and CT_{reg} as an estimate for inter-scan differences. Here, the beam depth is defined as the radial distance between isocentre and body contour. The definition of isocentre is dependent on the registration between image modalities. Note that, as specified in the introduction, when referring to inter-scan differences we consider also potential image registration errors.

We evaluated inter-scan variability in terms of beam depth of the five beam angles and in all radial directions. The beam depth of the five beams was directly extracted from each control point of the IMRT plans. The beam depth in all the radial directions was obtained by planning a single 10 MV 360° arc in Monaco and linearly interpolating at 1° intervals the radial beam depth extracted from the control points of the plan.

For each patient, the mean of the beam depth difference between CT_{reg} and MR_{sCT} over a complete 360° -arc, and over the five beams were estimated. Figure 2.3 shows an example of the radial representation of the beam depth (top) over a complete 360° -arc, and the beam depth difference between CT_{reg} and MR_{sCT} (bottom) for one of the patients.

The average and standard deviation (σ) over the whole population of the mean beam depth differences for the five beams and in all the radial directions were calculated. Single sample t-tests at $p = 0.01$ significance level were also conducted.

2.2.5 Dosimetric comparison

Lastly, we carried out a dosimetric evaluation to quantify the relative contribution of the three confounding factors (*inter-scan differences*, *synthetic-CT generation* and *electron density conversion*). To estimate their dosimetric contributions, the voxel-by-voxel relative percentage dose difference (RelDiff) between two sCT was calculated as follows:

$$\text{RelDiff}[\%] = \frac{\text{Test} - \text{Ref}}{\max(\text{Ref})} * 100$$

where $\max(\text{Ref})$ refers to the maximum dose value of Ref of each patient. To disentangle the individual confounding factors, we considered Ref and Test dose distributions as here presented:

- **Inter-scan differences.** CT_{water} and MR_{water} differ only due to *set-up & positioning differences* and *MR-related geometric inaccuracy*, and *registration errors* (inter-scan differences) when the dose calculation is performed using the

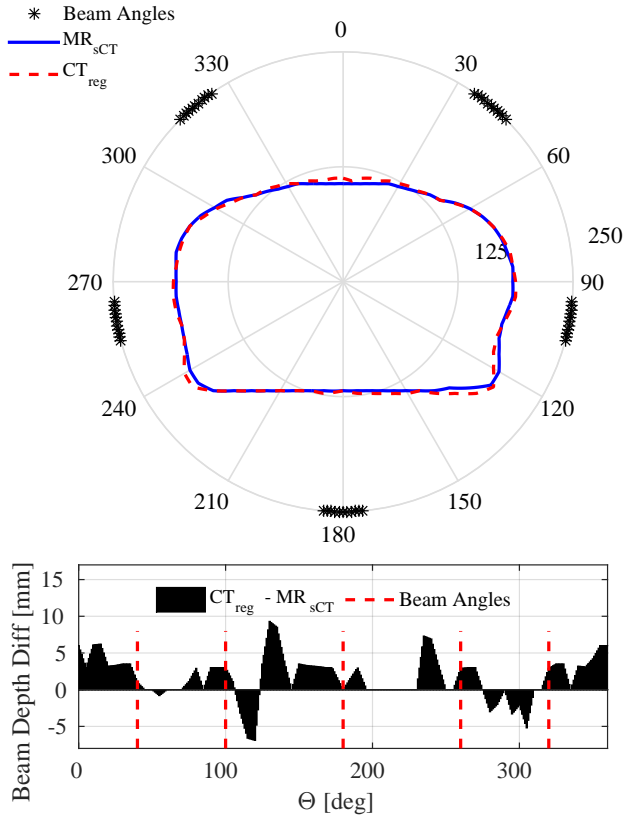


Figure 2.3 (Top) Beam depth (in mm) from isocentre to body contour of MR_{sCT} (blue continuous line) and CT_{reg} (red dashed line) for one patient. (Bottom) Difference between beam depth on CT_{reg} and MR_{sCT} in all the directions as function of the beam angle Θ for the shown patient. The location of the five beam angles is also represented as a 10° arc in the polar plot (top) and as vertical dashed (red) lines in the bar plot (bottom).

same calibration curve (*Clini* in this case). The “inter-scan differences” factor was estimated by considering CT_{water} as Ref and MR_{water} as Test.

- **Synthetic-CT generation.** CT_{strat} is immune to inter-scan differences with respect to CT_{reg} . To estimate the “synthetic-CT generation” factor, we considered CT_{reg} as Ref and CT_{strat} as Test converting synthetic-HU into electron density with the *Clini* calibration curve for both datasets.
- **Electron density conversion.** To estimate the “electron density conversion” factor, we considered the dose on CT_{reg} planned with the *Clini* calibration curve as Ref and the dose on CT_{reg} planned with the *MRcal* as Test.

To estimate the systematic contribution and error of each confounding factor, we calculated the average and σ among all the patients of the mean $RelDiff$ in the CTV and in the V_{Body} . The CTV was considered to represent the high dose region (where the largest dose difference is expected to be found), while the V_{Body}

was considered to represent the largest anatomical region common to MR- and CT-based sCT (CTV included). V_{Body} was defined as intersection of the body contour of the MR_{sCT} and the CT_{reg} . The resulting contour was isotropically eroded by 1.5 cm in each transverse slice to exclude build-up regions which are compromised by a steep dose gradient.

We also investigated the scenario taking into account the sum of **all the factors**, by considering CT_{reg} as Ref and MR_{sCT} as Test. Here, we considered two scenarios: one with different electron density conversions (*Clini* and *MRcal*), and one with the same electron density conversion (both *MRcal*). A third possible scenario (same electron density conversion: both *Clini*) has not been considered since the vendor suggests the use of MR_{sCT} in combination with *MRcal*. For these scenarios, we performed the same statistical analysis as described above.

2.3 RESULTS

2.3.1 Evaluation of inter-scan differences

The beam depth difference (CT_{reg} minus MR_{sCT}) was 0.9 ± 0.7 mm (1σ , $p < 0.01$), and 0.2 ± 1.5 mm ($p = 0.63$) when calculated over the complete 360° -arc and the five beam angles, respectively.

As shown in Figure 2.4 considering the average (and σ) of the beam depth differences between CT_{reg} and MR_{sCT} over all patients for the complete 360° -arc, the largest variations of beam depth differences occur at Θ about 130° and 240° . These angles correspond to the locations where the patient contour is not in contact with the flat table top, as Figure 2.3 (top) clearly illustrates. As this trend is seen after averaging over fourteen patients, the large variations may relate to a systematic positioning error, e.g. due to inclination of the in-house-built flat table top at MR, or due to a systematically different positioning of the patient legs between CT and MR imaging sessions.

2.3.2 Dosimetric comparison

A summary of the quantification of confounding factors described in Section 2.2.5 is reported in Table 2.2 as means ($\pm 1 \sigma$) over all fourteen patients in view of mean RelDiff to CTV and V_{Body} .

Considering “all factors” combined (first two rows of Table 2.2), the electron density conversion on CT_{reg} and MR_{sCT} was carried out using the *Clini* and *MRcal* calibration curve, respectively. We found (first row of Table 2.2) a dose overestimation of $1.0 \pm 0.6\%$ (1σ) when considering the overall dose difference (MR_{sCT} minus CT_{reg}). The observed dose overestimation more than halved when omitting the *electron density conversion* factor (second row of Table 2.2): the average RelDiff between CT_{reg} and MR_{sCT} was $0.33 \pm 0.39\%$ when the electron density conversion was performed using the *MRcal* calibration curve for both datasets. The dose comparison considering all the factors (first and second rows of Table 2.2) for each patients is reported in the Supplementary Material.

When comparing the possible confounding factors separately, the *electron density conversion* (row three of Table 2.2) was found to contribute the largest relative

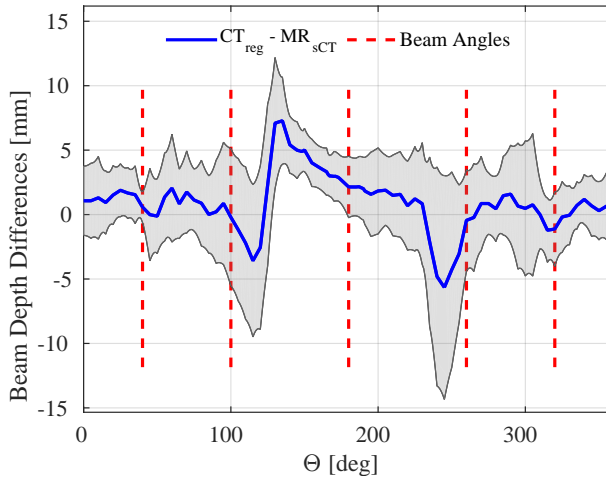


Figure 2.4 Beam depth (in mm) difference in all radial directions between CT_{reg} minus MR_{sCT} as an average over the patient population. The (blue) continuous line and the grey region indicate the average and the σ over the patient population, respectively. The five beam angles are represented by vertical (red) dashed lines.

dose difference ($0.7 \pm 0.2\%$), followed by the *synthetic-CT generation* (row four of Table 2.2) into five bulk-assigned tissue classes ($0.16 \pm 0.13\%$). For these two confounding factors the dose difference was within two σ s to zero.

The *set-up & positioning differences* and *MR-related geometric inaccuracy* (last row of Table 2.2) were the only confounding factors within one σ to zero: the average RelDiff was $0.01 \pm 0.35\%$ between CT_{water} and MR_{water} in the CTV.

Table 2.2 Confounding factors estimation in terms of average of the relative dose difference (RelDiff $\pm 1 \sigma$) over all patients for CTV and V_{Body} between the Test and Ref datasets. The calibration curves to convert the Test and Ref datasets (*MRcal* or *Clini*) into electron density are indicated in the columns “Calibration”.

sCT compared		Calibration		Confounding Factors	RelDiff $\pm 1 \sigma$ [%]	
Ref	Test	Ref	Test		CTV	V_{Body}
		<i>Clini</i>	<i>MRcal</i>		1.0 ± 0.6	0.14 ± 0.07
CT_{reg}	MR_{sCT}	<i>MRcal</i>	<i>MRcal</i>	All factors	0.33 ± 0.39	0.04 ± 0.06
CT_{reg}	CT_{reg}	<i>Clini</i>	<i>MRcal</i>	ED conversion	0.7 ± 0.2	0.10 ± 0.03
CT_{reg}	CT_{strat}	<i>Clini</i>	<i>Clini</i>	Synthetic-CT generation	0.16 ± 0.13	-0.03 ± 0.02
CT_{water}	MR_{water}	<i>Clini</i>	<i>Clini</i>	Inter-scan differences	0.01 ± 0.35	0.00 ± 0.06

2.4 DISCUSSION

In radiotherapy, a high level of accuracy is required to deliver clinically effective treatments [Mijnheer *et al.* 1987, Thwaites 2013]. To comply with such a requirement, institutions interested in introducing an MR-only workflow into their clinic should evaluate whether (and how) MR-planning impact the geometric and dosimetric accuracy of the radiotherapy treatment.

As part of such an evaluation, the present study was designed to verify the accuracy of MR-only dose calculations focusing on the case of prostate cancer patients. Additionally, we were interested in disentangling factors which may confound the results of this evaluation and that were described in the Introduction (Section 2.1). The key aspect of our approach was the generation of a series of CT-based sCT to circumvent the intrinsic geometric distortions in MRI, possible set-up and positioning differences, and registration errors (so called inter-scan differences). This allowed the quantification of the sole effect of the synthetic-CT generation technique. More specifically, we compared CT-based dose calculations to MR-only based dose calculations that were enabled by a commercially available solution known as MRCAT (Philips Healthcare, Vantaa, Finland).

The contribution of the aforementioned confounding factors was successfully identified, finding that the *electron density conversion*, and *synthetic-CT generation* contributed within two σ s of zero to the observed dose differences, while *inter-scan differences* within one σ of zero.

In particular, the largest confounding factor was the *electron density conversion* (0.7% dose difference in the CTV). Note that inaccuracy due the use of different calibration curves to convert HU (or synthetic-HU) in electron density has been already reported in literature as a possible source of inaccuracy in CT-based dose calculations, causing comparable dose differences [Thomas 1999, Inness *et al.* 2014]. The *electron density conversion* is a factor which is not specific of all sCT generation methods, however the fact that this was the largest contributing factor in our study highlights the importance of its evaluation during the introduction of an MR-only workflow.

The second-largest factor was the *synthetic-CT generation* (0.2% dose difference in the CTV). [Siversson *et al.* 2015] reported dose differences to the CTV of $0.0 \pm 0.2\%$ between registered CT and MR-based sCT images. Siversson *et al.* circumvented *inter-scan differences*, employing non-rigid registration, which is a different method to isolate the *synthetic-CT generation* factor with respect to the one adopted in the present study. However, the contribution of the *synthetic-CT generation* to the relative dose difference is consistent with their observation.

When focusing on the impact of *set-up & positioning differences*, *MR-related geometric inaccuracy*, and *images registration errors*, we found that such confounding factors resulted in a dose difference within one σ of zero ($0.01 \pm 0.35\%$). As a result, we concluded that residual discrepancies in inter-scan body outline between MR and CT imaging sessions did not contribute to the dose inaccuracy when planning with IMRT. [Lambert *et al.* 2011] quantified *inter-scan differences*, comparing doses planned on homogeneously assigned water-equivalent CT- and MR-based sCT images. The authors observed a dose difference of 1.3%. This difference is larger than what has been found in the present study. However, [Lam-

bert *et al.* 2011] did not use coil support during MRI. In this way, the skin surface of the patient may be compressed, possibly leading to the larger observed differences. [Sun *et al.* 2015] showed that external body deformation due to lack of coil support resulted in an observed dose difference of approximately 0.6 Gy, which corresponds to about 0.9% of the prescribed dose. This is comparable with our findings, and shows that the MR-simulator configuration adopted in this study minimises inter-scan differences.

From a geometric perspective, we found differences in body shapes that may originate from an inclination of the in-house built flat table top or from consistently different patient positioning on the CT and MR scanners. Further research will investigate the possible causes taking also into consideration that *MR-related geometric* inaccuracy and registration errors could play a role. In any case, even if systematic set-up errors and incorrect patient positioning may have occurred, contributing to observed beam depth differences, they did not contribute to observed dose differences.

Within our study, we demonstrated that exclusion of the *electron density conversion* factor (planning on the same calibration curve) reduced the difference between CT-based and sCT-based dose calculations from about 1% to 0.3%. In previous work, several authors concluded that comparable, or even higher observed dose differences would enable accurate MR-only dose calculations [Dowling *et al.* 2012, Korhonen *et al.* 2014, Kim *et al.* 2015, Siverson *et al.* 2015]. We concluded that MRCAT enables accurate MR-based dose calculation to the target.

A limitation of the present study is that for each patient a large number of plans (6) needs to be recalculated. In this regard, we believe that the proposed strategy is suitable mainly for initial evaluations of the MR-only workflow.

It would be desirable to show in future work a generalisation of the approach to other sCT generation techniques and anatomies. We believe that the application of the proposed approach is independent of the chosen sCT generation technique. This hypothesis is supported by the fact that the identification of confounding factors relies on the generation of CT-based sCT images that emulate MR-based sCT images: in principle the strategy is not dependent of irradiation modalities, or anatomical locations. Continuing this thought, we foresee as a straightforward possible application the situation in which MR-only planning merely relies on bulk assignment-based sCT generation techniques. Note however that the image processing pipeline to generate CT_{strat} would require optimisations for any sCT generation other than MRCAT.

Finally, we would like to underline that the here presented dose accuracy evaluation of an MR-only sCT generation method is not sufficient to introduce MR-only radiotherapy in the clinic. The clinical introduction of MR-only radiotherapy involves more steps, e.g. evaluation of MR-only delineations, and evaluation of MR-based position verification. These steps also contribute to the overall dose delivery accuracy and have to be taken into consideration by institutions interested in MR-only radiotherapy.

2.5 CONCLUSION

In this work, factors confounding accurate MRI-based dose calculation in the prostate were identified and quantified. This is a crucial step when aiming to introduce MR-only treatment planning into the clinic. With this regard, the method presented to quantify the confounding factors will be valuable for institutions interested in introducing MR-only dose planning in their clinical practice.

2.6 APPENDIX: CT-BASED SCT SIMILARITY

In this section we demonstrate the similarity between the CT-based (CT_{strat}) and the MR-based (MR_{sCT}) sCT images. This will justify using CT_{reg} and CT_{strat} to quantify the contribution of the *synthetic-CT generation* confounding factor. To quantify the similarity we used metrics (1) applicable to any sCT generation technique, and (2) applicable only to bulk assignment-based sCT generation techniques.

(1) MR_{sCT} served as reference for CT_{strat} and CT_{reg} . We assumed that the registration of CT (and CT-based sCT images) minimises *inter-scan differences*. For each patient, mean HU, and mean absolute error (MAE) was calculated within the body intersection of CT_{strat} and MR_{sCT} [Rank *et al.* 2013, Johansson *et al.* 2012, Siversson *et al.* 2015]. MAE was calculated for all N voxels within the body contour as follows:

$$\text{MAE} = \frac{1}{N} \sum_{i=1}^N |sCT_i - MR_{\text{sCT}_i}|,$$

The average and standard deviation (σ) of mean HU and MAE over all the patients was considered as representative of similarity among sCT images. We conducted a double sample t-test at $p = 0.01$ significance level on the MAE.

(2) A voxelwise comparison of the tissue classification between CT_{strat} and MR_{sCT} was carried out. Such a comparison was enabled by the voxelwise spatial relationship among CT-based sCT and MR-based sCT images. We performed (i) a volumetric, and (ii) a classification analysis.

(i) The mean relative volume percentage of each tissue class in the two datasets for each patient was calculated. The average and σ over the whole patient population were reported, and a double sample t-test at $p = 0.01$ significance level was conducted for each class.

(ii) A confusion matrix [Kohavi & Provost 1998] in terms of percentage of the body volume body intersection of CT_{strat} and MR_{sCT} was calculated: the tissue class for each voxel of MR_{sCT} was compared to CT_{strat} tissue class, considering the voxels MR_{sCT} as being correctly classified. The average and σ of the confusion matrix were calculated for each combination of classes of CT_{strat} and MR_{sCT} over all the patients. To preliminarily evaluate the impact on the dose, differences in radiological path length were examined for the five beam angles (see Section 2.2.3) for CT_{strat} and MR_{sCT} . Radiological beam paths were calculated in the treatment planning system (Monaco), using the *Clini* calibration curve. Statistical significance of the radiological path length differences was tested conducting a t-test at $p = 0.01$ significance level.

(1) The mean HU difference over all patients was -8.3 ± 5.2 HU (1σ), and -12.4 ± 3.3 HU for the body contour intersection between CT_{reg} and MR_{sCT} , and between CT_{strat} and MR_{sCT} , respectively. The corresponding MAE was 57.8 ± 8.0 HU (1σ), and 36.7 ± 5.9 HU. A double sample t-test for MAE resulted in a p -value < 0.01 , which indicates that the difference between the two populations is statistically significant.

Since the MAE is lower when calculated on CT_{strat} than when calculated on CT_{reg} , we conclude that MR_{sCT} is more similar to CT_{strat} than to CT_{reg} . The value obtained in terms of MAE (36.7 ± 5.9 HU) between CT_{strat} and MR_{sCT} is comparable to the findings reported by [Siverson *et al.* 2015] (36.5 ± 4.1 HU - in the body contour after non rigid registration).

(2i) Table 2.3: the result of the volumetric analysis performed in CT_{strat} and MR_{sCT} shows that only the volume of the compact bone class is statistically compatible between the two datasets (see further for possible explanation).

(2ii) Table 2.4 reports the average and σ of the confusion matrix over all the patients. The classification into tissue classes between MR_{sCT} and CT_{strat} was consistent (sum of the values along the diagonal) for $79.6 \pm 11.2\%$ of the body intersection volume. Misclassification between muscle and fat occurred for $16.3 \pm 2.1\%$ of the body intersection volume. The misclassification may originate from the *set-up & positioning differences*, and the *MR-related geometric inaccuracy* factors, but also from internal motion. Furthermore, misclassification may originate also from the image processing proposed to generate CT_{strat} , in case it does not correctly emulate the voxel content of MR_{sCT} . No statistically significant dose differences were

Table 2.3 Relative percentage volume of each tissue class in MR_{sCT} and CT_{strat} within the CT body \cap MR body.

Classes	CT_{strat} [%]	MR_{sCT} [%]	p -value
Outside Air	0	0	
Fat	45.4 ± 8.5	39.4 ± 8.3	< 0.001
Muscle	46.2 ± 7.5	49.9 ± 6.9	< 0.001
Spongy Bone	6.9 ± 1.2	9.2 ± 1.4	< 0.001
Compact Bone	1.4 ± 0.4	1.6 ± 0.5	0.2

Table 2.4 Confusion Matrix within CT body \cap MR body of the tissue classification in CT_{strat} vs. The percentage of voxels in the body contour intersection that belong to a specific class of MR_{sCT} and of CT_{strat} .

		CT_{strat}			
		Fat	Muscle	Spongy Bone	Compact Bone
MR_{sCT}	Fat	33.8 ± 8.7	5.5 ± 1.3	0.1 ± 0.1	0.01 ± 0.01
	Muscle	10.8 ± 1.6	38.7 ± 6.9	0.3 ± 0.2	0.05 ± 0.05
	Spongy Bone	0.7 ± 0.2	1.8 ± 0.4	6.2 ± 1.0	0.5 ± 0.1
	Compact Bone	0.11 ± 0.05	0.3 ± 0.1	0.30 ± 0.09	0.9 ± 0.3

observed due to inter-scan variability (Section 2.3), and the range used to stratify CT_{reg} into tissue classes (Table 2.1) has been arbitrarily chosen. The range could be further optimised, as well as the image processing proposed to generate CT_{strat} . However, the correct classification rate obtained ($\sim 80\%$) was considered satisfactory.

To understand whether the dissimilarity still present between CT_{strat} and MR_{sCT} may contribute to dose differences, and whether further optimisation of the proposed image processing would be required, we investigated the radiological path lengths. The difference in terms of average over all the patients of the radiological path lengths between CT_{strat} and MR_{sCT} was 0.01 ± 1.14 mm ($p = 0.98$). Thus, we conclude that the proposed image processing enables the generation of CT-based sCT sufficiently similar to MR_{sCT} .

We believe that the results here discussed demonstrate that CT_{strat} and CT_{reg} can be used to estimate the contribution of the *synthetic-CT generation* confounding factor.

Table 2.5 Dose comparison between MR_{sCT} (on *MRcal*) and CT_{reg} (on *Clini*) in terms of mean and standard deviation (σ), gamma pass rate (abbreviated as GPR) for $\gamma_{2mm/2\%}$ ($\gamma_{3mm/3\%}$) in the CTV for each patient. The last two rows of the table present the mean and σ over all patients, and the 95% confidence interval of the gamma pass rate for the γ analysis.

Patient	# Voxel	RelDiff [%]		GPR [%]	
		Mean	σ	$\gamma_{3mm/3\%}$	$\gamma_{2mm/2\%}$
1	2168	0.66	0.72	98.9	97.0
2	3078	1.26	0.81	98.9	91.6
3	2347	0.50	0.71	99.5	98.6
4	6399	1.43	1.05	96.8	76.6
5	1827	1.19	0.83	98.0	93.6
6	4657	1.25	0.77	99.1	92.8
7	4439	0.84	0.73	99.6	97.4
8	2744	0.84	0.94	98.0	95.7
9	2819	1.01	0.73	99.2	97.1
10	2991	1.16	0.80	98.9	94.1
11	2438	1.22	0.71	100	94.1
12	2710	1.91	0.86	96.2	71.1
13	2251	1.16	0.81	99.1	96.7
14	1845	-0.49	0.67	99.6	98.9
All		1.00 \pm 0.55		98.7	92.5
				[96.3;99.9]	[72.2;98.8]

2.7 SUPPLEMENTARY MATERIAL: GAMMA ANALYSIS

We here present supplementary data reporting the dosimetric comparison without disentanglement of the confounding factors in terms of γ analysis [Low *et al.* 1998]. As shown in Table 2.5 and 2.6, the data are presented for each patient reporting 2%/2 mm (and 3%/3 mm for Table 2.5) γ analysis in terms of percentage gamma pass rate.

Table 2.6 Dose comparison between MR_{sCT} (on MR_{cal}) and CT_{reg} (on MR_{cal}) in terms of mean and standard deviation (σ), gamma pass rate (abbreviated as GPR) for $\gamma_{2mm/2\%}$ in the CTV for each patient. The last two rows of the table present the mean and σ over all patients, and the 95 % confidence interval of the gamma pass rate for the γ analysis.

Patient	# Voxel	RelDiff [%]		GPR [%]
		Mean	σ	$\gamma_{2mm/2\%}$
1	2168	0.16	0.70	98.4
2	3078	0.36	0.64	99.3
3	2347	0.08	0.68	99.2
4	6399	0.48	0.87	98.3
5	1827	0.33	0.69	98.4
6	4657	0.68	0.66	99.0
7	4439	0.14	0.62	99.6
8	2744	0.39	0.79	97.8
9	2819	0.35	0.64	99.3
10	2991	0.46	0.65	98.9
11	2438	0.52	0.61	99.3
12	2710	0.88	0.72	97.5
13	2251	0.59	0.69	99.9
14	1845	-0.78	0.63	98.9
All		0.33 \pm 0.39		98.8
				[97.5; 99.5]

A γ analysis 2%/2 mm was performed for each confounding factor, in a similar way as reported in Table 2.2, and described in Section 2.2.5. As shown in Table 2.7, the γ values are reported in terms of average and 95% confidence interval of the percentage gamma pass rate over the patient population.

Table 2.7 Confounding factors estimation in terms of average gamma pass rate ($\gamma_{2\text{mm}/2\%}$, abbreviated as GPR) and 95% confidence interval (within squared brackets) over all patients for CTV and V_{Body} . The calibration curves to convert the Test and Ref datasets (MR_{cal} or $Clini$) into electron density are indicated in the columns “Calibration”.

sCT compared		Calibration		Confounding Factors	GPR [%]	
Ref	Test	Ref	Test		CTV	V_{Body}
		<i>Clini</i>	MR_{cal}	All factors	92.5 [72.2; 98.8]	96.7 [94.6; 98.0]
CT_{reg}	MR_{sCT}	MR_{cal}	MR_{cal}		98.8 [97.5; 99.5]	98.8 [97.0; 99.5]
CT_{reg}	CT_{reg}	<i>Clini</i>	MR_{cal}	ED conversion	99.9 [99.5; 100]	99.4 [98.9; 99.7]
CT_{reg}	CT_{strat}	<i>Clini</i>	<i>Clini</i>	Synthetic-CT generation	99.1 [98.2; 99.9]	99.7 [99.6; 99.9]
CT_{water}	MR_{water}	<i>Clini</i>	<i>Clini</i>	Inter-scan differences	99.9 [99.48; 100]	99.5 [97.6; 99.9]

Synthetic CT for proton radiotherapy

3

This chapter is based on:

Maspero, M., van den Berg, C. A. T., Landry, G., Belka, C., Parodi, K., Seevinck, P. R., Raaymakers, B. W., & Kurz, C. (2017). **Feasibility of MR-only proton dose calculations for prostate cancer radiotherapy using a commercial pseudo-CT generation method.** *Phys. Med. Biol.*, 62(24), 7981-8002 <https://doi.org/10.1088/1361-6560/aa9677> [Maspero *et al.* 2017].

Abstract

Background A magnetic resonance (MR)-only radiotherapy workflow can reduce cost, radiation exposure and uncertainties introduced by computed tomography (CT)/magnetic resonance imaging (MRI) registration. A crucial prerequisite is generating the so called synthetic CT (sCT) images for accurate dose calculation and planning. Many sCT generation methods have been proposed in the scope of photon radiotherapy. This work aims at verifying for the first time whether a commercially available photon-oriented sCT generation method can be employed for accurate intensity-modulated proton therapy (IMPT) dose calculation.

Methods A retrospective study was conducted on ten prostate cancer patients. For sCT generation from MR images, a commercial solution for creating bulk-assigned sCT images, called MR for calculating attenuation (MRCAT), was employed. The assigned synthetic-hounsfield unit (HU) values were adapted to yield an increased agreement to the reference CT in terms of proton range. Internal air cavities were copied from CT images to minimise inter-scan differences. CT- and MRCAT-based dose calculations for opposing beam IMPT plans were compared by gamma analysis and evaluation of clinically relevant target and organ at risk dose volume histogram (DVH) parameters. The proton range in beam's eye view (BEV) was compared using single field uniform dose plans.

Results On average, a (2%, 2 mm) gamma pass rate of 98.4% was obtained using a 10% dose threshold after adaptation of the synthetic-HU values. Mean differences between CT- and MRCAT-based dose in the DVH parameters were below 1 Gy (< 1.5%). The median proton range difference was 0.1 mm, with on average 96% of all BEV dose profiles showing a range agreement better than 3 mm.

Conclusion Results suggest that accurate MR-based proton dose calculation using an automatic commercial bulk-assignment sCT generation method, originally designed for photon radiotherapy, is feasible following adaptation of the assigned synthetic-HU values.

Keywords: **magnetic resonance, proton therapy, radiotherapy, bulk-assignment, pseudo CT, prostate cancer**

3.1 INTRODUCTION

Radiotherapy is one of the effective treatment modalities for prostate cancer patients [Thariat *et al.* 2013]. Among all the radiotherapy treatment techniques, external beam photon therapy is the most common [Jermann 2015, Durante *et al.* 2017]. However, over the last years, there has been growing interest in investigating proton therapy for prostate cancer. In particular, intensity-modulated proton therapy (IMPT) promises highly conformal prostate irradiation at reduced integral dose in comparison to conventional photon therapy [Trofimov *et al.* 2007, Durante *et al.* 2017] thanks to the favourable physical properties of protons [Durante & Loeffler 2010].

To ensure accurate treatment planning in photon and proton radiotherapy, X-ray computed tomography (CT) is the primary imaging modality [Chernak *et al.* 1975, Pereira *et al.* 2014]. CT provides a geometrically accurate representation of the patient anatomy [Zaorsky *et al.* 2017] and allows for the conversion of hounsfield unit (HU) values to relative electron density (in the case of photon therapy) or stopping power ratio relative to water (rSPR, in the case of proton therapy) which are crucial for dose calculation. Nevertheless, especially when focusing on prostate cancer treatment, magnetic resonance imaging (MRI) is playing an increasingly important role in radiotherapy since it enables imaging at superior soft tissue contrast with respect to CT [Debois *et al.* 1999, Dirix *et al.* 2014, Brock & Dawson 2014] and thereby facilitates accurate delineation of target regions and critical structures [Khoo & Joon 2006, Sciarra *et al.* 2011]. In consequence, radiotherapy treatment planning is nowadays often based on a hybrid workflow during which patients undergo both CT and magnetic resonance (MR) imaging with subsequent image registration [Kagawa *et al.* 1997].

In the last decades, solely MR-based radiotherapy planning - also called “MR-only”, or “MR-alone” - has been proposed to reduce systematic spatial uncertainties introduced when registering CT and MRI images [Fraass *et al.* 1987, Lee *et al.* 2003, Edmund & Nyholm 2017]. In addition, an MR-only workflow would reduce costs of the treatment due to fewer imaging sessions and minimise patient exposure to ionising radiation [Karlsson *et al.* 2009]. MR-only treatment planning is particularly desirable in the context of MR-guided photon [Raaymakers *et al.* 2004, Dempsey *et al.* 2005, Fallone *et al.* 2009, Karlsson *et al.* 2009] and eventually proton [Raaymakers *et al.* 2008, Schippers & Lomax 2011, Moteabbed *et al.* 2014, Hartman *et al.* 2015, Oborn *et al.* 2017] radiotherapy. To fully exploit the potential advantages offered by MR-only radiotherapy, high-accuracy is required in MR-based dose calculation and treatment planning [Nyholm *et al.* 2009, Jonsson *et al.* 2010, Kapanen *et al.* 2013]. This way, an MR-only workflow may eventually allow for frequent pre-treatment imaging and potentially, in the future, for MR-guided online treatment adaptation [Schippers & Lomax 2011, Oborn *et al.* 2017] at no further dose burden to the patient. With an MR-guided treatment scenario, the impact of inter-fraction motion could be considerably reduced, which is deemed particularly favourable in proton therapy when compared to conventional photon radiotherapy [Lomax 2008, Soukup *et al.* 2009, Bert & Durante 2011].

The main challenge in the context of MR-based dose calculation is the generation of accurate electron density or relative stopping power ratio (rSPR) maps by

the use of solely MR images. These maps, usually called synthetic CT (sCT) ¹, can then serve as CT surrogates [Edmund & Nyholm 2017] and can be employed for dose calculation.

While for prostate cancer photon radiotherapy several methods to generate sCTs resulting in dosimetric accurate plans have been proposed [Lee *et al.* 2003, Chen *et al.* 2004, Dowling *et al.* 2012, Johansson *et al.* 2012, Korhonen *et al.* 2014, Kim *et al.* 2015, Siversson *et al.* 2015, Prior *et al.* 2016], sCTs evaluation for MR-only prostate proton radiotherapy is up to now scarce. Two studies investigated the feasibility of proton radiotherapy for brain tumours. Rank *et al.* [Rank *et al.* 2013] obtained dose differences between sCTs and CTs within 2% for three patients when using a classification-based tissue segmentation method. Edmund *et al.* [Edmund *et al.* 2014] investigated the use of multiple sCT-generation methods showing an overall average dose deviation to CT below 2% for five patients. More recently, Koivula *et al.* [Koivula *et al.* 2016] reported a dosimetric comparison for proton therapy leading to an average 2%/2 mm gamma pass rate (using a 10% dose cut-off) above 98% for ten prostate and ten brain patients when employing a dual model conversion with heterogeneous tissue representation. Their study also investigated the accuracy of dose calculations using a simplified dual bulk density assignment, which yielded an average gamma pass rate above 97%.

Although the results of these investigations are promising, Koivula and coworkers reported that the need for manual bone segmentation may complicate the adoption of the method into the clinic, where it may be desirable to use a fully-automatic, commercially available and certified solution for sCT generation. In the scope of conventional photon radiotherapy, such commercial methods exist and were proven suitable for high accuracy dose calculation and clinical implementation [Siversson *et al.* 2015, Tyagi *et al.* 2016, Maspero *et al.* 2017, Persson *et al.* 2017].

The aim of this contribution was to explore for the first time whether a current commercially available photon-oriented sCT generation method may easily be adopted to enable accurate proton dose calculation and eventually MR-only proton radiotherapy. In particular, we conducted a retrospective study on ten prostate cancer patients comparing CT-based and MR-only based dose calculations for proton radiotherapy treatment planning. The study is divided into four parts. First, we collected patient data of previously acquired CT and MR images (Section 3.2.1). Second, we generated a series of MR-based sCTs to evaluate the dosimetric accuracy of the sCT (Section 3.2.2). Particular attention was given to generating valuable reference data by minimising the inter-scan difference (outer patient contour and internal air cavities). Third, we performed range calculations and treatment planning (Section 3.2.3). Finally, we evaluated the range deviations and dosimetric accuracy (Section 3.2.4) from the plans calculated with sCT and CT images.

¹In this article, the abbreviation sCT will be used to refer to these MR-based images, however, a variety of other terms, e.g., “pseudo-CT”, or “substitute-CT”, have been suggested in the literature.

3.2 MATERIALS AND METHODS

3.2.1 Patient data collection

Ten prostate cancer patients originally treated with intensity-modulated radiotherapy at the University Medical Center Utrecht between March and July 2015 were included in this study in accordance with the regulation from the local ethical committee. They were diagnosed with intermediate and high-risk prostate carcinoma staged T1c-T3b according to Ash *et al.* [Ash *et al.* 2000] and Gleason Score > 7 . The included patients were between 57.0 and 78.2 years old. Their mean age was 69.6 years with an inter-quartile range of 66.3-73.4 years. Within the patient population, body mass index was on average 26.4 kg/m^2 and ranged from 21.6 to 30.4 kg/m^2 with the inter-quartile range of $25.3\text{-}27.2 \text{ kg/m}^2$.

Patients underwent both CT (Brilliance CT Big Bore, Philips Healthcare, Best, The Netherlands) and 3T MR imaging (Ingenia Omega HP, Philips Healthcare, Best, The Netherlands) for radiotherapy treatment planning.

CT scans were performed with the following imaging parameters: 120 kV, exposure time = 923 ms, tube current between 121 and 183 mA, in-plane matrix = 512×512 pixels, and 3 mm slice thickness. In-plane resolution was variable depending on the field of view (FOV) used, with a typical pixel size of $0.98 \times 0.98 \text{ mm}^2$. Patients were positioned using a flat table and knee wedges.

MR scans were performed within 2.5 hours (mean time = 1.4 hours, a minimum time of 1 hour, inter-quartile range = 1.2-1.3 hours) after the CT scans. To simulate treatment positioning, patients were marked with three skin tattoos at the CT scanner, which were then used to reposition the patient at the MR scanner, using an in-house-built flat table top and liquid fiducial markers (PinPoint ref 128, Beekley Medical, Bristol, CT, USA). Patients were scanned using anterior and posterior phased array coils (dS Torso and Posterior coils, 28 channels, Philips Healthcare, Best, The Netherlands). To avoid compression of the patients, two in-house-built coil bridges supported the anterior coil.

For the generation of MR-based sCTs, a dual echo three-dimensional (3D) Cartesian radio-frequency (RF) spoiled gradient-recalled echo (SPGR) sequence was added to the standard MR exam. In particular, MR images were acquired with the following parameters: echo times = 1.21/2.53 ms, repetition time = 3.93 ms, flip angle = 10° , FOV = $477 \times 477 \times 300 \text{ mm}^3$, acquisition matrix = $248 \times 281 \times 120$, reconstructed matrix = $480 \times 480 \times 120$, bandwidth = 1083 Hz and acquisition time of 2 min 13 s. A Dixon [Dixon 1984] reconstruction [Eggers *et al.* 2011] was performed obtaining in-phase, fat, and water images (Figure 3.1b).

For position verification purposes, each patient received three intra-prostatic cylindrical gold fiducial markers (HA2 Medizintechnik GmbH, Germany) measuring 1.0 mm (diameter) by 5 mm. CT and MR images were registered based on the fiducial marker localisations annotated by a radiotherapy technician (RTT). Delineations of the target were drawn by a radiotherapist on the MR images, while delineations of organs at risk were drawn by an RTT on CT images and checked by a radiotherapist. The margins used for photon-based radiotherapy were maintained in this study. In particular, an isotropic clinical target volume (CTV) to planning target volume (PTV) margin of 4 mm

was used in combination with an anisotropic margin of 5 mm, applying no margin in the dorsal and cranial direction. Margin reductions were considered on a patient-specific basis in the proximity of rectum or bladder.

3.2.2 sCT generation

Using the acquired MR images, sCTs were generated with a commercially available vendor solution tailored to prostate patients and called MR for calculating attenuation (MRCAT) (rev. 257, Philips Healthcare, Vantaa, Finland). A detailed description of the MRCAT approach is given in [Köhler *et al.* 2015]. In the following, we will briefly outline the main ideas of the approach. MRCAT is a bulk assignment sCT generation method based on sequential intensity- and model-based segmentation techniques [Schadewaldt *et al.* 2014]. In particular, MRCAT segments the images from the dedicated MRsequence (see Section 3.2.1) into 5 classes, and assigns each class the synthetic-HU values specified in Table 3.1 (middle column). MRCAT uses a constrained shape model to estimate the body contour and segment bone structures. Within the determined bone structures, two classes are assigned, based on the intensities of the in-phase MRI: spongy and compact bone. Similarly, soft tissue structures are assigned either to fat or muscle. MRCAT classifies the implanted gold fiducial markers and air compartments within the patient as soft tissues. The assigned synthetic-HU values can be converted to electron density or, in the case of proton therapy, to rSPR either on the basis of the calibration curve provided by the vendor together with MRCAT (optimised for the use in photon radiotherapy) or on the basis of user specific calibration curves. In this study, for improved consistency, we opted for using the same user specific HU to rSPR calibration curve for conversion of CT and MRCAT images to proton rSPR. In the following, we use the term “original” with the abbreviation $\text{MRCAT}_{\text{org}}$ (see Figure 3.1c) to refer to the dataset as produced directly by the vendor MRCAT solution.

For analysis, the diagnostic CT was automatically rigidly registered and re-sampled to $\text{MRCAT}_{\text{org}}$, as described in [Maspero *et al.* 2017]. For the purpose of accurately testing dose discrepancies within the body arising due to the synthetic-HU value assignment, differences in the patient outer contour due to repositioning between CT and MRimaging were eliminated by using the CT-based body

Table 3.1 The synthetic-HU values assigned to the five tissue classes of $\text{MRCAT}_{\text{org}}$ and $\text{MRCAT}_{\text{adp}}$ (after synthetic-HU value optimisation).

Classes	$\text{MRCAT}_{\text{org}}$ synthetic-HU [HU]	$\text{MRCAT}_{\text{adp}}$ synthetic-HU [HU]
<i>Outside air</i>	-968	-968
<i>Internal air</i>	not present	-600
<i>Fat</i>	-86	-86
<i>Muscle</i>	42	42
<i>Spongy bone</i>	198	250
<i>Compact bone</i>	949	1250

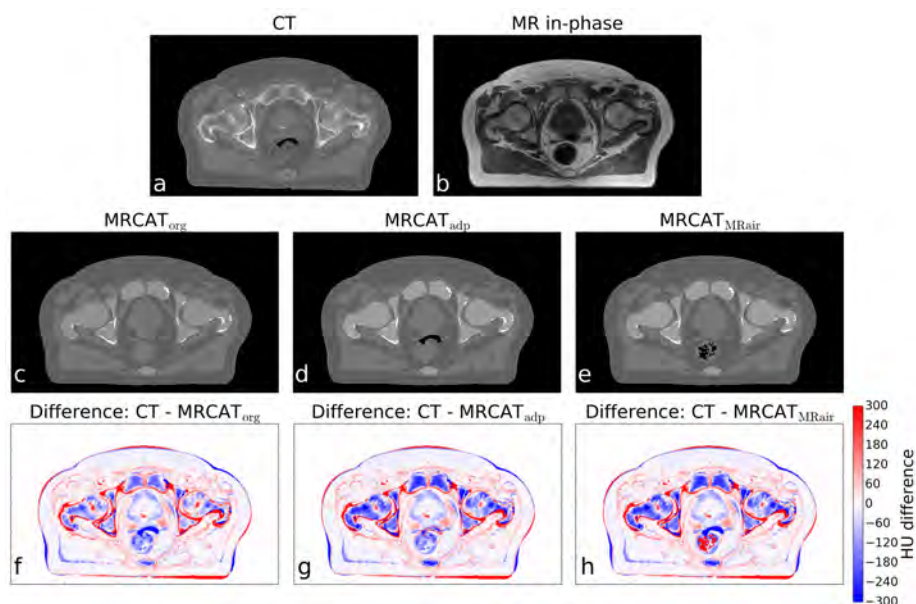


Figure 3.1 Images considered in this study for the identical transverse plane of an exemplary patient (P6). The registered and resampled reference CT and in-phase MR are shown in panels a and b. The retrieved sCTs images, i.e. MRCAT_{org}, MRCAT_{adp} and MRCAT_{MRAir}, are displayed in panels c to e, with their differences to the reference CT depicted in panels f to h.

contour for CT- and MR-based dose calculation, as already proposed by Koivula *et al.* [Koivula *et al.* 2016]. Regions of the MRCAT which were outside the CT body contour were truncated and regions which were between MRCAT_{org} and CT contour were filled by fat tissue (HU = -86). An alternative solution could be matching the two images by deformable image registration. However, this approach was not considered, since it would have introduced additional geometric uncertainties, due to registration errors [Thor *et al.* 2011, Thor *et al.* 2013], that we preferred to avoid in this study. Particularly in the pelvic region, substantial inter-scan differences in the soft tissue, e.g., in the rectum and bladder, may not be accurately modelled by deformable image registrations. Moreover, it can not be excluded that non-negligible geometric inaccuracies in the bony structures are introduced by deformable image registrations due to the signal void of cortical bones in the MR images. The same procedure has been conducted in the study by [Koivula *et al.* 2016].

Since the absence of rectal air cavities in close vicinity to the PTV in MRCAT_{org} has an impact on the calculated proton dose distribution [Soukup *et al.* 2009], additional sCTs were generated from MRCAT_{org} by inserting air cavities within body contour as found on the CT. In this way, the observed inter-scan differences in air pocket locations between CT and MR imaging session were minimised (see Figure 3.1a and b). Air pockets on the CT were identified by thresholding the images at -200 HU and obtaining a mask from morphologically connected regions (26 neighbourhood points) along the superior inferior direction having volumes

larger than 75 ml. A synthetic-HU value of -600 was assigned to voxels in the CT-based air mask. This value was chosen as an estimate of the population based average of the HU value found within the rectum. To ensure that bone tissue on $\text{MRCAT}_{\text{org}}$ was not substituted with air, the resulting images were visually inspected for each patient case.

In $\text{MRCAT}_{\text{org}}$, as specified by the vendor [Köhler *et al.* 2015], the synthetic-HU values were found averaging literature values and a specific patient population in the scope of photon radiotherapy. In line with these considerations, we deemed that synthetic-HU values could also be further optimised for the application to proton therapy as investigated in this work. Consequently, the assigned synthetic-HU values were adapted on the basis of a proton range analysis (see Section 3.2.3 for details) considering only the two patients having the lowest air volume in the vicinity of the target volume on the CT and MRimages (P₃ and P₄). Based on the estimated range differences and the length of traversed spongy and compact bone, an iterative manual adaptation of the synthetic-HU values assigned to these two components was performed aiming at minimising proton range differences and yielding the values given in the right column of Table 3.1. In the following, we use the term “adapted” with the abbreviation $\text{MRCAT}_{\text{adp}}$ to refer to the dataset as derived by MRCAT after synthetic-HU value modification and insertion of CT-based air pockets (see Figure 3.1d).

While for this study air pockets within the sCT were copied from the available CT, for the sake of generating consistent reference sCT data for comparison to the CT, it should be noted that an MR-only workflow may necessitate detecting internal air cavities on MRimages. To investigate the feasibility of generating bulk-assigned sCT with internal air cavities, we implemented an image processing pipeline using the acquired MRimages (in-phase, water and fat) to locate air pockets. For each patient, a water fraction image was calculated by dividing each voxel of the water image by the sum of the water and fat images. The in-phase image was normalised to its maximum. Voxels were considered being air if their intensity values were lower than 0.1 in the normalised in-phase image outside the MRCAT bone mask (expanded by a 15 mm margin) and their intensity value was larger than 0.85 in the water fraction image. Only air voxels contained in regions which were connected along the superior inferior direction and larger than 75 ml were bulk assigned to -600 synthetic-HU. For each patient, the geometrically accurate assignment of air pockets was ensured by visual inspection. The obtained dataset is shown in Figure 3.1e, labelled as $\text{MRCAT}_{\text{MRair}}$. The modification of $\text{MRCAT}_{\text{org}}$ was performed in Matlab (R2015a, MathWorks, Natick, MA, USA) and the time necessary to perform the automatic image processing pipeline was below 30 s per patient. The code used to generate $\text{MRCAT}_{\text{MRair}}$ has been made publicly available at <https://matteomaspero.github.io/MRonlyProton-pCTwithAir/>.

3.2.3 Treatment planning

For evaluating the accuracy of the retrieved sCT images in terms proton range, single field uniform dose proton treatment plans at 90° and 270° gantry angle on the International Electrotechnical Commission scale were generated using a research version of the commercial treatment planning system RayStation (version

4.99, RaySearch Laboratories, Stockholm, Sweden). Dose prescriptions aimed at a median dose of 70 Gy in 35 treatment fractions to the PTV. The plan optimisation was performed on the reference CT, setting the dose grid to the resolution of the resampled CT (reference), i.e. $1.0 \times 1.0 \times 2.5 \text{ mm}^3$, for high accuracy proton range probing. All single field uniform dose plans were recalculated on $\text{MRCAT}_{\text{org}}$, $\text{MRCAT}_{\text{adp}}$ and $\text{MRCAT}_{\text{MRair}}$ for proton range comparison in beam's eye view (BEV).

To infer the dosimetric accuracy of the sCT images in a more clinical scenario, opposing field (90° and 270° gantry angle) IMPT plans were generated using a standard $3 \times 3 \times 3 \text{ mm}^3$ dose grid, aiming at 70 Gy median dose to the PTV. Dose to the rectum and bladder was controlled using maximum equivalent uniform dose (EUD_{max}) constraints of 64 Gy and 63 Gy with parameter $a = 12$ and $a = 8$, respectively. The final plans were ensured not to violate the dose-volume constraints outline presented in the QUANTEC guidelines [Marks *et al.* 2010] for rectum $V_{50,60,65 \text{ Gy}}$ and bladder $V_{60,65 \text{ Gy}}$. For each patient, the opposing field IMPT plans obtained on CT were recalculated on $\text{MRCAT}_{\text{org}}$ and $\text{MRCAT}_{\text{adp}}$.

For all treatment plans, pencil beam scanning at a constant lateral spot spacing of 3 mm was used in combination with the implemented model of the dedicated IBA (Louvain-La-Neuve, Belgium) proton delivery system. HU values were converted to proton rSPR during dose calculation using the *Generic CT* model. The treatment isocentre was placed at the centre of mass of the PTV.

3.2.4 sCT evaluation

IMAGE EVALUATION. To characterise differences between CT and the retrieved sCTs, $\text{MRCAT}_{\text{org}}$, $\text{MRCAT}_{\text{adp}}$ and $\text{MRCAT}_{\text{MRair}}$ were compared to the reference CT by evaluation of the mean error and the mean absolute error in terms of HU. To study differences between CT and sCT images in terms of proton rSPR, the HU values of each image were also converted to rSPR. The difference of the MRCAT minus the reference CT rSPR values were calculated in percentage of the average rSPR value of the reference CT. In the following, this quantity will be referred to as "error rSPR". All the analyses were restricted to the treatment field by considering only voxels with at least 10% of the prescribed dose for the generated IMPT plan on the CT. For additional evaluation of HU values in the bone regions, the femurs were manually delineated for all the patients on CT and MR-based sCTs.

PROTON RANGE COMPARISON. To assess the accuracy of the retrieved sCTs in terms of proton range, a BEV range comparison was performed using the generated single field uniform dose plans. Proton range was defined at the 80% distal dose falloff and only dose profiles with a maximum of at least 80% of the prescribed dose were considered. The median range difference between dose distributions on the CT and $\text{MRCAT}_{\text{org}}/\text{MRCAT}_{\text{adp}}/\text{MRCAT}_{\text{MRair}}$ was determined, just as the percentage of profiles with a range agreement better than 3 mm and half the 2.5% to 97.5% inter-percentile range of the range difference distribution.

DOSIMETRIC COMPARISON. To determine the dosimetric accuracy achieved with the sCTs, the dose distributions of the generated IMPT plans recalculated on $\text{MRCAT}_{\text{org}}$ and $\text{MRCAT}_{\text{adp}}$ were compared to that on the CT by means of different 3D global

gamma criteria: (3%,3 mm) with 50% dose threshold, (2%,2 mm) with 50% dose threshold and, for comparison to [Koivula *et al.* 2016], (2%,2 mm) with 10% dose threshold. CTV and PTV D_{98} , D_2 and V_{95} , as well as median PTV dose, were compared for the dose calculations on the CT and $MRCAT_{org}/MRCAT_{adp}$, as well as rectum $V_{50,60,65 Gy}$ and bladder $V_{60,65 Gy}$. Given the impact of inter-scan air cavity mismatches on the calculated proton dose, $MRCAT_{MRair}$ was not further considered in the dosimetric analysis.

3.3 RESULTS

3.3.1 Image evaluation

Figure 3.1 shows the acquired reference CT (panel a) and in-phase MRI (b) for an exemplary patient (P6), as well as the different sCT images: $MRCAT_{org}$ (c), $MRCAT_{adp}$ (d) and $MRCAT_{MRair}$ (e). Differences of the respective MRCAT dataset to the CT are depicted in the bottom row (f - h). CT and MRI showed substantial inter-scan differences regarding position, size and shape of rectal air pockets. The difference images illustrate that copying the internal air cavities from the CT ($MRCAT_{adp}$) minimises differences between CT and MRCAT in the vicinity of the rectum, where $MRCAT_{org}$ (no internal air compartments) and $MRCAT_{MRair}$ (air extracted from MRimages) show deviations to the CT reference. Besides, differences to the CT are most pronounced for the bones. In general, the volume of bony structures was found smaller on the MRCAT images. For the contoured femurs (truncated to the PTV slices) an average volume difference of -11% to the CT was observed for all patients. On $MRCAT_{org}$ this leads to generally overestimated proton ranges (see Section 3.3.2), which was compensated by increasing the assigned synthetic-HU values for spongy and cortical bone in $MRCAT_{adp}$ and $MRCAT_{MRair}$ (cf. Table 3.1). For the femurs, the average HU was increased from 252 ($MRCAT_{org}$) to 336 ($MRCAT_{adp}/MRCAT_{MRair}$), while the average femur HU for the CT was 271. As shown in Figure 3.2, the adaptation of the bone synthetic-HU increased the average mean absolute error when comparing CT and MRCAT from 76 to 83, but reduced the average mean error from -15 to 2, as intended. An increased mean absolute error of 89 was observed for $MRCAT_{MRair}$, likely due to the mismatch of internal air cavities between CT and MRimages. The proton rSPR differences between CT and MRCAT images were on average below 1%, with the smallest average difference of 0.1% for $MRCAT_{adp}$, compared to -0.8% for $MRCAT_{org}$ and -0.4% for $MRCAT_{MRair}$. $MRCAT_{adp}$ also showed the smallest variation between different patients ($\sigma = 0.3\%$).

3.3.2 Proton range comparison

Figure 3.3 shows the dose distribution of the single field uniform dose plan at 90° gantry angle for another exemplary patient (P9). Dose calculated on the CT (used for optimisation, panel a), on $MRCAT_{org}$ (b), $MRCAT_{MRair}$ (e) and $MRCAT_{adp}$ (g) is displayed. The dose difference image in panel c indicates the overestimated proton range on $MRCAT_{org}$ with respect to the CT in the anterior part of the PTV where the beam transverses the femur and the hip bone. At the same time, proton

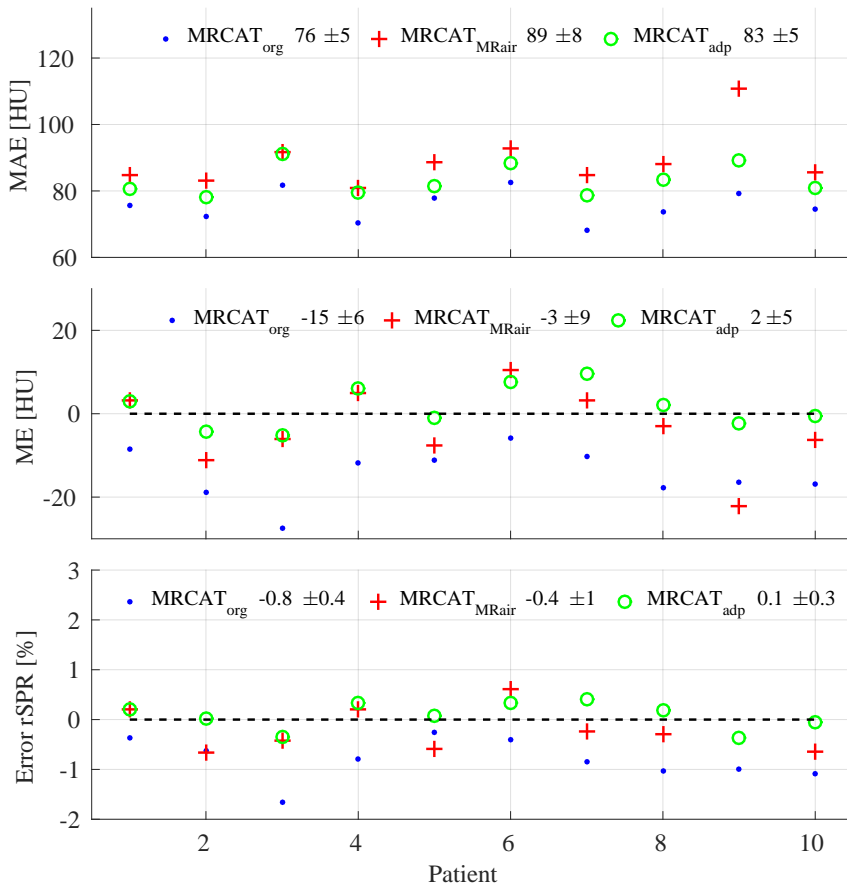


Figure 3.2 Mean absolute error (top, abbreviated as MAE), mean error (middle, abbreviated as ME) and proton rSPR error (bottom) between CT and MRCAT_{org} (blue dots), MRCAT_{adp} (red crosses) and MRCAT_{MRair} (green circles) for all patients in the region with at least 10% of the prescribed dose for the IMPT plan on the CT. Mean \pm one standard deviation (σ) over all patients are given in the legend.

range is underestimated in the posterior part of the PTV, close to the rectum, due to the lack of internal air cavities for MRCAT_{org}. For this patient, the median range difference to the CT was -2.2 mm, with 63% of all dose profiles in BEV having a range agreement better than 3 mm. Adaptation of the bone synthetic-HU considerably diminished the dose differences in the anterior part of the PTV for MRCAT_{MRair} (f) and MRCAT_{adp} (h). Due to pronounced changes in rectum filling between CT and MRI (d), however, the percentage of profile within 3 mm range ($PP_{3\text{mm}}$), was 57% for MRCAT_{MRair}, with a median range difference of -1.8 mm. Copying the rectal air cavities from the CT (MRCAT_{adp}), range agreement is substantially improved, with a $PP_{3\text{mm}}$ of 94% at a median range difference of -0.2 mm to the CT. Residual differences to the CT in the posterior part of the PTV can be attributed to the simplified filling of rectal air cavities by a substitute synthetic-HU value of -600 on MRCAT_{adp}.

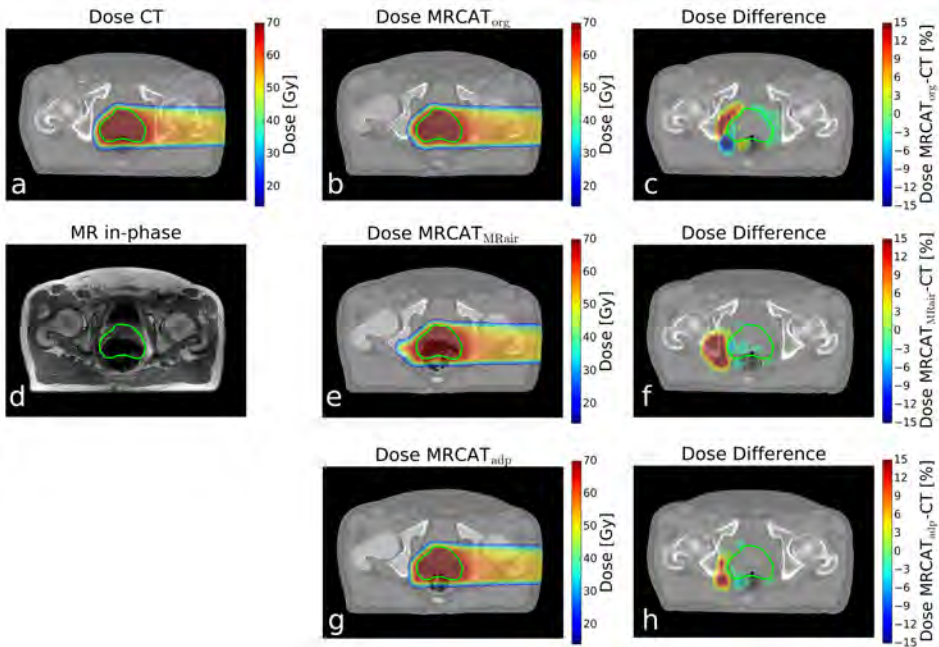


Figure 3.3 Single field uniform dose distribution in a transverse plane as optimised for 90° gantry angle on the CT (a) and recalculated on $MRCAT_{org}$ (b), $MRCAT_{MRair}$ (e) and $MRCAT_{adp}$ (g) for patient P9. Differences between MRCAT- and CT-based dose calculations are shown in panels c, f and h in percent of the prescribed dose. The MR-in-phase image is shown in panel d. The PTV is depicted in green.

A more detailed overview of the range analysis results for all the patients and for the 90° and 270° gantry angle single field uniform dose plans is given in Table 3.2. On $MRCAT_{org}$, the proton range was on average 1.7 mm larger than on the CT, with on average 76% of all BEV profiles having a range agreement better than 3 mm.

The inter-percentile range of the range difference distributions was comparably large, on average 5.1 mm, mainly due to substantial range differences close

Table 3.2 Comparison of single field uniform dose (here abbreviated as SFUD) proton ranges on CT and MR-based sCTs for 90° and 270° gantry angle. Percentage of profiles within 3 mm ($PP_{3\text{mm}}$), median and inter-percentile range (IPR) of the range difference (RD) distributions were considered. For each quantity, mean value, minimum and maximum are calculated over all the patients.

		$MRCAT_{org}$			$MRCAT_{adp}$			$MRCAT_{MRair}$		
		$PP_{3\text{mm}}$ (%)	Median RD (mm)	IPR RD (mm)	$PP_{3\text{mm}}$ (%)	Median RD (mm)	IPR RD (mm)	$PP_{3\text{mm}}$ (%)	Median RD (mm)	IPR RD (mm)
SFUD 90°	Mean	75.4	-1.7	5.1	95.3	0.1	2.7	82.4	-0.2	5.3
	Min	52.1	-2.5	1.7	90.3	-0.5	2.1	57.2	-1.8	2.5
	Max	99.3	-0.4	15.4	99.9	1.4	3.3	97.6	2.0	10.8
SFUD 270°	Mean	76.9	-1.6	5.1	96.5	0.1	2.5	82.2	-0.2	5.8
	Min	51.8	-2.6	1.8	88.4	-0.9	1.8	55.4	-1.9	2.7
	Max	98.2	-0.7	14.7	99.7	1.4	3.7	97.2	1.4	11.6

to the rectum where no internal air is modelled. Thus, 3 mm range pass rates ($PP_{3\text{mm}}$) were as low as 52% for a few cases. After adaptation of the assigned bone synthetic-HU value, the average $PP_{3\text{mm}}$ increased to 87%, with a minimum pass rate of 67% due to missing internal air cavities, which led to an inter-percentile range of 5.3 mm (these intermediate results are not displayed in Table 3.2). Range agreement to the CT was further improved by not only adapting the synthetic-HU but also copying the internal air pockets from the CT: the average range difference between CT and $MRCAT_{\text{adp}}$ was 0.1 mm, with 96% of the BEV dose profiles within 3 mm range. The inter-percentile range of the range difference distribution was considerably reduced to 2.6 mm. In the worst case, a median range difference of 0.9 mm to the CT was found at a 3 mm range pass rate of 88%. The range difference of $MRCAT_{\text{MRair}}$ to the CT was comparable to $MRCAT_{\text{adp}}$ in terms of the median range difference, while the average $PP_{3\text{mm}}$ was 82.3%. Due to inter-scan differences in the air pocket location on CT and MRI, the minimal $PP_{3\text{mm}}$ for $MRCAT_{\text{MRair}}$ was, however, 55% and the average inter-percentile range of the range difference distribution was comparably large (5.5 mm).

3.3.3 Dosimetric comparison

The pass rates obtained for the comparison of the IMPT dose distributions calculated on the CT and $MRCAT_{\text{org}}/MRCAT_{\text{adp}}$ are given for each patient in Table 3.3 for all three considered gamma criteria. Focusing on the high dose region (50% dose cut-off) and the gamma analysis with the most stringent criteria, for $MRCAT_{\text{org}}$, the average $(2\%, 2\text{mm})_{50\%}$ pass rate was 75% [58%, 96%]. Higher pass rates were found for $MRCAT_{\text{adp}}$ with an average $(2\%, 2\text{mm})_{50\%}$ pass rate of 92% [84%, 97%], despite potential residual anatomical inter-scan differences. Only for a single patient (P7), gamma pass rates were lower for $MRCAT_{\text{adp}}$ than for $MRCAT_{\text{org}}$, since this patient had a comparably low bone density on the CT,

Table 3.3 Percentage pass rates for the comparison of IMPT dose distributions on CT and $MRCAT$ using different gamma criteria and dose thresholds (50% and 10% of D_{prescr}). Pass rates for each patient and the mean, standard deviation (σ), minimum and maximum values are calculated over all the patients.

Patient	$MRCAT_{\text{org}}$			$MRCAT_{\text{adp}}$		
	$(3\%, 3\text{mm})_{50\%}$	$(2\%, 2\text{mm})_{50\%}$	$(2\%, 2\text{mm})_{10\%}$	$(3\%, 3\text{mm})_{50\%}$	$(2\%, 2\text{mm})_{50\%}$	$(2\%, 2\text{mm})_{10\%}$
P1	88.3	79.9	95.1	98.1	88.4	97.7
P2	78.4	58.4	89.5	94.9	84.0	96.4
P3	91.4	73.3	94.6	98.4	91.7	98.8
P4	97.3	85.5	96.8	99.5	97.0	99.6
P5	79.7	57.5	89.2	99.0	94.6	99.0
P6	93.0	82.5	96.0	98.7	92.5	98.5
P7	99.4	96.3	99.6	96.3	85.5	97.2
P8	93.7	77.5	94.6	99.3	95.1	99.3
P9	87.7	65.1	91.9	97.6	91.1	98.0
P10	91.2	72.5	94.0	99.4	96.8	99.7
Mean	90.0	74.8	94.1	98.1	91.7	98.4
σ	6.4	11.6	3.0	1.4	4.3	1.0
Min	78.4	57.5	89.5	94.9	84.0	96.4
Max	99.4	96.3	99.6	99.4	97.0	99.7

such that increasing the MRCAT bone synthetic-HU value reduced dosimetric agreement.

The impact of the observed dose differences on clinically relevant DVH parameters for target volumes and organs at risk (OARs) is illustrated in Figures 3.4 and 3.5, respectively. For the target volumes, deviations of up to 10 Gy in PTV D_{98} and up to 15% in CTV $V_{95\%}$ with respect to the CT-based dose were observed for MRCAT_{org} (Figure 3.4, top row), mainly due to missing air pockets in the rectum. Differences were considerably reduced for MRCAT_{adp}, with all investigated DVH parameters agreeing better than approximately 2 Gy ($\sim 2.9\%$ of the prescribed dose) with the CT. The mean/median difference was below 1 Gy ($\sim 1.4\%$ of the prescribed dose). It should be noted that the median PTV dose (D_{50}) was on average underestimated on MRCAT_{org} because of the too low synthetic-HU value. For MRCAT_{adp} there is on average no difference to the CT in PTV D_{50} .

For the rectum and the bladder, differences in DVH parameters were generally smaller. For MRCAT_{org} DVH parameters were mostly within 2% of the CT, for MRCAT_{adp} they were within 1%.

3.4 DISCUSSION

For accurate dose calculation and treatment planning in photon and proton radiotherapy, CT imaging is the primary modality [Pereira *et al.* 2014]. However, many methods have been proposed to enable MR-only radiotherapy in the scope

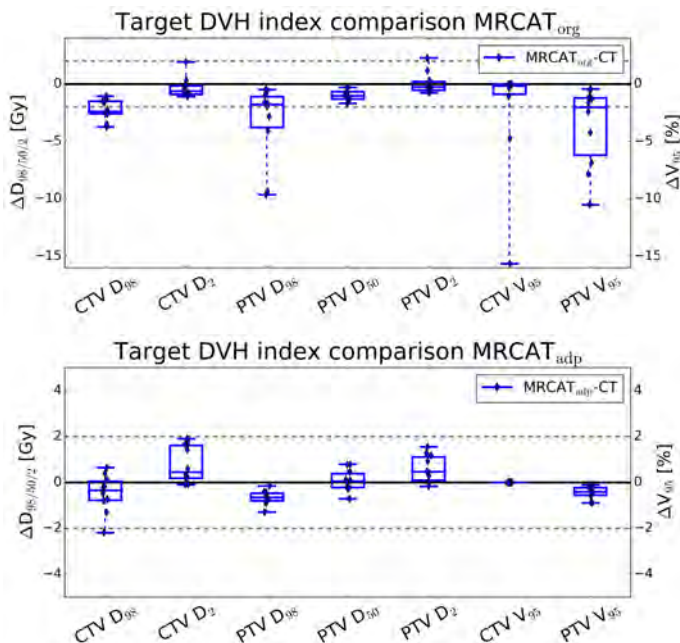


Figure 3.4 Boxplots of target DVH parameter differences between CT and MRCAT_{org} (top), as well as CT and MRCAT_{adp} (bottom). The values refer to the whole course of fractionated treatment. Note the different axis scaling in the two figures.

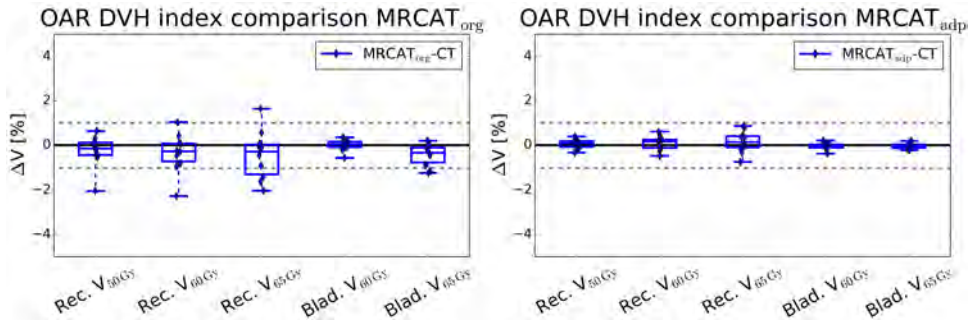


Figure 3.5 Boxplots of absolute OARs DVH parameter differences between CT and MRCAT_{org} (left), as well as CT and MRCAT_{adp} (right).

of photon radiotherapy. This study investigated for the first time whether a commercially available photon-oriented bulk assigned sCT generation method may also be employed for accurate proton therapy treatment planning.

The results showed that MR-only proton treatment planning using directly the commercially available sCT generation method, as originally designed for MR-only photon radiotherapy (MRCAT_{org}), is not sufficiently accurate. In the performed proton range analysis using single field uniform dose plans, the proton range was on average overestimated by 1.7 mm in comparison to the CT reference. This was mainly attributed to an underestimation of the bone volume on MRCAT_{org} with respect to the CT (on average by 11% for the femurs). In addition, substantial discrepancies emerged due to missing internal air cavities: for few cases, not more than 52% the proton depth dose profiles in BEV agreed better than 3 mm in range with the CT and dosimetric deviations of up to 15% to the CT in CTV V₉₅ appeared. Adapting the assigned synthetic-HU values in bones and copying internal air cavities from the reference CT in order to minimise inter-scan differences yielded considerably increased proton dose calculation accuracy (MRCAT_{adp}). Mean differences between CT- and MRCAT_{adp}-based dose calculation in the considered DVH parameters for target volumes and OARs were below 2 Gy and 1 Gy, respectively. The average proton range difference was reduced to 0.1 mm, with on average 96% of all BEV dose profiles showing a range agreement better than 3 mm to the CT. Gamma analysis (2%, 2 mm) at 10% dose cut-off showed an average acceptance rate of 98.4% for all the patients in our study (compared to 94.1% for MRCAT_{org}). This is comparable with the results obtained by [Koivula *et al.* 2016], yielding an average pass rate of 98.6% for the same gamma criterion using a heterogeneous bone model. In terms of the proton rSPR, the average difference between CT and MRCAT_{adp} was $0.1 \pm 0.3\%$ in the region with at least 10% of the prescribed dose. Consequently, based on our patient population, 95% of all pixels have an rSPR error of below $\pm 0.7\%$ (two σ). In comparison, the uncertainty in converting HU values to proton rSPR was estimated in the order of 3.0% (95th percentile) for prostate cancer patients by [Yang *et al.* 2012].

It should be noted that in the scope of this study, only gantry angles of 90° and 270° have been considered since these beam directions provide improved treatment robustness and are the current state of the art in clinical proton therapy for

prostate cancer. Nevertheless, recently also the option of treating patients with anterior-oblique proton beams has been investigated [Moteabbed *et al.* 2017]. For such beam orientations, the amount of bone transversed by the proton beam before reaching the target is smaller than for gantry angles of 90° and 270° . Given the fact that differences between MRCAT_{adp} and the CT were found most pronounced for bony structures, but were minor for soft tissue, we anticipate that the MRCAT synthetic-CT generation approach may provide a similar, or even improved, level of accuracy for treatment scenarios using anterior-oblique beams.

In this contribution, the adaptation of the synthetic-HU values has been obtained based on two out of the ten patients included in the study, and it has been then evaluated for the whole patient population. This proves the feasibility of the methodology. However, further investigations are necessary in order to extend the approach to a larger population and ensure optimal accuracy in proton dose calculation.

Although the bulk assigned sCTs with internal air demonstrated a good agreement to the reference CT, MRCAT generally underestimated the bone volumes. In this work, these differences were compensated by increasing the assigned synthetic-HU in MRCAT_{adp}, yielding a high agreement in terms of the proton range. Still, differences in the shape of the bones may be responsible for the observed small remaining differences between MRCAT_{adp} and CT images, e.g., in CTV and PTV D₉₈ and D₂. Also the copying of air cavities from the CT with a single bulk synthetic-HU value of -600 may contribute to these differences.

A further limitation of the MRCAT approach, being a bulk-assignment method, is the inability to correctly model potential inter-patient variabilities in terms of the bone density, as expressed by the CT. Especially in the femoral region a high inter-patient variability of shape and bone composition has been previously shown in the literature [Carballido-Gamio *et al.* 2013, Hazrati Marangalou *et al.* 2014]. In the context of MR-only radiotherapy, the fact that the method may need adaptation based on a patient population and could encounter difficulties in accommodating inter-patient variability can be deemed as a general limitation, but further investigations on a larger and independent population may be required to clarify these aspects.

Internal air cavities have previously been reported as possible factor confounding dose calculation for repetitive CT imaging sessions [Soukup *et al.* 2009]. Also in this study, it was observed that internal air cavities in the vicinity of prostate cancer patients' PTVs substantially impact the proton range and dose distribution. In particular, we found an average reduction of 14% in terms of percentage of range profiles within 3 mm when comparing sCTs with air cavities deduced either from CT or MR imaging. Due to this, we have proposed a method to automatically detect and insert air cavities as visible during MR acquisition, aiming at representing the patients' anatomy consistently to their actual state. In particular, the availability of a bone model along with the MRCAT approach allows for a straight forward separation of internal air and bone, which may otherwise require non standard MRI sequences with sufficient air bone contrast [Edmund *et al.* 2014], as also pointed out by [Koivula *et al.* 2016]. A full evaluation of the air localisation method was deemed beyond the scope of this work and may be the object of future investigations. Such a study would, however, require highly

correlated MRI and CT data, with internal air cavities at the same position for a direct comparison of air compartments on the CT and MR images. Preferably, the patient should not be repositioned and the two scans should be taken within the typical time scales of changes in the rectum anatomy of few minutes [Kleijnen *et al.* 2016]. In this work, the geometrically accurate assignment of air from the available MR images was assured by visual inspection of the in-phase image and the retrieved $MRCAT_{MRair}$. In clinical practice, the impact of inter-fractional differences in the air cavities may be further reduced, e.g., by using rectal balloons or inserting spacer gel between prostate and rectum [Smeenk *et al.* 2010, Ng *et al.* 2014]. Robust planning is another approach that could be taken into account to mitigate inter-scan differences and calculation uncertainties. This study deliberately avoids the calculation of robust IMPT plans to verify the dose difference between CT and sCTs in a setting which may be more susceptible to density variations between sCT and CT.

To deliver accurate radiotherapy, another aspect, beyond the scope of our investigation, that should be taken into consideration in an MR-only workflow is the geometric accuracy of the sCTs. In this study, the patients' body contours in the sCT images have been matched to the contour of the CT images to minimise inter-scan differences due to patient repositioning. This can positively influence the results obtained. Up to now, geometric accuracy has been investigated in the scope of photon therapy, yielding geometric distortions within ± 1 mm inside the body contour with the same commercial sCT generation method employed in this work [Tyagi *et al.* 2016].

The method proposed in this study is fully automatic and can be performed with an image acquisition and reconstruction time below 4 minutes. This fact may, in the future, enable its application in an online adaptive MRI-guided IMPT scenario [Schippers & Lomax 2011, Oborn *et al.* 2017].

3.5 CONCLUSION

This study shows that accurate MR-based proton dose calculation for prostate cancer treatment could be performed using a commercial solution originally designed for photon radiotherapy, following adaptation of synthetic-HU values. The correct modelling of internal air cavities was found crucial. For this, a novel method to detect air cavities in an MR-only workflow was proposed. The investigated method may be of interest to facilitate MR-only proton therapy and potentially, in the future, online adaptive MR-guided IMPT at considerably reduced imaging dose burden to the patient in comparison to state of the art CT-based IMPT. Clinical implementation of the proposed method will, however, require further investigations on the basis of a considerably larger patient group. In particular, the questions if the assigned bulk synthetic HU values found in this work are also optimal for a larger patient cohort and if they allow for clinically sufficiently accurate proton dose calculation for patients with bone densities values lower or higher than average have to be carefully addressed.

Part II

Patient Positioning

Automatic gold fiducial marker localisation

4

This chapter is based on:

Maspero, M., van den Berg, C. A. T., Zijlstra, F., Sikkes, G. G., de Boer, H. C. J., Meijer, G. J., Kerkmeijer, L. G. W., Viergever, M. A., Lagendijk, J. J. W., Meijer, G. J., & Seevinck, P. R. (2017). **Evaluation of an automatic MR-based gold fiducial marker localisation method for MR- only prostate radiotherapy.** *Phys. Med. Biol.*, 62(20), 7981-8002 <http://doi.org/10.1088/1361-6560/aa875f> [Maspero *et al.* 2017].

Abstract

Background A magnetic resonance (MR)-only radiotherapy planning workflow would reduce cost, radiation exposure and uncertainties introduced by computed tomography (CT)/magnetic resonance imaging (MRI) registrations. In the case of prostate treatment, one of the remaining challenges currently withholding implementation of a radiotherapy planning workflow is the MR-based localisation of intraprostatic gold fiducial marker (FM), which is crucial for accurate patient positioning.

Currently, MR-based FM localisation is clinically performed manually. This is sub-optimal as manual interaction increases workload. Attempts to perform automatic FM detection often relies on detecting signal voids induced by the FMs in magnitude images. However, signal voids may not always be sufficiently specific, hampering accurate and robust automatic FM localisation.

Methods Here, we present an approach that aims at automatic MR-based FM localisation. This method is based on template matching using a library of simulated complex-valued templates, and exploiting the behaviour of the complex MR signal in the vicinity of the FM. Clinical evaluation was performed on seventeen prostate cancer patients undergoing external beam radiotherapy treatments. Automatic MR-based FM localisation was compared to manual MR-based and semi-automatic CT-based localisation (the current gold standard) in terms of detection rate and spatial precision of localisation.

Results The proposed method correctly detected all the three FMs in 15/17 patients. The spatial accuracy (mean) and precision (σ) were 0.9 mm and 0.6 mm respectively, which is below the voxel size of $1.1 \times 1.1 \times 1.2 \text{ mm}^3$ and comparable to MR-based manual localisation. FM localisation failed (3/51 FMs) in the presence of bleeding or calcifications in the direct vicinity of the FM.

Conclusion The method was found to be spatially accurate and precise, which is essential for clinical use. To overcome any missed detection, we envision the use of the proposed method along with verification by an observer. This will result in a semi-automatic workflow facilitating the introduction of an MR-only workflow.

Keywords: **magnetic resonance, radiotherapy, position verification, template matching, MRI simulation, fiducial marker localization**

4.1 INTRODUCTION

Magnetic resonance imaging (MRI)-based radiotherapy radiotherapy planning - also called “magnetic resonance (MR)-only” - has been proposed for several reasons including the reduction of systematic spatial uncertainties introduced when registering computed tomography (CT) and MRI, reduction of costs of the treatment and reduction of patient exposure to ionising radiation [Fraass *et al.* 1987, Lee *et al.* 2003, Karlsson *et al.* 2009, Edmund & Nyholm 2017]. To fully exploit the possible advantages offered by MR-only radiotherapy, several challenges need to be addressed: (1) performing MRI in the radiotherapy treatment position, (2) enabling MR-based dose planning, and (3) generating MR-based reference images for position verification of image-guided radiotherapy (IGRT) treatments [Kapanen *et al.* 2013].

The first point has been addressed through the “MR-simulator”, which utilises dedicated devices as flat table tops [Mcjury *et al.* 2011], coil supports [Kapanen *et al.* 2013, Sun *et al.* 2014], skin markers and lasers [Schmidt & Payne 2015] to facilitate a reproducible patient positioning.

The second point has been investigated through the estimation of MR-based electron density maps, which are called synthetic CT (sCT) ¹ images since they are generated to substitute CT images in the current workflow allowing for calculation of the attenuation of radiation in the body [Edmund & Nyholm 2017]. For prostate cancer radiotherapy, several methods to generate sCTs have been proposed [Lee *et al.* 2003, Chen *et al.* 2004, Dowling *et al.* 2012, Johansson *et al.* 2012, Korhonen *et al.* 2014, Kim *et al.* 2015, Siversson *et al.* 2015, Prior *et al.* 2016] resulting in acceptable treatment plans.

To address the third challenge, we first identify which position verification techniques have clinically been adopted for IGRT [Das *et al.* 2014, Nabavizadeh *et al.* 2016]. IGRT for prostate cancer can be performed based on the location of the prostate itself (usually using cone beam CT), anatomical landmarks, or prostate surrogates, e.g intraprostatic gold fiducial markers (FMs) and implanted electromagnetic transponders [Bujold *et al.* 2012, Ng *et al.* 2014, Zaorsky *et al.* 2017]. Most of the MR-only oriented investigations have so far focused on the MR-based generation of digitally reconstructed radiographs for bone alignment [Chen *et al.* 2004, Dowling *et al.* 2012, Korhonen *et al.* 2014, Kim *et al.* 2015, Tyagi *et al.* 2016]. Nevertheless, it has been shown that bone-based landmarks represent an unreliable surrogate of the true prostate position due to the motion of the prostate with respect to the pelvic bones [Schallenkamp *et al.* 2005], demanding larger planning target volume (PTV) margin recipes with respect to FM-based alignment [Beard *et al.* 1996, van Herk *et al.* 1995, Greer *et al.* 2008]. Previous research has established that implanted FMs permit significantly improved localisation of the target [Fuller & Scarbrough 2006, van der Heide *et al.* 2007, Kupelian *et al.* 2008]. Therefore, MR-based localisation of intraprostatic gold FMs is crucial for accurate prostate irradiation.

Gold FMs are usually cylindrically shaped, with the diameter ranging between 0.5 and 1.5 mm and the length between 2 and 10 mm. Typically three markers

¹In this article, the abbreviation sCT will be used to refer to these MR-based images, however, a variety of other terms, e.g. “pseudo-CT”, or “substitute-CT”, have been suggested in the literature.

are implanted in the prostate prior to the treatment and permanently remain in the target after completion of the treatment [Habermehl *et al.* 2013, Ng *et al.* 2014, Tanaka *et al.* 2016]. During treatment planning, the FMs are easily localised on CT images thanks to their high signal and the specific streaking artefacts [Nederveen *et al.* 2000, Habermehl *et al.* 2013, Chan *et al.* 2015]. In MRI, FMs are depicted as signal voids in magnitude images, and the appearance of these voids varies according to imaging parameters [Vonken *et al.* 2013, Lim *et al.* 2016] and the FM orientation with respect to the magnetic field [Jonsson *et al.* 2012]. In current clinical practice, MR-based manual FM localisation is performed by radiotherapy technicians (RTTs) [Parker *et al.* 2003, Ung & Wee 2011, Kapanen *et al.* 2013]. As the signal void in magnitude images is not highly specific, manual FM localisation can be a challenging task [Chan *et al.* 2015], as calcifications or blood clots may resemble FMs [Hong *et al.* 2012, Ng *et al.* 2014]. To ease MR-based FM localisation, RTTs usually estimate the position of gold FMs after initial localisation on CT, which easily facilitates distinction from calcifications and bleedings.

However, in an MR-only workflow CT images are not available, therefore methods that enhance FM visibility or even enable localisation are demanded to identify the reference patient position that is used during radiotherapy treatment.

Up to now, several groups proposed to support manual FM localisation by enhancing metal object visibility on MRI through positive contrast [Seevinck *et al.* 2011, Varma *et al.* 2011, Zhu *et al.* 2011, Vonken *et al.* 2013, Dong *et al.* 2015], or sequence parameter optimisation [Lim *et al.* 2016]. Attempts to pursue automatic MR-based FM localisation have been scarce. A semi-automatic localisation algorithm was proposed by [van Dalen *et al.* 2003], while fully automatic methods for MR-based FM localisation were only recently presented [Ghose *et al.* 2016, Dinis Fernandes *et al.* 2017]. A key feature of Ghose *et al.*'s method is the use of template matching [Brunelli 2009] between in-vivo data and a manifold template on manually segmented FMs. [Dinis Fernandes *et al.* 2017] investigated the use of a logistic regression model on individual and combined sequences, obtaining the most promising results when a combination of sequences was employed.

Although the results of these approaches have been promising, we see room for improvement, hypothesising that a more accurate fiducial localisation may be achieved by increasing the information available, e.g. using the complex MR images. In this sense, recently, a template matching method based on phase correlation for metal object localisation was proposed [Zijlstra *et al.* 2017], inspired by [Wachowicz *et al.* 2006] and [Kuglin & Hines 1975], which was applied in several brachytherapy applications [Zijlstra *et al.* 2017, Beld *et al.* 2016]. Instead of merely using spin dephasing information presented in magnitude images, this method exploits the phase dispersion induced by susceptibility markers, which is hopefully detectable when employing complex-valued MR images. Furthermore, detailed knowledge of the objects to be localised (geometry, orientation, magnetic susceptibility and B_0 distortion) as well as of the MR imaging parameters are incorporated in this approach. In this way, we aim to exploit all available prior knowledge.

In this study, we will apply this approach for FM localisation after performing the adaptations necessary to enable gold FMs localisation. In particular, we generated a new template specific for the gold FM and designed an image processing

pipeline that allows selection of candidates and eventually identification of FMs. We will present a clinical evaluation of the method against MR-based manual localisation and the gold standard in the clinical practice: CT-based localisation.

4.2 MATERIALS AND METHODS

We conducted a study to assess the performance of the MR-based automatic FM localisation approach here proposed. The study has been performed on prostate cancer patients undergoing external beam radiotherapy treatments to evaluate performances in a clinical setting. This study is divided into four parts. First, we acquired CT and MR images (Section 4.2.1) including a dedicated MR sequence for FM localisation purposes. Second, we obtained locations of the FMs as it was estimated from CT images in clinical practice (Section 4.2.2). Third, we performed both manual and automatic MR-based localisation (Section 4.2.3). Finally, we evaluated the detection rate, accuracy and precision of the automatic FM localisation and compared it to the outcome of the clinical CT-based, and of the MR-based manual localisation method (Section 4.2.4).

4.2.1 Patient data collection

Seventeen consecutive prostate patients (61.5-82 years, mean age = 68.8 years, median age = 68.4 years) underwent both CT (Brilliance CT Big Bore, Philips Healthcare, Best, The Netherlands) and 3T MRI (Ingenia Omega HP, Philips Healthcare, Best, The Netherlands) for radiotherapy planning at the University Medical Center Utrecht (The Netherlands) between September and October 2015 after prostate carcinoma diagnosis. One of the patients (#14) had a hip implantation. The study has been conducted in accordance with the regulation from the local ethical committee.

CT scans were performed with the following imaging parameters: 120 kV, exposure time = 923 ms, tube current between 121 and 183 mA, in-plane matrix = 512×512 pixels, and 3 mm slice thickness. The resolution was variable depending on the field of view (FOV) used. The typical size of the FOV was $500 \times 500 \times 300$ mm³, which corresponds to an in-plane resolution of 0.98×0.98 mm². Patient positioning at CT was conducted simulating the treatment, e.g. using a flat table, knee wedges and tattooing the patient with the aid of laser alignment.

The MR scans were performed within 1-2 hours after the CT scans. A dedicated sequence was designed to locate FMs with MRI. The sequence was a three-dimensional (3D) Cartesian radio-frequency (RF) spoiled dual gradient-recalled echo (GRE). Imaging parameters were: $TE_1/TE_2/TR = 1.4/2.7/4.6$ ms, flip angle = 10° , FOV = $449 \times 449 \times 90$ mm³, acquisition matrix = $376 \times 376 \times 75$, reconstruction matrix = $400 \times 400 \times 75$, bandwidth = 1142 Hz/voxel, readout direction (frequency encoding) = anterior-posterior, and acquisition time = 2 min 10 s. Complex images (magnitude, phase, real and imaginary) were stored for both echoes. Patient setup at MR was performed using a knee wedge, but without a flat table top and without laser-aided positioning. Patients were scanned using anterior and posterior phased array coils (dStream Anterior and Posterior 28 channel coils, Philips

Healthcare, Best, The Netherlands). To avoid compression of patient's anatomy, two in-house-built coil bridges supported the anterior coil.

After the imaging sessions, CT and MR images were registered based on the manual FM localisations, obtained by manual annotation by a RTT. To allow treatment planning, delineations of the target were drawn by a radiotherapist on MR images, while delineations of organs at risk were drawn by an RTT on CT images and then checked by a radiotherapist. Patients underwent intensity-modulated radiotherapy, using 5 beams of 10 MV, with a prescribed dose of 77 Gy to the entire prostate in 35 fractions (further clinical prescriptions are specified in [Lips *et al.* 2008]).

For position verification purposes, each patient received three intraprostatic cylindrical gold FMs (HA2 Medizintechnik GmbH, Germany) measuring 1.0 mm (diameter) by 5 mm. The FMs were transperineally implanted by a physician at least one week prior to the imaging session using two 18-gauge needles placed in a template. The FM implantation was guided by ultrasound imaging and the physician intentionally positioned FMs away from calcifications and keeping a distance between needles larger than 1.5 cm in the lateral direction. The use of FMs allowed online patient position verification and alignment using MV portal imaging projections that were acquired before each treatment fraction: the FM location obtained from CT was matched with the FM location obtained from MV-based digitally reconstructed radiographs as it was calculated in the software used to perform the patient alignment (TheraView NT/CL 5.2.6, TheraView Technology, Leusden, The Netherlands).

4.2.2 Clinical fiducial marker localisation

Clinical FM localisation was based on CT images and it was aimed to provide the reference position of FMs for patient alignment. To generate reference images for the online alignment, digitally reconstructed radiographs were produced in the treatment planning system (Monaco v5.10.00, Elekta AB, Stockholm, Sweden).

The FM positions used during the alignment were semi-automatically extracted from CT. In particular, the localisation consisted of two steps. First, FM locations and orientations were automatically extracted using an in-house tool [Bol *et al.* 2003]. More specifically, the tool selected regions having 6-neighbourhood connected voxels with hounsfield unit (HU) thresholded between 2800 and 3071 measuring a volume between 3.9 and 11.8 mm³, which correspond to 5 and 15 times the volume of a FM. After selection of the regions, the centre and orientation of FMs were extracted calculating the average and the vector of the first principal component [Jolliffe 2002] of each region, respectively. The position of tops and bottoms were calculated from the centre, orientation and length of each FM. The FM locations were used to visualise FMs on digitally reconstructed radiographs in Theraview. Second, an RTT visually checked the consistency of FMs location on digitally reconstructed radiographs keeping CT images as ground truth. In case the RTT noted discrepancies in FM location between CT and digitally reconstructed radiographs, the FM(s) was (were) manually repositioned on digitally reconstructed radiographs under the supervision of a medical physicist. For the purpose of this study, the locations of centre, top and bottom of each FM was

pooled from the clinical database. For simplicity, the term “CT” was used to refer to the FM locations as it was clinically calculated on CT images.

4.2.3 MR-based fiducial marker localisation

MR-based manual and automatic FM localisation was performed on the second echo of the GRE sequence.

Manual localisation

An experienced RTT manually localised FMs by clicking the apparent top and bottom of the marker on magnitude images. Subsequently, the centre of the FM was calculated as the mean position between the top and bottom, and the orientation of the vector connecting top and bottom. Note that the apparent location of the top and bottom of each FM coincided with the centre of a voxel in the GRE sequence, nevertheless, the calculated centre of the FM may have been positioned with subvoxel resolution. The actual position of top and bottom was finally assigned knowing the position of the centre, orientation and length of the FM. The term “MR_{man}” was used to refer to the FM locations performed on MR images by the manual observer.

Automatic localisation

We here describe a method that localises FMs using complex images (real and imaginary) of the GRE sequence. [Zijlstra *et al.* 2017] have recently developed and presented this method for brachytherapy seeds localisation. Here, we present an adaptation of the approach for gold FMs localisation purposes. For clarity, all the steps of the method will be introduced in this section and the details that may be useful to reproduce the method has been provided in the 4.6. During the algorithm design, we assumed that the number of implanted FMs (3) and the target delineations were available prior to FM localisation. To assess the specificity of the approach, the algorithm was allowed to search for a maximum of 4 FMs, even if only 3 FMs were implanted. The approach has been subdivided into four main steps: 1) library generation, 2) template matching, 3) reduction of candidates and 4) selection of FMs.

With respect to the previous work [Zijlstra *et al.* 2017], a new template library specific for the gold fiducials and scan parameters has been generated. Furthermore the image processing pipeline described at point 3) and 4) is novel. Note that in these steps some parameters involved in candidate reduction and selection have been determined empirically after heuristic optimisation, which may have influenced the results in a positive way due to overfitting. Figure 4.1 shows these steps organised according to their chronological order within the patient study. Here, it follows a description of each of the four steps:

- (1) **Library generation.** First of all, the artefact generated by a FM in the GRE sequence was simulated in two steps: (i) calculating of the B_0 perturbation induced by a FM and (ii) simulating the resulting MR signal in the proximity of the FM within the frameworks presented by [Bouwman & Bakker 2012, Zijlstra *et al.* 2017]. In particular, during the calculations, a 3D analytical model of the gold FM in a uniform background was used. The term

“template” was used to refer to the output of the simulation. Note that the output of the simulation was complex-valued data. To allow the localisation of the FM along with its orientation, several templates were generated orienting the FM along different orientations with respect to the main magnetic field direction. This collection of templates was referred to as “library”. Note that the library generation step was performed only one time during the whole study and is specific for the sequence and the FMs employed.

- (2) **Template matching.** For each patient, a region of interest (abbreviated only for this appendix as ROI) was defined as the smallest volume containing the clinical delineation of the prostate after an isotropic expansion of 1.5 cm. A phase correlation [Kuglin & Hines 1975] was performed between the image in the ROI and each template in the library. The template with the highest phase correlation within the library was associated to each voxel in the ROI, such that to each voxel a FM orientation with respect to the main magnetic field was associated.
- (3) **Reduction of candidates.** In principle, all the voxels in the ROI may be selected as FM candidates. To reduce the number of candidates two sub-steps were performed. (i) We hypothesised that the voxels with the highest phase correlation have the highest probability to contain a FM. The first 250 voxels with the highest phase correlation were selected as FM candidates. (ii) To further reduce the number of candidates, we discarded the voxels that were located in hypointense regions having a volume much larger than the hypointense region induced by a FM.
- (4) **Selection of FMs.** The remaining candidates were sorted minimising the error calculated by a local linear regression between the in-vivo data and the template. Afterwards, for each FM candidate, a smoothness criterion was applied on the phase image starting with the candidate having lowest linear regression error until the criterion was satisfied for a maximum of four voxels.

The output of the algorithm was a centre, top and bottom for each FM. The total time to simulate a library of templates was below 7 seconds, and the maximum time needed to locate FMs for a single patient was about 20 seconds in Matlab (R2015a, MathWorks, Natick, MA, USA) and using a quad core 3.4 GHz commercial CPU. The term “MR_{auto}” was used to refer to the FM locations performed on MR images by the here proposed method.

4.2.4 Evaluation

The performances of the proposed MR-based automatic FM localisation approach (MR_{auto}) were compared against performances of clinical CT-based (CT), and of manual MR-based (MR_{man}) localisation. The detection rate and inter-marker distances (IDs) between the FM positions were determined.

Figure 4.2 shows an example, for one patient, of the FM location as obtained by the three approaches in their respective frame of reference. Since the frames of reference differ between localisation methods, FMs were labelled (from 1 to 3)

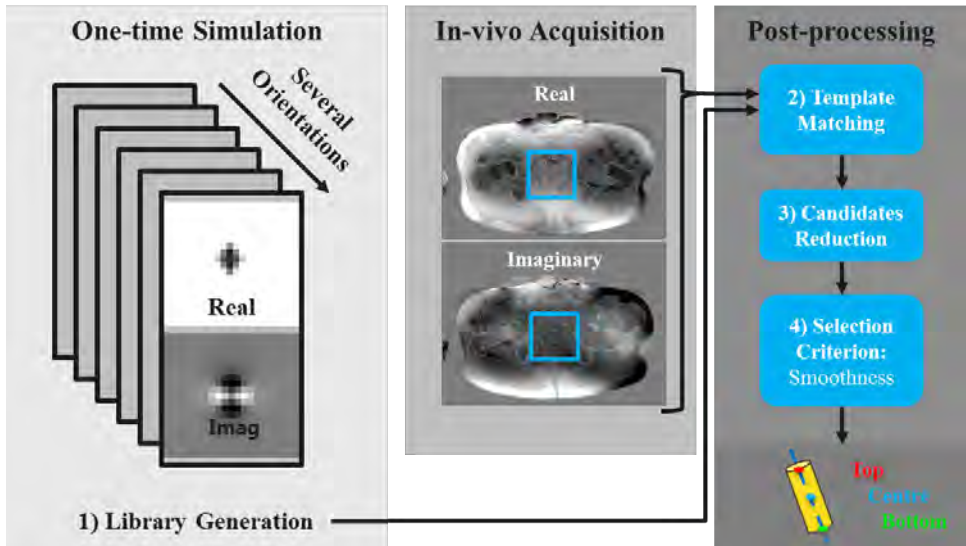


Figure 4.1 **MR-based automatic fiducial marker localisation.** 1) A library was generated from a single simulation containing the complex images of the artefact generated in the proximity of a FM. The library contains simulations of one FM having several orientations with respect to B_0 . For each patient, after the in-vivo acquisition, post-processing was performed: 2) the simulated template was matched with the in-vivo data, 3) possible FM candidates were reduced, and 4) selected according to a smoothness criterion on the phase image. A maximum of 4 FMs was allowed as the output of the method, in terms of centre, top and bottom of the FMs to verify the specificity of the proposed post-processing.

according to the position of their centre along the craniocaudal direction prior to comparison. In case FMs were in the same transverse plane, the left-right direction was used for labelling.

For the three FM localisation approaches, the *apparent detection rate* was calculated as the number of located FMs divided by the number of implanted FMs (51, since 3 FMs were implanted for each patient). We define such detection rate as “apparent” since, at this stage, no check has been performed in terms of false or positive FM detection.

Geometrical evaluation and detection rate

The ID between two FMs was calculated, referring to ID_{ij} as the distance between FMs with label i and j (with $i, j = 1, 2, 3$ and $i \neq j$). To compare the FM location of the three localisation approaches, the differences between IDs with the same label between all FM localisation modalities were calculated as $ID_{MR_{man}} - ID_{CT}$, $ID_{MR_{auto}} - ID_{CT}$, and $ID_{MR_{man}} - ID_{MR_{auto}}$. As these differences can be both positive and negative, a value of zero is to be expected when calculating the mean, assuming no non-rigid deformations. The absolute values for the ID differences were also calculated. To test the precision of the FM detection with respect to CT, each FM was considered as correctly localised when the associated absolute

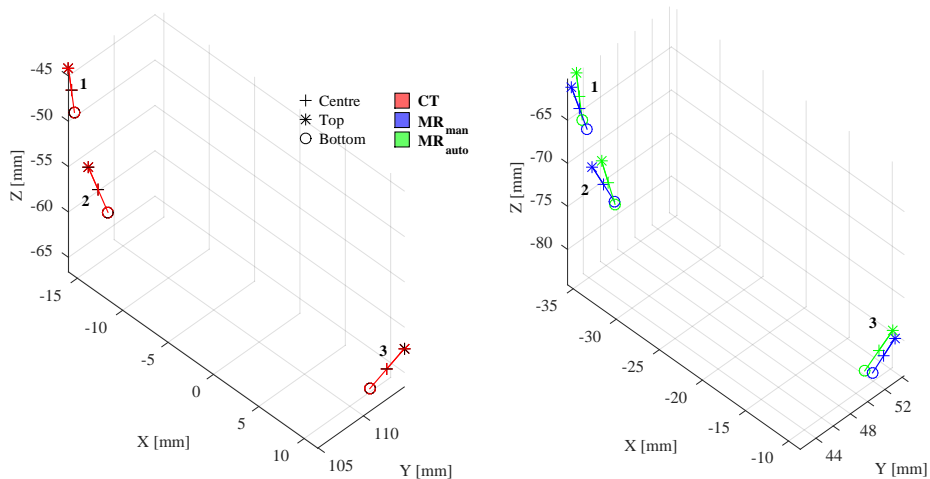


Figure 4.2 **Schematic representation of the FMs for a patient (#12)**. Each of the FMs is labelled (1,2,3) and represented by a line, and by three points that indicate the top (*), centre (+) and bottom (o) of the FM. The figure presents the FM localisation as obtained by the three methods: CT-based clinical localisation (left, red), and MR-based manual (right, blue) and automatic localisation (right, green). MR-based localisations were performed on the same sequence, therefore they are also presented in an identical frame of reference. The directions X, Y and Z of the reference systems correspond to the anterior-posterior, right-left and feet-head directions, respectively.

difference ID_s^2 were < 5 mm (= the length of a FM). We considered the mean and σ of $ID_{MR_{man}} - ID_{CT}$ and $ID_{MR_{auto}} - ID_{CT}$ excluding the IDs associated with incorrectly localised FMs to verify whether MR-based localisation was biased with respect to the clinical gold standard (CT). Furthermore, we considered the σ of the absolute value of $ID_{MR_{man}} - ID_{CT}$ and $ID_{MR_{auto}} - ID_{CT}$ as representative of the **precision** of the MR-based localisation with respect to the clinical gold standard (CT). To allow for the complete comparison among localisation approaches, mean and σ were calculated also between $ID_{MR_{auto}} - ID_{MR_{man}}$. Note that precision of IDs between MR-based FM localisation and CT-based are expected to be larger than IDs between MR-based FM localisation approaches due to the possible presence of non-rigid inter-scan motion.

The benefit of these metrics is that IDs are independent of the absolute position of the FMs in the coordinates used during the localisation, therefore it allows comparison between imaging modality with different frames of reference without recurring to image registration. However, there are certain drawbacks associated with the use of these metrics, since mislocalisation of one FM may bias two inter-marker distances. To provide additional metrics that are independent of inter-marker distances, the euclidean distance between FMs with the same label was calculated between MR_{auto} and MR_{man} , as well as the difference of the FM positions in each direction (X, Y, Z). The advantage of these metrics is that the MR-based localisation is intrinsically performed on an identical frame of reference. This enables estimating the accuracy of FM localisation of MR_{auto} against

²Note that for each FM two IDs are associated in case all the FMs have been detected.

MR_{man} . Mean, maximum difference and σ among all the patients and corresponding FMs were calculated. We considered the mean and σ as representative of the **accuracy** and **precision**, respectively, of localisation between MR-based localisation approaches. Finally, a t-test at 1% significance level was conducted on the difference between each of the components of $MR_{\text{auto}}-MR_{\text{man}}$ to verify whether any bias was observed in terms of FM localisation.

In addition, the *detection rate* was calculated for MR_{man} and MR_{auto} as the number of correctly localised FMs divided by the total number of implanted FMs (51). A case-study based on observation of CT and MR images for all the patients was chosen to obtain further in-depth information on the causes of the incorrect detection and to verify whether false positive FM were detected. The cases with further positive FM were reported. Furthermore, the patient #14 was also reported to highlight the performance of FM localisation in the presence of hip implantation.

Impact on patient alignment

To compare the two MR-based localisation methods (MR_{man} and MR_{auto}) and investigate the possible influence of their difference on the patient alignment, we performed, for each patient, registration between CT and both MR-based localisation methods. This was done by matching the centre of FMs between CT and MR_{man} and between CT and MR_{auto} . The matching of the FMs was performed by only applying translations to realistically mimic the patient alignment at the linear accelerator. More specifically, for each patient, the centre of mass (average among the three FMs) of the FMs localised by MR_{man} and MR_{auto} was aligned (translation only) with the centre of mass of the FMs localised on CT. To compare the differences between registrations, we assess the quality of the registrations in terms of root mean square of the residual mismatch between FMs with the same label [Ung & Wee 2011], referred to the root mean square error, which was calculated for each patient after the registration. In case the root mean square error was larger than 2.5 mm, the quality of registration was considered poor, and the registered FMs were visually checked to assess the origin of the poor registration. In addition, the difference of the translation vectors obtained aligning MR_{man} to CT and MR_{auto} to CT in each direction (X,Y,Z) was calculated for each patient using mean, σ and range over the patient population. A t-test at 1% significance level was calculated for each component of the difference between translation vectors over the patient population to verify whether any systematic shift has been introduced between registration based on the two MR-based localisation modalities.

4.3 RESULTS

4.3.1 *Detection rates*

Table 4.1 provides the summary statistics for detection rates obtained by the three approaches introduced in Sections 4.2.2 and 4.2.3. From the first column of the table, it appears that the localisation clinically performed on CT, as well as the manually performed on MR (MR_{man}), detected all the FMs implanted. Interestingly, the here proposed MR-based automatic approach (MR_{auto}) never located > 3 FMs

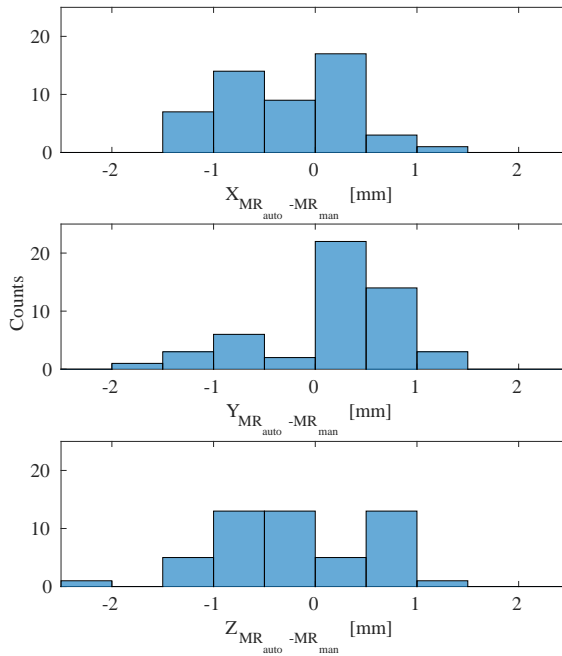


Figure 4.3 Histogram of the difference $MR_{auto} - MR_{man}$ of the position of corresponding FMs (with same label) for all the three directions: (top) X = anterior-posterior, (centre) Y = right-left, (bottom) Z = feet-head.

for any of the patients, even if the detection of a maximum of 4 FMs was allowed. For one patient (#1) two FMs were localised resulting in an apparent detection rate of 0.98. Considering the incorrectly detected FMs, it resulted that one FM was not correctly localised for the patient #4 both by MR_{man} and MR_{auto} , lowering the detection rate for both the MR-based localisation approaches with respect to their apparent detection rate.

4.3.2 Geometric accuracy and precision

MR_{man} vs MR_{auto} The euclidean distance between FMs with the same label between MR_{auto} and MR_{man} were 0.91, 0.53, and 3.14 mm in terms of mean, σ and maximum among all the patients and FMs, respectively. Both the spatial accuracy (mean) and precision (σ) between MR-based localisation approaches appears to Table 4.1 Apparent detection rate (first column), and detection rate (second column) for the CT-based clinical localisation (CT), MR-based manual (MR_{man}) and MR-based automatic (MR_{auto}).

	Apparent Detection Rate	Detection Rate
CT	51/51 = 1	ground truth
MR_{man}	51/51 = 1	50/51 = 0.98
MR_{auto}	50/51 = 0.98	49/51 = 0.96

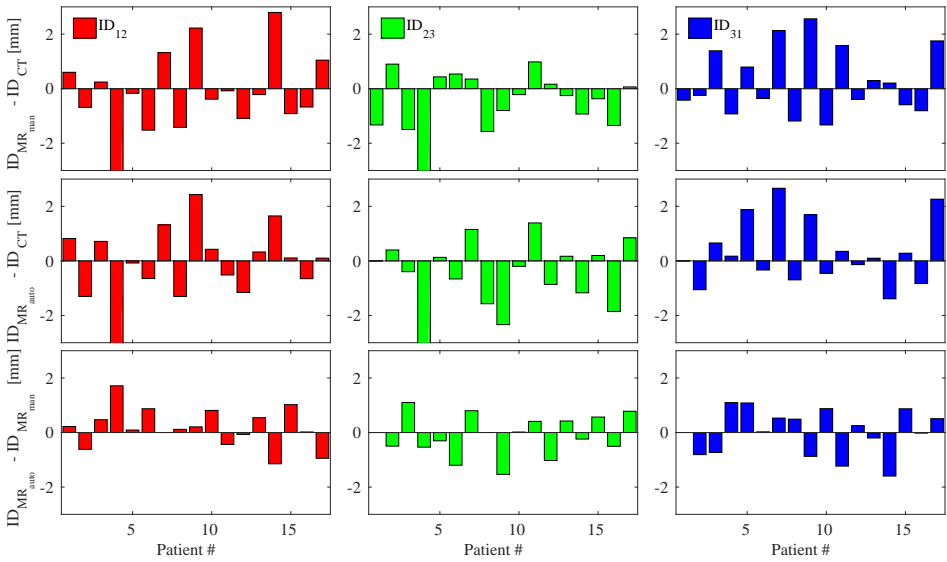


Figure 4.4 Barplot of the difference of inter-marker distance (ID) of corresponding FMs between MR_{man} -CT (top), MR_{auto} -CT (centre), and MR_{auto} - MR_{man} (bottom). The left plots (red) refer to the ID between FM 1 and 2, the centre plots to the ID between FM 2 and 3, while the right plots to the ID between FM 3 and 1. The IDs relative to MR_{auto} for the FM 3 and were not plotted since the FM was not detected.

be below the image resolution ($1.1 \times 1.1 \times 1.2 \text{ mm}^3$). The maximum difference value occurred for patient #4 and FM #2, but as outlined in the previous section, for this FM an incorrect detection occurred. Excluding this FM from the statistics, the maximum value obtained was reduced to 1.73 mm, which is a distance $< 2.5 \text{ mm}$ (2 voxels). Figure 4.3 shows the histogram of the difference MR_{auto} - MR_{man} of the position of corresponding FMs (with the same label) for all the three directions. From the figure, it stands out that the maximum difference observed between manual and automatic MR-based FM localisation approaches was within 2 voxels. The null hypothesis was rejected ($p < 0.001$) in the anterior-posterior ($X = \text{readout}$ direction) direction according to the result of the t-test. This result suggests that FM localisation between the manual observer and the automatic approach along X direction significantly differed. In particular, in terms of average among all the FMs, the absolute difference in X was $0.26 \pm 0.49 \text{ mm}$ (1σ).

INTER-MARKER DISTANCES Figure 4.4 shows the difference of IDs of the corresponding (having the same label) FMs between localisation approaches. From this figure, we can see that the patient #4 has ID differences $> 5 \text{ mm}$ for the FM #2 for both the MR-based localisation approaches. This suggests that such FM was incorrectly located by MR_{man} and MR_{auto} , resulting in a false positive detection. Furthermore, ID differences relative to the FM #3 localised with MR_{auto} are not plotted for the patient #1 in Figure 4.4, since such FM was not located (false negative detection).

In summary, Figure 4.4 highlights that: for patient #1 MR_{auto} the FM #3 resulted in a false negative detection for the MR_{auto} approach, while for patient #4 the FM #3 resulted in a false positive detection for the MR_{man} and the MR_{auto}

approaches. These FMs are considered as outliers and a more detailed analysis is given in the following section. As reported in Table 4.2, averaging the ID differences among true positive detected FMs over all the patients, the mean and σ were about 0 mm and <1.2 mm for all the compared FM localisation approaches. We concluded that the ID metric was not biased over the patient population. We identified the σ over the absolute values of ID differences as indicative of the precision of the FM localisation. It is apparent from Table 4.2 that the precision of the localisation was comparable between approaches. Therewith, the precision resulted from comparing all the three methods was lower than the voxel size ($1.1 \times 1.1 \times 1.2$ mm²) of the GRE sequence. From the table, it can be seen that maximum ID difference obtained was < 3 mm when localisation was performed between different imaging modality, and < 2 mm between MR-based FM localisation approaches.

4.3.3 Outliers of MR-based FM localisation

To understand possible origins of the false negative, and false positive detections, we present the CT and MR images of the patient #1 and #4. As shown in Figure 4.5 (left), the false negative detection on the patient #1 occurred in the proximity of a large hypointense signal around the FM on GRE (circle on the bottom left image). To further understand the origin of such large hypointense signal, we checked all the MR sequences acquired during the imaging session. From a 3D T1 weighted sequence, we concluded that bleedings result in enlarging the dimension of the hypointense region in proximity of the FM. This may explain the false positive detection, since the artefact generated by the FM may, in this case, do not match with the simulation due to the presence of blood. Figure 4.5 (right) shows the scenario for the patient #4: a hyperintense area on CT (within the square), which is not characterised by CT streaking artefacts was localised as FM on MR images, but it was not detected as a FM on CT. Such hyperintense area on CT occurred in the proximity of a calcification. We hypothesised that the presence of calcifications contributed to the false positive and negative detection for the patient #4. During the inspection of all the patients, we did not notice any further false positive detection.

Table 4.2 Statistics of the correctly detected FMs in terms of inter-marker distance (ID) differences and its absolute value between localisation approaches (CT, MR_{man} and MR_{auto}). The results are expressed in mm.

	ID difference		ID difference		
	Mean	σ	Mean	σ	Maximum
ID _{MR_{man}} -ID _{CT}	0.01	1.13	0.90	0.66	2.80
ID _{MR_{auto}} -ID _{CT}	0.00	1.14	0.89	0.70	2.66
ID _{MR_{man}} -ID _{MR_{auto}}	0.03	0.77	0.62	0.45	1.71

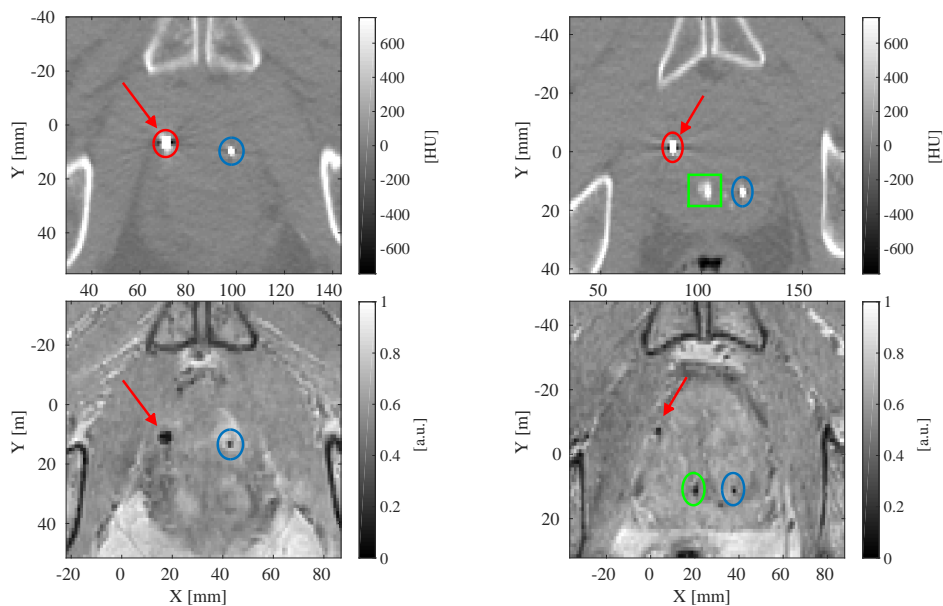


Figure 4.5 Corresponding transverse planes of CT (top) and MR images (bottom) of patient #1 (left) and patient #4 (right) in the proximity of intraprostatic FMs. The center of the circles indicate the position of the FM in the selected plane as localised by the CT (top) and MR_{auto} (bottom) approach. The colours of the circles highlight which FMs have the same label. For the patient #1 (left) and #4 (right), the arrows highlight the position of the FMs that resulted in false negative detections. For the patient #4 (right) the square on CT indicates the location of the calcification that led to FM false positive detections with the MR_{man} and MR_{auto} approach.

4.3.4 Impact on patient alignment

As shown in Figure 4.6 (left), the quality of registrations, only taking into account translation, was comparable between the MR-based methods for all the patients. For the patient #4, a poor quality of the registration was found. As already observed in the previous section (4.3.3), for such patient false positive and negative detection occurred. Interestingly, even for this patient (#4), when considering the centre of mass, the patient alignment seems to be acceptable (Figure 4.6, right).

As it can be seen from the Table 4.3 the range of differences between translation vector is within the voxel resolution, and therefore we can conclude that the patient alignment based on FM location obtained with the here proposed method was comparable (within 1 voxel) to the patient alignment based on FM location obtained by a manual observer.

Nevertheless, the p -value highlights that a systematic shift occurred in the anterior-posterior direction (X), which is the frequency encoding direction. This is in accordance with the results reported in Section 4.3.2, and it reveals that the FM localisation difference impacted also the patient alignment along the readout direction. In the following section, we will elaborate on the possible causes of such reported difference.

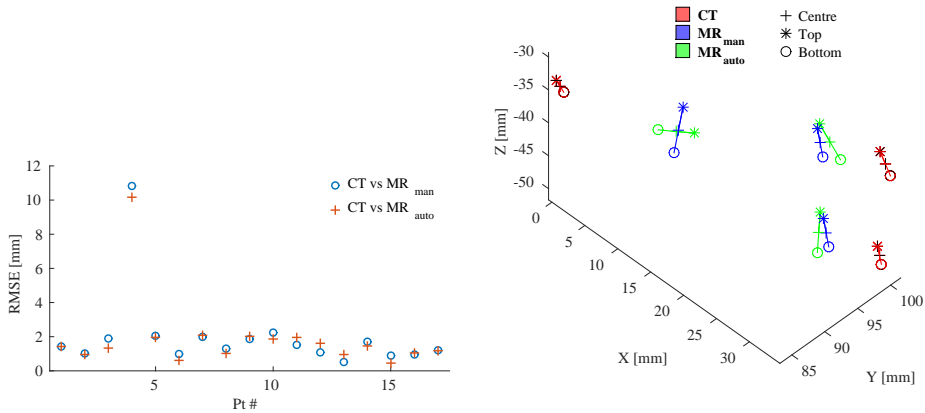


Figure 4.6 (Left) Root mean square error (RMSE) of the mismatch between corresponding (with the same label) FMs after registration (translation only) of MR_{man} (○) and MR_{auto} to CT (+). (Right) Schematic representation of the FMs as localised by the three localisation methods after registration for the patients #4: CT-based clinical localisation (red), and MR-based manual (blue) and automatic localisation (green).

4.4 DISCUSSION

State of the art IGRT of prostate cancer within an MR-only workflow requires the localisation of gold FMs [Fuller & Scarbrough 2006, van der Heide *et al.* 2007, Kupelian *et al.* 2008].

To facilitate MR-based FM localisation, we proposed an MR-based automatic gold FM localisation approach which relies on a template matching method applied to the complex MRI data, aiming to fully exploit the signal behaviour in the vicinity of a FM. The here proposed method performed similarly to an operator resulting in 50/51 FMs automatically localised within 2 voxels (2.4 mm) the manually localised FMs. In addition, when compared to the clinical standard (CT), the automatic MRI-based FM localisation resulted in all the 3 FMs being correctly de-

Table 4.3 Statistics in terms of mean, σ , range and t-test over the patient population of the difference between the translation vectors obtained with the two MR-based localisation approaches. The statistics, except for the p -values, are expressed in mm.

Translation vector			
MR _{auto} - MR _{man}			
	X	Y	Z
Mean	0.28	-0.08	0.17
σ	0.33	0.39	0.42
Minimum	-0.37	-0.75	-0.20
Maximum	0.75	0.56	1.20
p -value	0.003*	0.41	0.12

* p -value < 0.01 = the null hypothesis is rejected.

tected for 15 out of 17 patients and with precision < 1 mm. When comparing our approach to the clinical standard, inter-scan motion may have occurred between the two imaging sessions [Beard *et al.* 1996, van Herk *et al.* 1995, McPartlin *et al.* 2016, Kupelian *et al.* 2008]. To minimise the effect of inter-scan motion, we used inter-marker distances (IDs) as a metric, which is insensitive to rigid-body transformation but is sensitive to prostate deformation [Kupelian *et al.* 2005, van der Heide *et al.* 2007]. The difference of IDs between automatic MR-based localisation and the clinical standard resulted in a mean of 0 mm and a σ of 1.14 mm. This result may indicate that prostate deformation was not observed in our study over the patient population. This is in line with previous research when considering IDs variation between irradiation sessions [Kupelian *et al.* 2005].

To understand the performance of FM localisation in presence of a hip implant, we manually inspected the FM location for the patient #14. No evidence was found for the systematic difference between MR-based FM localisation, and between MR- and CT-based. The result is surprising and it encourages future research for these cases, nevertheless, these findings cannot be extrapolated to all hip implants patients.

When considering the false detections, bleedings and calcifications were among the reported causes. This is in line with previous research [Hong *et al.* 2012, Ng *et al.* 2014]. More specifically, calcifications are expected to occur in about 40% of the cases [Hong *et al.* 2012]. Given the high rate, finding correct FM location for such cases is highly demanded to facilitate clinical implementation. Previous studies showed that susceptibility weighted imaging may help to identify calcifications and bleedings [Wu *et al.* 2009, Bai *et al.* 2013, Chen *et al.* 2014, Berberat *et al.* 2014], thus an approach that foresees integration of susceptibility weighted imaging with the here presented approach may be of interests for a future study.

To date, two studies have investigated performances of MR-based approaches for gold FMs localisations. [Ghose *et al.* 2016] proposed to exploit manifold learning and spectral clustering to localise gold markers from manually segmented volumes. Their method showed promising results, however, it required manual interaction to generate references for data training. The manual interaction may need to be repeated when varying the MR image parameters or type of FMs. [Dinis Fernandes *et al.* 2017] investigated the use of logistic regression, obtaining the most promising results when several MR sequences were employed. In terms of detection rate our study resulted in an higher number of correctly detected FMs with respect to the just presented studies.

An aspect that is important for MR-only radiotherapy is the accuracy of FM localisation. MR images may be subject to geometric distortions caused by the system and/or the patient [Fransson *et al.* 2001, Walker *et al.* 2014, Weygand *et al.* 2016]. When considering MR-simulators, strict geometric fidelity tests are mandatory to ensure that system-dependent geometric distortions are minimised [Kapainen *et al.* 2013]. Note that, since system-related distortions increase proportionally with the distance from the isocentre of the MR scanner, we expect that geometric fidelity is higher than 1 mm within a distance of 10 cm from the isocentre [Wang *et al.* 2004, Sun *et al.* 2014, Xing *et al.* 2016]. If the patient is positioned with the prostate in the centre of the FOV, we could expect accuracy of the same order. Nevertheless, patient-related distortions may also contribute, especially

when metallic objects are present [Hargreaves *et al.* 2011], or when the rectum is filled with air, as both metal and air induce magnetic susceptibility related field changes. Previous studies demonstrated that gold FMs may cause small position deviations (< 1 mm) of the imaged marker positions with respect to the actual marker positions [Jonsson *et al.* 2012]. As [Jonsson *et al.* 2012] showed, deviations can be mitigated by the MR imaging parameters. We believe that geometric accuracy is crucial for MR-only radiotherapy, therefore we utilised a method that provides the original location of the FM by taking into account the FM-induced B_0 distortion. By doing so, potential geometric distortions related to interference between local field inhomogeneities caused by the fiducials and the readout gradients are mitigated. In addition, the dedicated GRE sequence used in our study had high bandwidth (1142 Hz/voxel) minimising possible distortions in the readout direction to a sub-voxel level. Surprisingly, a statistically significant difference in the readout direction (anterior-posterior, or X) between MR-based localisation approaches was found. A possible explanation for this might be that the observer perceived that the signal void was shifted with respect to the real position of the FM, whereas the automatic method incorporated these effects. As [Jonsson *et al.* 2012] underlined, a deviation of about 0.5 mm was reported for susceptibility induced by a gold marker and bandwidth = 1200 Hz/voxel. This is compatible with the observed deviation along X, and it is in line with previously accepted distortion for MR-based FM localisation [Tyagi *et al.* 2016, Dinis Fernandes *et al.* 2017]. In our study, we considered the MR-based manual FM localisation as a standard without further questioning its precision and geometric accuracy. Unfortunately, the availability of studies to quantify inter-observer variability in gold FM localisation is limited when excluding x-rays-based studies. [Huisman *et al.* 2005] reported that inter-observer variability resulted in uncertainties within 0.4-0.6 mm. The uncertainties were calculated as σ at the centre of the prostate between CT-MR registration. In our study, uncertainties (σ) impacting the translation was in a range of 0.3-0.4 mm, which is in line with the results of the previous study [Huisman *et al.* 2005].

The FM localisation has been demonstrated only with a single centre dataset; hence, a generalisation of the method across scanners and different shapes of gold FMs requires further tests. In any case, the here proposed method is, in principle, applicable to different FMs as long as the shape, dimensions and composition of the FMs are known. In addition, our method is flexible since it may be employed for different MR sequences. In principle, a different sequence may possibly impact gold FM appearances and performances of markers localisation. In this sense, an optimisation of the image parameters might result beneficial to reduce false positive or false negative detection and might be the object of future studies. Note that if a different combination of MR sequence and FM is employed, a new template library will need to be generated.

We believe that the proposed approach will facilitate MR-only radiotherapy workflows by reducing manual interaction. Moreover, such method could also be applied in a standard MR-CT workflow to reduce workload for registration purposes. To ensure patient alignment, 3 FMs needs to be at least localised [Ung & Wee 2011]. The results obtained in terms of false positive detection would not allow patient alignment for 2/15 patient. This rate is considered too high to ac-

cept a fully automatic procedure. In this sense, we believe that a semi-automatic scenario would still be favourable to reduce workload and limit FM localisation variability [van Dalen *et al.* 2003]. In particular, the proposed sequence has already been shown to facilitate manual depiction of FM with respect to single echo GRE and fast spin echo sequences [Schieda *et al.* 2015]. Further speculating, a scenario that could facilitate the automatic FM localisation could be by introducing a 4th intraprostatic FM. This could be performed without creating additional patient discomfort since, for each needle insertions, two FMs can be released as it is already currently performed for two of the FMs. In this way, the automatic algorithm may still ensure target localisation on reference images in case 1 out of 4 FMs will be falsely detected. This may enable a safer introduction of the automatic FM localisation. Another approach that it is worthed investigation is automatic quantification of the correctness of FM localisation. Interestingly, Ghose *et al.* 's designed an automatic warning that was raised to recall attention for possible incorrectly detected FMs. We believe that such a feature facilitates clinical implementation of MR-based automatic FM localisation. In this sense, our experience suggests that the phase correlation could help to quantify the confidence of detection since high correlation corresponds to a high match but further investigations are required.

As a final note, we would like to stress the fact that, in this article, FM localisation has been performed in a separate sequence with respect to the sequences used for sCT generation or target delineation. Ideally, to minimise intra-scan motion and to ensure geometric fidelity, the sequence used for target delineation and FM localisation should be performed in a single scan with acquisition time in the order of 2/3 min since intra-scan motion increases with the treatment time [McPartlin *et al.* 2016]. In this sense, we believe that MR-only would not benefit from a multi-sequence approach [Dinis Fernandes *et al.* 2017]. The proposed method can be, in principle, applied to any GRE sequence, therefore it could be integrated with the sequence used for sCT generation or for target delineation. Actually, the sequence here presented is similar to what has been already used by other groups [Tyagi *et al.* 2016] and by our group [Maspero *et al.* 2017] for sCT generation. In any case, when it is not possible to incorporate the FM localisation with the sequence used for sCT generation or target delineation, our suggestion is to acquire the three sequences one after each other such that intra-scan motion is as low as possible and the relative position of the prostate among the sequence is consistent.

4.5 CONCLUSION

This project was undertaken to design an MR-based automatic method to localise intraprostatic gold fiducial markers and evaluate its performances. The results of this study indicate that gold FMs were automatically localised with detection rate, accuracy and precision comparable to a human expert. We envision that the method may facilitate the introduction of MR-only radiotherapy workflow reducing the manual workload and ensuring geometric fidelity.

4.6 APPENDIX: PERFORMANCES OF MR-BASED AUTOMATIC FM LOCALISATION

In this section details that may result useful to reproduce the work are presented along with an evaluation of the discriminative power of the Fiducial Marker (FM) selection. In particular, the steps (1) and (2) have already been presented elsewhere [Zijlstra *et al.* 2017] and represent an adaptation of the previous method for matching with gold FMs. The details follow maintaining the division into steps presented already in Section 4.2.3:

- (1) **Library generation.** (i) The B_0 perturbation (ΔB_0) induced by one FM was obtained by fast forward field-shift calculations [Bouwman & Bakker 2012]. During the calculations, the 3D analytical model of the gold FM consists of a cylinder with diameter = 1 mm and length = 5 mm. The uniform background simulated was water. To perform the ΔB_0 calculation, the magnetic susceptibility (χ) were set to -9 ppm in the background (water) and to -34 ppm in the FM (gold). (ii) To simulate the signal in the proximity of a FM for the GRE sequence employed during the in-vivo data acquisition, we used the FORECAST framework [Zijlstra *et al.* 2017]. This framework simulates the off-resonance artefacts for steady-state GRE sequences with a lower computational complexity than full Bloch simulations. During the simulation, the proton density relative to water was set to 1 in the background and to 0 in the FM. In addition, the T_2 value of the background was set to 50 ms. Fast forward ΔB_0 simulations were performed on a grid with resolution $0.07 \times 0.07 \times 0.08$ mm³ and an FOV of $23.6 \times 23.7 \times 25.2$ mm³. The resolution of the ΔB_0 calculation was chosen to be higher than typical MR scan resolution to avoid, at least at this stage, partial volume effect. When employing the FORECAST framework, the resolution of the simulation was matched to the GRE sequence. During the generation of the library, a total of 321 template were generated resulting in an angular resolution of approximately 8° . Note that the FM is cylindrically symmetric, therefore during the library generation any orientations with respect to B_0 with symmetry degeneracy was not considered.
- (2) **Template matching.** The phase correlation [Kuglin & Hines 1975] was performed between the image (I) in the ROI and each template (T) in the library. Mathematically, phase correlation (here abbreviated as PC) was implemented as follows:

$$PC = \mathfrak{F}^{-1} \frac{\mathfrak{F}(I)^* \cdot \mathfrak{F}(T)}{|\mathfrak{F}(I)^* \cdot \mathfrak{F}(T)| + \epsilon}$$

where \mathfrak{F} refers to the fast Fourier transform, $*$ refers to the complex conjugation, and $\epsilon = 2.2 \cdot 10^{-16}$ was the floating point accuracy during the calculation that was added to the denominator to avoid singularities in case both T and I were zero.

- (3) **Reduction of candidates.** After the selection of the first 250 candidates (i) we performed image further reduction using a method inspired by [Vonken

et al. 2013]. In particular, an heuristic approach was used to define the volume of a hypointense region induced by a FM. First of all magnitude images were thresholded (25% of the maximum intensity in the ROI) and regions were defined in the binary masks according to their connectivity (26-neighbourhood connected components). Second, the volume of one hypointense region was calculated from the simulated library since the size of the region may change according to the orientation [Jonsson *et al.* 2012]: for each template the volume of the hypointense region was calculated as the number of voxels having intensity lower than the average value in the template minus five times its standard deviation (σ). Averaging the volumes over the whole library, we estimated that the hypointense region was about 46 voxels ($\sim 70 \text{ mm}^3$). Finally, the candidates in regions having a volume larger than 184 voxels, which corresponds to four times (= maximum amount of FMs that we searched for) the volume of a hypointense region in the proximity of a FM, were excluded.

- (4) **Selection of FMs.** The linear regression was locally performed on 3D patches having the same size of the template. The smoothness criterion was applied on patches having the size of the template and the candidate as centre. In particular, the criterion was defined as follows: FMs were selected only if the local smoothness (S) of the image phase ($\phi_{I(x,y,z)}$) was increased after voxelwise subtracting the template phase ($\phi_{T(x,y,z)}$). More specifically, S over the image (I) was calculated as:

$$S(\phi_{I(x,y,z)}) = \left| \frac{\partial e^{i\phi_{I(x,y,z)}}}{\partial x} \right|$$

where (x) represents here the phase encoding direction (transverse plane, left-right). The criterion can be mathematically written as:

$$\sum [S(\phi_{I(x,y,z)}) - S(\phi_{I(x,y,z)} - \phi_{T(x,y,z)})] > 0$$

where \sum indicates the voxelwise sum over the patch. The smoothness criterion was calculated only over the phase encoding direction after heuristically observing that this direction maximised the specificity of the selection.

The discriminative power of the candidate selection during the step 3 and 4 is reported in Table 4.4 in terms of number of voxel considered as a FM candidate. As shown in the table, the step 4 (i.e. smoothness criterion) reveals to have the highest discriminative power. Furthermore, the σ of step 3 (ii) is large since such step is applied only in case a patients presents large signal voids that are usually generated by calcifications. Since not all the patients present intraprostatic calcifications, the discriminative power of such step is variable.

Table 4.4 Discriminative power of the steps of the algorithm, expressed in terms of number of voxels. The last row reports also the mean and σ over the patient population. The steps (1) and (2) are not reported since refers to the template generation and matching and no candidate selection is performed.

Patient #	Step 3(i)	Step 3(ii)	Step 4
1	250	249	2
2	250	243	3
3	250	249	3
4	250	236	3
5	250	166	3
6	250	234	3
7	250	246	3
8	250	207	3
9	250	144	3
10	250	216	3
11	250	247	3
12	250	238	3
13	250	245	3
14	250	250	3
15	250	242	3
16	250	209	3
17	250	220	3
Mean$\pm\sigma$	250 \pm 0	226 \pm 30	2.9 \pm 0.2

Manual gold fiducial marker localisation

5

This chapter is based on:

Maspero, M., Seevinck, P. R., Willems, N. J. W., Sikkes, G. G., de Kogel, G. J., de Boer, H. C. J., van der Voort van Zyp, J. R. N., & van den Berg, C. A. T. (2017). **Evaluation of manual gold Fiducial Marker localisation for Magnetic Resonance-only prostate Radiotherapy.** *Radiat. Oncol.*, submitted, [Maspero *et al.* 2018].

Abstract

Background The use of intraprostatic gold fiducial markers (FMs) ensures highly accurate and precise image-guided radiation therapy for patients diagnosed with prostate cancer due to the easy detection of FMs on photon-based imaging, such as computed tomography (CT) images. Recently, magnetic resonance (MR)-only has been proposed for radiotherapy treatment planning to simplify the workflow and reduce possible systematic uncertainties. A critical, determining factor in the accuracy of such an MR-only simulation will be correct localisation of FMs using sole MR images. *Purpose* The aim of this study is to evaluate the performances of manual MR-based FM localisation within a clinical environment.

Methods We designed a study in which 5 clinically involved radiotherapy technicians (RTTs) independently localised gold FMs implanted in 16 prostate cancer patients. Two scenarios were investigated: employing a single MR sequence or a combination of sequences. For both scenarios, inter-observer precision and accuracy were assessed for localisation in terms of 95% limit of agreement on single FMs (LoA)/ centre of mass (LoA_{CM}) and inter-marker distances (IDs), respectively.

Results The number of precisely located FMs (LoA < 2 mm) increased from 38/48 to 45/48 FMs when localisation was performed using multiple sequences instead of a single sequence. When performing localisation on multiple sequences, imprecise localisation of the FMs (3/48 FMs) occurred for 1/3 implanted FMs in three different patients. In terms of precision, we obtained LoA_{CM} within 0.25 mm in all directions over the precisely located FMs. In terms of accuracy, IDs difference of manual MR-based localisation versus CT-based localisation was on average ($\pm 1 \sigma$) 0.6 ± 0.6 mm.

Conclusions For both the investigated scenarios, the results indicate that when FM classification was correct, precision and accuracy were high and comparable to CT-based FM localisation. We found that use of multiple sequences led to better localisation performances when compared to use of a single sequence. However, we observed that, due to the presence of calcification and patient motion, the risk of mislocated patient positioning is still too high for sole manual MR-based FM localisation. Finally, strategies to possibly overcome the current challenges were proposed.

Keywords: **magnetic resonance imaging, radiotherapy treatment planning, MR-only treatment planning, pre-treatment positioning, fiducial marker localization, manual detection, accuracy, precision**

5.1 INTRODUCTION

The use of intraprostatic fiducial markers (FMs) ensures highly accurate and precise image-guided radiotherapy (IGRT) for patients diagnosed with prostate cancer [Zaorsky *et al.* 2017]. Specifically, it has been shown that markers enable for a safe reduction of planning target volume (PTV) margin [Wu *et al.* 2001, Schallenkamp *et al.* 2005, Beltran *et al.* 2008, Greer *et al.* 2008]. To accurately position patients based on the target location, a set of three non-co-linear markers centred in the prostate is the minimum requirement allowing triangulation and measurement of the prostate position in different planes [Schmidt & Payne 2015]. Most markers are made of inert metals (gold and titanium, for example). For prostate cancer, gold FMs are generally employed and their use allows accurate prostate localisation [Ng *et al.* 2014] on photon-based images thanks to their high density, which increases radio opacity [Gall *et al.* 1993]. Markers usually have a cylindrical shape, a diameter ranging between 0.5 and 1.5 mm and length between 2 and 10 mm; they remain in the patient permanently [Ng *et al.* 2014]. To ensure geometrically accurate IGRT treatments, FMs are localised on computed tomography (CT) during treatment simulation and they are localised on kV/MV imaging before patient irradiation to verify and eventually match the pre-treatment patient position with the planned position [Balter *et al.* 1995, Vigneault *et al.* 1997]. The localisation is performed based on a distinct image contrast the FM induce in the CT as well as kV/MV images [Habermehl *et al.* 2013]. The distinctness of the contrast ensures that false classification of FMs, e.g. due the presence of calcifications, is unlikely.

Recently, magnetic resonance imaging (MRI) and its superior soft tissue contrast with respect to photon-based imaging [Debois *et al.* 1999, Dirix *et al.* 2014] enabled more accurate delineation of the prostate [Roach *et al.* 1996, Rasch *et al.* 1999, Villeirs *et al.* 2005]. To exploit the advantages offered by this imaging modality, the use of MRI in radiotherapy planning is rapidly expanding [Schmidt & Payne 2015]. Nowadays, the treatment simulation is generally based on CT and MRI images. Before treatment target delineation, CT and magnetic resonance (MR) images are registered based on the location of FMs on both image modalities [Parker *et al.* 2003, Huisman *et al.* 2005]. The accuracy of the registration is generally considered as being within 1 mm [Jonsson *et al.* 2011].

More recently, MRI-based radiotherapy - also called MR-only radiotherapy - has been proposed [Fraass *et al.* 1987, Lee *et al.* 2003, Edmund & Nyholm 2017] to reduce systematic spatial uncertainties introduced when registering CT and MRI images [Nyholm *et al.* 2009]. Moreover, an MR-only workflow would reduce costs of the treatment and patient exposure to ionising radiation [Karlsson *et al.* 2009]. Additionally, MR-only treatment planning is particularly desirable in the context of MR-guided photon [Raaymakers *et al.* 2004, Dempsey *et al.* 2005, Fallone *et al.* 2009] and eventually proton [Raaymakers *et al.* 2008, Moteabbed *et al.* 2014, Oborn *et al.* 2017] radiotherapy. Up to now, research to such an MR-only workflow has mainly focused upon generation of so-called synthetic-CT images to allow dose calculation based on MR image information alone. Less attention has been paid to the issue of MR-based FM localisation, which is a major determining factor in obtaining accurate radiation treatment for prostate cancer.

In MRI, FMs are depicted as signal voids in magnitude images since they do not produce nuclear magnetic resonance signal [Zangger & Armitage 1999]. The appearance of FM voids varies according to imaging parameters [Lim *et al.* 2016] and the FM orientation with respect to the magnetic field [Jonsson *et al.* 2012]. Up to now, to minimise manual interaction, automated MR-based FM localisation methods have been proposed [Ghose *et al.* 2016, Dinis Fernandes *et al.* 2017, Gustafsson *et al.* 2017, Maspero *et al.* 2017]. These methods are promising, resulting in acceptable accuracy and relatively high detection rates ranging from 84% to 96%. However, we can not rely on the fact that all FMs will be automatically localised, leaving to manual observers the burden to correct for missed detections. These missed detections can derive from classifying blood clots or calcification into FMs since they all appear as signal voids in MR images [Hong *et al.* 2012, Ng *et al.* 2014]. Therefore, in addition to the requirement of achieving a high localisation accuracy, the risk of misclassification of signal voids (i.e. false positives) should be very low as this could result in systematic errors in patient positioning [Ung & Wee 2011].

In current clinical practice, MR-based manual FM localisation is performed by radiotherapy technicians (RTTs) for registering MR to CT images [Parker *et al.* 2003, Ung & Wee 2011]. In such a setting, the presence of CT images greatly aids the RTT to discern whether signal voids in MR images can be classified as FM, calcifications or blood clots.

While this MR-based FM localisation for CT/MR simulation is clinically accepted, no previous study has investigated the reliability of a solely MR-based FM localisation by manual observers, which is the expected scenario within MR-only radiotherapy.

The aim of this study is to evaluate the performance of manual MR-based FM localisation during the planning of prostate cancer patients' external beam radiotherapy treatments. Furthermore, since in a clinical environment multiple sequences are usually available, we aim at investigating whether the use of multiple sequences may impact the manual FM localisation. We conducted a study to assess the inter-observer precision and accuracy of the MR-based FM localisation among clinically involved observers. Furthermore, we evaluated in our patients' group the occurrence of misclassification of FMs.

5.2 MATERIALS AND METHODS

This study is divided into three parts. First, we selected patients and acquired CT and MR images (Section 5.2.1). Second, we performed a multi-observer manual MR-based localisation (Section 5.2.2). Finally, we evaluated the precision and accuracy of the manual FM localisation and investigated whether the observer agreement may lead to a precise and accurate patient alignment (Section 5.2.3).

5.2.1 *Patient preparation and selection*

The study was performed in patients with prostate carcinoma diagnosis who underwent radiotherapy planning at the University Medical Center Utrecht (The

Netherlands) between September and October 2015. The study has been conducted in accordance with regulations from the local ethical committee.

For position verification purposes, each patient received three intraprostatic cylindrical gold FMs (HA2 Medizintechnik GmbH, Germany) measuring 1 mm (diameter) by 5 mm (length). The FMs were transperineally implanted under ultrasound guidance by a physician prior to the imaging session using two 18-gauge needles placed in a template under ultrasound imaging guidance.

Patient positioning at CT scan (Brilliance CT Big Bore, Philips Medical Systems, Cleveland, Ohio, USA) was conducted simulating the treatment, i.e. using a flat table, knee wedges, positioning arms on the chest and tattooing the patient with the aid of laser alignment.

Patient setup at 3T MR scan (Ingenia Omega HP, Philips Healthcare, Best, The Netherlands) was performed using a knee wedge, but without a flat table top, without positioning arms on the chest and without laser-aided positioning. Patients were scanned using anterior and posterior phased array coils (dS Torso and Posterior coils, 28 channels, Philips Healthcare, Best, The Netherlands). To avoid compression of patients' anatomy, two in-house-built coil bridges supported the anterior coil. The location of FMs from CT images was obtained as previously described in [Maspero *et al.* 2017] (see Section 4.2.2). No rectum or bladder preparation protocol was applied before imaging sessions.

Criteria for selecting the subjects were: patients had gold FMs implanted prior to the imaging sessions, patients underwent CT and MRI on the same day acquiring three specific MR sequences (see next section for further details) and were without metallic implants. CT scans were performed with the following imaging parameters: 120 kV, exposure time = 923 ms, tube current between 121 and 183 mA, in-plane matrix = 512x512 pixels, and 3 mm slice thickness. The resolution was variable depending on the field of view (FOV) used. The typical size of the FOV was 500x500x300 mm³, which corresponds to an in-plane resolution of 0.98x0.98 mm².

5.2.2 MR-based fiducial marker localisation

Among the acquired MR images, we tested manual FM localisation on the three following sequences, which imaging parameters are reported in Table 5.1:

1. a three-dimensional (3D) cartesian balanced steady-state free precession (bSSFP) sequence with spectral attenuated inversion recovery to obtain fat suppression and highlight prostate boundaries. The images acquired with this sequence were used by the physician to perform prostate delineations. The vendor's name for this sequence was "3D balanced turbo field echo".
2. a 3D cartesian T₁-weighted dual radio-frequency (RF) spoiled gradient-recalled echo (SPGR) sequence. The SPGR sequence was acquired right after the bSSFP and used by the physician to distinguish bleedings from the primary lesion. The vendor's name for this sequence was "3D T₁ fast field echo".
3. a 3D cartesian dual gradient-recalled echo (GRE) sequence. This sequence was acquired at the end of the examination to have an independent sequence

for FM localisation. The FOV was reduced to the sole target reducing acquisition time as well as making this sequence less prone to motion artefacts. The vendor’s name for this sequence was “3D fast field echo”.

The sequences were selected as best candidates for FM identification after inspection of images from previously acquired patients. The rationale underlying the choice was the high contrast between FM location and surrounding tissues and the spatial high resolution (voxel size $< 1.2 \times 1.2 \times 1.5 \text{ mm}^3$). Furthermore, they were expected to preserve geometric accuracy thanks to the 3D acquisition and large bandwidth ($> 900 \text{ Hz/pixel}$); similar sequences were used also by other institutions for FM localisation [Dinis Fernandes *et al.* 2017, Tyagi *et al.* 2017]. Five RTTs independently performed manual localisation of FMs by identifying the top and bottom of the markers on magnitude images of the bSSFP sequence. The RTTs were requested to follow standardised instructions regarding zoom and window/level of the images. The provided instructions are available as supplementary material (see Section 5.6.1). The RTTs involved in the study had varying experience as technicians: 11, 6.5, 5, 5 and 10 years. They all had experience with position verification. Four RTTs (all the observers except the first observer), had experience with image registration between MR and CT images of: 0, 2, 2, 2.5 and 2.5 years, respectively. They were new to MR-only FM localisation since this procedure was initiated with this study. The observers were asked to report for which patients the FM localisation was perceived as being problematic. In such cases, the RTTs could localise a minimum of three and a maximum of four markers. In case the observers identified four FMs, the RTTs indicated which FM was the most difficult to distinguish. The FM centre was calculated as the mean position between the manually identified top and bottom positions. Note that the observed length of the FM may not correspond to the nominal length of the FM (5mm). The term “apparent” location was used to refer to the location of top and bottom as identified by the observers. Note that apparent location of the

Table 5.1 Image parameters of the sequences used for manual gold FMs localisation: the second column provides the details for the balanced steady-state free precession (bSSFP) sequence, the third column for the RF SPGR sequence acquired right after the bSSFP and the fourth column for the gradient-recalled echo (GRE) sequence acquired at the end of the examination. The terms FOV refers to the field of view, while AP to anterior-posterior.

Imaging parameters	bSSFP	SPGR	GRE
$TE_1/(TE_2)/TR$ [ms]	1.98/3.96	1.4/2.7/4.4	1.4/2.7/4.6
Flip Angle [°]	40	10	10
FOV* [mm ³]	250x250x90	467x467x300	449x449x90
Acquisition Matrix*	252x234x90	312x314x200	376x376x75
Reconstruction Matrix*	512x512x90	320x320x200	400x400x75
Reconstructed Voxel* [mm ³]	0.5x0.5x1.0	1.5x1.5x1.5	1.1x1.1x1.2
Bandwidth [Hz/voxel]	945	1078	1142
Readout direction	AP	AP	AP
Acquisition time	4 min 29 s	4 min 1 s	2 min 10 s

*expressed in terms of anterior-posterior, right-left and superior-inferior directions.

top and bottom of each FM coincided with the centre of a voxel, thus, the calculated centre of the FMs may be located with the resolution higher than a single voxel. For completeness, the following metrics were also recorded: the apparent length as characterised in each sequence and by the different observers, the time required by each observer to complete the FM localisation and the number of FMs for which the localisation was perceived as being problematic. These results are reported as part of the online supplementary material (see Section 5.6.2).

To investigate whether the use of multiple sequences impacts the FM localisation, the RTTs repeated the FM localisation using images of the bSSFP, the second echo of the SPGR and of the GRE sequences immediately after localisation using images of the sole bSSFP sequence. In the case of inter-scan FM motion, the RTTs were instructed to consider the position of the FMs on the bSSFP as a reference.

5.2.3 Statistical analysis

The analysis was performed on the FM centres as located using both a “single” sequence (bSSFP) and “multiple” MRI sequences (bSSFP, SPGR and GRE). In case four FMs were identified, the FM located with the lowest reliability was excluded from the statistical analysis. To generate a consistent FM marker labelling among observers, FMs were numbered (from 1 to 3) according to the position of their centre along the superior-inferior direction. In case FMs were located in the same transverse plane, the left-right direction was used for labelling. To keep the consistency of the labelling among the observers, the labelling was manually checked and, when necessary, corrected. The analysis was performed in Matlab (R2015a, the MathWorks Inc., Natick, Massachusetts, United States).

Inter-observer agreement or spatial precision

SINGLE FM LOCATIONS For each observer, the number of detected FMs was reported. An agreement position was defined as the mean position among all the five observers. To assess the precision among the five observers, FM locations were compared calculating a 95% limit of agreement ($= 1.96$ times the standard deviation (σ) [Jones *et al.* 2011]) of the distance to the mean position (LoA) in the three directions ($X =$ anterior-posterior, $Y =$ right-left and $Z =$ superior-inferior). For comparison with [Deegan *et al.* 2015], a threshold for clinical acceptability was set to $95\% \text{ LoA} \leq 2 \text{ mm}$. Bar plots providing a visual assessment of the inter-observer variability were created reporting also a more stringent LoA threshold of 1 mm . An investigation on the CT and MRI images was performed on patient-base to investigate the causes underlying imprecise localisation of FMs; schematic representations of the inter-observer localisation were also examined.

CENTRE OF MASS LOCATIONS To verify the impact on patient alignment, the location of the centre of mass (CM) among all the FMs was calculated for each patient and observer. For each patient, the 95% limit of agreement ($= 1.96$ times the standard deviation (σ) [Jones *et al.* 2011]) with the average position of the CMs (LoA_{CM}) was calculated among all the observers in the three directions [Deegan *et al.* 2015]. To assess agreement of the CM position among the observers a threshold of $\text{LoA}_{\text{CM}} < 2 \text{ mm}$ was used for comparison with [Deegan *et al.* 2015]. To verify clinical CM agreement, the threshold $\text{LoA}_{\text{CM}} < 1 \text{ mm}$ was employed.

Bar plots providing a visual assessment of the inter-observer agreement variability were created. Note that patient alignment is generally performed on the centre of mass location [Ung & Wee 2011]; therefore, this is considered as the final metric to assess inter-observer precision.

Intra-observer agreement

To evaluate whether, over all the observers, a statistically significant variation of FM location occurred between localisation using only the bSSFP sequence and the combination of bSSFP, SPGR and GRE sequences, we performed Wilcoxon rank-sum test at the confidence level of 95% in the three directions on LoA and LoA_{CM}.

Spatial accuracy

The difference of inter-marker distances (IDs) between the FMs located in CT and MRI were calculated for the precisely located (LoA < 2 mm) markers using single and multiple sequences. For each observer and over all the observers, the absolute difference between the ID of MRI and CT were calculated as in [Gustafsson *et al.* 2017] and characterised in terms of mean, median, standard deviation (σ) and range ([minimum;maximum]).

5.3 RESULTS

Seventeen consecutive prostate patients (61.4-81.9 years, mean age = 68.7 years, median age = 68.3 years, inter-quartile range = 66.1-70.8 years) were considered for inclusion in the study. All the patients were staged as T1c-3b, Gleason score ≥ 6 and one of the patients (P14) had a hip implant and was excluded from the analysis (the localisation and images for this patient are presented as supplementary material in Figure 5.8) within Section 5.6.3). Within the patient population, the average prostate volume during imaging sessions was 56.8 ml (range = 32.1-117.3 ml, median volume = 54.8 ml, inter-quartile range = 42.9-70.9 ml) and body mass index was on average 26.4 kg/m² (range = 19.9-30.7 kg/m², inter-quartile range = 24.9-28.7 kg/m²). No patient received adjuvant hormonal therapy.

Patients underwent intensity-modulated radiotherapy, using 5 beams of 10 MV, with a prescribed dose of 77 Gy to the entire prostate in 35 fractions (2.2 Gy per fraction). Other clinical prescriptions are specified in [Lips *et al.* 2008]. Each of the patients had three FMs implanted leading to a total of 48 FMs and 580 FM localisations (16 patients \times 3 FMs \times 5 observers \times 2 sequence scenarios) performed over all the observers. The FMs were implanted at least one week prior to imaging.

During the pre-planning imaging session, MRI scans were performed within maximum 70 min (mean time = 45 min, minimum time of 20 min and inter-quartile range = 34-50 min) after the CT scans. For all the patients, the bSSFP and SPGR sequences were acquired one after each other with a maximum time difference of 5 min, while the GRE sequence was acquired at least 15 min after the SPGR sequence. Figure 5.1 shows an axial slice of CT, bSSFP, SPGR and GRE images for patient P1 (top) and P9 (bottom) in the neighbourhood of the FMs.

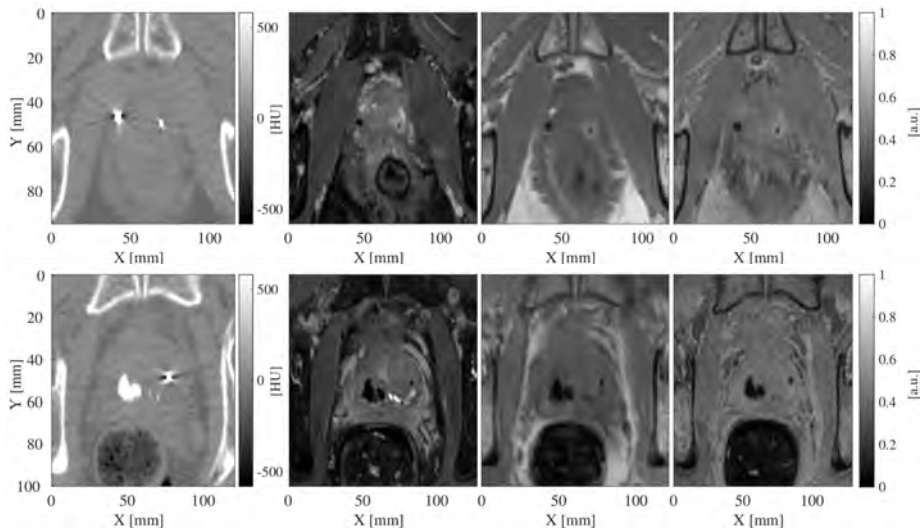


Figure 5.1 Zoom of an axial slice of CT (left), bSSFP (centre-left), SPGR (centre-right) and GRE (right) images for patients P1 (top) and P9 (bottom) before image registration. The axes X and Y indicate the anterior-posterior and right-left directions. The intensity of CT image is in HU, while of MRI images are normalised to the maximum over the whole dataset. Note the presence of calcification for the patient P9; they are visible as high intensity on CT and signal void on MR images.

5.3.1 Single FM locations

All the observers detected three FMs for all the patients, except one observer (Obs₁) who detected four FMs for two patients (P₄ and P₁₇) when using the bSSFP sequence. When also the SPGR and GRE sequences were employed, all the RTTs localised three FMs. Figure 5.2 provides a schematic representation of the centres of the FMs as localised by all the FMs for patients P₁ and P₉ using multiple sequences. The agreement position is also shown. For example, taking into consideration the FM with the largest spread for patient P₁ (FM₁), the LoA were 0.69, 0.57, 0.84 mm in X (anterior-posterior), Y (right-left) and Z (superior-inferior) directions, respectively. The bar plots of LoA for all the patients over the five RTTs is shown in Figure 5.3. The LoA was found to be higher than 2 mm in one of the three directions for 10/48 and 3/48 FMs when the observers located on a single (bSSFP) and multiple (bSSFP, SPGR and GRE) sequences, respectively. This resulted in an increased agreement (45/48) when the observers located on multiple sequences with respect to a single sequence (38/48). Over all the three directions, the Wilcoxon rank-sum test at 95 % confidence interval resulted in significantly different LoA when comparing FM location obtained with one or multiple sequences. In particular, as shown in Figure 5.3 with the use of multiple sequences for two patients (P₇ and P₁₇) the LoA decreased below 2 mm. When localising using a single sequence over all the patients, LoA was found > 2 mm for more than one FM per patient, while when localisation was performed on multiple sequences LoA was > 2 mm only for one FM per patient. Focusing on the scenario with the largest agreement (localisation performed using

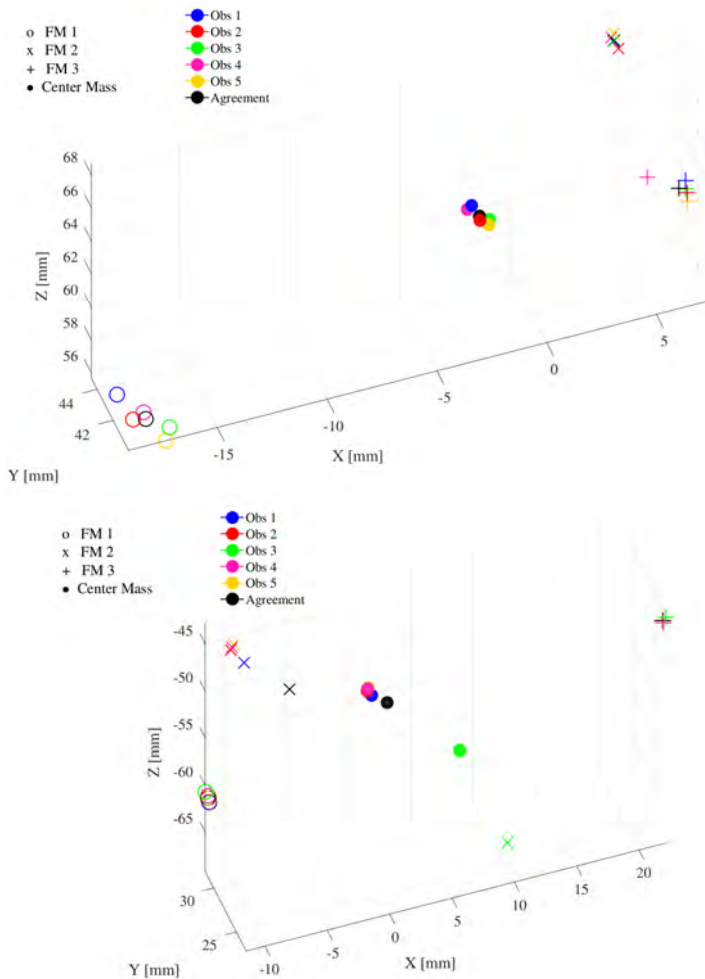


Figure 5.2 Schematic representation of the centres of the FMs as localised by all the observers for patient P1 (top) and P9 (bottom) using multiple sequences (bSSFP, SPGR and GRE). The labelling of the FM is indicated by the marker: \circ , \times , $+$ and \bullet for FM having number 1, 2, 3 and for agreement position, respectively. For patient P1 (top), the LoA_{CM} of FM1 over the five RTTs was 0.27, 0.31 and 0.38 mm in X, Y and Z, respectively, which was considered clinically acceptable; for patient P9 (bottom), the LoA_{CM} for FM2 over the five observers was 11.17, 0.99 and 13.70 mm in X, Y and Z, respectively, which was considered clinically unacceptable.

multiple sequences), localisation of maximum one FM was found imprecise for 3/16 patients: P4, P6 and P9. Excluding these 3 FMs (considering, therefore, 45/48 FMs), the average ($\pm 1 \sigma$) LoA was 0.19 ± 0.15 , 0.18 ± 0.12 and 0.30 ± 0.31 mm in anterior-posterior, right-left and superior-inferior directions, respectively.

After the investigation of the images acquired for the patients resulting in an imprecise FM localisation, we observed that patients P4 (Figure 5.6) and P9 (Figure 5.1 and 5.2 bottom) were characterised by the presence of large (> 2 mm

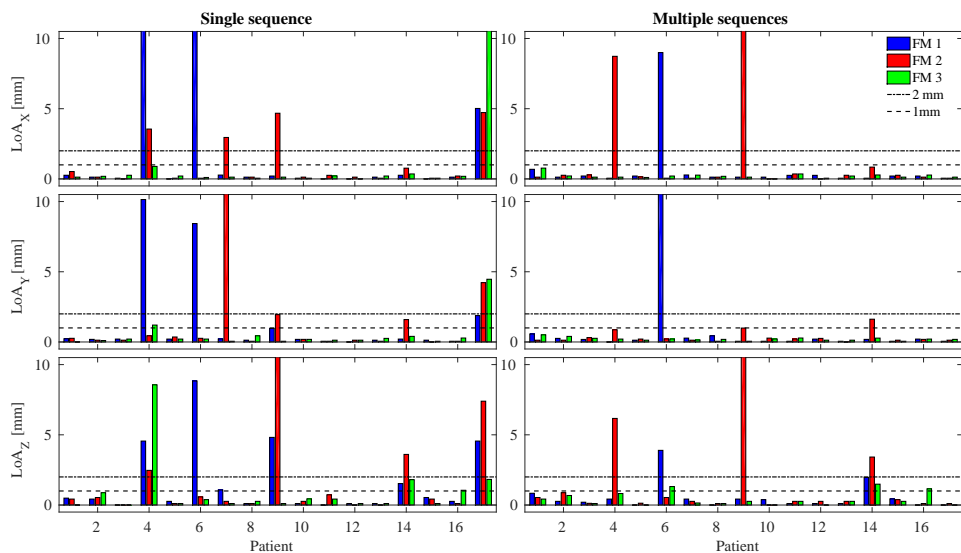


Figure 5.3 The 95% limit of agreement (LoA) calculated, for each patient, over the five observers for the single FM in the three directions, where X = anterior-posterior (top), Y = right-left (center) and Z = superior-inferior (bottom). On the left is shown the FM localisation as performed using the bSSFP sequence only, while on the right the FM localisation as performed using multiple sequences. The dotted and dashed lines represent the LoA of 2 mm, while the dotted lines represent the LoA of 1 mm. Note that patient P14 had hip implant and the results are here presented but were excluded in the statistical analysis.

in diameter) intra-prostatic calcifications. In both cases, $1/5$ RTTs (Obs₁ for P₄ and Obs₃ for P₉) localised one of the FMs far away from the other four observers. Figure 5.2 shows that a misclassification occurred for patient P₉ when considering the FM₂ and Obs₃. The same occurred for FM₂ and Obs₁ for patient P₄ (Figure 5.6 bottom). After observing the location of the misclassified FMs as reported by the two observers in the MR and CT images, we found that the FMs was located in correspondence of calcifications. For one patient (P₆, as shown in Figure 5.6), one of the FMs was not visible on bSSFP but appeared on SPGR and GRE; we hypothesised that motion reduced the visibility of the FM on the bSSFP impacting reliability of the localisation for this FM. Considering the results from a different perspective, for the total 240 (16 patients \times 5 observers \times 3 FMs) single observer localisations using multiple sequences, 2 times calcifications were marked as FMs by one of the RTTs and no agreement could be found for one FM among all the five RTTs. This would result in misclassification for 7 out of the 240 single observer localisations, or $7/80$ (16 patients \times 5 observers) single observer localisation of the CM in the case the outliers cannot be eliminated.

5.3.2 Center of mass locations

Figure 5.4 presents the bar plot of the 95% LoA_{CM} for all the patients over the five RTTs. The LoA_{CM} was found higher than 1 mm in one of the three directions (X, Y or Z) for 5/16 and 3/16 patients when the observers located on a single (bSSFP)

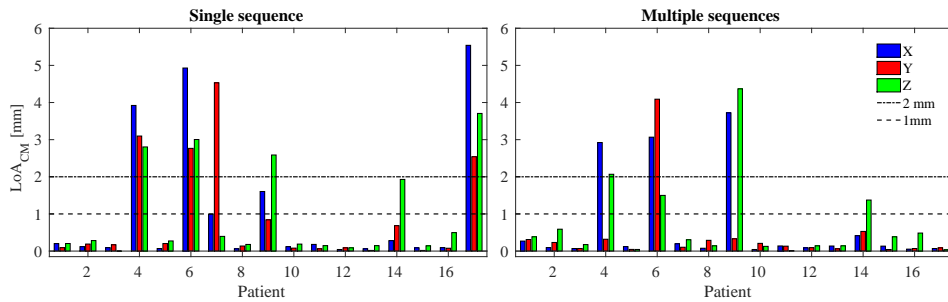


Figure 5.4 The 95% limit of agreement of the centre of mass (LoA_{CM}) calculated, for each patient, over the five observers for a single fiducial marker (FM) in the three directions, where X = anterior-posterior (blue), Y = right-left (red) and Z = superior-inferior (green). On the left is shown the localisation of the CM as performed using the bSSFP sequence only, while on the right the localisation of the CM as performed using multiple sequences. The dotted and dashed lines represent the LoA of 2 mm, while the dotted lines represent the LoA of 1 mm. Note that patient P14 had hip implant and the results are here presented but were excluded in the statistical analysis.

and multiple (bSSFP, SPGR and GRE) sequences, respectively. Over all the three directions, the Wilcoxon rank-sum test at 95 % confidence interval resulted in significantly different LoA when comparing FM locations obtained with one or multiple sequences. Excluding the imprecisely located CMs, the average ($\pm 1 \sigma$) LoA_{CM} when localisation was performed with single sequence was 0.10 ± 0.05 , 0.10 ± 0.06 and 0.19 ± 0.13 mm in anterior-posterior, right-left and superior-inferior directions, respectively; the average ($\pm 1 \sigma$) LoA_{CM} when localisation was performed with multiple sequences was 0.11 ± 0.06 , 0.13 ± 0.09 and 0.23 ± 0.18 mm in anterior-posterior, right-left and superior-inferior directions, respectively. In all the directions, the average LoA_{CM} is < 0.25 mm.

5.3.3 Spatial accuracy

Table 5.2 shows the mean, median, σ and range of the absolute difference in the ID of the precisely located FMs ($LoA < 2$ mm) using single and multiple sequences. Among all the observers, the average ID difference is slightly lower (0.5 ± 0.6 mm) when locating with multiple sequences with respect to with a single sequence (0.7 ± 0.6 mm).

5.4 DISCUSSION

The precision and accuracy of manual localisation of intraprostatic gold FMs on sole MR images was evaluated in the context of an MRI-only simulation workflow. Note that this fundamentally differs from localisation of FMs on MR images in the current CT-MR simulation workflow for registration purposes as the CT images can be used to minimise misclassification on the MR images. In this sense, this study was conducted to verify whether an MR-only simulation could facilitate a robust positioning workflow comparable to current CT-based positioning in the totality of the cases.

Sixteen patients were considered in the study. During the investigation, manual FM localisation was evaluated for two scenarios: 1) employing a single MRI sequence (bSSFP) and 2) a combination of multiple sequences (bSSFP, SPGR and GRE). In this study, the use of multiple sequences led to precise localisation ($LoA < 2$ mm) in more patients and of more FMs (13/16 patients and 45/48 FMs) than localisation with a single sequence only (11/16 patients and 38/48 FMs). For both scenarios, the precision calculated as the average of LoA_{CM} in all the directions on the precise localised FMs was within 0.25 mm. The results are in good agreement with others [Huisman *et al.* 2005, Ullman *et al.* 2006, Deegan *et al.* 2013, Deegan *et al.* 2015]. Huisman *et al.* [Huisman *et al.* 2005] obtained a precision of 0.5 mm in the centroid of the prostate on a cohort of 21 patients when assessing registration of CT and MR images. Ullman *et al.* [Ullman *et al.* 2006] reported a mean inter-observer variability of 0.9 ± 0.6 mm when performing registration on photon-based portal images. Deegan *et al.* [Deegan *et al.* 2013] reported that inter-observer LoA on the applied registration, which is comparable to the LoA_{CM} , was in the range of about ± 2 mm. Literature reporting single FM localisation precision has not been found.

In general, in our study, when FMs were precisely localised, they were also accurately localised. In particular, we found an inter-observer accuracy of 0.7 mm with the single sequence and of 0.6 mm with the multiple sequences. These results are slightly more accurate than what presented when comparing a human observatory to automatic FM localisation by Gustafsson *et al.* [Gustafsson *et al.* 2017] and in line with the accuracy previously considered acceptable for the CM localisation performed with photon-based imaging (0.6 mm) [van der Heide *et al.* 2007].

However, for a single FM in 3/16 cases, precise localisation was not achieved. That implies that a correct positioning in these patients can not be guaranteed.

Table 5.2 The mean, median, standard deviation (σ) and range ([min;max]) of the absolute difference in the IDs of the precisely located FM between CT and MRI for all the single observers and for all the five observers. The results were calculated excluding 10/48 and 3/48 FMs for the localisation performed on a single and multiple sequences, respectively. All the values are expressed in mm.

Sequence	Observer	Mean	Median	σ	Range
Single	1	0.8	0.6	0.7	[0.1;3.1]
	2	0.6	0.5	0.5	[0.0;2.5]
	3	0.7	0.6	0.5	[0.0;2.1]
	4	0.7	0.6	0.6	[0.1,2.9]
	5	0.7	0.5	0.6	[0.1,2.5]
	All	0.7	0.6	0.6	[0.0,3.1]
Multiple	1	0.7	0.4	0.6	[0.0,2.7]
	2	0.6	0.4	0.6	[0.0,3.0]
	3	0.7	0.5	0.7	[0.0;2.5]
	4	0.7	0.5	0.6	[0.0;2.8]
	5	0.7	0.6	0.5	[0.0;2.5]
	All	0.6	0.5	0.6	[0.0;3.0]

Based on the thorough investigation of the images of these specific patients, we concluded that the following two causes may have led to imprecise FM localisation: (1) presence of calcifications misclassified as FM and (2) motion during the bSSFP sequence. (1) Previous studies reported the presence of calcifications in 40 to 88% of prostate cancer patients [Suh *et al.* 2008, Hong *et al.* 2012, Ng *et al.* 2014, Gustafsson *et al.* 2017]. In our study, for 2/16 patients the presence of calcifications led to misclassified FM localisation for 1/5 RTT. Interestingly, the observers seemed to be aware of the difficulties and they reported that the localisation procedure for such patients was problematic (see Figure 5.5 within the supplementary material in Section 5.6.2). (2) Motion as a possible cause of hampered accuracy of FM localisation has already been reported in the literature for the bSSFP sequence [Tyagi *et al.* 2017]. The readout of this sequence was 3D leading to typical acquisition times of 2-3 minutes, and thus motion blurring is likely to occur.

To obtain accurate localisation for all the patient cases, we believe that redundancy should be added in the localisation procedure to lower the risk of FM misclassification. In this sense, we foresee the following as possible ways to increase the redundancy:

- *multiple observers localisation.* Whenever an RTT would have low confidence in the FM localisation, an independent observer could perform localisation and assess a posteriori the initially found position. In this scenario, the experience of the RTT may influence the outcome. Further investigations are necessary to evaluate whether such scenario will lead to accurate localisation in the totality of the cases.
- *implantation of a fourth marker.* The use of a fourth FM could be easily performed without increasing the patient discomfort: the fourth FM could be collinearly placed with the third FM avoiding a new needle insertion. In case of FM misclassification, the RTTs may explicitly exclude one of the FM when correcting patient set-up, remaining with a sufficient number of FMs to enable the procedure. On the other hand, with four FMs several permutations of 3 FMs could be considered and the RTTs would need to consistently choose the FMs between imaging modalities to obtain identical set-up corrections.
- *resorting to automatic localisation.* Given the promising results obtained with automatic gold FM localisation methods [Ghose *et al.* 2016, Dinis Fernandes *et al.* 2017, Gustafsson *et al.* 2017, Maspero *et al.* 2017], recurring to a combination of manual and automated MR-based FM localisation methods may ensure safe MR-based simulation of patient position.

In our institution further investigation is undergoing to verify that using automatic localisation [Maspero *et al.* 2017] is a viable approach including also the insertion of a fourth FM. Alternatively to the redundancy options above proposed, another centre [Tyagi *et al.* 2017] reported that using kV radiography after FM implantation provided independent images that facilitated MR-based FM localisation. Similarly to this approach, we could also speculate about designing a workflow that foresees referring the patients to CT in case of dubious manual FM

localisation at the MR scan. Performing a low dose CT for all the patients for the sole scope of FM localisation could be another possibility.

Strategies to possibly solve FM misclassification other than adding redundancy may involve 1) further MR sequence optimisation and 2) employing different MR sequences. 1) Further MR sequence optimisation could, for example, be employed to diminish the susceptibility to the motion by reducing the acquisition time of the employed sequences. In addition, sequence optimisation may impact visualisation and also manual localisation performance. 2) Among the available MRI sequences, only the images of one echo of the gradient-echo sequences have been taken into consideration in this study. It may occur that acquiring with different image parameters or MR sequences may result in more favourable manual FM localisation performances. For example, recently, the use of multi-echo images showed promising results, thanks to the increasing size of a signal void when increasing the echo time [Gustafsson *et al.* 2017]; Future studies could investigate whether MR sequence optimisation or the use of other sequences may be more suitable for FM localisation verifying accuracy and precision performances.

From a general perspective, in our study, five RTTs were involved in the study, making the findings representative of a realistic situation. As the observers were not familiar with MR-only FM localisation, it may be expected that better results may be obtained by training the observers for this specific context. In this sense, it may be interesting to verify, in a future study, the influence of clinical experience on the manual localisation performance.

Comparing our study to previous research, a limitation of the presented cohort is its size, although, no other research has been presented to assess manual FM localisation with such details and reporting localisation performances within a realistic clinical environment. Recently, Gustafsson *et al.* [Gustafsson *et al.* 2017] presented results of the accuracy of manual FM localisation and a larger cohort (44 patients). Unfortunately, the precision has not been reported.

In the perspective of MR-only Radiotherapy, the use of multiple sequences would enable manual marker localisation for precise and accurate simulation of prostate cancer patients' position prior to irradiation in almost the totality of the cases. Nevertheless, believing that an MR-only simulation should facilitate a robust positioning workflow, we think the risk of mislocated patient positioning is still too high and that additional redundancy is essential to enable a safe clinical practice.

5.5 CONCLUSION

We studied inter-observer precision and accuracy of manual gold FM localisation for MR-only prostate cancer external beam therapy simulation over five RTTs for two scenarios: employing a single MRI sequence (bSSFP) or a combination of multiple sequences (bSSFP, SPGR and GRE). The use of multiple sequences (bSSFP, SPGR and GRE) led to better localisation performances compared with the use of a single sequence (bSSFP). For both the scenarios, the results indicate that when FM classification was correct, the precision and accuracy are high and comparable to CT-based FM localisation. However, the risk of mislocated patient positioning due to FM misclassification is still too high to allow the sole use of manual FM

localisation. For future work, we hypothesise that further increasing redundancy by increasing the number of FM per patient and by setting up a system to rely on multiple observers or automatic localisation is necessary to increase the detection rate and warrant clinical introduction.

5.6 SUPPLEMENTARY MATERIAL

5.6.1 *Instructions provided to the clinical observers*

As part of the supplementary material is possible to download¹ a repository (InstructionPackage.zip) containing the instructions provided to the RTTs before performing the manual FM localisation. In particular, the repository contains the following files:

1. [1.] *GeneralGuidelineFMloc.pdf* which presents a short description of the procedure;
2. [2.] *PracticalInstructionFMloc.pdf* which describes step-by-step the procedure;
3. [3.] *Checklist_Obs.pdf* which is aimed at supporting the RTTs during the procedure in keeping track and annotate for which patient the localisation was found problematic.

5.6.2 *Annotations on the FM localisation*

As part of the supplementary material, we report the apparent length of the FMs for each observer and the time spent by each observer performing the FM localisation over all the patients. In particular, Table 5.3 shows the mean, standard deviation (σ), range [min, max] of the apparent length, expressed in mm. The weighted mean over all the observer is 7.5 ± 0.6 mm and 7.7 ± 0.7 mm for localisation using a single and multiple sequences, respectively. Note that the apparent length was longer than the nominal length of the FM (5 mm).

Table 5.4 reports the mean, σ and range of the time needed by each observer to perform the FM localisation. The weighted mean over all the observer is 5.8 ± 1.4 min.

In addition, a histogram reporting the frequency of unreliable FM localisation, as perceived by the RTTs is shown in Figure 5.5 for four out of five observers; one of the observers did not report the reliability of the localisation. The observers reported the perceived reliability without distinction between localisation performed employing a single and multiple sequences.

¹Upon acceptance of the manuscript, the material will be made publicly available. Before that moment, it is possible to directly contact the author of this thesis.

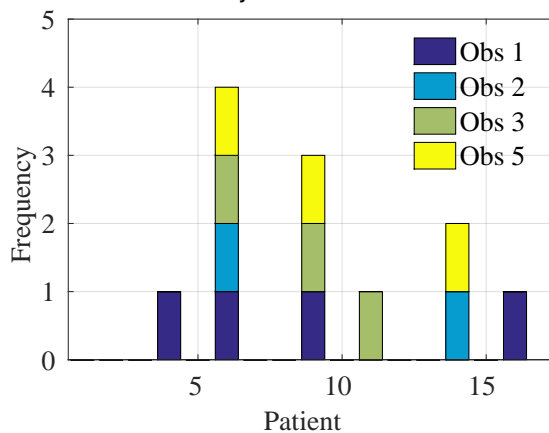
Table 5.3 Apparent detection length of the FMs as obtained performing the localisation using a single (bSSFP) or multiple (bSSFP, SPGR and GRE) sequences for each observer. All the values are expressed in mm.

Sequence	Observer	mean	σ	Range
Single	1	8.3	1.9	[3.1;15.2]
	2	7.6	1.4	[5.0;13.2]
	3	7.1	1.3	[3.0;9.2]
	4	7.4	1.8	[3.2;13.3]
	5	7.8	1.6	[4.1;15.2]
Multiple	1	8.3	1.6	[4.1;14.2]
	2	7.7	1.5	[4.0;14.2]
	3	7.2	1.3	[3.0;9.1]
	4	7.4	1.8	[3.2;13.3]
	5	7.7	1.2	[4.0;10.0]

Table 5.4 The mean, standard deviation (σ) and maximum time needed for the FM localisation procedure of each observer over all the FMs, expressed in minutes.

Observer	mean	σ	Maximum
1	8.7	3.4	15
2	7.8	3.2	15
3	4.4	2.5	10
4	5.0	3.4	14
5	3.8	3.5	13

Figure 5.5 Frequency of reported unreliable FM localisation according to four out of five observers. Note that patient P14 had hip implant and the results are here presented but were excluded in the statistical analysis.



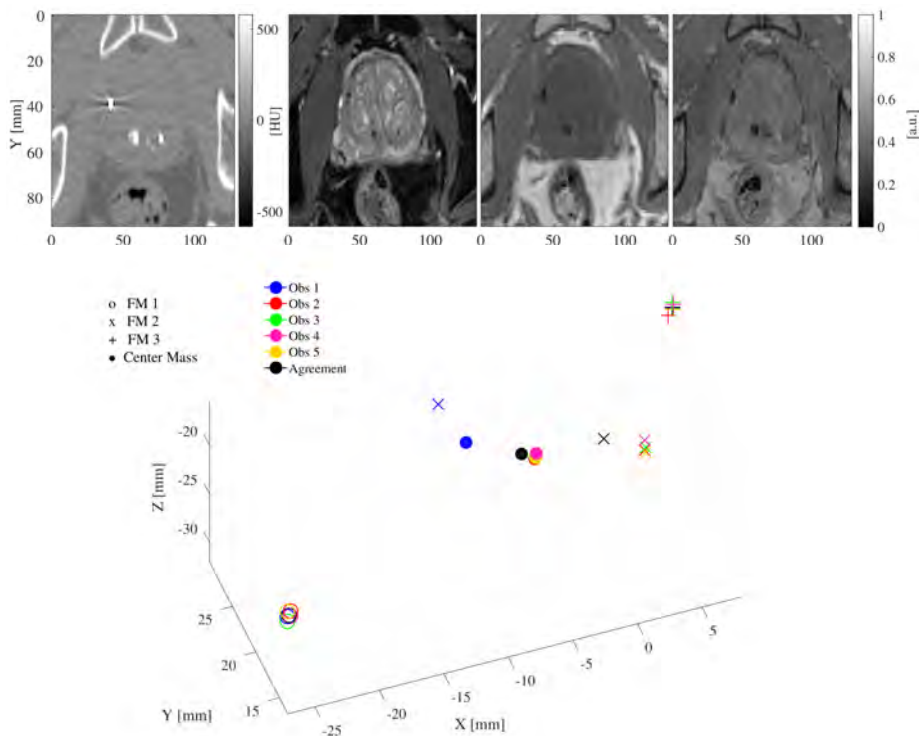


Figure 5.6 (Top) Zoom of an axial slice of CT (left), bSSFP (centre-left), SPGR (centre-right) and GRE (right) images for patient P4 before image registration. The axes X and Y indicate the anterior-posterior and right-left directions. The intensity of CT image is in HU, while of MRI images are normalised to the maximum over the whole dataset. (Bottom) Schematic representation of the centres of the FMs as localised by all the observers for patient P4 using multiple sequences (bSSFP, SPGR and GRE). The labelling of the FM is indicated by the marker: \circ , \times , $+$ and \bullet for FM having number 1, 2, 3 and for agreement position, respectively. For this patient (P4), the LoA_{CM} for FM2 was 8.73, 0.87 and 6.17 mm in X, Y and Z, respectively, which was considered clinically unacceptable.

5.6.3 Single patient investigation

As a supplementary material, we report CT and MRI images for the patients P4 and P6, which were found having $LoA > 2$ mm in maximum one of the three FMs for localisation performed with multiple sequences. Zoom of an axial slice of CT (top left), bSSFP (top centre-left), SPGR (top centre-right) and GRE (top right) images for the patients P4, P6 before image registration as well as schematic representations of the centres of the FMs as localised by all the observers (bottom) are shown in Figure 5.6 and Figure 5.7, respectively. For completeness, we report also the CT and MRI images along with the schematic representation of the centres of the FM for patient P14 in Figure 5.8. Note that this patient was not considered during the analysis since had a hip implant.

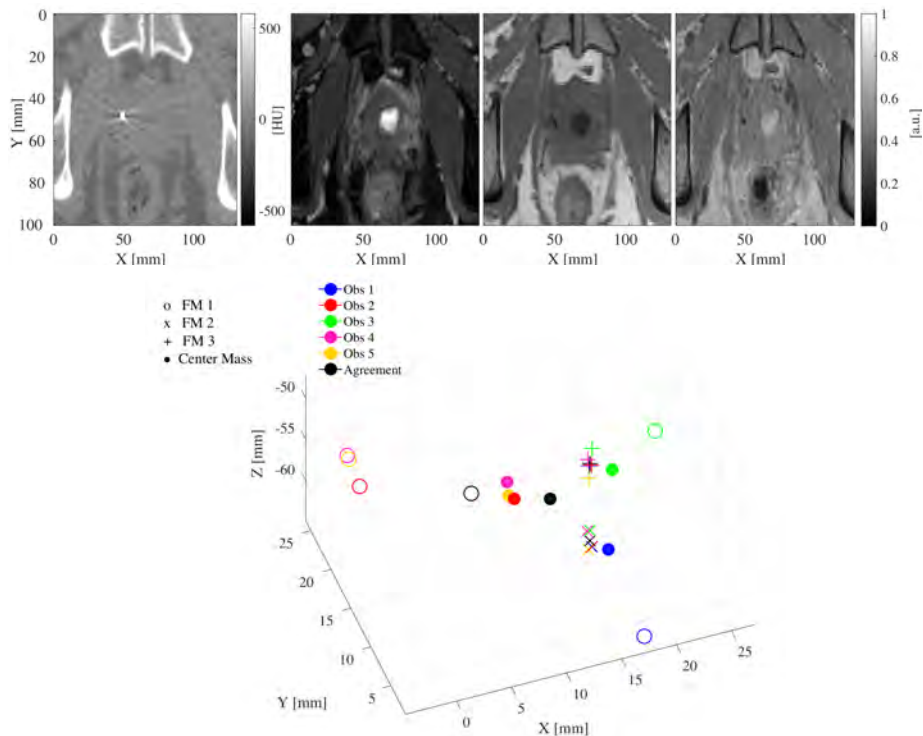


Figure 5.7 (Top) Zoom of an axial slice of CT (left), bSSFP (centre-left), SPGR (centre-right) and GRE (right) images for patient P6 before image registration. The axes X and Y indicate the anterior-posterior and right-left directions. The intensity of CT image is in HU, while of MRI images are normalised to the maximum over the whole dataset. (Bottom) Schematic representation of the centres of the FMs as localised by all the observers for patient P6 using multiple sequences. The labelling of the FM is indicated by the marker: \circ , \times , $+$ and \bullet for FM having number 1, 2, 3 and for agreement position, respectively. For this patient (P6), the LoA_{CM} for FM1 was 8.99, 12.19 and 3.89 mm in X, Y and Z, respectively, which was considered clinically unacceptable.

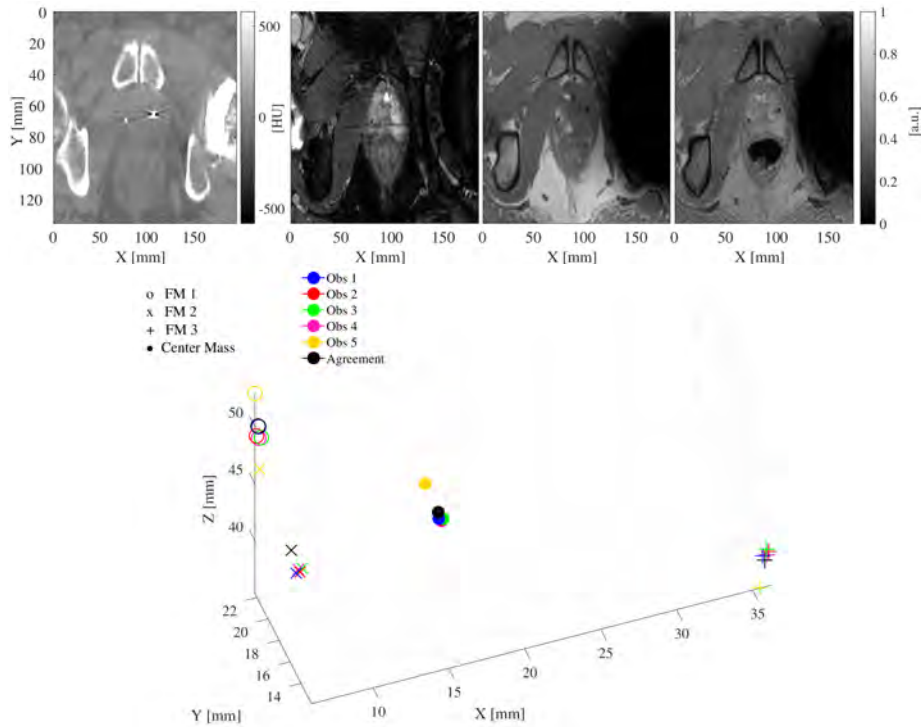


Figure 5.8 (Top) Zoom of an axial slice of CT (left), bSSFP (centre-left), SPGR (centre-right) and GRE (right) images for patient P14 before image registration. The axes X and Y indicate the anterior-posterior and right-left directions. The intensity of CT image is in HU, while of MRI images are normalised to the maximum over the whole dataset. (Bottom) Schematic representation of the centres of the FMs as localised by all the observers for patient P14 using multiple sequences. The labelling of the FM is indicated by the marker: ○, ×, + and ● for FM having number 1, 2, 3 and for agreement position, respectively. For this patient (P14), the LoA_{CM} for FM2 was 0.84, 1.62 and 3.42 mm in X, Y and Z, respectively, which was considered clinically unacceptable. The statistics relative to this patients have not been considered in the study due to the presence of the hip implant.

Part III

Discussion and Summaries

Discussion

6

Stante, dunque, ciò, mi par che nelle dispute di problemi naturali non si dovrebbe cominciare dalle autorità di luoghi delle Scritture, ma dalle sensate esperienze e dalle dimostrazioni necessarie.

**Galileo Galilei,
Letter to Christina of Lorraine**

In radiotherapy, a high level of accuracy is required to deliver clinically effective treatments [Mijnheer *et al.* 1987, Thwaites 2013, Zaorsky *et al.* 2017]. Such a requirement entails that whenever a clinic has achieved a clinical standard, any change needs to be justified and validated by proving that a “high level of accuracy” is maintained.

This thesis focuses on magnetic resonance (MR)-only radiotherapy for prostate cancer. To achieve MR-only radiotherapy, modifications to the clinical pathway are necessary. Therefore, this thesis investigated whether such modifications can be done maintaining the clinical standards.

Section 6.1 considers the accuracy of magnetic resonance imaging (MRI)-based dose calculations (as presented in **Part I**), while Section 6.2 describes the feasibility of image-guided radiotherapy (IGRT) using MR images as reference for set-up corrections (as shown in **Part II**). The contributions that were presented in the previous chapters are shortly described and compared with results by other groups. Assuming the point of view of a clinic interested in implementing an MR-only pathway for prostate radiotherapy, Section 6.3 speculates on the solutions and practices that are required to perform MR-only simulations and examines organs at risk (OARs) delineations in an MR-only pathway. Finally, Section 6.4 begins with possible applications of MR-only for sites other than prostate and looks at the perspective of MRI-guided radiotherapy (MRIgRT).

6.1 MR-BASED DOSE CALCULATIONS

Synthetic CT (sCT) images are generated to enable dose calculations in an MR-only pathway. To prove that using sCT for dose calculations is safe compared to the gold standard, i.e. computed tomography (CT)-based calculations, dosimetric studies are performed [Edmund & Nyholm 2017]. The dosimetric comparisons described in this thesis aimed at investigating the use of sCT images generated with MR for calculating attenuation (MRCAT) (Philips Healthcare, The Netherlands). MRCAT is a five classes bulk-assigned sCT generation approach that utilises a model to segment bones robustly. The model was pre-trained by the vendor on a large cohort using multi-contrast MR images. To ensure robustness, generation of sCT was conducted at the MR scanner using a three-dimensional

(3D) spoiled gradient-recalled echo (SPGR) sequence with fixed image parameters¹. The final images produced with MRCAT are sCT images with voxels in (synthetic-)hounsfield unit (HU) values. The vendor suggested using a calibration curve to convert HU into electron density, which is the quantity required to enable dose calculations. The accuracy of MRCAT-based dose calculation was assessed for photon and proton radiotherapy in two different studies. The following paragraphs further elaborate on such studies.

To facilitate a comparison of the results obtained in this thesis with the results obtained by other groups, an overview of the performances related to sCT images for prostate MR-only radiotherapy is presented in Table 6.1. This table is an update of Table 1.1 that includes the results described in **Part I** of this thesis.

Photon radiotherapy

Chapter 2 reports the results of the dosimetric comparison undertaken to assess the accuracy of dose calculations with MRCAT in photon-based radiotherapy. Fourteen patient were included in the study, and a mean dose difference of approximately 1% was found over the population with respect to CT-based dose calculations. In the study, possible confounding factors contributing to dose difference were further investigated successfully disentangling three factors. The largest confounding factor leading to dose differences was the calibration curve to convert (synthetic-)HU into electron density: in our institute, a different curve was used with respect to the curve suggested by the vendor for use with MRCAT (0.7%). The second largest factor was the use of bulk-assigned sCT images: the use of stratified CT instead of CT images with a continuous range of HU (0.2-0.3%). The last factor, which is the combination of inter-scan differences due to patient repositioning, MR-related geometric inaccuracy, and registration errors to body contours, did not significantly contribute to dose differences (0.01%) [Maspero *et al.* 2017]. The identification of the confounding factors enabled the reduction of the initially found dose difference from 1% to 0.3% by adopting an identical calibration curve for conversion of HU into electron density.

The dose differences found in the study should be reviewed in the light of the total uncertainty accepted in radiation therapy. When considering the complete radiotherapy pathway, including uncertainties in beam calibration, relative dosimetry, dose calculations, and dose delivery, the International Commission on Radiation Protection estimated a standard uncertainty of 5% in a clinical setup [ICRP 2000]. The added uncertainty of an MR-based dose calculation, shown in our study to differ by only fractions of a percent from CT-based dose calculations, is negligible in comparison to the total uncertainty. Our study enabled to shed light on the factors contributing to dose differences, possibly facilitating a clinic to understand where to counteract for reducing such differences, if considered necessary. For example, following the findings presented in Chapter 2, the staff at the University Medical Centre Utrecht decided to adopt a new phantom and calibration curve for conversion of HU into electron density before proceeding with the clinical use of MRCAT. Preliminary dose assessments using the new

¹The field of view (FOV) was the only image parameter that could be chosen: two FOV sizes were available 477x477x300 mm³ or 552x552x300 mm³. The total acquisition time was about 2.5 min.

phantom/calibration curve were conducted in Utrecht demonstrating that dose differences decreased from 1% to about 0.3%, which is consistent with the results previously reported.

Other groups, as shown in Table 6.1, performed a comparable assessment of MR-based dose calculation using MRCAT reporting dose differences well within 1% [Tyagi *et al.* 2016, Kemppainen *et al.* 2017, Christiansen *et al.* 2017]. The results reported in Chapter 2 are in line with what was presented by similar studies from different institutions, underlining the validity of our results.

Table 6.1 Overview of sCT generation approaches for prostate radiotherapy, along with their performances in terms of percent dose difference (DD), mean absolute error (MAE) and gamma pass rate on gamma 2%,2mm (if not differently specified). For each approach, the classification class, type of radiation involved - photon (γ) or proton (p) -, the number of patients included in the study and the associated reference have been specified.

Approach	Radiation	Pt	Performance metrics			Reference
			DD [%]	MAE [HU]	$\gamma_{2\%,2mm}$ [%]	
bulk	γ	5	<2			[Lee <i>et al.</i> 2003]
bulk	γ	15	<2.5			[Chen <i>et al.</i> 2004]
bulk	γ	10	<1			[Eilertsen <i>et al.</i> 2008]
bulk	γ	10	<1			[Jonsson <i>et al.</i> 2010]
bulk	γ	39	1.3			[Lambert <i>et al.</i> 2011]
bulk	γ	21	<2			[Korsholm <i>et al.</i> 2014]
bulk	γ	10	<1			[Doemer <i>et al.</i> 2015]
atlas	γ	37	1.5			[Dowling <i>et al.</i> 2012]
atlas	γ	39	0.3	40.5	100	[Dowling <i>et al.</i> 2015]
atlas	γ	15	<0.7	50	97.1	[Guerreiro <i>et al.</i> 2017]
hybrid	γ	39	0.3	108	99.6/94.2 ^a	[Ghose <i>et al.</i> 2017]
voxel	γ	15	<1		97 ^a	[Kim <i>et al.</i> 2015]
voxel	γ	10	0.4	54	99/97 ^a	[Andreassen <i>et al.</i> 2016]
voxel	γ	10	<0.8		>99/93 ^a	[Korhonen <i>et al.</i> 2014]
voxel	γ	15	0.2		>99	[Korhonen <i>et al.</i> 014b]
voxel	p	10	0.6	42	98.6/95 ^a	[Koivula <i>et al.</i> 2016]
voxel	γ	35	0.3-2	135	93 ^a	[Koivula <i>et al.</i> 2017]
Vendors' solutions						
hybrid	γ	10	0.4	36.5	99.9 ^b	[Siversson <i>et al.</i> 2015]
hybrid	γ	170	0.3		99.1	[Persson <i>et al.</i> 2017]
bulk ^c	γ	25	<0.6			[Tyagi <i>et al.</i> 2016]
bulk ^c	γ	5	0.7		100/99.1 ^a	[Kemppainen <i>et al.</i> 2017]
bulk ^c	γ	29			99.8/97.3 ^a	[Christiansen <i>et al.</i> 2017]
This thesis						
bulk ^c	γ	14	0.3	58 ^d	98.8	[Maspero <i>et al.</i> 2017]
bulk ^{c,e}	p	10	<1	83 ^f	98.4	[Maspero <i>et al.</i> 2017]

^a $\gamma_{1\%,1mm}$; ^b $\gamma_{2\%,1mm}$; ^cBulk assignment using a model for bone segmentation; ^dData integrated for this thesis; ^eAfter adaptation of the synthetic-HU; ^fin the region with dose > 10% of the prescribed dose.

Chapter 3 aimed at verifying whether MRCAT, which was initially designed for photon radiotherapy, may enable accurate dose calculation for proton radiotherapy as well. Our study showed that accurate MR-based proton dose calculation for prostate cancer treatment could be performed with MRCAT over a population of ten prostate cancer patients. A 98.4% gamma pass rate at 2%/2mm tolerance and a dose difference of 0.7% in the dose volume histogram (DVH) parameters (population mean on CTV) were obtained. However, it should be clarified that such accuracies could only be achieved when recurring to minimisation of inter-scan differences by copying the internal air cavities as localised on CT and adapting synthetic-HU values of the bones. Such adaptation of sCT images aimed at minimising proton range differences between CT and sCT images. Without minimising inter-scan differences and adapting the synthetic-HU, dose differences larger than 2% were obtained. This shows that correct modelling of internal air cavities and varying synthetic-HU is crucial. To facilitate modelling of internal air, a novel method to detect air cavities based on MRCAT was proposed in Chapter 3, and made available under an open source license [Maspero *et al.* 2017].

To date, as also notable in Table 6.1, studies to assess the accuracy of MR-based dose calculations mainly focused on photon radiotherapy [Oborn *et al.* 2017]. The first, and only, study on MR-based proton dose calculations was by Koivula *et al.* The group demonstrated the feasibility of using MRI for dose calculation in the brain as well as prostate proton radiotherapy on a total of twenty patients requiring manual bone segmentation [Koivula *et al.* 2016].

The results obtained in our study are comparable to the findings by Koivula and coworkers [Koivula *et al.* 2016], which makes MRCAT a promising approach to generate sCT images for accurate MR-based proton dose calculations. Moreover, in Chapter 3, it was shown for the first time that accurate MR-based proton dose calculation based on an automatic bulk-assigned sCT generation approach is feasible.

To sum up, the studies presented in **Part I** demonstrated that the use of MRCAT enables MR-based dose calculations both for photon and proton prostate radiotherapy with an accuracy higher than 1%. Such results can support the safe introduction of MRCAT into the clinic addressing the challenge of MR-based dose calculations.

6.2 MR-BASED SET-UP CORRECTIONS

Set-up corrections during an IGRT treatment aim at ensuring that a patient may assume an identical posture and position during an irradiation session and the simulation session. An institute that introduces an MR-only pathway needs to assess whether set-up correction during IGRT can be accurately performed if sCT images or MR-based surrogates of the target position are utilised as references.

For IGRT of patients with prostate cancer, several methods have been proposed and utilised [Das *et al.* 2014, Nabavizadeh *et al.* 2016]. At the University Medical Centre Utrecht, intraprostatic gold fiducial markers (FMs) are used to perform set-up corrections. Therefore, we considered MR-based localisation of the markers as crucial to ensure accuracy on IGRT. In **Part II** of this thesis, automatic and manual localisation of FMs was investigated.

Manual

To verify whether manual FM localisation can be reliably performed when based solely on MR images, we designed and conducted an inter-observer study, which was presented in **Chapter 5**.

In the study, the use of three different MR sequences was investigated in terms of precision, accuracy and agreement among five radiotherapy technicians (RTTs) on 16 patients. The most reliable manual localisation was obtained when the observers could perform the procedure with the aid of multiple (three) 3D MR sequences: a balanced steady-state free precession (bSSFP) which was acquired for prostate delineation, the SPGR sequence already proposed for sCT generation with MRCAT and a gradient-recalled echo (GRE) sequence. In such a case, agreement among all the observers was found for 45/48 FMs. Over the FMs having an agreement among all the observers, a precision of 0.25 mm and an accuracy within 0.6 mm was found for the centre of mass of the three implanted FMs. This is in line with previous research [Schieda *et al.* 2015, Ghose *et al.* 2016, Tyagi *et al.* 2016, Gustafsson *et al.* 2017]. Moreover, this complies with the accuracy necessary in the clinical practice which is about 0.6 mm for the centre of mass of the implanted FMs [van der Heide *et al.* 2007].

Consensus among observers was not obtained over all the five RTTs for 1/3 FMs implanted in three patients. For these three patients, it was observed that FMs localisation was hampered by the presence of calcifications or patient motion. In total, all the observers mislocated the FM localisation in 7/80=8.75% of the cases (5 observers x 16 patients).

The results are promising, especially considering the detection rate but they demonstrated that patient localisation is not feasible for all the patients: 13/16 patients had all the implanted markers correctly located with a detection rate of 0.94 when considering the single FM. Within clinical practice, if all the three gold FMs are not correctly located, patient set-up may be subject to errors. In this sense, it would be desirable to increase redundancy in the procedure such that the probability of locating less than three FMs for one patient may be decreased. To possibly overcome the current challenges, the following strategies were proposed: recurring to multiple-observer localisation, implanting a fourth marker or combining automatic and manual FM localisation.

Currently, at the University Medical Center Utrecht, four FMs are implanted to verify whether implanting an additional marker may be a viable solution to the underlined challenges.

In **Chapter 4** a method to perform automatic localisation of the FMs was presented and assessed considering spatial accuracy, precision and missed localisations. The novelty of the method resides in the use of prior information, i.e. MRI sequence parameters and size/orientations of a FM in the magnetic field. With such *a priori* knowledge, a template of a marker was simulated enabling localisation via template matching using complex MRI images. The working principle of this approach is based on the hypothesis that using both phase and magnitude images during matching may increase the information available and also the specificity of the procedure. A criterion was then set to select as FMs the voxels that were correlating with the template. The proposed method performed similarly to an operator resulting in 50/51 FMs automatically and correctly localised compared to the manually localised FMs. The spatial accuracy of the automatic method (mean) was 0.9 mm, while precision (standard deviation) was 0.6 mm against manual localisation. Both are below the voxel size of the MR sequence used for automatic localisation [Maspero *et al.* 2017]. The accuracy of the automatic localisation of the FM centre of mass was <0.3 mm compared to manual localisation. This was obtained considering the impact on the patient alignment allowing for sole translations.

The results are in line with literature reporting manual CT-based FM localisation, which is considered as the gold standard [Huisman *et al.* 2005, Ullman *et al.* 2006, Deegan *et al.* 2013, Deegan *et al.* 2015]. Huisman *et al.* obtained a precision of 0.5 mm in the centroid of the prostate localised on MR images on a cohort of 21 patients when assessing registration of CT and MR images [Huisman *et al.* 2005]. Ullman *et al.* reported a mean inter-observer variability of 0.9 ± 0.6 mm when performing registration on photon-based portal images [Ullman *et al.* 2006]. Thus far, literature reporting single MR-based FM localisation accuracy was not found by the author. When considering automatic CT-based localisation, Nederveen *et al.* obtained a detection rate of 0.95 and localisation accuracy larger than 0.6 mm for all the different markers investigated [Nederveen *et al.* 2000]. The results of our study are comparable in terms of detection rate and slightly worse in terms of spatial accuracy when compared to automatic localisation of FM on CT images.

To facilitate a comparison of the results obtained in this thesis with the literature on automatic MR-based FM localisation, Table 6.2 was compiled summarising the performance of the three automatic methods presented so far. Ghose *et al.* proposed to exploit manifold learning and spectral clustering to localise gold markers from manually segmented volumes [Ghose *et al.* 2016]. Their method required manual interaction to generate references for data training. Dinis Fernandes *et al.* investigated the use of a logistic regression model on several combinations of MR sequences. They obtained the most promising results when combining multi-parametric MRI and a bSSFP sequence [Dinis Fernandes *et al.* 2017]. Lastly, Gustafsson *et al.* developed a model based on an image processing pipeline able to select a FM in case its signal void increased over gradient echo images with increasing echo times [Gustafsson *et al.* 2017]. As visible in Table 6.2, the study presented within this thesis demonstrated slightly better performances with respect to the aforementioned studies in terms of correctly detected FMs. A limitation of our study was that we did not develop and evaluate the method on

a completely independent dataset, possibly being subject to overfitting. To fully evaluate the method, future work will apply the approach to an independent cohort.

In general, we can state that the results are promising. Nevertheless, the method presented in Chapter 4 does not enable automatic gold FM localisation for all the markers implanted in the patients: for 2/17 patients one of the three implanted markers were incorrectly localised when compared to localisation on CT images, which is in line with previous works. To enable IGRT in such cases, prostate localisation on MR images may also rely on manual localisation in parallel with automatic localisation. In this sense, studies are being conducted to verify whether the automatic approach proposed in Chapter 4 [Maspero *et al.* 2017] may improve overall localisation performances in a semi-automatic setting when four FMs are implanted.

To sum-up, the studies presented in **Part II** resulted in accurate and precise gold FM localisation. However, considering the need of ensuring robustness in the perspective of a clinical adoption of MR-based FM localisation at our insti-

Table 6.2 Overview of the methods for automatic and manual (when presented in the same contribution) FM localisation, along with their performances in terms of patients having all the implanted markers correctly detected (Pt), number and percent of FMs classified as true positive (TP), false negative (FN), false positive (FP) and mean \pm standard deviation [min; max] of the metric used to characterised the distance of the FM centres against the reference (Distance).

Reference	Pt	Performance metrics					
		Comparison	Pt	TP	FN	FP	Distance ^a [mm]
[Ghose <i>et al.</i> 2016]	15	Auto vs Man	10	38/41 92.7%	7	0	0.5 \pm 0.5 [0.0;0.8]
		Man	11	41/45 91.1%	4	0	0.6 \pm 0.6 [0.0;2.0]
[Dinis Fernandes <i>et al.</i> 2017]	32	Auto vs CT	26	88/94 93.7%	6	6	1.6
[Gustafsson <i>et al.</i> 2017]	40	Auto vs Man	24	98/117 83.8%	19	14	1.28 \pm 1.25 [0.0;6.0]
		4 Obs vs Man	41.5				1.14 \pm 1.06 [0.0;6.0]
		This thesis					
[Maspero <i>et al.</i> 2017]	17	Auto vs CT	15	48/51 94.1%	3	0	0.9 \pm 0.6 [0.0;2.7]
		Man vs CT	15	49/51 96.1%	2	0	0.9 \pm 0.7 [0.0;2.8]
		Auto vs Man	16	50/51 98.0%	1	0	0.6 \pm 0.5 [0.0;1.7]
		Man vs Man					

^a Each contribution may provide slightly different metrics, please consider the original reference for more details.

tutions, further investigations are needed. In this sense, verifications are already undergoing to verify the efficacy of increasing redundancy during the FM localisation. When considering the modification to the imaging protocol required to perform MR-based FM localisation, we obtained the most promising results acquiring a 3D GRE sequence for automatic and manual localisation, in combination with the SPGR sequence already acquired for sCT generation and a bSSFP which is usually acquired for prostate delineation. This configuration required adding the GRE sequence to the MR protocol resulting in the extra imaging time of about 2.5 min.

6.3 PRACTICAL CONSIDERATIONS: A CLINICAL PERSPECTIVE

The implementation of an MR-only workflow presents a new set of logistical challenges for the clinical institutions interested in introducing this pathway.

Given the fact that the use of a dedicated MRI simulator is a requirement for an MR-only pathway, personnel needs to be trained and gain experience with such a configuration [Rai *et al.* 2017]. Limited availability of experienced staff is a major hurdle in wide application of an MR-only pathway, especially if no previous knowledge on the use of MRI in radiotherapy is present within an institute [Batumalai *et al.* 2016]. Moreover, quality control of the MRI scanner should be arranged, with special attention to the geometrical accuracy of the MR images and the assessment of image quality for the sequences used for tissue delineation [Paulson *et al.* 2015]. All these considerations are valid for MR-only pathways as well as for the use of MRI in radiotherapy. A specific point for MR-only pathways is the introduction of control procedures to ensure that the quality of sCT images is not degraded over time resulting in inaccurate dose calculations [Frantzen-Steneker 2015].

Clinical institutions should also consider any implementation of algorithms to make the workflow as streamlined as possible. For example, no standard is defined within the digital imaging and communication in medicine (DICOM) concerning the data format of sCT images [Torresin *et al.* 2015]. Particularly, sCT images are acquired from an MR scanner but are expressed in HU and need to comply with the DICOM standard of CT images to be accepted for dose calculations in treatment planning systems. In my opinion, such a situation is confusing since the standard is currently improperly used. Modifications of the current DICOM may solve this situation.

Institutions also need to define clear rules for patient inclusion in the MR-only pathways and be able to recur to a CT-based pathway in case of patients' ineligibility. For example, to date, MR-only prostate radiotherapy is contra-indicated for patients with hip implants.

6.3.1 MR protocol optimisation: an example from Utrecht

MRI is traditionally considered as a slow imaging technique compared to, for example, CT and ultrasound [Brix *et al.* 2014]. A typical imaging session at an MR scanner for a prostate investigation lasts maximum 30 min for diagnostic

purposes and maximum 45 min for treatment simulation [Hegde *et al.* 2013]. In such a time period, intra-scan motion may occur [McPartlin *et al.* 2016] potentially undermining the advantages offered by an MR-only pathway.

Ideally, to minimise the likelihood of intra-scan motion [Tree *et al.* 2012, McPartlin *et al.* 2016], the total acquisition time comprising the sequences used for delineation, sCT generation and FM localisation purposes should be as short as possible. Moreover, all these sequences should have high bandwidth to ensure geometric fidelity of the MRI images. As an example of protocol optimised to comply with the needs of an MR-only patient simulation, Table 6.3 reports the sequences presented in this thesis. Currently, such a protocol is considered for use in the MR-only radiotherapy pathway at Utrecht. This protocol includes sequences for target and OARs delineation, sCT generation and gold FM localisation. The imaging time comprising three sequences is about 10 min, which is comparable to the time necessary to deliver an intensity-modulated radiotherapy (IMRT) plan [Teoh *et al.* 2011]. This makes the imaging time acceptable to facilitate consistency of organs' position during acquisition, in case the three sequences are acquired consecutively.

Table 6.3 MRI sequences proposed in this thesis for a prostate MR-only simulation as on a 3 T MR scanner (Ingenia, Philips). Image parameters are expressed in terms of: weighting (W), field of view (FOV), acquisition matrix (acq matrix), reconstructed resolution (recon res), echo time(s) and relaxation time (TE₁.../TR), flip angle (FA), bandwidth per voxel (BW/vox) and acquisition time (acq time).

Goal	Sequence	W	FOV ^a [mm ³]	Acq ^a Matrix	Recon ^a Res	TE ₁ .../TR [ms]	FA [°]	BW/vox [Hz]	Acq Time
Prostate delineation & man FM	3D bSSFP Fat sat	T ₂ /T ₁	25 25 9	252 234 90	0.5 0.5 1	1.98/3.96	40	945	4 min 40 s
sCT generation & man FM	3D SPGR dixon	~T ₁	55.2 55.2 30	376 376 120	1.1 1.1 2.5	1.2/2.5/3.9	10	1083	2 min 13 s
auto FM man FM	3D GRE	~T ₁	45 45 9	376 376 75	1.1 1.1 1.2	1.4/2.7/4.6	10	1142	2 min 34 s

^aexpressed in terms of anterior-posterior, right-left and superior-inferior directions. The readout direction is in bold.

6.3.2 MR-only delineations for OARs

A crucial step for an MR-only pathway that has not yet been discussed is fully MR-based OARs delineation.

Recently, centres involved in introducing an MR-only pathway took the initiative of defining protocols for MR-only-based delineations. Comparing the practices adopted by these centres (when fully reported²), it is noticeable that to enable MR-only-based delineations, the FOV of the images should be enlarged to include

²An interesting initiative regarding standardisation of MRI for use in radiotherapy that comprehends some guidelines and full report of MR protocols is within the Swedish consortium called Gentle: <http://gentleradiotherapy.se/>

contouring of all the OARs as currently defined on CT images. To comply with this requirement, the FOV of T2 weighted images is extended such that delineation of target and OARs can be performed in a single sequence. This approach was suggested by experts' consensus [Paulson *et al.* 2016]. Moreover, other groups with interest in an MR-only pathway followed the same approach. Christiansen *et al.* reported acquiring in 7 min 26 s a 3D T2 weighted (probably spin echo) sequence with FOV of 368x552x300 mm³ for OARs delineation [Christiansen *et al.* 2017]. Tyagi *et al.* reported acquiring three two-dimensional (2D) fast spin echo sequences with sagittal, axial and coronal orientations and different FOV coverage for the same scope. Moreover, the MR images acquired for sCT generation (MRCAT) were used to support delineation in case the coverage of the FOV on T2 weighted images was not sufficient [Tyagi *et al.* 2017]. In total, about 25 min were required for contouring, sCT generation and gold FM localisation.

Currently, in the hybrid CT/MRI simulation pathway adopted in Utrecht, the delineation of the target is performed on MR images, while OARs are delineated on CT. For future use in an MR-only pathway, the SPGR sequence (MRCAT) may be an excellent candidate to perform OARs delineations given the large FOV, bandwidth and considering that the sequence is already used for patient simulation (see 6.3). This sequence is particularly interesting because it produces multi-contrast images via a Dixon reconstruction [Eggers *et al.* 2011] that may facilitate delineation. Also, the SPGR sequence is used for sCT generation which ensures consistency of delineated structures and dose calculation. Currently, to validate such a hypothesis, investigations are undergoing to assess whether the SPGR sequence is suitable for OARs delineation.

6.4 FUTURE PERSPECTIVES

Currently, independent investigations are undergoing in Utrecht to verify the logistical implementation of the pathway for prostate cancer patients based on the indications proposed in this thesis. To warrant MR-based set-up correction based on MR images for the totality of the patients in Utrecht, a pathway composed by the use of manual and automatic FM localisation of four FMs is being assessed. In the near future an MR-only radiotherapy for prostate cancer patients will be clinically implemented in Utrecht if this configuration will prove its robustness.

6.4.1 ...beyond prostate treatments

In general, the future of MR-only radiotherapy pathways is strictly linked to the use of MRI in radiotherapy: recurring to an MR-only pathway is justified only for anatomical locations where signs of evidence supported the use of MRI during the treatment planning, e.g. target/OAR delineation or primary tumour identification. The use of MRI in radiotherapy seems to improve target delineation for pelvis, brain, breast and head and neck tumours [Dirix *et al.* 2014, Paulson *et al.* 2016]. For these anatomical sites, it may be justified to design MR-only pathways.

WITHIN THE PELVIC AREA Considering that sCT image generation is the biggest challenge when designing an MR-only pathway [Torresin *et al.* 2015], MR-only

for general pelvis may be easily designed extending or re-using sCT generation techniques adopted for prostate treatment.

In case the current commercial sCT generation approaches designed for treatment of prostate cancer patient could be utilised for the whole pelvis, MR-only pathways for the pelvic region may be soon clinical practice in our institution. Kemppainen *et al.* have already shown that MR-based calculations for cervical and rectal cancer patients using MRCAT is feasible [Kemppainen *et al.* 2017]. Currently, at the University Medical Centre Utrecht, we are investigating MR-only for rectal cancer patients with MRCAT, obtaining promising results [Maspero *et al.* 2018]. For this anatomical site, position verification is generally based on bone match [Gwynne *et al.* 2012, Nijkamp *et al.* 2012], which may make easier clinical implementation given the fact that there is no need to develop a technique to localise gold FMs as for prostate cancer patients.

OTHER SITES The use of MRI during treatment planning of **brain** tumours is standard of practice since the beginning of the millennium [Creak *et al.* 2011, Majithia *et al.* 2016]. For this reason, several methods for sCT generations were presented for this anatomical site [Edmund & Nyholm 2017, Johnstone *et al.* 2017] making brain the anatomical location having the largest amount of methods proposed for sCT generation.

Feasibility of MR-only pathways for **head and neck** was investigated, mostly using bulk-assignment sCT generation techniques [Johnstone *et al.* 2017]. Recently, we have presented methods based on T1-weighted gradient echo images [Maspero *et al.* 2015], and the site is the current object of further investigations in our institute [Wolterink *et al.* 2017].

The feasibility of MR-based dose calculation with bulk-assignment was investigated for other locations, e.g. for **lung** [Prior *et al.* 2017], **pancreas** [Prior *et al.* 2016] and **liver** [Bredfeldt *et al.* 2017]. The results are promising and pave the way for more sophisticated approaches such that higher accuracy may be achieved during dose calculations.

So far, there was little discussion about other sites, and it may be interesting to deepen the matter in future studies. Perhaps, the reason why sCT generation techniques were mostly presented for pelvis and brain is the fact that these locations are minimally affected by motion [Tree *et al.* 2012, McPartlin *et al.* 2016, Majithia *et al.* 2016]. When present, motion is a problem because it can significantly degrade the images [Koay *et al.* 2017] making structure delineations and sCT generation challenging. In my opinion, the ultimate challenge for MR-only radiotherapy is the application to mobile organs. Perhaps, such a challenge can be considered as the most rewarding as well since for mobile organs misregistration of CT and MR images can be expected to be higher than for non-moving tumours.

6.4.2 MR-only for MRI-guided radiotherapy

Another interesting application of MR-only radiotherapy is MRigRT, where the use of MR-based dose calculations could enable acquisition of daily anatomy to deal with inter-fraction differences as well as streamlined intra-fractional plan adaptations. One of the prerequisite to reaching such a goal is the fast generation of sCT images.

To date, only few sCT generation approaches can create images in a matter of minutes. Among the few methods, the atlas-based sCT generation approaches seem to be the best performing, showing sCT generation in the order of 3 min [Dowling *et al.* 2014].

Recently, machine learning-based sCT generation were also presented [Han 2017, Wolterink *et al.* 2017] enabling sCT generations of a full 3D volume below a minute (acquisition time is about 4 min). Moreover, we have recently presented a contribution for fast generation of sCT for general pelvis radiotherapy using multi-contrast MR images acquired with a single acquisition. The results obtained were promising and a full 3D volume was generated in 5.6 s with an acquisition time of less than 2.5 min [Savenije *et al.* 2018, Maspero *et al.* 2018].

So far MR-based dose calculations were assessed only in the absence of magnetic field. For MRIGRT, dose calculations may require particular attention because the presence of a magnetic field affects the dose distribution in patients. This phenomenon is known as electron return effect, and it was shown that the dose distribution could be disturbed especially when a photon beam traverses tissue interfaces [Raaijmakers *et al.* 2008].

Within an MR-only radiotherapy pathway, taking into account the electron return effect means that sCT images should correctly model air-tissue interfaces. Future studies should focus on assessing the accuracy of MR-based dose calculations including the contribution of the magnetic field.

In principle, position verification with MRIGRT system could be based solely on MR images enabling corrections directly on soft tissue for the prostate case. Future studies are necessary to assess which may be the best position verification technique given the new possibilities offered by MRIGRT.

6.5 CONCLUSION

This thesis presented an investigation to facilitate the introduction of an MR-only radiotherapy for prostate cancer patients within the University Medical Centre Utrecht. In **Part I**, MR-based dose calculation was demonstrated to be feasible. In **Part II** strategies to perform MR-based gold FM localisation were assessed. In the light of the work here presented, we found that:

- MR-based dose calculations for photon-based radiotherapy performed on MRCAT is accurate. We obtained a dose difference $<0.5\%$ against CT-based calculations.
- MR-based dose calculations for proton-based radiotherapy performed on MRCAT is accurate upon modification of HU and minimising inter-scan differences in the positions of air pocket between sCT and CT images. With this study, we showed, for the first time, that automatic bulk-assigned sCT image generation enables MR-based calculations for proton MR-only radiotherapy. Also, we presented an automatic method to insert air pocket in MRCAT which can be applied in an MR-only pathway.
- manual MR-based FM localisation performed better when multiple MR sequences are available. In such a case, an accuracy higher than 0.6 mm was

obtained, which is comparable to the gold standard represented by CT-based localisation.

- manual FM localisation resulted in mislocating patient positioning due to FM misclassification in $7/80=8.75\%$ of all the single observer localisations performed (5 observers \times 16 patients). We believe that the risk of misclassification is too high to allow recurring solely to human observers and we proposed adding redundancy to the procedure to decrease the risk.
- the newly proposed automatic method for FM localisation can achieve a detection rate of 94% and a spatial accuracy of 0.9 mm with respect to CT-based localisation.

In addition, we proposed the use of a fast MR protocol enabling patient simulation based solely on MR images. In this protocol, the sequence used for sCT generation and manual and automatic FM localisation are acquired within 10 min.

Ultimately, the work presented in this thesis contributed to shaping the implementation of the clinical pathway in Utrecht aiming at ensuring a safe introduction of MR-only radiotherapy for prostate cancer patients.

Summaries

SAMENVATTING

Radiotherapie is een lokale behandeling waarbij gebruik wordt gemaakt van het celdodende effect van ioniserende straling om kanker te genezen. Dit effect is echter globaal en niet specifiek gericht op het beschadigen van kankercellen en het sparen van gezonde cellen. Daarom zijn veel ontwikkelingen in radiotherapie gericht op het verminderen van onzekerheden in de behandeling, zodanig dat er een therapeutische stralingsdosis kan worden afgeleverd aan een kwaadaardige tumor terwijl de dosis in het gezonde weefsel zo laag mogelijk blijft. De recente ontwikkelingen in beeldvormende technieken hebben een grote impact op de radiotherapie strategieën.

In westerse landen is prostaatkanker één van de meest gediagnosticeerde kankersoorten bij mannen en radiotherapie één van de meest gebruikte behandelingen voor prostaatkankerpatiënten. Omdat de prostaat een klier is die bestaat uit zacht weefsel, wordt het voordeel van MRI voor radiotherapie erkent: het vergroot de precisie waarmee we het doelwit kunnen vastleggen.

Tot op heden wordt computertomografie (CT) beschouwd als de primaire modaliteit in radiotherapie. Dit levert een gepersonaliseerd patiëntmodel op om de stralingsattenuatie bij mensen vast te stellen. Ook wordt in toenemende mate magnetische resonantie beeldvorming (MRI) gebruikt bij het plannen van radiotherapeutische behandelingen. In het bijzonder voor het bepalen van tumoren vanwege het superieure weke delencontrast in vergelijking met CT.

Om een bestralingsplan te creëren gebruikt men op dit moment zowel CT- als MRI-beelden. Doordat de CT en MRI op de verschillende momenten worden gemaakt geeft dit onzekerheid en kan het fouten induceren in de positionering van de patiënt.

Om mogelijke positioneringsverschillen te elimineren, is *MR-only* radiotherapie voorgesteld. MR-only radiotherapie biedt praktische en logistieke voordelen zoals het vereenvoudigen van het behandelingstraject door de totale kosten en werklust te verlagen en de blootstelling van patiënten aan schadelijke CT straling te verminderen. Bij MR-only radiotherapie worden alleen MR-beelden gebruikt voor intekening, dosisplanning en als referentiebeelden voor positionering van de patiënt tijdens de bestraling. MRI verschaft echter geen informatie over de verzwakking van straling in het lichaam en het kan geometrische vervormingen geven die de nauwkeurigheid van de positionering van de patiënt beïnvloeden.

Om dergelijke uitdagingen het hoofd te bieden zijn in dit proefschrift strategieën onderzocht voor het uitvoeren van radiotherapie voor prostaatkankerpatiënten op basis van MRI. Dit onderzoek maakt een toekomstige klinische implementatie mogelijk. Het onderzoek is in twee delen verricht.

In **Deel I** concentreert het proefschrift zich op de evaluatie van de dosimetrische nauwkeurigheid. Deze nauwkeurigheid is bepaald door planningen te ma-

ken op MRI en CT en deze met elkaar te vergelijken. Vanuit klinisch perspectief is de nauwkeurigheid van de dosisberekening, met als basis MRI, onderzocht. Hiervoor gebruiken we een commerciële oplossing, genaamd MRCAT (Philips Healthcare). Deze oplossing is bruikbaar voor zowel fotonen- (Hoofdstuk 2) als protonenbestraling (Hoofdstuk 3).

Deel II onderzocht of beeldgestuurde radiotherapie (IGRT) haalbaar is als de correctie van de patiënt positionering uitsluitend berust op MRI als referentie-beeldvormingsmodaliteit. IGRT voor prostaatpatiënten is gebaseerd op de lokalisatie van goudmarkers geïmplanteerd in de prostaat. Dit maakt het belangrijk om deze goed te visualiseren. De verschillen tussen waarnemers zijn geëvalueerd (Hoofdstuk 5). Tevens is er een automatische methode voorgesteld die leidt tot een detectiegraad die vergelijkbaar is met die van een handmatige waarnemer (Hoofdstuk 4).

Uiteindelijk heeft het werk wat in het proefschrift is gepresenteerd bijgedragen aan het vormgeven van de klinische implementatie van de MR-only radiotherapie in het UMC Utrecht, met als doel een veilige introductie voor prostaatkankerpatiënten te garanderen.

RIASSUNTO

La radioterapia utilizza radiazioni ionizzanti per trattare neoplasie (uso curativo), alleviare il dolore dei pazienti (uso palliativo), ridurre la probabilità di recidiva tumorale o aumentare l'efficacia di altri trattamenti come chemioterapia o intervento chirurgico. La radioterapia è un trattamento così diffuso che attualmente viene utilizzato per il 50 ed il 65% di tutti i pazienti affetti da neoplasie.

Durante la radioterapia la radiazione ionizzante viene diretta verso il tumore rilasciando una dose capace di danneggiare i tessuti interessati. Tuttavia, in prossimità di neoplasie si possono trovare anche tessuti sani. Per far sì che tali tessuti non siano danneggiati o che il loro danneggiamento sia limitato, i cosiddetti "piani di trattamento" radioterapico vengono ottimizzati per ogni paziente. Per facilitare la personalizzazione dei piani di trattamento, svariate modalità di imaging diagnostico sono attualmente utilizzate. La principale modalità di imaging in uso per scopi radioterapici è la tomografia computerizzata (TC): la TC permette, infatti, di misurare accuratamente l'attenuazione della radiazione, attraverso il calcolo della radiazione rilasciata nel corpo dei pazienti ed in alcuni casi anche tramite la localizzazione del tumore.

Negli ultimi decenni, la risonanza magnetica (RM) è sempre più utilizzata in radioterapia. RM offre un eccellente contrasto per i tessuti molli come muscoli o massa grassa ed ha dimostrato di poter localizzare più accuratamente le regioni tumorali rispetto al solo uso di TC. In particolare, ciò è valido per il cancro alla prostata, oggetto di studio di questa tesi.

Nei moderni dipartimenti di radioterapia i vantaggi offerti dalla RM sono sfruttati durante la fase di simulazione sottoponendo i pazienti sia a TC che a RM. Tuttavia, durante due differenti esami diagnostici un paziente può essere posizionato in modo differente o il target radioterapico può essere diversamente posizionato rispetto ai tessuti circostanti inducendo errori sistematici tra le due sessioni di imaging.

Per tentare di minimizzare incertezze ed errori di localizzazione, è stato proposto l'uso della sola RM in fase di simulazione del paziente. Tale proposta presenta anche dei vantaggi dal punto di vista logistico: eliminando una sessione di imaging (TC) la procedura radioterapica può risultare in una generale diminuzione dei costi ed in una diminuzione della dose di radiazione ionizzante rilasciata nel paziente. Tuttavia, utilizzare solamente la RM in fase di simulazione comporta una serie di problemi. Il primo risiede nel fatto che la fisica della RM non è legata all'attenuazione della radiazione ionizzante nella materia. Ciò non rende possibile la pianificazione di un piano di trattamento direttamente da immagini di RM, poiché non è possibile calcolare la dose di radiazione ionizzante rilasciata nel paziente. Per ovviare a tale impedimento sono stati sviluppati metodi per sintetizzare immagini equivalenti a TC a partire da RM.

Nella **Parte I** di questa tesi viene considerato uno dei metodi disponibili a livello commerciale e certificato per uso medico. Il metodo è chiamato MR for calculating attenuation (MRCAT) e permette di produrre immagini di TC segmentando automaticamente i tessuti ed assegnando ad essi designati valori di attenuazione.

Nel **Capitolo 2** di questa tesi si discute se MRCAT permetta l'accurato calcolo della dose rilasciata nel paziente, nel caso di radioterapia con fotoni; mentre nel **Capitolo 3** viene trattata la radioterapia con protoni. In entrambi i casi, MRCAT ha permesso di calcolare la dose in modo accurato rispetto alla dose calcolata con TC. In aggiunta, nel **Capitolo 2** sono stati quantificati con uno studio su 14 pazienti i diversi fattori che inducono differenze tra dose calcolata con MRCAT e TC. Il fattore preponderante che contribuisce a queste differenze in dose calcolata è riconducibile all'uso di diverse curve di calibrazione tra hounsfield unit (HU) e densità elettronica (usata per calcolare l'attenuazione della radiazione nel corpo) rispetto alla curva in uso in Utrecht e quella suggerita per MRCAT. Tale fattore ha contribuito per circa 0.7% a differenze tra la dose calcolata con MRCAT rispetto alla dose calcolata con TC. Utilizzando la medesima curva di calibrazione le differenze sono state ridotte a circa 0.3%. Tale differenza è stata considerata accettabile per uso clinico ed in accordo con i risultati riportati in letteratura da altri gruppi di ricerca.

Nel **Capitolo 3** si è dimostrato che è possibile utilizzare MRCAT anche per radioterapia con protoni. In particolare, uno studio retrospettivo condotto su dieci pazienti affetti da cancro alla prostata ha dimostrato differenze inferiori all'1% tra dosi calcolate con MRCAT e TC. Questo studio ha presentato, per la prima volta, l'accuratezza di dosi calcolate sulla base di immagini con RM, utilizzando un surrogato della TC automaticamente generato e costituito da un fissato (5) numero di HU. Tuttavia, nello studio, è stato dimostrato che per raggiungere tale accuratezza i valori di HU assegnati per MRCAT devono essere adattati rispetto a quanto in uso per terapia fotonica e che il contributo dovuto a differenze nella posizione di aree contenenti gas nel paziente deve essere minimizzato. Inoltre nello studio si è presentato un metodo per ottenere in modo automatico la posizione delle aree gassose nel paziente a partire da immagini di RM.

Nella **Parte I** della tesi si è approfondito il posizionamento del paziente a partire da simulazioni con RM. In particolare, nel caso di trattamento alla prostata guidato da immagini, dei marker d'oro vengono impiantati nella prostata e permettono un accurato e preciso posizionamento del paziente. Infatti tali marker fungono da surrogato della prostata e sono facilmente visibili con imaging a base di fotoni. Tuttavia, i marker non producono in RM e la loro visibilità, accuratezza e precisione di localizzazione non è quindi assicurata.

Per verificare che i marker siano visibili e accuratamente localizzati su immagine di RM, nel **Capitolo 5** si è presentato uno studio che coinvolge cinque osservatori e valuta la precisione di localizzazione manuale dei marker su immagini di RM provenienti da sedici pazienti aventi ciascuno tre marker. Le sequenze in cui i marker sono localizzati più accuratamente sono state individuate, ottenendo un accordo (valutato a posteriori) sulla posizione che 45 dei 48 marker sono stati localizzati da tutti e cinque gli osservatori. Una precisione di 0.25 mm ed accuratezza di 0.6 mm sono stati trovati per i marker localizzati in accordo tra gli osservatori. Consenso non è stato ottenuto tra i tecnici di radioterapia a causa della presenza di calcificazioni (2 marker) o movimento del paziente (1 marker) in fase di acquisizione dell'immagine. Rispetto alla posizione dei marker localizzata nella clinica a partire da TC, $7/80=8.75\%$ delle localizzazioni su RM ha una distanza superiore ai 2.5 mm rispetto a quanto trovato su TC. Tali risultati sono

promettenti, tuttavia un numero troppo alto di errate localizzazioni dei marker su RM rischia di indurre errori sistematici nella localizzazione del paziente. In tal senso, metodi quali l'aggiunta di un quarto marker o il ricorrere a localizzazione automatica dei marker sono stati ipotizzati per ridurre la probabilità di errato posizionamento dei marker. Questi metodi sono attualmente oggetto di studi.

Nel **Capitolo 4** viene presentato un metodo per la localizzazione automatica dei marker; esso sfrutta la conoscenza di informazioni riguardanti la forma dei marker e la sequenza di RM utilizzata. A partire da tali informazioni, le immagini di RM vengono simulate per ottenere la posizione dal marker correlando le immagini simulate e quelle acquisite. Il metodo proposto è stato valutato rispetto alla localizzazione di un osservatore su RM e alla localizzazione dei marker su TC precedentemente eseguita per scopi clinici. In 49/51 dei marker (su 17 pazienti) il metodo ha localizzato i marker ad una distanza inferiore ai 2.5 mm rispetto alla posizione utilizzata per scopi clinic. Accuratezza e precisione del metodo sono comparabili con metodi automatici precedentemente proposti e comparabili con le performance di un singolo operatore.

Attualmente (dicembre 2017) in Utrecht è in corso l'implementazione della preparazione della radioterapia utilizzando la sola RM nella fase di simulazione. Questa tesi ha contribuito a verificare i metodi necessari per tale implementazione.

Part IV

Index

Bibliography

- [Adjeiwaah *et al.* 2017] Adjeiwaah, M., Bylund, M., Lundman, J. A., Thellenberg Karlsson, C., Jonsson, J. H., & Nyholm, T. (2017). Quantifying the effect of 3T MRI residual system and patient-induced susceptibility distortions on radiotherapy treatment planning for prostate cancer. *Int. J. Radiat. Oncol. Biol. Phys.* (Cited on page 12.)
- [Andreasen *et al.* 2016] Andreasen, D., Van Leemput, K., & Edmund, J. M. (2016). A patch-based pseudo-CT approach for MRI-only radiotherapy in the pelvis. *Med. Phys.*, 43(8Part1), 4742–4752. (Cited on pages 11 and 103.)
- [Andreychenko *et al.* 2017] Andreychenko, A., Kroon, P. S., Maspero, M., Jürgenliemk-Schulz, I., De Leeuw, A. A. C., Lam, M. G. E. H., Lagendijk, J. J. W., & van den Berg, C. A. T. (2017). The feasibility of semi-automatically generated red bone marrow segmentations based on MR-only for patients with gynecologic cancer. *Radiother. Oncol.*, 123(1), 164–168. (Cited on page 153.)
- [Ash *et al.* 2000] Ash, D., Flynn, A., Battermann, J., de Reijke, T., Lavagnini, P., & Blank, L. (2000). ESTRO/EAU/EORTC recommendations on permanent seed implantation for localized prostate cancer. *Radiother. Oncol.*, 57(3), 315–321. (Cited on page 41.)
- [Bai *et al.* 2013] Bai, Y., Wang, M.-Y., Han, Y.-H., Dou, S.-W., Lin, Q., Guo, Y., Li, W., Ding, D.-G., Dai, J.-P., Qin, W., Shi, D.-P., Tian, J., & Dai, Y.-M. (2013). Susceptibility Weighted Imaging: A New Tool in the Diagnosis of Prostate Cancer and Detection of Prostatic Calcification. *PLoS ONE*, 8(1), e53237. (Cited on page 73.)
- [Baldwin *et al.* 2007] Baldwin, L. N., Wachowicz, K., Thomas, S. D., Rivest, R., Fallone, B. G., Tg, A., Wachowicz, K., Thomas, S. D., Rivest, R., & Fallone, B. G. (2007). Characterization, prediction, and correction of geometric distortion in 3 T MR images. *Med. Phys.*, 34(2), 388–99. (Cited on page 26.)
- [Balter *et al.* 1995] Balter, J. M., Lam, K. L., Sandler, H. M., Littles, J., Bree, R. L., & Ten Haken, R. K. (1995). Automated localization of the prostate at the time of treatment using implanted radiopaque markers: Technical feasibility. *Int. J. Radiat. Oncol. Biol. Phys.*, 33(5), 1281–1286. (Cited on page 81.)
- [Barentsz *et al.* 2012] Barentsz, J. O., Richenberg, J., Clements, R., Choyke, P., Verma, S., Villeirs, G., Rouviere, O., Logager, V., Fütterer, J. J., & European Society of Urogenital Radiology (2012). ESUR prostate MR guidelines 2012. *Eur. Radiol.*, 22(4), 746–757. (Cited on page 8.)
- [Baskar *et al.* 2012] Baskar, R., Lee, K. A., Yeo, R., & Yeoh, K.-W. (2012). Cancer and Radiation Therapy: Current Advances and Future Directions. *Int. J. Med. Sci.*, 9(3), 193–199. (Cited on page 4.)
- [Batumalai *et al.* 2016] Batumalai, V., Holloway, L., Kumar, S., Dundas, K., Jameson, M., Vinod, S., & Delaney, G. (2016). PO-1017: Survey of image-guided radiation therapy use in Australia. *Radiother. Oncol.*, 119, S492–S493. (Cited on page 108.)
- [Beard *et al.* 1996] Beard, C. J., Kijewski, P., Bussière, M., Gelman, R., Gladstone, D., Shaffer, K., Plunkett, M., Costello, P., & Coleman, C. (1996). Analysis of prostate and seminal vesicle motion: Implications for treatment planning. *Int. J. Radiat. Oncol. Biol. Phys.*, 34(2), 451–458. (Cited on pages 13, 59, and 73.)
- [Beavis *et al.* 1998] Beavis, A. W., Gibbs, P., Dealey, R. A., & Whitton, V. J. (1998). Radiotherapy treatment planning of brain tumours using MRI alone. *Brit. J. Radiol.*, 71(845), 544–548. (Cited on pages 9 and 10.)

- [Beld *et al.* 2016] Beld, E., Moerland, M. A., Zijlstra, F., Lagendijk, J. J., Viergever, M. A., & Seevinck, P. R. (2016). Automatic high temporal and spatial resolution position verification of an HDR brachytherapy source using subpixel localization and SENSE. In *Proc. Intl. Soc. Magn. Reson. Med.*, number 3585 in 24. (Cited on page 60.)
- [Beltran *et al.* 2008] Beltran, C., Herman, M. G., & Davis, B. J. (2008). Planning Target Margin Calculations for Prostate Radiotherapy Based on Intrafraction and Interfraction Motion Using Four Localization Methods. *Int. J. radiat. Oncol. Biol. Phys.*, 70(1), 289–95. (Cited on page 81.)
- [Berberat *et al.* 2014] Berberat, J., Grobholz, R., Boxheimer, L., Rogers, S., Remonda, L., & Roelcke, U. (2014). Differentiation Between Calcification and Hemorrhage in Brain Tumors Using Susceptibility-Weighted Imaging: A Pilot Study. *Am. J. Roentgenol.*, 202(4), 847–50. (Cited on page 73.)
- [Bert & Durante 2011] Bert, C. & Durante, M. (2011). Motion in radiotherapy: particle therapy. *Phys. Med. Biol.*, 56(16), R113–R144. (Cited on page 39.)
- [Bol *et al.* 2003] Bol, G. H., Kotte, A. N. T. J., & Lagendijk, J. J. W. (2003). Volumetool: an image evaluation, registration, and delineation system for radiotherapy. *Phys. Med.*, 19, 80. (Cited on page 62.)
- [Bouwman & Bakker 2012] Bouwman, J. G. & Bakker, C. J. G. (2012). Alias subtraction more efficient than conventional zero-padding in the Fourier-based calculation of the susceptibility induced perturbation of the magnetic field in MR. *Magn. Res. Med.*, 68(2), 621–630. (Cited on pages 63 and 76.)
- [Bredfeldt *et al.* 2017] Bredfeldt, J. S., Liu, L., Feng, M., Cao, Y., & Balter, J. M. (2017). Synthetic CT for MRI-based liver stereotactic body radiotherapy treatment planning. *Phys. Med. Biol.*, 62(8), 2922–2934. (Cited on page 111.)
- [Brierley *et al.* 2017] Brierley, J., Gospodarowicz, M. K., & Wittekind, C. (2017). *TNM classification of malignant tumours* (8 ed.). Wiley-Blackwell. (Cited on page 3.)
- [Brix *et al.* 2014] Brix, L., Sørensen, T. S., Berber, Y., Ries, M., Stausbøl-Grøn, B., & Ringgaard, S. (2014). Feasibility of interactive magnetic resonance imaging of moving anatomy for clinical practice. *Clin. Physiol. Funct. Imaging*, 34(1), 32–38. (Cited on page 108.)
- [Brock & Dawson 2014] Brock, K. K. & Dawson, L. A. (2014). Point: Principles of Magnetic Resonance Imaging Integration in a Computed Tomography-Based Radiotherapy Workflow. *Semin. Radiat. Oncol.*, 24(3), 169–74. (Cited on pages 19 and 39.)
- [Brown *et al.* 2014] Brown, R. W., Cheng, Y.-C. N., Haacke, E. M., Thompson, M. R., & Venkatesan, R. (2014). *Magnetic resonance imaging: physical properties and sequence design*. Wiley. (Cited on page 10.)
- [Brunelli 2009] Brunelli, R. (2009). *Front Template Matching Techniques in Computer Vision*. Chichester, UK: John Wiley & Sons, Ltd. (Cited on page 60.)
- [Bujold *et al.* 2012] Bujold, A., Craig, T., Jaffray, D., & Dawson, L. A. (2012). Image-Guided Radiotherapy: Has It Influenced Patient Outcomes? *Semin. Radiat. Oncol.*, 22(1), 50–61. (Cited on pages 13 and 59.)
- [Carballido-Gamio *et al.* 2013] Carballido-Gamio, J., Harnish, R., Saeed, I., Streeper, T., Sigurdsson, S., Amin, S., Atkinson, E. J., Therneau, T. M., Siggeirsdottir, K., Cheng, X., Melton, L. J., Keyak, J., Gudnason, V., Khosla, S., Harris, T. B., Lang, T. F., & Lang, T. F. (2013). Proximal femoral density distribution and structure in relation to age and hip fracture risk in women. *J. Bone Min. Res.*, 28(3), 537–46. (Cited on page 52.)

- [Chan *et al.* 2015] Chan, M. F., Cohen, G. N., & Deasy, J. O. (2015). Qualitative Evaluation of Fiducial Markers for Radiotherapy Imaging. *Technol. Cancer. Res. Treat.*, 14(3), 298–304. (Cited on page 60.)
- [Chen *et al.* 2004] Chen, L., Price, R. a., Nguyen, T.-B., Wang, L., Li, J. S., Qin, L., Ding, M., Palacio, E., Ma, C.-M., & Pollack, a. (2004). Dosimetric evaluation of MRI-based treatment planning for prostate cancer. *Phys. Med. Biol.*, 49(22), 5157–70. (Cited on pages 11, 13, 19, 20, 40, 59, and 103.)
- [Chen *et al.* 2014] Chen, W., Zhu, W., Kovanlikaya, I., Kovanlikaya, A., Liu, T., Wang, S., Salustri, C., & Wang, Y. (2014). Intracranial Calcifications and Hemorrhages: Characterization with Quantitative Susceptibility Mapping. *Radiol.*, 270(2), 496–505. (Cited on page 73.)
- [Chernak *et al.* 1975] Chernak, E. S., Rodriguez-Antunez, A., Jelden, G. L., Dhaliwal, R. S., & Lavik, P. S. (1975). The use of computed tomography for radiation therapy treatment planning. *Radiol.*, 117(3 Pt 1), 613–14. (Cited on pages 19 and 39.)
- [Christiansen *et al.* 2017] Christiansen, R. L., Jensen, H. R., & Brink, C. (2017). Magnetic resonance only workflow and validation of dose calculations for radiotherapy of prostate cancer. *Acta Oncol.*, 56(6), 787–791. (Cited on pages 11, 103, and 110.)
- [Constantinou *et al.* 1992] Constantinou, C., Harrington, J. C., & DeWerd, L. A. (1992). An electron density calibration phantom for CT-based treatment planning computers. *Med. Phys.*, 19(2), 325–27. (Cited on pages 5 and 21.)
- [Cooperberg *et al.* 2010] Cooperberg, M. R., Broering, J. M., & Carroll, P. R. (2010). Time trends and local variation in primary treatment of localized prostate cancer. *J. Clin. Oncol.*, 28(7), 1117–23. (Cited on page 6.)
- [Creak *et al.* 2011] Creak, A., Tree, A., & Saran, F. (2011). Radiotherapy Planning in High-grade Gliomas: a Survey of Current UK Practice. *Clin. Oncol.*, 23(3), 189–198. (Cited on page 111.)
- [Das *et al.* 2014] Das, S., Liu, T., Jani, A. B., Rossi, P., Shelton, J., Shi, Z., & Khan, M. K. (2014). Comparison of Image-guided Radiotherapy Technologies for Prostate Cancer. *Am. J. Clin. Oncol.*, 37(6), 616–623. (Cited on pages 13, 59, and 105.)
- [Dawson & Jaffray 2007] Dawson, L. A. & Jaffray, D. A. (2007). Advances in image-guided radiation therapy. *J. Clin. Oncol.*, 25(8), 938–46. (Cited on page 6.)
- [Dearnaley *et al.* 2016] Dearnaley, D., Syndikus, I., Mossop, H., Khoo, V., Birtle, A., Bloomfield, D., Graham, & ..., & Investigators CHHiP (2016). Conventional versus hypofractionated high-dose intensity-modulated radiotherapy for prostate cancer: 5-year outcomes of the randomised, non-inferiority, phase 3 CHHiP trial. *Lancet Oncol.*, 17(8), 1047–1060. (Cited on page 7.)
- [Debois *et al.* 1999] Debois, M., Oyen, R., Maes, F., Verswijvel, G., Gatti, G., Bosmans, H., Feron, M., Bellon, E., Kutcher, G., Van Poppel, H., & Vanuytsel, L. (1999). The contribution of magnetic resonance imaging to the three-dimensional treatment planning of localized prostate cancer. *Int. J. Radiat. Oncol. Biol. Phys.*, 45(4), 857–65. (Cited on pages 19, 39, and 81.)
- [Deegan *et al.* 2015] Deegan, T., Owen, R., Holt, T., Fielding, A., Biggs, J., Parfitt, M., Coates, A., & Roberts, L. (2015). Assessment of cone beam CT registration for prostate radiation therapy: Fiducial marker and soft tissue methods. *J. Med. Imag. Radiat. Oncol.*, 59(1), 91–98. (Cited on pages 85, 91, and 106.)
- [Deegan *et al.* 2013] Deegan, T., Owen, R., Holt, T., Roberts, L., Biggs, J., McCarthy, A., Parfitt, M., & Fielding, A. (2013). Interobserver variability of radiation therapists aligning to fiducial markers for prostate radiation therapy. *J. Med. Imaging Radiat. Oncol.*, 57(4), 519–23. (Cited on pages 91 and 106.)

- [Dempsey *et al.* 2005] Dempsey, J., Benoit, D., Fitzsimmons, J., Haghghat, A., Li, J., Low, D., Mutic, S., Palta, J., Romeijn, H., & Sjoden, G. (2005). A device for realtime 3D image-guided IMRT. *Int. J. Radiat. Oncol. Biol. Phys.*, 63, S202. (Cited on pages 9, 19, 39, and 81.)
- [Devic 2012] Devic, S. (2012). MRI simulation for radiotherapy treatment planning. *Med. Phys.*, 39(11), 6701. (Cited on pages 8, 9, 12, and 19.)
- [Dinis Fernandes *et al.* 2017] Dinis Fernandes, C., Dinh, C. V., Steggerda, M. J., ter Beek, L. C., Smolic, M., van Buuren, L. D., Pos, F. J., & van der Heide, U. A. (2017). Prostate fiducial marker detection with the use of multi-parametric magnetic resonance imaging. *Phys. Imag. Radiat. Oncol.*, 1, 14–20. (Cited on pages 60, 73, 74, 75, 82, 84, 92, 106, and 107.)
- [Dirix *et al.* 2014] Dirix, P., Haustermans, K., & Vandecaveye, V. (2014). The Value of Magnetic Resonance Imaging for Radiotherapy Planning. *Semin. Radiat. Oncol.*, 24(3), 151–9. (Cited on pages 7, 12, 19, 39, 81, and 110.)
- [Dixon 1984] Dixon, W. T. (1984). Simple proton spectroscopic imaging. *Radiology*, 153(1), 189–94. (Cited on pages 23 and 41.)
- [Doemer *et al.* 2015] Doemer, A., Chetty, I. J., Glide-Hurst, C., Nurushev, T., Hearshen, D., Pantelic, M., Traughber, M., Kim, J., Levin, K., Elshaikh, M. A., Walker, E., & Movsas, B. (2015). Evaluating organ delineation, dose calculation and daily localization in an open-MRI simulation workflow for prostate cancer patients. *Radiat. Oncol.*, 10(1), 37. (Cited on pages 11 and 103.)
- [Dong *et al.* 2015] Dong, Y., Chang, Z., Xie, G., Whitehead, G., & Ji, J. X. (2015). Susceptibility-based positive contrast MRI of brachytherapy seeds. *Magn. Res. Med.*, 74(3), 716–726. (Cited on page 60.)
- [Dowling *et al.* 2014] Dowling, J. A., Burdett, N., Greer, P. B., Sun, J., Parker, J., Pichler, P., Stanwell, P., Chandra, S., Rivest-Hénault, D., Ghose, S., Salvado, O., & Fripp, J. (2014). Automatic Atlas Based Electron Density and Structure Contouring for MRI-based Prostate Radiation Therapy on the Cloud. *J. Phys.*, 489(1), 012048. (Cited on page 112.)
- [Dowling *et al.* 2012] Dowling, J. A., Lambert, J., Parker, J., Salvado, O., Fripp, J., Capp, A., Wratten, C., Denham, J. W., & Greer, P. B. (2012). An atlas-based electron density mapping method for magnetic resonance imaging (MRI)-alone treatment planning and adaptive MRI-based prostate radiation therapy. *Int. J. Radiat. Oncol. Biol. Phys.*, 83(1), e5–11. (Cited on pages 11, 13, 19, 20, 31, 40, 59, and 103.)
- [Dowling *et al.* 2015] Dowling, J. A., Sun, J., Pichler, P., Rivest-Hénault, D., Ghose, S., Richardson, H., Wratten, C., Martin, J., Arm, J., Best, L., Chandra, S. S., Fripp, J., Menk, F. W., & Greer, P. B. (2015). Automatic Substitute Computed Tomography Generation and Contouring for Magnetic Resonance Imaging (MRI)-Alone External Beam Radiation Therapy From Standard MRI Sequences. *Int. J. Radiat. Oncol. Biol. Phys.*, 93(5), 1144–1153. (Cited on pages 11 and 103.)
- [Durante & Loeffler 2010] Durante, M. & Loeffler, J. S. (2010). Charged particles in radiation oncology. *Nat. Rev. Clin. Oncol.*, 7(1), 37–43. (Cited on pages 2 and 39.)
- [Durante *et al.* 2017] Durante, M., Orecchia, R., & Loeffler, J. S. (2017). Charged-particle therapy in cancer: clinical uses and future perspectives. *Nat. Rev. Clin. Oncol.*, 14, 483–495. (Cited on page 39.)
- [Edmund *et al.* 2014] Edmund, J. M., Kjer, H. M., Van Leemput, K., Hansen, R. H., Andersen, J. A., & Andreasen, D. (2014). A voxel-based investigation for mri-only radiotherapy of the brain using ultra short echo times. *Phys. Med. Biol.*, 59(23), 7501. (Cited on pages 40 and 52.)

- [Edmund & Nyholm 2017] Edmund, J. M. & Nyholm, T. (2017). A review of substitute CT generation for MRI-only radiation therapy. *Radiat. Oncol.*, 12(1), 28. (Cited on pages 10, 11, 39, 40, 59, 81, 101, and 111.)
- [Eggers *et al.* 2011] Eggers, H., Brendel, B., Duijndam, A., & Herigault, G. (2011). Dual-echo Dixon imaging with flexible choice of echo times. *Magn. Reson. Med.*, 65(1), 96–107. (Cited on pages 23, 41, and 110.)
- [Eilertsen *et al.* 2008] Eilertsen, K., Nilsen Tor Arne Vestad, L., Geier, O., & Skretting, A. (2008). A simulation of MRI based dose calculations on the basis of radiotherapy planning CT images. *Acta Oncol.*, 47(7), 1294–1302. (Cited on pages 11 and 103.)
- [Faddegon *et al.* 2015] Faddegon, B. A., Shin, J., Castenada, C. M., Ramos-Méndez, J., & Daftari, I. K. (2015). Experimental depth dose curves of a 67.5 MeV proton beam for benchmarking and validation of Monte Carlo simulation. *Med. Phys.*, 42(7), 4199–4210. (Cited on page 3.)
- [Fallone *et al.* 2009] Fallone, B. G., Murray, B., Rathee, S., Stanescu, T., Steciw, S., Vidakovic, S., Blosser, E., & Tymofichuk, D. (2009). First MR images obtained during megavoltage photon irradiation from a prototype integrated linac-MR system. *Med. Phys.*, 36(6), 2084–8. (Cited on pages 9, 19, 39, and 81.)
- [Fraass *et al.* 1987] Fraass, B. A., McShan, D. L., Diaz, R. F., Ten Haken, R. K., Aisen, A., Gebarski, S., Glazer, G., & Lichter, A. S. (1987). Integration of magnetic resonance imaging into radiation therapy treatment planning: i. technical considerations. *Int. J. Radiat. Oncol. Biol. Phys.*, 13(12), 1897–908. (Cited on pages 19, 39, 59, and 81.)
- [Fransson *et al.* 2001] Fransson, A., Andreo, P., & Pötter, R. (2001). Aspects of MR Image Distortions in Radiotherapy Treatment Planning. *Strahlenther. Onkol.*, 177(2), 59–73. (Cited on pages 12, 20, and 73.)
- [Frantzen-Stenecker 2015] Frantzen-Stenecker, M. (2015). SP-0022: Routine QA of an MR-only workflow. *Radiother. Oncol.*, 115, S12. (Cited on page 108.)
- [Fuller & Scarbrough 2006] Fuller, C. D. & Scarbrough, T. J. (2006). Fiducial Markers in Image-guided Radiotherapy of the Prostate. *Oncol. Hematol. Rev.*, 00(02), 75. (Cited on pages 59 and 72.)
- [Gall *et al.* 1993] Gall, K. P., Verhey, L. J., & Wagner, M. (1993). Computer-assisted positioning of radiotherapy patients using implanted radiopaque fiducials. *Med. Phys.*, 20(4), 1153–1159. (Cited on page 81.)
- [Ghose *et al.* 2017] Ghose, S., Greer, P. B., Sun, J., Pichler, P., Rivest-Henault, D., Mitra, J., Richardson, H., Wratten, C., Martin, J., Arm, J., Best, L., & Dowling, J. A. (2017). Regression and statistical shape model based substitute CT generation for MRI alone external beam radiation therapy from standard clinical MRI sequences. *Phys. Med. Biol.*, 62(22), 8566–8580. (Cited on pages 11 and 103.)
- [Ghose *et al.* 2016] Ghose, S., Mitra, J., Rivest-Hénault, D., Fazlollahi, A., Stanwell, P., Pichler, P., Sun, J., Fripp, J., Greer, P. B., & Dowling, J. A. (2016). MRI-alone radiation therapy planning for prostate cancer: Automatic fiducial marker detection. *Med. Phys.*, 43(5), 2218–28. (Cited on pages 60, 73, 82, 92, 105, 106, and 107.)
- [Goldin *et al.* 2012] Goldin, G. H., Goldin, G. H., Meyer, A.-M., Wu, Y., Chang, Y., Stürmer, T., Holmes, J. A., Reeve, B. B., Godley, P. A., Carpenter, W. R., & Chen, R. C. (2012). Intensity-Modulated Radiation Therapy, Proton Therapy, or Conformal Radiation Therapy and Morbidity and Disease Control in Localized Prostate Cancer. *JAMA*, 307(15), 1611. (Cited on page 7.)

- [Greer *et al.* 2008] Greer, P., Dahl, K., Ebert, M., Wratten, C., White, M., & Denham, J. (2008). Comparison of prostate set-up accuracy and margins with off-line bony anatomy corrections and online implanted fiducial-based corrections. *J. Med. Imaging Radiat. Oncol.*, 52(5), 511–516. (Cited on pages 13, 59, and 81.)
- [Grimm *et al.* 2012] Grimm, P., Billiet, I., Bostwick, D., Dicker, A. P., Frank, S., Immerzeel, J., Keyes, M., Kupelian, ., Vera, R., & Langley, S. (2012). Comparative analysis of prostate-specific antigen free survival outcomes for patients with low, intermediate and high risk prostate cancer treatment by radical therapy. results from the prostate cancer results study group. *BJU Int*, 109, 22–29. (Cited on page 6.)
- [Guerreiro *et al.* 2017] Guerreiro, F., Burgos, N., Dunlop, A., Wong, K., Petkar, I., Nutting, C., Harrington, K., Bhide, S., Newbold, K., Dearnaley, D., DeSouza, N., Morgan, V., McClelland, J., Nill, S., Cardoso, M., Ourselin, S., Oelfke, U., & Knopf, A. (2017). Evaluation of a multi-atlas CT synthesis approach for MRI-only radiotherapy treatment planning. *Phys. Med.*, 35, 7–17. (Cited on pages 11 and 103.)
- [Gundersen & Tepper 2016] Gundersen, L. L. & Tepper, J. E. (2016). *Clinical Radiation Oncology* (4 ed.). Elsevier. (Cited on page 1.)
- [Gupta & Narayan 2012] Gupta, T. & Narayan, C. (2012). Image-guided radiation therapy: Physicians perspectives. *J. Med. Phys.*, 37(4), 174. (Cited on page 3.)
- [Gustafsson *et al.* 2017] Gustafsson, C., Korhonen, J., Persson, E., Gunnlaugsson, A., Nyholm, T., & Olsson, L. E. (2017). Registration free automatic identification of gold fiducial markers in MRI target delineation images for prostate radiotherapy. *Med. Phys.*, (in press). (Cited on pages 82, 86, 91, 92, 93, 105, 106, and 107.)
- [Gwynne *et al.* 2012] Gwynne, S., Webster, R., Adams, R., Mukherjee, S., Coles, B., & Staffurth, J. (2012). Image-guided Radiotherapy for Rectal Cancer - A Systematic Review. *Clin. Oncol.*, 24(4), 250–260. (Cited on page 111.)
- [Habermehl *et al.* 2013] Habermehl, D., Henkner, K., Ecker, S., Jäkel, O., Debus, J., & Combs, S. E. (2013). Evaluation of different fiducial markers for image-guided radiotherapy and particle therapy. *J. Radiat. Res.*, 54(Suppl 1), i61–8. (Cited on pages 60 and 81.)
- [Han 2017] Han, X. (2017). MR-based synthetic CT generation using a deep convolutional neural network method. *Med. Phys.*, 44(4), 1408–1419. (Cited on page 112.)
- [Hargreaves *et al.* 2011] Hargreaves, B. A., Worters, P. W., Pauly, K. B., Pauly, J. M., Koch, K. M., & Gold, G. E. (2011). Metal-Induced Artifacts in MRI. *Am. J. Roentgenol.*, 197(3), 547–55. (Cited on page 74.)
- [Hartman *et al.* 2015] Hartman, J., Kontaxis, C., Bol, G. H., Frank, S. J., Legendijk, J. J. W., van Vulpen, M., & Raaymakers, B. W. (2015). Dosimetric feasibility of intensity modulated proton therapy in a transverse magnetic field of 1.5 T. *Phys. Med. Biol.*, 60(15), 5955–5969. (Cited on page 39.)
- [Hazrati Marangalou *et al.* 2014] Hazrati Marangalou, J., Ito, K., Taddei, F., & van Rietbergen, B. (2014). Inter-individual variability of bone density and morphology distribution in the proximal femur and T12 vertebra. *Bone*, 60, 213–220. (Cited on page 52.)
- [Hegde *et al.* 2013] Hegde, J. V., Mulkern, R. V., Panych, L. P., Fennessy, F. M., Fedorov, A., Maier, S. E., & Tempany, C. M. C. (2013). Multiparametric MRI of prostate cancer: an update on state-of-the-art techniques and their performance in detecting and localizing prostate cancer. *J. Magn. Res. Imaging*, 37(5), 1035–54. (Cited on pages 8 and 109.)
- [Helle *et al.* 2014] Helle, M., Schadewaldt, N., Frantzen-Stenekker, M., Schulz, H., Stehning, C., van der Heide, U., & Renisch, S. (2014). Evaluation of Dixon based Soft Tissue and Bone Classification in the Pelvis for MR-only-based Radiation Therapy Planning. *Proc. Intl. Soc. Mag. Reson. Med.*, 22(4238). (Cited on page 24.)

- [Hong *et al.* 2012] Hong, C. G., Yoon, B. I., Choe, H.-S., Ha, U.-S., Sohn, D. W., & Cho, Y.-H. (2012). The Prevalence and Characteristic Differences in Prostatic Calcification between Health Promotion Center and Urology Department Outpatients. *Kor. J. Urol.*, 53(5), 330. (Cited on pages 60, 73, 82, and 92.)
- [Huisman *et al.* 2005] Huisman, H. J., Fütterer, J. J., van Lin, E. N. J. T., Welmers, A., Scheenen, T. W. J., van Dalen, J. a., Visser, A. G., Witjes, J. a., & Barentsz, J. O. (2005). Prostate cancer: precision of integrating functional MR imaging with radiation therapy treatment by using fiducial gold markers. *Radiology*, 236(1), 311–17. (Cited on pages 74, 81, 91, and 106.)
- [IAEA 2008] IAEA (2008). *The Role of PET/CT in Radiation Treatment Planning for Cancer Patient Treatment*, volume 1063. International Atomic Energy Agency (IAEA). (Cited on page 20.)
- [IAEA & Izewska 2008] IAEA & Izewska, J. (2008). *Setting up a radiotherapy programme : clinical, medical physics, radiation protection, and safety aspects*. International Atomic Energy Agency (IAEA). (Cited on page 1.)
- [IAEA & Podgorsak 2005] IAEA & Podgorsak, E. D. (2005). *Radiation oncology physics : a handbook for teachers and students*. International Atomic Energy Agency (IAEA). (Cited on page 3.)
- [IAEA *et al.* 2017] IAEA, Rosenblatt, E., & Zubizarreta, E. (2017). *Radiotherapy in Cancer Care*. International Atomic Energy Agency (IAEA). (Cited on pages 1, 2, 4, and 5.)
- [ICRP 2000] ICRP (2000). *International Commission on Radiation Protection: Prevention of Accidents to Patients Undergoing Radiation Therapy*, volume 86. Elsevier Health Sciences. (Cited on page 102.)
- [ICRU 1989] ICRU (1989). *Report 44. Tissue Substitutes in Radiation Dosimetry and Measurement*. International Commission on Radiation Units and Measurements (ICRU). (Cited on page 25.)
- [ICRU 1992] ICRU (1992). *Report 46. Photon, electron, proton, and neutron interaction data for body tissues*. International Commission on Radiation Units and Measurements (ICRU). (Cited on page 25.)
- [ICRU 2010] ICRU (2010). Prescribing, Recording, and Reporting Photon-Beam Intensity-Modulated Radiation Therapy (IMRT). *J. ICRU*, 10(1), NP. (Cited on page 5.)
- [Inness *et al.* 2014] Inness, E. K., Moutrie, V., & Charles, P. H. (2014). The dependence of computed tomography number to relative electron density conversion on phantom geometry and its impact on planned dose. *Australas. Phys. Eng. Sci. Med.*, 37(2), 385–91. (Cited on page 30.)
- [Jaffray 2012] Jaffray, D. A. (2012). Image-guided radiotherapy: from current concept to future perspectives. *Nat. Rev. Clin. Oncol.*, 9(12), 688–699. (Cited on page 1.)
- [Jermann 2015] Jermann, M. (2015). Particle Therapy Statistics in 2014. *Int. J. Part. Ther.*, 2(1), 50–54. (Cited on pages 2 and 39.)
- [Jezzard 2000] Jezzard, P. (2000). Physical basis of spatial distortions in magnetic resonance images. In Bankman, I. N. (Ed.), *Handbook of Medical Imaging*, (pp. 425–438)., Orlando, FL, USA. Academic Press, Inc. (Cited on page 12.)
- [Johansson *et al.* 2012] Johansson, A., Karlsson, M., Yu, J., Asklund, T., & Nyholm, T. (2012). Voxel-wise uncertainty in CT substitute derived from MRI. *Med. Phys.*, 39(6), 3283–90. (Cited on pages 19, 20, 32, 40, and 59.)

- [Johnstone *et al.* 2017] Johnstone, E., Wyatt, J. J., Henry, A. M., Short, S. C., Sebag-Montefiore, D., Murray, L., Kelly, C. G., McCallum, H. M., & Speight, R. (2017). A systematic review of synthetic CT generation methodologies for use in MRI-only radiotherapy. *Int. J. Radiat. Oncol. Biol. Phys.* (Cited on page 111.)
- [Joiner & van der. Kogel 2009] Joiner, M. & van der. Kogel, A. (2009). *Basic Clinical Radiobiology*. CRC Press. (Cited on pages 1 and 2.)
- [Jolliffe 2002] Jolliffe, I. (2002). *Principal component analysis*. Wiley Online Library. (Cited on page 62.)
- [Jones *et al.* 2011] Jones, M., Dobson, A., & O'Brien, S. (2011). A graphical method for assessing agreement with the mean between multiple observers using continuous measures. *Int. J. Epidemiol.*, 40(5), 1308–1313. (Cited on page 85.)
- [Jonsson *et al.* 2011] Jonsson, J. H., Brynolfsson, P., Garpebring, A., Karlsson, M., Söderström, K., & Nyholm, T. (2011). Registration accuracy for MR images of the prostate using a subvolume based registration protocol. *Radiat. Oncol.*, 6(1), 73. (Cited on page 81.)
- [Jonsson *et al.* 2012] Jonsson, J. H., Garpebring, A., Karlsson, M. G., & Nyholm, T. (2012). Internal Fiducial Markers and Susceptibility Effects in MRI-Simulation and Measurement of Spatial Accuracy. *Int. J. radiat. Oncol. Biol. Phys.*, 82(5), 1612–1618. (Cited on pages 60, 74, 77, and 82.)
- [Jonsson *et al.* 2010] Jonsson, J. H., Karlsson, M. G., Karlsson, M., & Nyholm, T. (2010). Treatment planning using MRI data: an analysis of the dose calculation accuracy for different treatment regions. *Radiat. Oncol.*, 5(1), 62. (Cited on pages 11, 19, 21, 39, and 103.)
- [Kagawa *et al.* 1997] Kagawa, K., Lee, W., Schultheiss, T. E., Hunt, M. A., Shaer, A. H., & Hanks, G. E. (1997). Initial clinical assessment of CT-MRI image fusion software in localization of the prostate for 3D conformal radiation therapy. *Int. J. Radiat. Oncol. Biol. Phys.*, 38(2), 319–325. (Cited on page 39.)
- [Kalbasi *et al.* 2015] Kalbasi, A., Li, J., Berman, A. T., Swisher-McClure, S., Smaldone, M., Uzzo, R. G., Small, D. S., Mitra, N., & Bekelman, J. E. (2015). Dose-Escalated Irradiation and Overall Survival in Men With Nonmetastatic Prostate Cancer. *JAMA Oncol.*, 1(7), 897. (Cited on page 6.)
- [Kapanen *et al.* 2013] Kapanen, M., Collan, J., Beule, A., Seppl, T., Saarilahti, K., & Tenhunen, M. (2013). Commissioning of MRI-only based treatment planning procedure for external beam radiotherapy of prostate. *Magn. Reson. Med.*, 70(1), 127–35. (Cited on pages 19, 20, 39, 59, 60, and 73.)
- [Karlsson *et al.* 2009] Karlsson, M., Karlsson, M. G., Nyholm, T., Amies, C., & Zackrisson, B. (2009). Dedicated Magnetic Resonance Imaging in the Radiotherapy Clinic. *Int. J. Radiat. Oncol. Biol. Phys.*, 74(2), 644–51. (Cited on pages 9, 19, 39, 59, and 81.)
- [Kemppainen *et al.* 2017] Kemppainen, R., Suilamo, S., Tuokkola, T., Lindholm, P., Deppe, M. H., & Keyriläinen, J. (2017). Magnetic resonance-only simulation and dose calculation in external beam radiation therapy: a feasibility study for pelvic cancers. *Acta Oncol.*, 56(6), 792–798. (Cited on pages 11, 103, and 111.)
- [Khoo *et al.* 1997] Khoo, V. S., Dearnaley, D. P., Finnigan, D. J., Padhani, A., Tanner, S. F., & Leach, M. O. (1997). Magnetic resonance imaging (MRI): considerations and applications in radiotherapy treatment planning. *Radiother. Oncol.*, 42(1), 1–15. (Cited on pages 9, 10, and 19.)

- [Khoo & Joon 2006] Khoo, V. S. & Joon, D. L. (2006). New developments in MRI for target volume delineation in radiotherapy. *Br. J. Radiol.*, 79(special issue_1), S2–S15. (Cited on pages 8 and 39.)
- [Kim *et al.* 2015] Kim, J., Glide-Hurst, C., Doemer, A., Wen, N., Movsas, B., & Chetty, I. J. (2015). Implementation of a novel algorithm for generating synthetic CT images from magnetic resonance imaging data sets for prostate cancer radiation therapy. *Int. J. Radiat. Oncol. Biol. Phys.*, 91(1), 39–47. (Cited on pages 11, 13, 19, 20, 31, 40, 59, and 103.)
- [Kim & Tannock 2005] Kim, J. J. & Tannock, I. F. (2005). Repopulation of cancer cells during therapy: an important cause of treatment failure. *Nat. Rev. Cancer*, 5(7), 516–525. (Cited on page 4.)
- [Kim *et al.* 2011] Kim, S., Shen, S., Moore, D., Shih, W., Lin, Y., Li, H., Dolan, M., Shao, Y., & Lu-Yao, G. L. (2011). Late Gastrointestinal Toxicities Following Radiation Therapy for Prostate Cancer. *Eur. Urol.*, 60(5), 908–916. (Cited on page 7.)
- [Kleijnen *et al.* 2016] Kleijnen, J.-P. J. E., van Asselen, B., Burbach, J. P. M., Intven, M., Philippens, M. E. P., Reerink, O., Lagendijk, J. J. W., & Raaymakers, B. W. (2016). Evolution of motion uncertainty in rectal cancer: implications for adaptive radiotherapy. *Phys. Med. Biol.*, 61(1), 1–11. (Cited on page 53.)
- [Klein *et al.* 2009] Klein, S., Pluim, J. P. W., Staring, M., & Viergever, M. A. (2009). Adaptive Stochastic Gradient Descent Optimisation for Image Registration. *Int. J. Comput. Vision*, 81(3), 227–39. (Cited on page 23.)
- [Klein *et al.* 2010] Klein, S., Staring, M., Murphy, K., Viergever, M. A., & Pluim, J. P. (2010). Elastix: A Toolbox for Intensity-Based Medical Image Registration. *IEEE Trans. Med. Imaging*, 29(1), 196–205. (Cited on page 23.)
- [Knöös *et al.* 1986] Knöös, T., Nilsson, M., & Ahlgren, L. (1986). A method for conversion of hounsfield number to electron density and prediction of macroscopic pair production cross-sections. *Radiother. Oncol.*, 5(4), 337–45. (Cited on pages 5 and 20.)
- [Koay *et al.* 2017] Koay, E. J., Hall, W., Park, P. C., Erickson, B., & Herman, J. M. (2017). The role of imaging in the clinical practice of radiation oncology for pancreatic cancer. *Abdom. Radiol.*, 1–11. (Cited on page 111.)
- [Kohavi & Provost 1998] Kohavi, R. & Provost, F. (1998). Glossary of terms. *Machine Learning*, 30(2-3), 271–74. (Cited on page 32.)
- [Köhler *et al.* 2015] Köhler, M., Varra, T., Van Grootel, M., Hoogeveen, R., Kempainen, R., & Renisch, S. (2015). Philips MRCAT for prostate dose calculation using only MRI data. *Philips white paper*. (Cited on pages 42 and 44.)
- [Koivula *et al.* 2017] Koivula, L., Kapanen, M., Seppälä, T., Collan, J., Dowling, J. A., Greer, P. B., Gustafsson, C., Gunnlaugsson, A., Olsson, L. E., Wee, L., *et al.* (2017). Intensity-based dual model method for generation of synthetic CT images from standard T2-weighted MR images—Generalized technique for four different MR scanners. *Radiother. Oncol.*, 125(3), 411–419. (Cited on pages 11 and 103.)
- [Koivula *et al.* 2016] Koivula, L., Wee, L., & Korhonen, J. (2016). Feasibility of MRI-only treatment planning for proton therapy in brain and prostate cancers: Dose calculation accuracy in substitute CT images. *Med. Phys.*, 43(8Part1), 4634–4642. (Cited on pages 11, 40, 43, 46, 51, 52, 103, and 104.)
- [Korhonen *et al.* 2014] Korhonen, J., Kapanen, M., Keyriläinen, J., Seppälä, T., & Tenhunen, M. (2014). A dual model HU conversion from MRI intensity values within and outside of bone segment for MRI-based radiotherapy treatment planning of prostate cancer. *Med. Phys.*, 41(1), 011704. (Cited on pages 11, 13, 19, 20, 31, 40, 59, and 103.)

- [Korhonen *et al.* 014b] Korhonen, J., Kapanen, M., Keyriläinen, J., Seppälä, T., Tuomikoski, L., & Tenhunen, M. (2014b). Influence of MRI-based bone outline definition errors on external radiotherapy dose calculation accuracy in heterogeneous pseudo-CT images of prostate cancer patients. *Acta Oncol.*, 53(8), 1100–1106. (Cited on pages 11 and 103.)
- [Korhonen *et al.* 2016] Korhonen, J., Visapää, H., Seppälä, T., Kapanen, M., Saarilahti, K., & Tenhunen, M. (2016). Clinical experiences of treating prostate cancer patients with magnetic resonance imaging–only based radiation therapy treatment planning workflow. *Int. J. Radiat. Oncol. Biol. Phys.*, 96(2), S225. (Cited on page 12.)
- [Korsholm *et al.* 2014] Korsholm, M. E., Waring, L. W., & Edmund, J. M. (2014). A criterion for the reliable use of MRI-only radiotherapy. *Radiat. Oncol.*, 9(16). (Cited on pages 11, 12, 20, and 103.)
- [Kuglin & Hines 1975] Kuglin, C. D. & Hines, D. C. (1975). The phase correlation image alignment method. *Proceed. Int. Conf. Cybernetics and Society*, 163–165. (Cited on pages 60, 64, and 76.)
- [Kupelian & Meyer 2011] Kupelian, P. & Meyer, J. L. (2011). Image-Guided, Adaptive Radiotherapy of Prostate Cancer: Toward New Standards of Radiotherapy Practice. volume 43 (pp. 344–368). KARGER. (Cited on page 7.)
- [Kupelian *et al.* 2008] Kupelian, P. A., Langen, K. M., Willoughby, T. R., Zeidan, O. A., & Meeks, S. L. (2008). Image-Guided Radiotherapy for Localized Prostate Cancer: Treating a Moving Target. *Semin. Radiat. Oncol.*, 18(1), 58–66. (Cited on pages 59, 72, and 73.)
- [Kupelian *et al.* 2005] Kupelian, P. A., Willoughby, T. R., Meeks, S. L., Forbes, A., Wagner, T., Maach, M., & Langen, K. M. (2005). Intraprostatic fiducials for localization of the prostate gland: Monitoring intermarker distances during radiation therapy to test for marker stability. *Int. J. Radiat. Oncol. Biol. Phys.*, 62(5), 1291–96. (Cited on page 73.)
- [Legendijk *et al.* 2014] Legendijk, J. J. W., Raaymakers, B. W., Van den Berg, C. A. T., Moerland, M. A., Philippens, M. E., & van Vulpen, M. (2014). MR guidance in radiotherapy. *Phys. Med. Biol.*, 59(21), R349–R369. (Cited on page 9.)
- [Lambert *et al.* 2011] Lambert, J., Greer, P. B., Menk, F., Patterson, J., Parker, J., Dahl, K., Gupta, S., Capp, A., Wratten, C., Tang, C., Kumar, M., Dowling, J., Hauville, S., Hughes, C., Fisher, K., Lau, P., Denham, J. W., & Salvado, O. (2011). MRI-guided prostate radiation therapy planning: Investigation of dosimetric accuracy of MRI-based dose planning. *Radiother. Oncol.*, 98(3), 330–34. (Cited on pages 11, 21, 30, 31, and 103.)
- [Lee *et al.* 2003] Lee, Y. K., Bollet, M., Charles-Edwards, G., Flower, M. A., Leach, M. O., McNair, H., Moore, E., Rowbottom, C., & Webb, S. (2003). Radiotherapy treatment planning of prostate cancer using magnetic resonance imaging alone. *Radiother. Oncol.*, 66(2), 203–216. (Cited on pages 9, 11, 19, 20, 21, 39, 40, 59, 81, and 103.)
- [Lim *et al.* 2016] Lim, T. Y., Kudchadker, R. J., Wang, J., Stafford, R. J., MacLellan, C., Rao, A., Ibbott, G. S., & Frank, S. J. (2016). Effect of pulse sequence parameter selection on signal strength in positive-contrast MRI markers for MRI-based prostate postimplant assessment. *Med. Phys.*, 43(7), 4312–4322. (Cited on pages 60 and 82.)
- [Lips *et al.* 2008] Lips, I. M., Dehnad, H., van Gils, C. H., Boeken Kruger, A. E., van der Heide, U. A., & van Vulpen, M. (2008). High-dose intensity-modulated radiotherapy for prostate cancer using daily fiducial marker-based position verification: acute and late toxicity in 331 patients. *Radiat. Oncol.*, 3, 15. (Cited on pages 62 and 86.)
- [Lomax 2008] Lomax, A. J. (2008). Intensity modulated proton therapy and its sensitivity to treatment uncertainties 2: the potential effects of inter-fraction and inter-field motions. *Phys. Med. Biol.*, 53(4), 1043–1056. (Cited on page 39.)

- [Low 2017 (Chapter MRI Guided Radiotherapy)] Low, D. A. (2017). *Advances in Radiation Oncology*, chapter MRI Guided Radiotherapy, (pp. 41–67). Cancer Treatment and Research,. Springer. (Cited on page 9.)
- [Low *et al.* 1998] Low, D. A., Harms, W. B., Mutic, S., & Purdy, J. A. (1998). A technique for the quantitative evaluation of dose distributions. *Med. Phys.*, 25(5), 656–61. (Cited on page 35.)
- [Majithia *et al.* 2016] Majithia, L., Walston, S., Guiou, M., Gupta, N., & Chakravarti, A. (2016). Use of Neuroimaging for Radiation Therapy Planning. In *Handbook of Neuro-Oncology Neuroimaging* (pp. 231–241). Elsevier. (Cited on page 111.)
- [Marks *et al.* 2010] Marks, L. B., Yorke, E. D., Jackson, A., Haken, R. K. T., Constine, L. S., Eisbruch, A., Bentzen, S. M., Nam, J., & Deasy, J. O. (2010). Use of normal tissue complication probability models in the clinic. *Int. J. Radiat. Oncol. Biol. Phys.*, 76(3), S10 – S19. Quantitative Analyses of Normal Tissue Effects in the Clinic. (Cited on page 45.)
- [Maspero *et al.* 2015] Maspero, M., Berra, A., Conti, V., Giannini, G., Ostinelli, A., Prest, M., & Vallazza, E. (2015). A real time scintillating fiber Time of Flight spectrometer for LINAC photoproduced neutrons. *Nucl. Instr. Meth. Phys. Res. A*, 777, 154–160. (Cited on page 153.)
- [Maspero *et al.* 2018] Maspero, M., Savenije, M. H. F., Dinkla, M. A., Seevinck, P. R., W., I. M. P., Jurgenliemk-Schulz, I. M., Kerkmeijer, L. G. W., & van den Berg, C. A. T. (2018). Fast synthetic CT generation with deep learning for general pelvis MR-only Radiotherapy. *Phys. Med. Biol.* Submitted and available on airXiv. (Cited on page 112.)
- [Maspero *et al.* 2015] Maspero, M., Seevinck, P., Meijer, G., Lagendijk, J., Viergever, M., & van den Berg, C. (2015). SU-E-J-219: A Dixon Based Pseudo-CT Generation Method for MR-Only Radiotherapy Treatment Planning of the Pelvis and Head and Neck. *Med. Phys.*, 42(6Part10), 3316–3316. (Cited on page 111.)
- [Maspero *et al.* 2017] Maspero, M., Seevinck, P. R., Schubert, G., Hoesl, M. A. U., van Asselen, B., Viergever, M. A., Lagendijk, J. J. W., Meijer, G. J., & van den Berg, C. A. T. (2017). Quantification of confounding factors in MRI-based dose calculations as applied to prostate IMRT. *Phys. Med. Biol.*, 62(3), 948–965. (Cited on pages 17, 40, 42, 75, 102, 103, and 153.)
- [Maspero *et al.* 2018] Maspero, M., Seevinck, P. R., Willems, N. J., Sikkes, G. G., de Kogel, G. J., de Boer, H. C. J., van der Voort van Zyp, J. R. N., & van den Berg, C. A. T. (2018). Evaluation of manual gold Fiducial Marker localisation for Magnetic Resonance-only prostate Radiotherapy. *Radiat. Oncol*, 0(0), -. Submitted. (Cited on pages 79 and 154.)
- [Maspero *et al.* 2018] Maspero, M., Tyyger, M. D., Seevinck, P. R., Tijssen, R. H. N., Intven, M. P. W., & van den Berg, C. A. T. (2018). E37-0820: Feasibility of MR-only rectum radiotherapy using a commercial prostate sCT generation solution. In *ESTRO 37*. In press. (Cited on page 111.)
- [Maspero *et al.* 2017] Maspero, M., van den Berg, C. A. T., Landry, G., Belka, C., Parodi, K., Seevinck, P. R., Raaymakers, B. W., & Kurz, C. (2017). Feasibility of MR-only proton dose calculations for prostate cancer radiotherapy using a commercial pseudo-CT generation method. *Phys. Med. Biol.*, 62(24), 9159–9176. (Cited on pages 37, 103, 104, and 153.)
- [Maspero *et al.* 2017] Maspero, M., van den Berg, C. A. T., Zijlstra, F., Sikkes, G. G., de Boer, H. C. J., Meijer, G. J., Kerkmeijer, L. G. W., Viergever, M. A., Lagendijk, J. J. W., Meijer, G. J., & Seevinck, P. R. (2017). Evaluation of an automatic MR-based gold fiducial marker localisation method for MR-only prostate radiotherapy. *Phys. Med. Biol.*, 62(20), 7981–8002. (Cited on pages 57, 82, 83, 92, 106, 107, and 153.)

- [Mcjury *et al.* 2011] Mcjury, M., O'Neill, A., Lawson, M., Mcgrath, C., Grey, A., Page, W., & O'Sullivan, J. M. (2011). Assessing the image quality of pelvic MR images acquired with a flat couch for radiotherapy treatment planning. *Brit. J. Radiol.*, 84(1004), 750–755. (Cited on pages 8, 20, and 59.)
- [McLaughlin *et al.* 2005] McLaughlin, P. W., Troyer, S., Berri, S., Narayana, V., Meirowitz, A., Roberson, P. L., & Montie, J. (2005). Functional anatomy of the prostate: Implications for treatment planning. *Int. J. Radiat. Oncol. Biol. Phys.*, 63(2), 479–491. (Cited on page 8.)
- [McPartlin *et al.* 2016] McPartlin, A. J., Li, X., Kershaw, L. E., Heide, U., Kerkmeijer, L., Lawton, C., Mahmood, U., Pos, F., van As, N., van Herk, M., *et al.* (2016). MRI-guided prostate adaptive radiotherapy - A systematic review. *Radiother. Oncol.*, 119(3), 371–80. (Cited on pages 7, 73, 75, 109, and 111.)
- [McRobbie *et al.* 2006] McRobbie, D. W., Moore, E. A., Graves, M. J., & Prince, M. R. (2006). *MRI from Picture to Proton*. Cambridge: Cambridge University Press. (Cited on page 10.)
- [Ménard & van der Heide 2014] Ménard, C. & van der Heide, U. A. (2014). Introduction: Magnetic resonance imaging comes of age in radiation oncology. *Semin. Radiat. Oncol.*, 24(3), 149–50. (Cited on page 7.)
- [Metcalf *et al.* 2013] Metcalf, P., Liney, G. P., Holloway, L., Walker, A., Barton, M., Delaney, G. P., Vinod, S., & Tome, W. (2013). The potential for an enhanced role for MRI in radiation-therapy treatment planning. *Technol. Cancer Res. Treat.*, 12(5), 429–46. (Cited on pages 7 and 8.)
- [Mijnheer *et al.* 1987] Mijnheer, B. J., Battermann, J. J., & Wambersie, A. (1987). What degree of accuracy is required and can be achieved in photon and neutron therapy? *Radiat. Oncol.*, 8(3), 237–52. (Cited on pages 30 and 101.)
- [Mitchell 2013] Mitchell, G. (2013). The Rationale for Fractionation in Radiotherapy. *Clin. J. Oncol. Nurs.*, 17(4), 412–417. (Cited on page 4.)
- [Mizowaki *et al.* 1996] Mizowaki, T., Nagata, Y., Okajima, K., Murata, R., Yamamoto, M., Kokubo, M., Hiraoka, M., & Abe, M. (1996). Development of an MR simulator: experimental verification of geometric distortion and clinical application. *Radiol.*, 199(3), 855–860. (Cited on page 8.)
- [Moteabbed *et al.* 2014] Moteabbed, M., Schuemann, J., & Paganetti, H. (2014). Dosimetric feasibility of real-time MRI-guided proton therapy. *Med. Phys.*, 41(11), 111713. (Cited on pages 39 and 81.)
- [Moteabbed *et al.* 2017] Moteabbed, M., Trofimov, A., Sharp, G. C., Wang, Y., Zietman, A. L., Efstathiou, J. A., & Lu, H.-M. (2017). Proton therapy of prostate cancer by anterior-oblique beams: implications of setup and anatomy variations. *Phys. Med. Biol.*, 62(5), 1644–1660. (Cited on page 52.)
- [Mottet *et al.* 2017] Mottet, N., Bellmunt, J., Bolla, M., Briers, E., Cumberbatch, M. G., De Santis, M., Fossati, N., Gross, T., ..., & Cornford, P. (2017). EAU-ESTRO-SIOG Guidelines on Prostate Cancer. Part 1: Screening, Diagnosis, and Local Treatment with Curative Intent. *Eur. Urol.*, 71(4), 618–629. (Cited on page 6.)
- [Nabavizadeh *et al.* 2016] Nabavizadeh, N., Elliott, D. A., Chen, Y., Kusano, A. S., Mitin, T., Thomas, C. R., & Holland, J. M. (2016). Image Guided Radiation Therapy (IGRT) Practice Patterns and IGRT's Impact on Workflow and Treatment Planning: Results From a National Survey of American Society for Radiation Oncology Members. *Int. J. radiat. Oncol. Biol. Phys.*, 94(4), 850–57. (Cited on pages 13, 59, and 105.)
- [Nederveen *et al.* 2000] Nederveen, A., Lagendijk, J., & Hofman, P. (2000). Detection of fiducial gold markers for automatic on-line megavoltage position verification using a

- marker extraction kernel (MEK). *Int. J. Radiat. Oncol. Biol. Phys.*, 47(5), 1435–1442. (Cited on pages 60 and 106.)
- [Newhauser & Zhang 2015] Newhauser, W. D. & Zhang, R. (2015). The physics of proton therapy. *Phys. Med. Biol.*, 60(8), R155–R209. (Cited on page 3.)
- [Ng *et al.* 2014] Ng, M., Brown, E., Williams, A., Chao, M., Lawrentschuk, N., & Chee, R. (2014). Fiducial markers and spacers in prostate radiotherapy: current applications. *BJU Int.*, 113(S2), 13–20. (Cited on pages 13, 53, 59, 60, 73, 81, 82, and 92.)
- [Nijkamp *et al.* 2012] Nijkamp, J., Haustermans, K., & Marijnen, C. A. M. (2012). What Is the Role of IMRT and IGRT in Rectal Cancer? In *Multidisciplinary Management of Rectal Cancer* (pp. 129–148). Berlin, Heidelberg: Springer Berlin Heidelberg. (Cited on page 111.)
- [Njeh 2008] Njeh, C. F. (2008). Tumor delineation: The weakest link in the search for accuracy in radiotherapy. *J. Med. Phys.*, 33(4), 136–40. (Cited on page 8.)
- [Nyholm & Jonsson 2014] Nyholm, T. & Jonsson, J. (2014). Counterpoint: Opportunities and Challenges of a Magnetic Resonance Imaging-Only Radiotherapy Work Flow. *Semin. Radiat. Oncol.*, 24(3), 175–80. (Cited on page 19.)
- [Nyholm *et al.* 2009] Nyholm, T., Nyberg, M., Karlsson, M. G., & Karlsson, M. (2009). Systematisation of spatial uncertainties for comparison between a MR and a CT-based radiotherapy workflow for prostate treatments. *Radiat. Oncol.*, 4(1), 1–9. (Cited on pages 8, 9, 19, 21, 39, and 81.)
- [Oborn *et al.* 2017] Oborn, B. M., Dowdell, S., Metcalfe, P. E., Crozier, S., Mohan, R., & Keall, P. J. (2017). Future of Medical Physics: Real-time MRI guided Proton Therapy. *Med. Phys.*, 44, e77–e90. (Cited on pages 39, 53, 81, and 104.)
- [Okamoto *et al.* 1993] Okamoto, Y., Imanaka, I., Sakaguchi, T., Kushima, T., & Kono, M. (1993). Fundamental Study on development of MRI simulation system for Radiotherapy planning. *Int. J. Radiat. Oncol. Biol. Phys.*, 27(1), 303. (Cited on page 8.)
- [Parker *et al.* 2003] Parker, C., Damyanovich, A., Haycocks, T., Haider, M., Bayley, A., & Catton, C. (2003). Magnetic resonance imaging in the radiation treatment planning of localized prostate cancer using intra-prostatic fiducial markers for computed tomography co-registration. *Radiother. Oncol.*, 66(2), 217–224. (Cited on pages 60, 81, and 82.)
- [Patkar *et al.* 2011] Patkar, V., Acosta, D., Davidson, T., Jones, A., Fox, J., & Keshtgar, M. (2011). Cancer multidisciplinary team meetings: evidence, challenges, and the role of clinical decision support technology. *Int. J. Breast Cancer*, 2011, 831605. (Cited on page 3.)
- [Paulson *et al.* 2016] Paulson, E. S., Crijns, S. P. M., Keller, B. M., Wang, J., Schmidt, M. A., Coutts, G., & van der Heide, U. A. (2016). Consensus opinion on MRI simulation for external beam radiation treatment planning. *Radiother. Oncol.*, 121(2), 187–192. (Cited on page 110.)
- [Paulson *et al.* 2015] Paulson, E. S., Erickson, B., Schultz, C., & Allen Li, X. (2015). Comprehensive MRI simulation methodology using a dedicated MRI scanner in radiation oncology for external beam radiation treatment planning. *Med. Phys.*, 42(1), 28–39. (Cited on pages 19 and 108.)
- [Pereira *et al.* 2014] Pereira, G. C., Traughber, M., & Muzic, R. F. (2014). The role of imaging in radiation therapy planning: past, present, and future. *Biomed. Res. Int.*, 2014(231090). (Cited on pages 19, 39, and 50.)
- [Persson *et al.* 2017] Persson, E., Gustafsson, C., Nordström, F., Sohlén, M., Gunnlaugsson, A., Petruson, K., Rintelä, N., Hed, K., Blomqvist, L., Zackrisson, B., *et al.* (2017). Mr-opera—a multi-center/multi-vendor validation of mri-only prostate treatment planning

- using synthetic ct images. *Int. J. Radiat. Oncol. Biol. Phys.*, 99(3), 692–700. (Cited on pages 11, 12, 40, and 103.)
- [Pouliot *et al.* 2004] Pouliot, J., Kim, Y., Lessard, E., Hsu, I.-C., Vigneron, D. B., & Kurhanewicz, J. (2004). Inverse planning for HDR prostate brachytherapy used to boost dominant intraprostatic lesions defined by magnetic resonance spectroscopy imaging. *Int. J. Radiat. Oncol. Biol. Phys.*, 59(4), 1196–1207. (Cited on page 8.)
- [Prior *et al.* 2016] Prior, P., Chen, X., Botros, M., Paulson, E. S., Lawton, C., Erickson, B., & Li, X. A. (2016). MRI-based IMRT planning for MR-linac: comparison between CT- and MRI-based plans for pancreatic and prostate cancers. *Phys. Med. Biol.*, 61(10), 3819–42. (Cited on pages 19, 20, 40, 59, and 111.)
- [Prior *et al.* 2017] Prior, P., Chen, X., Gore, E., Johnstone, C., & Li, X. A. (2017). Technical Note: Is bulk electron density assignment appropriate for MRI-only based treatment planning for lung cancer? *Med. Phys.*, 44(7), 3437–3443. (Cited on page 111.)
- [Raaijmakers *et al.* 2008] Raaijmakers, A. J. E., Raaymakers, B. W., & Lagendijk, J. J. W. (2008). Magnetic-field-induced dose effects in MR-guided radiotherapy systems: dependence on the magnetic field strength. *Phys. Med. Biol.*, 53(4), 909–923. (Cited on page 112.)
- [Raaymakers *et al.* 2017] Raaymakers, B. W., Jürgenliemk-Schulz, I. M., Bol, G. H., Glitzner, M., Kotte, A. N. T. J., van Asselen, B., de Boer, J. C. J., Bluemink, J. J., Hackett, S. L., Moerland, M. A., ..., & Lagendijk, J. J. W. (2017). First patients treated with a 1.5 T MRI-Linac: clinical proof of concept of a high-precision, high-field MRI guided radiotherapy treatment. *Phys. Med. Biol.*, 62(23), L41–L50. (Cited on page 9.)
- [Raaymakers *et al.* 2004] Raaymakers, B. W., Raaijmakers, A. J. E., Kotte, A. N. T. J., Jette, D., & Lagendijk, J. J. W. (2004). Integrating a MRI scanner with a 6 MV radiotherapy accelerator: dose deposition in a transverse magnetic field. *Phys. Med. Biol.*, 49(17), 4109–18. (Cited on pages 9, 19, 39, and 81.)
- [Raaymakers *et al.* 2008] Raaymakers, B. W., Raaijmakers, A. J. E., & Lagendijk, J. J. W. (2008). Feasibility of MRI guided proton therapy: magnetic field dose effects. *Phys. Med. Biol.*, 53(20), 5615–5622. (Cited on pages 39 and 81.)
- [Rai *et al.* 2017] Rai, R., Kumar, S., Batumalai, V., Elwadia, D., Ohanessian, L., Juresic, E., Cassapi, L., Vinod, S. K., Holloway, L., Keall, P. J., & Liney, G. P. (2017). The integration of MRI in radiation therapy: collaboration of radiographers and radiation therapists. *J. Med. Radiat. Sci.*, 64(1), 61–68. (Cited on page 108.)
- [Ramsey & Oliver 1998] Ramsey, C. R. & Oliver, A. L. (1998). Magnetic resonance imaging based digitally reconstructed radiographs, virtual simulation, and three-dimensional treatment planning for brain neoplasms. *Med. Phys.*, 25(10), 1928–1934. (Cited on pages 9 and 10.)
- [Rank *et al.* 2013] Rank, C. M., Tremmel, C., Hünemohr, N., Nagel, A. M., Jäkel, O., & Greilich, S. (2013). MRI-based treatment plan simulation and adaptation for ion radiotherapy using a classification-based approach. *Radiat. Oncol.*, 8, 51. (Cited on pages 32 and 40.)
- [Rasch *et al.* 1999] Rasch, C., Barillot, I., Remeijer, P., Touw, A., van Herk, M., & Lebesque, J. V. (1999). Definition of the prostate in CT and MRI: a multi-observer study. *Int. J. Radiat. Oncol. Biol. Phys.*, 43(1), 57–66. (Cited on pages 8, 19, and 81.)
- [Riches *et al.* 2014] Riches, S. F., Payne, G. S., Desouza, N. M., Dearnaley, D., Morgan, V. A., Morgan, S. C., & Partridge, M. (2014). Effect on therapeutic ratio of planning a boosted radiotherapy dose to the dominant intraprostatic tumour lesion within the prostate based on multifunctional MR parameters. *Br. J. Radiol.*, 87(1037), 20130813. (Cited on page 8.)

- [Roach *et al.* 1996] Roach, M. I., Faillace-Akazawa, P., Malfatti, C., Holland, J., & Hricak, H. (1996). Prostate volumes defined by magnetic resonance imaging and computerized tomographic scans for three-dimensional conformal radiotherapy. *Int. J. Radiat. Oncol. Biol. Phys.*, 35(5), 1011–18. (Cited on pages 8, 19, and 81.)
- [Roberson *et al.* 2005] Roberson, P. L., McLaughlin, P. W., Narayana, V., Troyer, S., Hixson, G. V., & Kessler, M. L. (2005). Use and uncertainties of mutual information for computed tomography/magnetic resonance (CT/MR) registration post permanent implant of the prostate. *Med. Phys.*, 32(2), 473–82. (Cited on page 21.)
- [Rosenblatt *et al.* 2013] Rosenblatt, E., Izewska, J., Anacak, Y., Pynda, Y., Scalliet, P., Boniol, M., & Autier, P. (2013). Radiotherapy capacity in European countries: an analysis of the Directory of Radiotherapy Centres (DIRAC) database. *Lancet Oncol.*, 14(2), e79–e86. (Cited on page 2.)
- [Sander *et al.* 2014] Sander, L., Langkilde, N. C., Holmberg, M., & Carl, J. (2014). MRI target delineation may reduce long-term toxicity after prostate radiotherapy. *Acta Oncol.*, 53(6), 809–814. (Cited on page 8.)
- [Savenije *et al.* 2018] Savenije, M. H. F., Maspero, M., Dinkla, M. A., Seevinck, P. R., & van den Berg, C. A. T. (2018). Feasibility of MR-only rectum radiotherapy using a commercial prostate sCT generation solution. In *ISMRM-ESMRB 2018*. 548. (Cited on page 112.)
- [Schadewaldt *et al.* 2014] Schadewaldt, N., Schulz, H., Helle, M., Frantzen-Stenekker, M., Heide, U., & Renisch, S. (2014). SU-EJ-141: Comparison of Dose Calculation On Automatically Generated MRBased ED Maps and Corresponding Patient CT for Clinical Prostate EBRT Plans. *Med. Phys.*, 41(6), 188. (Cited on pages 19, 20, 23, and 42.)
- [Schallenkamp *et al.* 2005] Schallenkamp, J. M., Herman, M. G., Kruse, J. J., & Pisansky, T. M. (2005). Prostate position relative to pelvic bony anatomy based on intraprostatic gold markers and electronic portal imaging. *Int. J. radiat. Oncol. Biol. Phys.*, 63(3), 800–11. (Cited on pages 13, 59, and 81.)
- [Schieda *et al.* 2015] Schieda, N., Avruch, L., Shabana, W. M., & Malone, S. C. (2015). Multi-echo gradient recalled echo imaging of the pelvis for improved depiction of brachytherapy seeds and fiducial markers facilitating radiotherapy planning and treatment of prostatic carcinoma. *J. Magn. Res. Imaging*, 41(3), 715–720. (Cited on pages 75 and 105.)
- [Schippers & Lomax 2011] Schippers, J. M. & Lomax, A. J. (2011). Emerging technologies in proton therapy. *Acta Oncol.*, 50(6), 838–850. (Cited on pages 39 and 53.)
- [Schmidt & Payne 2015] Schmidt, M. A. & Payne, G. S. (2015). Radiotherapy planning using MRI. *Phys. Med. Biol.*, 60(22), R323–61. (Cited on pages 7, 8, 9, 12, 19, 20, 59, and 81.)
- [Schulz-Ertner & Tsujii 2007] Schulz-Ertner, D. & Tsujii, H. (2007). Particle radiation therapy using proton and heavier ion beams. *J. Clin. Oncol.*, 25(8), 953–64. (Cited on page 2.)
- [Sciarra *et al.* 2011] Sciarra, A., Barentsz, J., Bjartell, A., Eastham, J., Hricak, H., Panebianco, V., & Witjes, J. A. (2011). Advances in magnetic resonance imaging: How they are changing the management of prostate cancer. *Europ. Urol.*, 59(6), 962–977. (Cited on pages 8 and 39.)
- [Seco & Evans 2006] Seco, J. & Evans, P. M. (2006). Assessing the effect of electron density in photon dose calculations. *Med. Phys.*, 33(2), 540–52. (Cited on page 19.)
- [Seevinck *et al.* 2011] Seevinck, P. R., de Leeuw, H., Bos, C., & Bakker, C. J. G. (2011). Highly localized positive contrast of small paramagnetic objects using 3D center-out radial sampling with off-resonance reception. *Magn. Res. Med.*, 65(1), 146–156. (Cited on page 60.)

- [Sefrova *et al.* 2012] Sefrova, J., Odrazka, K., Paluska, P., Belobradek, Z., Brodak, M., Dolezel, M., Prosvic, P., Macingova, Z., Vosmik, M., Hoffmann, P., Louda, M., & Nejedla, A. (2012). Magnetic Resonance Imaging in Postprostatectomy Radiotherapy Planning. *Int. J. Radiat. Oncol. Biol. Phys.*, 82(2), 911–918. (Cited on page 8.)
- [Siegel *et al.* 2016] Siegel, R. L., Miller, K. D., & Jemal, A. (2016). Cancer statistics, 2016. *CA Cancer. J Clin.*, 66(1), 7–30. (Cited on page 6.)
- [Singh *et al.* 2013] Singh, J., Greer, P. B., White, M. A., Parker, J., Patterson, J., Tang, C. I., Capp, A., Wratten, C., & Denham, J. W. (2013). Treatment-Related Morbidity in Prostate Cancer: A Comparison of 3-Dimensional Conformal Radiation Therapy With and Without Image Guidance Using Implanted Fiducial Markers. *Int. J. Radiat. Oncol. Biol. Phys.*, 85(4), 1018–1023. (Cited on page 7.)
- [Siversson *et al.* 2015] Siversson, C., Nordström, F., Nilsson, T., Nyholm, T., Jonsson, J., Gunnlaugsson, A., & Olsson, L. E. (2015). Technical Note: MRI only prostate radiotherapy planning using the statistical decomposition algorithm. *Med. Phys.*, 42(10), 6090–97. (Cited on pages 11, 19, 20, 30, 31, 32, 33, 40, 59, and 103.)
- [Skrzynski *et al.* 2010] Skrzynski, W., Zieliska-Dabrowska, S., Wachowicz, M., Slusarczyk-Kacprzyk, W., Kukolowicz, P. F., & Bulski, W. (2010). Computed tomography as a source of electron density information for radiation treatment planning. *Strahlenther. Onkol.*, 186(6), 327–33. (Cited on page 19.)
- [Smeenk *et al.* 2010] Smeenk, R. J., Teh, B. S., Butler, E. B., van Lin, E. N., & Kaanders, J. H. (2010). Is there a role for endorectal balloons in prostate radiotherapy? A systematic review. *Radiother. Oncol.*, 95(3), 277–282. (Cited on page 53.)
- [Soukup *et al.* 2009] Soukup, M., Shn, M., Yan, D., Liang, J., & Alber, M. (2009). Study of Robustness of IMPT and IMRT for Prostate Cancer Against Organ Movement. *Int. J. Radiat. Oncol. Biol. Phys.*, 75(3), 941–949. (Cited on pages 39, 43, and 52.)
- [Stanescu *et al.* 2012] Stanescu, T., Wachowicz, K., & Jaffray, D. A. (2012). Characterization of tissue magnetic susceptibility-induced distortions for MRIgRT. *Med. Phys.*, 39(12), 7185–93. (Cited on pages 12 and 20.)
- [Suh *et al.* 2008] Suh, J. H., Gardner, J. M., Kee, K. H., Shen, S., Ayala, A. G., & Ro, J. Y. (2008). Calcifications in prostate and ejaculatory system: a study on 298 consecutive whole mount sections of prostate from radical prostatectomy or cystoprostatectomy specimens. *Ann. Diagn. Pathol.*, 12(3), 165–170. (Cited on page 92.)
- [Sun *et al.* 2015] Sun, J., Dowling, J. A., Pichler, P., Parker, J., Martin, J., Stanwell, P., Arm, J., Menk, F., & Greer, P. B. (2015). Investigation on the performance of dedicated radiotherapy positioning devices for MR scanning for prostate planning. *Journal of applied clinical medical physics / American College of Medical Physics*, 16(2), 4848. (Cited on pages 20 and 31.)
- [Sun *et al.* 2014] Sun, J., Pichler, P., Dowling, J., Menk, F., Stanwell, P., Arm, J., & Greer, P. B. (2014). MR simulation for prostate radiation therapy: effect of coil mounting position on image quality. *Brit. J. Radiol.*, 87(1042), 20140325. (Cited on pages 20, 59, and 73.)
- [Tanaka *et al.* 2016] Tanaka, O., Komeda, H., Iida, T., Tamaki, M., Seike, K., Kato, D., Yokoyama, T., Hirose, S., Kawaguchi, D., & Yama, E. (2016). Usefulness of Iron-Containing Fiducial Marker for Prostate Radiotherapy. *Int. J. Med. Phys. Clin. Eng. Radiat. Oncol.*, 05(04), 348–354. (Cited on page 60.)
- [Tanderup *et al.* 2014] Tanderup, K., Viswanathan, A. N., Kirisits, C., & Frank, S. J. (2014). Magnetic resonance image guided brachytherapy. *Sem. Radiat. Oncol.*, 24(3), 181–91. (Cited on page 2.)

- [Teoh *et al.* 2011] Teoh, M., Clark, C. H., Wood, K., Whitaker, S., & Nisbet, A. (2011). Volumetric modulated arc therapy: a review of current literature and clinical use in practice. *Br. J. Radiol.*, *84*(1007), 967–96. (Cited on page 109.)
- [Thariat *et al.* 2013] Thariat, J., Hannoun-Levi, J.-M., Myint, A. S., Vuong, T., & Gérard, J.-P. (2013). Past, present, and future of radiotherapy for the benefit of patients. *Nat. Rev. Clin. Oncol.*, *10*(1), 52–60. (Cited on page 39.)
- [The Royal College of Radiologists 2016] The Royal College of Radiologists (2016). *Radiotherapy dose fractionation* (2 ed.). The Royal College of Radiologists. (Cited on pages 4 and 7.)
- [Thomas 1999] Thomas, S. J. (1999). Relative electron density calibration of CT scanners for radiotherapy treatment planning. *Br. J. Radiol.*, *72*(860), 781–86. (Cited on pages 21 and 30.)
- [Thompson *et al.* 2013] Thompson, J., Lawrentschuk, N., Frydenberg, M., Thompson, L., Stricker, P., & USANZ (2013). The role of magnetic resonance imaging in the diagnosis and management of prostate cancer. *BJU Int.*, *112*, 6–20. (Cited on page 8.)
- [Thor *et al.* 2013] Thor, M., Bentzen, L., Elstrøm, U. V., Petersen, J. B. B., & Muren, L. P. (2013). Dose/volume-based evaluation of the accuracy of deformable image registration for the rectum and bladder. *Acta Oncol.*, *52*(7), 1411–1416. (Cited on page 43.)
- [Thor *et al.* 2011] Thor, M., Petersen, J. B. B., Bentzen, L., Høyer, M., & Muren, L. P. (2011). Deformable image registration for contour propagation from CT to cone-beam CT scans in radiotherapy of prostate cancer. *Acta Oncol.*, *50*(6), 918–925. (Cited on page 43.)
- [Thwaites 2013] Thwaites, D. (2013). Accuracy required and achievable in radiotherapy dosimetry: have modern technology and techniques changed our views? *J. Phys.*, *444*(1), 012006. (Cited on pages 30 and 101.)
- [Torresin *et al.* 2015] Torresin, A., Brambilla, M. G., Monti, A. F., Moscato, A., Brockmann, M. A., Schad, L., Attenberger, U. I., & Lohr, F. (2015). Review of potential improvements using MRI in the radiotherapy workflow. *Zeit. Med. Phys.*, *25*(3), 210–220. (Cited on pages 108 and 110.)
- [Tree *et al.* 2012] Tree, A., Khoo, V., & van As, N. (2012). Prostate motion: Implications and management strategies. In *Robotic Radiosurgery. Treating Prostate Cancer and Related Genitourinary Applications* (pp. 51–65). Springer. (Cited on pages 7, 109, and 111.)
- [Trofimov *et al.* 2007] Trofimov, A., Nguyen, P. L., Coen, J. J., Doppke, K. P., Schneider, R. J., Adams, J. A., Bortfeld, T. R., Zietman, A. L., DeLaney, T. F., & Shipley, W. U. (2007). Radiotherapy Treatment of Early-Stage Prostate Cancer with IMRT and Protons: A Treatment Planning Comparison. *Int. J. Radiat. Oncol. Biol. Phys.*, *69*(2), 444–453. (Cited on page 39.)
- [Tyagi *et al.* 2017] Tyagi, N., Fontenla, S., Zelefsky, M., Chong-Ton, M., Ostergren, K., Shah, N., Warner, L., Kadbi, M., Mechalakos, J., & Hunt, M. (2017). Clinical workflow for mr-only simulation and planning in prostate. *Radiat. Oncol.*, *12*(1), 119. (Cited on pages 12, 84, and 92.)
- [Tyagi *et al.* 2016] Tyagi, N., Fontenla, S., Zhang, J., Cloutier, M., Kadbi, M., Mechalakos, J., Zelefsky, M., Deasy, J., & Hunt, M. (2016). Dosimetric and workflow evaluation of first commercial synthetic CT software for clinical use in pelvis. *Phys. Med. Biol.*, *62*(8), 2961–2975. (Cited on pages 11, 13, 40, 53, 59, 74, 75, 103, and 105.)
- [Tyagi *et al.* 2017] Tyagi, N., Fontenla, S., Zhang, J., Cloutier, M., Kadbi, M., Mechalakos, J., Zelefsky, M., Deasy, J., & Hunt, M. (2017). Dosimetric and workflow evaluation of first commercial synthetic CT software for clinical use in pelvis. *Phys. Med. Biol.*, *62*(8), 2961–2975. (Cited on page 110.)

- [Ullman *et al.* 2006] Ullman, K. L., Ning, H., Susil, R., Ayele, A., Jocelyn, L., Havelos, J., Guion, P., Xie, H., Li, G., Arora, B. C., Cannon, A., Miller, R. W., Norman, C. C., Camphausen, K., & Ménard, C. (2006). Intra- and inter-radiation therapist reproducibility of daily isocenter verification using prostatic fiducial markers. *Radiat. Oncol.*, 1(1), 2. (Cited on pages 91 and 106.)
- [Ung & Wee 2011] Ung, N. M. & Wee, L. (2011). Fiducial registration error as a statistical process control metric in image-guidance radiotherapy with fiducial markers. *Phys. Med. Biol.*, 56(23), 7473–85. (Cited on pages 60, 67, 74, 82, and 86.)
- [van Dalen *et al.* 2003] van Dalen, J. A., Huisman, H. J., Welmers, A., & Barentsz, J. O. (2003). Semi-automatic Image Registration of MRI to CT Data of the Prostate Using Gold Markers as Fiducials. In *Biomedical Image Registration: Second International Workshop, WBIR 2003, Philadelphia, PA, USA, June 23-24, 2003. Revised Papers* (pp. 311–320). Springer Berlin Heidelberg. (Cited on pages 60 and 75.)
- [Van den Berge *et al.* 2000] Van den Berge, D. L., Ridder, M. D., & Storme, G. A. (2000). Imaging in radiotherapy. *Eur. J. Radiol.*, 36(1), 41–48. (Cited on page 19.)
- [van der Heide *et al.* 2007] van der Heide, U. A., Kotte, A. N., Dehnad, H., Hofman, P., Lagenijk, J. J., & van Vulpen, M. (2007). Analysis of fiducial marker-based position verification in the external beam radiotherapy of patients with prostate cancer. *Radiother. Oncol.*, 82(1), 38–45. (Cited on pages 59, 72, 73, 91, and 105.)
- [van Herk *et al.* 1995] van Herk, M., Bruce, A., Kroes, A. P., Shouman, T., Touw, A., & Lebesque (1995). Quantification of organ motion during conformal radiotherapy of the prostate by three dimensional image registration. *Int. J. Radiat. Oncol. Biol. Phys.*, 33(5), 1311–20. (Cited on pages 13, 20, 59, and 73.)
- [Varma *et al.* 2011] Varma, G., Clough, R. E., Acher, P., SÉNégas, J., Dahnke, H., Keevil, S. F., & Schaeffter, T. (2011). Positive visualization of implanted devices with susceptibility gradient mapping using the original resolution. *Magn. Res. Med.*, 65(5), 1483–1490. (Cited on page 60.)
- [Verellen *et al.* 2008] Verellen, D., De Ridder, M., & Storme, G. (2008). A (short) history of image-guided radiotherapy. *Radiother. Oncol.*, 86(1), 4–13. (Cited on pages 4, 6, and 7.)
- [Verellen *et al.* 2007] Verellen, D., Ridder, M. D., Linthout, N., Tournel, K., Soete, G., & Storme, G. (2007). Innovations in image-guided radiotherapy. *Nat. Rev. Cancer*, 7(12), 949–960. (Cited on pages 4, 6, and 7.)
- [Vigneault *et al.* 1997] Vigneault, E., Pouliot, J., Laverdière, J., Roy, J., & Dorion, M. (1997). Electronic portal imaging device detection of radioopaque markers for the evaluation of prostate position during megavoltage irradiation: A clinical study. *Int. J. Radiat. Oncol. Biol. Phys.*, 37(1), 205–212. (Cited on page 81.)
- [Villeirs *et al.* 2005] Villeirs, G. M., Vaerenbergh, K., Vakaet, L., Bral, S., Claus, F., Neve, W. J., Verstraete, K. L., & Meerleer, G. O. (2005). Interobserver Delineation Variation Using CT versus Combined CT + MRI in Intensity-Modulated Radiotherapy for Prostate Cancer. *Strahlenther. Onkol.*, 181(7), 424–30. (Cited on pages 8, 19, and 81.)
- [Vonken *et al.* 2013] Vonken, E. P., Schär, M., Yu, J., Bakker, C. J., & Stuber, M. (2013). Direct in vitro comparison of six three-dimensional positive contrast methods for susceptibility marker imaging. *J. Magn. Res. Imaging*, 38(2), 344–357. (Cited on pages 60 and 77.)
- [Wachowicz *et al.* 2006] Wachowicz, K., Thomas, S. D., & Fallone, B. G. (2006). Characterization of the susceptibility artifact around a prostate brachytherapy seed in MRI. *Med. Phys.*, 33(12), 4459. (Cited on page 60.)

- [Walker *et al.* 2014] Walker, A., Liney, G., Metcalfe, P., & Holloway, L. (2014). MRI distortion: Considerations for MRI based radiotherapy treatment planning. *Australas. Phys. Eng. Sci. Med.*, 37(1), 103–13. (Cited on pages 12, 20, and 73.)
- [Wan *et al.* 2013] Wan, L., Pantel, K., & Kang, Y. (2013). Tumor metastasis: moving new biological insights into the clinic. *Nat. Med.*, 19(11), 1450–1464. (Cited on page 1.)
- [Wang *et al.* 2004] Wang, D., Strugnell, W., Cowin, G., Doddrell, D. M., & Slaughter, R. (2004). Geometric distortion in clinical MRI systems: Part I: evaluation using a 3D phantom. *Magn. Res. Imaging*, 22(9), 1211–21. (Cited on pages 12, 20, and 73.)
- [Weygand *et al.* 2016] Weygand, J., Fuller, C. D., Ibbott, G. S., Mohamed, A. S., Ding, Y., Yang, J., Hwang, K.-P., & Wang, J. (2016). Spatial Precision in Magnetic Resonance ImagingGuided Radiation Therapy: The Role of Geometric Distortion. *Int. J. Radiat. Oncol. Biol. Phys.*, 95(4), 1304–16. (Cited on page 73.)
- [Wolterink *et al.* 2017] Wolterink, J. M., Dinkla, A. M., Savenije, M. H. F., Seevinck, P. R., van den Berg, C. A. T., & Išgum, I. (2017). Deep MR to CT Synthesis Using Unpaired Data. In Tsafaris, S. A., Gooya, A., Frangi, A. F., & Prince, J. L. (Eds.), *Simulation and Synthesis in Medical Imaging*, (pp. 14–23)., Cham. Springer International Publishing. (Cited on pages 111 and 112.)
- [Wu *et al.* 2001] Wu, J., Haycocks, T., Alasti, H., Ottewell, G., Middlemiss, N., Abdolell, M., Warde, P., Toi, A., & Catton, C. (2001). Positioning errors and prostate motion during conformal prostate radiotherapy using on-line isocentre set-up verification and implanted prostate markers. *Radiother. Oncol.*, 61(2), 127–133. (Cited on page 81.)
- [Wu *et al.* 2009] Wu, Z., Mittal, S., Kish, K., Yu, Y., Hu, J., & Haacke, E. M. (2009). Identification of calcification with MRI using susceptibility-weighted imaging: a case study. *J. Magn. Res. Imaging*, 29(1), 177–82. (Cited on page 73.)
- [Xing *et al.* 2016] Xing, A., Holloway, L., Arumugam, S., Walker, A., Rai, R., Juresic, E., Cassapi, L., Goozee, G., & Liney, G. (2016). Commissioning and quality control of a dedicated wide bore 3T MRI simulator for radiotherapy planning. *Int. J. Canc. Ther. Oncol.*, 4(2). (Cited on page 73.)
- [Yang *et al.* 2012] Yang, M., Zhu, X. R., Park, P. C., Titt, U., Mohan, R., Virshup, G., Clayton, J. E., & Dong, L. (2012). Comprehensive analysis of proton range uncertainties related to patient stopping-power-ratio estimation using the stoichiometric calibration. *Phys. Med. Biol.*, 57(13), 4095–4115. (Cited on page 51.)
- [Zangger & Armitage 1999] Zangger, K. & Armitage, L. M. (1999). Silver and gold NMR. *Metal-based drugs*, 6(4-5), 239–245. (Cited on page 82.)
- [Zaorsky *et al.* 2017] Zaorsky, N. G., Davis, B. J., Nguyen, P. L., Showalter, T. N., Hoskin, P. J., Yoshioka, Y., Morton, G. C., & Horwitz, E. M. (2017). The evolution of brachytherapy for prostate cancer. *Nat. Rev. Urol.*, 14(7), 415–439. (Cited on page 2.)
- [Zaorsky *et al.* 2017] Zaorsky, N. G., Showalter, T. N., Ezzell, G. A., Nguyen, P. L., Assimos, D. G., D’Amico, A. V., Gottschalk, A. R., Gustafson, G. S., Keole, S. R., Liauw, S. L., Lloyd, S., McLaughlin, P. W., Movsas, B., Prestidge, B. R., Taira, A. V., Vapiwala, N., & Davis, B. J. (2017). ACR Appropriateness Criteria® external beam radiation therapy treatment planning for clinically localized prostate cancer, part I of II. *Adv. Radiat. Oncol.*, 2(1), 62–84. (Cited on pages 13, 39, 59, 81, and 101.)
- [Zelevsky *et al.* 2012] Zelevsky, M. J., Kollmeier, M., Cox, B., Fidaleo, A., Sperling, D., Pei, X., Carver, B., Coleman, J., Lovelock, M., & Hunt, M. (2012). Improved clinical outcomes with high-dose image guided radiotherapy compared with non-igrt for the treatment of clinically localized prostate cancer. *Int. J. Radiat. Oncol. Biol. Phys.*, 84(1), 125 – 129. (Cited on page 7.)

- [Zelevsky *et al.* 2008] Zelevsky, M. J., Levin, E. J., Hunt, M., Yamada, Y., Shippy, A. M., Jackson, A., & Amols, H. I. (2008). Incidence of Late Rectal and Urinary Toxicities After Three-Dimensional Conformal Radiotherapy and Intensity-Modulated Radiotherapy for Localized Prostate Cancer. *Int. J Radiat. Oncol. Biol. Phys.*, 70(4), 1124–1129. (Cited on page 6.)
- [Zhu *et al.* 2011] Zhu, H., Demachi, K., & Sekino, M. (2011). Phase gradient imaging for positive contrast generation to superparamagnetic iron oxide nanoparticle-labeled targets in magnetic resonance imaging. *Magn. Res. Imaging*, 29(7), 891–898. (Cited on page 60.)
- [Zijlstra *et al.* 2017] Zijlstra, F., Bouwman, J. G., Braškute, I., Viergever, M. A., & Seevinck, P. R. (2017). Fast fourier-based simulation of off-resonance artifacts in steady-state gradient echo mri applied to metal object localization. *Magn. Res. Med.*, 78(5), 2035–2041. (Cited on pages 60, 63, and 76.)
- [Zijlstra *et al.* 2017] Zijlstra, F., Moerland, M. A., van der Voort van Zyp, J. R. N., Noteboom, J. L., Viergever, M. A., & Seevinck, P. R. (2017). Challenges in MR-only seed localization for postimplant dosimetry in permanent prostate brachytherapy. *Med. Phys.*, 44(10), 5051–5060. (Cited on pages 60, 63, and 76.)

List of Figures

1.1	Percent Dose depth profile for electron and photon radiations beams	3
1.2	Flowchart of an ideal patient treatment with radiotherapy	4
1.3	CT and MR images for prostate cancer treatment planning	7
1.4	Overview of a radiotherapy pathway for prostate cancer treatments	9
1.5	Schematic overview of an MR-only radiotherapy pathway.	10
2.1	Schematic of the study	22
2.2	Calibration curves used to convert CT or sCT in electron density . .	25
2.3	Radial distance from the isocentre to body contour as on CT/sCT .	27
2.4	Radial beam depth difference between CT and sCT	29
3.1	Axial plane of the images considered in the study	43
3.2	Statistics of the image evaluation between CT and sCT images	47
3.3	Axial plane of a patient with superimposed dose distribution	48
3.4	Boxplots of target DVH parameter difference	50
3.5	Boxplot of organ at risks DVH parameters	51
4.1	Schematic of MR-based automatic fiducial marker localisation	65
4.2	Schematic representation of the automatic FM localisation	66
4.3	Histogram of the ID position between man and auto localisation . .	68
4.4	Barplot of the difference of ID of corresponding FMs	69
4.5	Axial plane of CT and MR images for two patients	71
4.6	Root mean square error between registered FMs	72
5.1	Axial slice of CT, and MRI images for patients P ₁ and P ₉	87
5.2	Representation of inter-observer marker localisation for P ₁ and P ₉ .	88
5.3	Barplot of the LoA in all the directions	89
5.4	Barplot of LoA _{CM} in all the directions	90
5.5	Frequency of reported unreliable FM localisation	95
5.6	Axial slice of CT and MRI images for patient P ₄	96
5.7	Axial slice of CT and MRI images for patient P ₆	97
5.8	Axial slice of CT and MRI images for patient P ₁₄	98

List of Tables

1.1	Overview of the sCT generation approaches and their performances	11
2.1	Synthetic-HU assigned to the five tissue classes	24
2.2	Confounding factor estimated as average of relative dose differences	29
2.3	Relative percentage volume of each tissue class in sCTs	33
2.4	Confusion Matrix of the tissue classification in sCT images	33
2.5	Gamma pass rates in CTV using the clinical calibration curve	34
2.6	Gamma pass rate in CTV using the sCT calibration curve	35
2.7	Confounding factor estimated in terms of gamma pass rates	36
3.1	The synthetic-HU values assigned to the five tissue classes	42
3.2	Proton range calculated on single field uniform dose	48
3.3	Gamma pass rates calculated on CT- and sCT-based doses	49
4.1	Detection rate for CT- and MR-based localisation	68
4.2	Statistics of the correctly detected FM	70
4.3	Statistics of the difference of the translation vectors	72
4.4	Discriminative power in each step of the algorithm	78
5.1	Image parameters in use for manual gold FMs localisation	84
5.2	Statistics of the absolute difference in the inter-marker distances	91
5.3	Inter-observer apparent detection length	95
5.4	Time needed to perform manual FM localisation for each observer	95
6.1	Updates on the sCT generation approaches and their performances	103
6.2	Overview of the methods for automatic FM localisation	107
6.3	Imaging protocol proposed for an MR-only pathway in Utrecht	109
7.1	Base units of the International System.	148
7.2	Derived units adopted in this thesis.	149
7.3	Prefixes	149

List of Abbreviations

2D	two-dimensional	7, 110
3D	three-dimensional	4, 5, 7, 11, 22, 41, 45, 61, 63, 70, 75, 76, 83, 91, 101, 105, 108–112
BEV	beam’s eye view	38, 44, 45, 47, 48, 51
bSSFP	balanced steady-state free precession	83–91, 93–98, 105, 106, 108, 109
CT	computed tomography	4–10, 12, 13, 18–25, 27–33, 38–53, 58–62, 65–67, 70–72, 74, 80–87, 90–93, 95–98, 101, 102, 104, 106–113
CTV	clinical target volume	5, 18, 23, 24, 27–30, 34, 35, 41, 45, 50–52
DVH	dose volume histogram	38, 49–51, 104
FA	flip angle	v
FM	fiducial marker	6, 12, 13, 58–77, 80–98, 105–113
FOV	field of view	12, 21, 22, 41, 61, 73, 75, 83, 84, 102, 109, 110
GRE	gradient-recalled echo	61–63, 70, 73–76, 83–89, 91, 93–98, 105, 108, 109
HU	hounsfield unit	4, 10, 19–21, 23–25, 27, 30–32, 38, 39, 41–46, 48, 50–53, 62, 87, 96–98, 102, 104, 108, 112, 118
ID	inter-marker distance	65, 66, 69, 70, 72, 80, 86, 90
IGRT	image-guided radiotherapy	5, 6, 12, 13, 59, 72, 81, 101, 104, 105, 107
IMPT	intensity-modulated proton therapy	38, 39, 44–46, 49, 52, 53
IMRT	intensity-modulated radiotherapy	6, 18, 24, 25, 30, 109
linac	linear accelerator	3, 5, 9
MR	magnetic resonance	7–13, 18–25, 27–33, 38–48, 50–53, 58–76, 80–84, 87, 91–93, 101–113
MRCAT	MR for calculating attenuation	10, 12, 18, 22–25, 30, 31, 38, 41, 42, 44–47, 49–52, 101–105, 110–112, 117, 118
MRI	magnetic resonance imaging	v, vi, 4, 5, 7–9, 11–13, 19, 23, 29–31, 38, 39, 42, 45, 48, 52, 53, 58–61, 72, 81, 83, 85–87, 90–93, 95–98, 101, 104, 106, 108–111

MRIgRT	MRI-guided radiotherapy	9, 101, 111, 112
OAR	organ at risk	5, 12, 50, 51, 101, 109, 110
PTV	planning target volume	5, 12, 41, 42, 44–48, 50, 52, 59, 81
RF	radio-frequency	3, 22, 41, 61, 83, 84
rSPR	relative stopping power ratio	39, 42, 45–47, 51
RTT	radiotherapy technician	3–5, 9, 13, 41, 59–62, 80, 82–84, 86–89, 91–94, 105
sCT	synthetic CT	10, 12, 13, 18–25, 27, 30–33, 38–45, 48, 50–53, 59, 74, 75, 101, 102, 104, 105, 108–113
SPGR	spoiled gradient-recalled echo	22, 41, 83–89, 91, 93–98, 101, 105, 108–110
TE	echo time	v
TR	relaxation time	v

UNITS AND SYMBOLS

In this thesis the International System established by the General Conference on Weights and Measures has been adopted. The international System is founded on seven base units for corresponding mutually independent quantities. The names and symbol of these base quantities are reported in Table 7.1. Derived units are

Table 7.1 Quantity, name and symbol of the International System base units.

Quantity	Name	Symbol
length	metre	m
mass	kilogram	kg
time	second	s
electric current	ampere	A
thermodynamic temperature	kelvin	K
amount of substance	mole	mol
luminous intensity	candela	cd

units which may be expressed in terms of base units by means of the mathematical symbols of multiplication (·) and division (/). Table 7.2 lists the derived quantities and associated units, names and symbols used in this thesis. Note that not all the units are adopted by the International System, e.g. Hounsfield Units (HU), which is somehow anyway recognised given its diffuse use.

The units can be accompanied by prefixes. The prefixes adopted in this thesis are as shown in Table 7.3.

Table 7.2 Names and symbols of the derived units used in this thesis as well as their correspondent in base units of the International System.

Quantity	Name	Symbol	Expressed in units
angle	radian	rad	$\text{m}\cdot\text{m}^{-1}$
angle	degree	$^{\circ}$	$1^{\circ} = (\pi/180) \text{ rad}$
area			m^2
volume			m^3
volume	litre	l	$1 \text{ l} = 1 (\text{dm})^3 = 10^{-3} \text{ m}^3$
time	minute	min	$1 \text{ min} = 60 \text{ s}$
time	hour	h	$1 \text{ h} = 60 \text{ min} = 3600 \text{ s}$
time	day		$1 \text{ day} = 24 \text{ h} = 86400 \text{ s}$
time	year		$365 \text{ day} = 365 \cdot 86400 \text{ s}$
frequency	Hertz	Hz	s^{-1}
force	Newton	N	$\text{m}\cdot\text{kg}\cdot\text{s}^{-2}$
energy	joule	J	$\text{N}\cdot\text{m} = \text{m}^2\cdot\text{kg}\cdot\text{s}^{-2}$
electric potential	volt	V	$\text{J}\cdot\text{m}^{-1}\cdot\text{A}^{-1} = \text{m}^2\cdot\text{kg}\cdot\text{s}^{-3}\cdot\text{A}^{-1}$
energy	electronvolt	eV	*
dose ^a	Gray	Gy	$\text{J}\cdot\text{kg}^{-1} = \text{m}^2\cdot\text{s}^{-2}$
magnetic field	tesla	T	$\text{kg}\cdot\text{s}^{-2}\cdot\text{A}^{-1}$

ionising radiation. * The electronvolt is the kinetic energy acquired by an electron in passing through a potential difference of 1 V in vacuum; $1 \text{ eV} = 1.60217733\text{e-}19 \text{ J}$ with a combined standard uncertainty of $0.0000049\text{e-}19 \text{ J}$.

Table 7.3 Prefixes used in the thesis.

Name	Symbol	Factor	Name	Symbol	Factor
milli	m	10^{-3}	kilo	k	10^3
centi	c	10^{-2}	mega	M	10^6
deci	d	10^{-1}			

Part V

Addendum

List of Publications

ARTICLES IN PEER-REVIEWED JOURNALS

Published

2017

- Maspero, M., van den Berg, C. A. T., Landry, G., Belka, C., Parodi, K., Seevinck, P. R., Raaymakers, B. W., & Kurz, C. (2017). **Feasibility of MR-only proton dose calculations for prostate cancer radiotherapy using a commercial pseudo-CT generation method.** *Phys. Med. Biol.*, 62(24), 9159-9176 <https://doi.org/10.1088/1361-6560/aa9677> [Maspero *et al.* 2017].
- Maspero, M., van den Berg, C. A. T., Zijlstra, F., Sikkes, G. G., de Boer, H. C. J., Meijer, G. J., Kerkmeijer, L. G. W., Viergever, M. A., Lagendijk, J. J. W., Meijer, G. J., & Seevinck, P. R. (2017). **Evaluation of an automatic MR-based gold fiducial marker localisation method for MR-only prostate radiotherapy.** *Phys. Med. Biol.*, 62(20), 7981-8002. <http://doi.org/10.1088/1361-6560/aa875f> [Maspero *et al.* 2017].
- Andreychenko, A., Kroon, P. S., Maspero, M., Jurgenliemk-Schulz, I., De Leeuw, A. A., Lam, M. G., Lagendijk, J. J. W. & van den Berg, C. A. T. (2017). **The feasibility of semi-automatically generated red bone marrow segmentations based on MR-only for patients with gynecologic cancer.** *Radiother. Oncol.*, 123(1), 164-168 <https://doi.org/10.1016/j.radonc.2017.01.020> [Andreychenko *et al.* 2017].
- Maspero, M., Seevinck, P. R., Schubert, G., Hoesl, M. A. U., van Asselen, B., Viergever, M. A., Lagendijk, J. J. W., Meijer, G. J., & van den Berg, C. A. T. (2017). **Quantification of confounding factors in MRI-based dose calculations as applied to prostate IMRT.** *Phys. Med. Biol.*, 62(3), 948-965 <http://dx.doi.org/10.1088/1361-6560/aa4fe7> [Maspero *et al.* 2017].

2015

- Maspero, M., Berra, A., Conti, V., Giannini, G., Ostinelli, A., Prest, M., & Vallazza, E. (2015). **A real time scintillating fiber Time of Flight spectrometer for LINAC photoproduced neutrons.** *Nucl. Instr. Meth. Phys. Res. A*, 777, 154-160 <https://doi.org/10.1016/j.nima.2014.12.101> [Maspero *et al.* 2015].

Submitted

2017

- Maspero, M., Seevinck, P. R., Willems, N. J. W., Sikkes, G. G., de Kogel, G. J., de Boer, H. C. J., van der Voort van Zyp, J. R. N., & van den Berg, C.

A. T. (2017). **Evaluation of manual gold Fiducial Marker localisation for Magnetic Resonance-only prostate Radiotherapy.** *Radiat. Oncol.*, [Maspero *et al.* 2018].

- Dinkla, A. M., Wolterink, J. M., Maspero, M., Savenije, M. H. F., Verhoeff, J. J. C., Isgum, I., Seevinck, P. R., Lagendijk, J. J. W. & van den Berg, C. A. T., since the manuscript is under review in a double-blind peer reviewed journal, we omit the title in accordance to the policy of the journal. *Int. Radiat. Oncol. Biol. Phys.*

2018

- Maspero, M., Savenije, M. H. F., Dinkla, A. M., Seevinck, P. R., M. P. W. Intven, I. M. Jurgenliem-Schulz, L. G. W. Kerkmeijer & van den Berg, C. A. T., **Fast synthetic CT generation with deep learning for general pelvis MR-only Radiotherapy.** *Phys. Med. Biol.*

In Preparation

- Maspero, M., Tyyger M. D., Veeneendaal, G., Seevinck, P. R., Tijssen, R. H. N., Intven, M. P. W., & van den Berg, C. A. T., Feasibility of MR-only rectum radiotherapy using a commercial solution for prostate.

ABSTRACTS AND CONFERENCE PROCEEDINGS

Upcoming

2018

- Maspero, M., Tyyger M. D., Seevinck, P. R., Tijssen, R. H. N., Intven, M. P. W., & van den Berg, C. A. T., Feasibility of MR-only rectum radiotherapy using a commercial prostate sCT generation solution, *ESTRO 37*.
- Savenije, M. H. F., Maspero, M.¹, Dinkla, A. M., Seevinck, P. R. & van den Berg, C. A. T., MR-based synthetic CT with conditional Generative Adversarial Network for prostate RT planning, *ESTRO 37*.
- Dinkla, A. M., Wolterink, J. M., Maspero, M., Savenije, M. H. F., Verhoeff, J. J. C., Isgum, I., Seevinck, P. R., Lagendijk, J. J. W. & van den Berg, C. A. T., Dosimetric evaluation of deep learning based synthetic-CT generation for MR-only brain radiotherapy, *ESTRO 37*.
- Kurz, C., Maspero, M., Landry, G., Belka, C., Parodi, K., Seevinck, P. R., Raaymakers, B. W., & van den Berg, C. A. T., Translation of a certified MR-only synthetic CT solution for prostate from photon to proton therapy, *ESTRO 37*.
- Savenije, M. H. F., Maspero, M.¹, Dinkla, A. M., Seevinck, P. R. & van den Berg, C. A. T., Fast synthetic CT generation using a conditional Generative Adversarial Network and Dixon imaging for general pelvis

¹Indicating the presenting author.

MR-based Radiotherapy planning, *Joint Annual Meeting ISMRM-ESMRMB 2018*.

- Dinkla, A. M., Wolterink, J. M., Maspero, M., Savenije, M. H. F., Verhoeff, J. J. C., Isgum, I., Seevinck, P. R., Lagendijk, J. J. W. & van den Berg, C. A. T., CT synthesis for MR-only brain radiotherapy treatment planning using convolutional neural networks, *Joint Annual Meeting ISMRM-ESMRMB 2018*.
- Meliaddò, E. F., Raaijmakers, A. J. E., Savenije, M. H. F., Sbrizzi, A., Maspero, M., Luijten, P. R. and van den Berg, C. A. T. On-line Subject-Specific Local SAR Assessment by Deep Learning, *Joint Annual Meeting ISMRM-ESMRMB 2018*.

Presented

2017

- Maspero, M., van den Berg, C. A. T., Zijlstra, F., de Boer, H. C., Meijer, G. J., Viergever, M. A., Lagendijk, J. J. W., Kerkmeijer, L. J. W. & Seevinck, P. R. Clinical evaluation of automatic localization of prostate gold Fiducial Markers for MR-only Radiotherapy. *Proc. Int. Soc. Mag. Res. Med.* 25, #5555 <http://dev.ismrm.org/2017/5555.html>.

2016

- Maspero, M., Seevinck, P. R., Schubert, G., Hoesl, M., Meijer, G. J., Viergever, M. A., Lagendijk, J. J. W. & van den Berg, C. A. T. (2016). MOFGCAM-PUSJeP204: Comparison study for CT and MR-only Prostate IMRT treatment planning: a framework for the estimation of relative contribution of body contour discrepancies, tissue stratification, and HURED conversion to the overall dose difference. *Med. Phys.*, 43(6), 3721-3722 <https://doi.org/10.1118/1.4957357>.
- Hoesl, M., Seevinck, P., Maspero, M., Meijer, G., Lagendijk, J., Raaymakers, B., & van den Berg, C., Fast generation of pseudo-CT in the head and neck for MR guided radiotherapy, *Proc. Int. Soc. Mag. Res. Med.* 24, #2115 dev.ismrm.org/2016/2115.html.
- Meliaddò, E. F., Raaijmakers, A., Restivo, M., Maspero, M., Luijten, P., & van den Berg, C., Database Construction for Local SAR Prediction: Preliminary Assessment of the Intra and Inter Subject SAR Variability in Pelvic Region. *Proc. Int. Soc. Mag. Res. Med.* 24, #3660 dev.ismrm.org/2016/3660.html.
- Andreychenko, A., Kroon, P. S., Maspero, M., Jurgenliemk-Schulz, I., de Leeuw, A., Lam, M., Lagendijk, J. J. W., & van den Berg, C. A. T. (2016), The feasibility of red bone marrow segmentation in the pelvis for MRI-only therapy planning, *Proc. Int. Soc. Mag. Res. Med.* 24, #3889 dev.ismrm.org/2016/3889.html.

- Maspero, M., Schubert, G., Lindstrom, M., Hoesl, M., Seevinck, P. R., Meijer, G. J., Lagendijk, J. J. W. & Van den Berg, C. A. T. (2016). EP-1841: Dose comparison study for CT and MR-only prostate IMRT treatment planning. *Radiother. Oncol.*, 119, S864-S865 [http://dx.doi.org/10.1016/s0167-8140\(16\)33092-4](http://dx.doi.org/10.1016/s0167-8140(16)33092-4).

2015

- Maspero, M., Seevinck, P. R., Meijer, G. J., Lagendijk, J. J. W., Viergever, M. A., & van den Berg, C. A. T. (2015). SUEJ219: A Dixon Based Pseudo-CT Generation Method for MR-Only Radiotherapy Treatment Planning of the Pelvis and Head and Neck. *Med. Phys.*, 42(6), 3316 <http://dx.doi.org/10.1118/1.4924305>.
- Maspero, M., Seevinck, P. R., Andreychenko, A., Crijns, S., Sbrizzi, A., Viergever, M., Lagendijk, J. W., van Den Berg, C. A. T, Improved cortical bone segmentation using a spectral-spatial selective pulse to reduce water/fat in-phase echo time, *Proc. Intl. Soc. Mag. Reson. Med.* 23, #0865 dev.ismrm.org/2015/0865.html.
- Maspero, M., Seevinck, P. R., Andreychenko, A., Crijns, S., Sbrizzi, A., Viergever, M., Lagendijk, J. J. W. & Van Den Berg, C. A. T. (2015). PO-0957: Improved automatic bone segmentation in pelvis using a customized excitation pulse on MR. *Radiother. Oncol.*, 115, S505 [http://dx.doi.org/10.1016/S0167-8140\(15\)40949-1](http://dx.doi.org/10.1016/S0167-8140(15)40949-1).

AWARDS & NOMINATIONS

- IOP Outstanding Reviewer Award, *Physics in Medicine and Biology*, 2016 http://iopscience.iop.org/journal/0031-9155/page/Reviewer_Awards_2016.
- IOP Outstanding Reviewer Award, *Physics in Medicine and Biology*, 2017 <https://publishingsupport.iopscience.iop.org/questions/physics-medicine-biology-2017-reviewer-awards/>.

MISCELLANEA

- Faurobert, M., Fang, C., Corbard, T., Sigismondi, C., Raponi, A., De Rosi, G., Bianda, M., Ramelli R., Caccia, M., Maspero, M., Negrini, L., & X. Wang (2012) Atmospheric fluctuations below 0.1 Hz during drift-scan solar diameter measurements. *EAS Publication Series*, 55, 381-383 <https://doi.org/10.1051/eas/1255054>.
- Caccia, M., Ebolese, A., Maspero, M., Santoro, R., Locatelli, M., Pieracci, M., & Tintori, C. (2011) Background removal procedure based on the SNIP algorithm for γ -ray spectroscopy with the CAEN Educational Kit. *Educational Note* ED3163.

Acknowledgements

*No man is an Iland, intire of itselfe; every man
is a peece of the Continent, a part of the maine;
if a Clod bee washed away by the Sea, Europe
is the lesse, as well as if a Promontorie were, as
well as if a Manor of thy friends or of thine
owne were; any mans death diminishes me,
because I am involved in Mankinde;
And therefore never send to know for whom
the bell tolls; It tolls for thee.*

John Donne
MEDITATION XVII,
Devotions upon Emergent Occasions

As already anticipated in the Forewords, this thesis could not be done without the contribution of many. I hope I will not forget anyone in the following lines².

THE GUIDES

First, I would like to thank Nico and Peter, *copromotoren* and weekly/daily guides. Thanks a lot for having managed to cope with me in the last four years: this thesis will surely not be there without the two of you, your assistance, guidance and comprehension.

Nico, your capability of putting together people and ideas at the right moment is merely impressive. You gave me the opportunity to get exposed to stimulating environments where I could meet so many interesting humans.

Peter, your enthusiasm and intuition have been so valuable during this time: smart solutions during scanning sessions, ideas for post-processing a specific image and the steps that should follow.

Thank you, both, for teaching me so much about the scientific world. You managed to highlight the flaw of my reasoning at the very beginning, showing me how to make effective use of time and words. If I have learned how to target a topic to a general audience, understanding how to try to get to the core of a subject, well, this is thanks to you.

Second, a big *thank you* goes to Jan and Max, *promotoren*.

Jan, your capabilities of having a clear “blue sky” vision and do not be shy to share it are something that I would love to bring along with me. You taught me that it is not necessary to use many words to communicate your opinion: thank you for such a lesson.

²If that will be the case, consider yourself invited for dinner at my place

Max, my profound gratitude for following the project: it has been an honour having the possibility to use some of your time to discuss the latest advances and knowing that your support could promptly be at hand.

My sincere gratitude goes to the members of the thesis assessment committee for their time and the constructive discussion: Marnix G.E.H Lam, Bas W. Raaymakers, Chrit T.W. Moonen, Ulke A. van der Heide and Mischa S. Hoogeman.

Thanks to Neelam Tyagi for joining the defence all the way from the USA and giving me the opportunity to visit MSKCC in New York and try out our automatic method on a challenging dataset.

In the section “guides”, I’d also like to mention six people that surely shaped my first scientific steps in the Physics world: Michela Prest, Erik Vallazza and Massimo Caccia (Università degli Studi dell’Insubria, Como, Italy). I would surely not be here without you! Your enthusiasm for particle physics and curiosity still follows me and positively influences my thoughts.

I’d like to thank Angelo Filippo Monti (Ospedale Niguarda Cá Granda, Milano, Italy) for being a personal reference point in the Italian radiotherapy community. Angelo, you have been always so keen in addressing my questions. Also, it is always a great pleasure to have occasion to meet you at ESTRO, and from there I still remember your words: “You will not come back [to Italy]”. I am curious whether your prophecy will become true, and, by the way: so far you were right!

Ewoud Smit, thank you for answering my questions about UMC Utrecht and its radiotherapy department. Marco Schwarz (Trento Proton therapy centre and INFN-TIFPA, Italy) thank you for the prompt call you offered after hearing that I could have a position in Utrecht and Nijmegen. Both of you, even if you probably do not know, played a crucial role in the decision of moving four years ago.

Such decision revealed to be a tough one, but I feel honoured to have had the privilege to get to know and use MRI in the practical realm of radiotherapy within UMC Utrecht.

I’d like to dedicate the conclusive lines of this section to my professors of Maths and Phys at the *Liceo*. You planted in me the seed of interest towards Science; I am still deeply thankful for the passion you demonstrated every day, dear: Stefania Tagliabue, Eddy Ostinelli and Giorgio Ballerini.

COLLEAGUES & FRIENDS

When thanking the colleagues, I’d like to remember the origin of this word. It comes from the Latin *col* = together with, and *legare* = to choose. So, even if it may sound odd: one decides to work with another one, according to the Latins³ ...

First, I’d like to thank the MR-only weekly group for the discussions and the learning moments. So, thanks to Anna, Mark, Nico & Peter, Gert, Hans, Christopher, Filipa and Daan. I wish you a great continuation with the meeting hoping to keep alive the collaboration wherever I will end up.

A big thanks for all the comments and feedback to all the co-authors (in order of appearance): Alessandro, Anna A, Sjoerd, Gerald, Michaela, Bram, Gert, Matti, Flavio, Alexander, Matthew, Peter, Petra, Marnix, Frank, Gonda, Hans, Linda,

³We, surely, do not want to move any objection against the Latins/Romans. Ah, in case you may find a different etymology, remember not to spoil a good story with facts.

Christopher, Guillaume, Katia, Bas, Nicole, Geja, Jochem, Mark, Anna, Martijn, Rob, Guus, Ina and Marcus.

For each paper, there is at least a person that deserve a special thanks.

Gerald, thanks to you I had a sneak preview of the dynamics of the industrial world. It has been my pleasure trying to get aligned on analysis and thanks for the deep scientific discussions that still we keep having now and then.

Frank, there would be no attempt to make the marker localisation automatic (at least in the way we did) if it was without you. Thanks for sharing your latest research trying to getting further into the clinic. I am not sure that the method will eventually be used, but it has been worth giving a shot.

Christopher, what a pleasure to collaborate and “milk” results for extending MR-only to the proton world.

Nicole, Gonda and Geja, your help in collecting data and extending the participation of the study to other colleagues have been simply perfect. If the study went so smoothly is thanks to you. Thanks once more to Nicole, Joske and Tiny for taking part in the study.

In the context of the project, I would love to thank Eveline Alberts, Marijn Kruiskamp, Gerald Schubert, Martin Deppe, Matti Tillander, Aleksii Halkola, Teeuvo Vaara, Matti Lindstrom, Max Köhler and Marieke van Grootel (Philips Healthcare) for the collaboration.

A big thanks to all the (PhD-or-PhD-to-be-but-not-only) colleagues. You all made the walk lighter, more interesting and I hope to have learned all the lessons imparted by each of you, in her/his special way. So, thanks to (this time, we do from z to a): Zorro (who does not exist, but as I said: this time we go from ‘z’), Yulia, Tristan, Tom, Tim, Tijn, Stefano, Stefan, Stan, Soraya, Sjoerd, Sieske, Robin, Remko, Ramona, Quincy, Pim, Peter, Oscar, Niek, Mike, Michaela, Mick, Metha, Maxence, Max P, Max B, Maureen, Matthew, Martijn, Marijn, Markus, Mark, Mariska, Mariolijn, Mario, Marieke, Lisa, Juliette, Joris, Joanne, Joana, Jeroen, Jean-Paul, Janot, Jaco, Ivana, Ivan, Ingmar, Hans, Hanne, Frank, Flavio, Filipa, Fieke, Federico, Ellis, Dennis, Deji, Daan, Cyril, Cornel, Clemens, Christel, Charis, Casper, Carlo, Boris, Bjorn, Baudouin, Bart, Arjan, Anneloes, Anna K, Anna D, Anna A, Anita, Alicia, Alice, Alexander, Alex, Alessandro and Alberto.

A special thanks to Christel, Bjorn, Michaela and Tom for being colleagues “in crime” sharing the same room & for making the time in the office a pleasant experience.

Bjorn and Mark, thanks for being my men of honour during this special day. When deciding who to chose for such a burden, I stick to the actual origin of the habit. *Paranifen* used to support the gentlemen, especially in the (not unlike) event of a discussion getting out of hand⁴. I thought you were just perfect knowing enough of the topic under discussion and enough of the native language to find your way through the burden ;)

If UMC Utrecht and its radiotherapy department is a special place, it is undoubtedly thanks to its staff: what a stimulant bunch of people to work with! Thanks for the input and attention to (this time we do from a to z): Alexis, André, Annette, Annika, Atousa, Astrid dL, Astrid vL, Bas, Bram, Daan, Dawit, Derrick, Eline, Ellart, Enrica, Eric, Erwin, Evert-Jan, Frans (& his music sessions) Gert,

⁴The person defending a doctorate was not allowed to carry weapons, the paranif yes. . .

Gery, Gijs, Guus. Hanneke, Hannick, Hans, Ilse, Jan K, Jan S, Jan-Willem, Jeroen, Jochem H, Jochem W, Joost, Kübra, Kees, Lieke, Linda, Loes, Louk, Marielle, Marie-Jose, Niels, Patricia, Petra, Rasa, Ric, Rien, Rob Ti, Rob Te, Rob U, Rogier, Sara, Simon, Stefan, Teun, Theo, Tiny, Tuan, Vincent, Wilfred and the rest of the Department. Thanks to the technicians at the department, with a mention of honour to Ellart and Tuan for being always at disposal.

A special thanks to the *secretariaat* of the radiotherapy department: Judith, Therèse, Yvette and Leonie, you have always been so kind to me, whatever question I could come up with; to Sylvia of the 7 T for arranging my pass to get access in the lab (to have some agar-cooking session with Stefano); to Renee from Imago, whom kindness and patience were so valuable on many occasions.

One of the reasons that attracted me to the Netherlands is that I knew the country beforehand since I had the opportunity to take part in a European Voluntary Service in the summer of 2012. The EVS has been an amazing experience and the primary key (no, this is not SQL!) to dare to move a step out of the comfort zone. My gratitude goes to the EU and the programme Erasmus plus for trying to make Europe smaller & creating occasions to meet other mindsets; to the Rijswijk Don Bosco Centrum, Biju, Marlies, Frouke, Thomas, Spela, Franka, Felix, Kayleigh, Martijn and the other volunteers for their joyful enthusiasm. A special thanks to the Brouwer family for being open-hearted and for their immense *gastorijheid*: Lilian and Tom thank you for being supportive and managing to keep having follow-ups on a regular basis.

Lisette, your creativity and dreaming attitude were a mind-opener during these years: thanks for the inspirational words of wisdom and kindness!

Un grosso grazie ai compagni di viaggio italiani: anche se sicuramente non è stato semplice starmi accanto da lontano, è sempre stato un piacere tornare a casa e chiaccherare cercando di comprendere a che punto le nostre vite erano giunte nel frattempo. Anna & Paolo, Carlo (chissà in che paese sei al momento), Chiara, Daniele, Federica, Filippo, Jhonny, Lilly, Matteo, Paolo F, Sara, Sebastiano, Stefano e Walter, grazie di cuore per l'interesse e la vicinanza.

Bilstraat has been my first Dutch home; it has been the door opening to a new world of people and relationships. It has been a pleasure to intersect life with: Anna, Mateuz, Romin, Firdose, João, Andreia, Paula, Silvia, Kostas & Maria, Ruben, Matteo, Sara & Sara, Simona, Matteo, Aisha, Nikos, Charlotte and Oghuzan.

Ruben, you have been the first person I met there, coincidence wants that we started the same day in UMC. You have always been a safe figure in this four years, even if we lost each other for some periods, to speak with you had always felt naturally good and reinvigorating: thanks Ruben for your support!

Maria and Kostas, the last four years have been an intense period. Even if on the 26th you will not be there, I am sure your presence will reach the Academieggebouw. Goodluck with beginning a new chapter in Greece!

Gaurav, thanks to the Dutch classes we met (for once: Ik dank de Nederlandse taal hier voor!). We struggled together through werkwoorden en nieuwe woorden. Thanks for making that experience lighter. From there, your kindness and creative spirit has always highly impressed and inspired me. Keep your spirit, Gaurav, and spread it around!

Ontzettend bedankt aan VV Boni, en Heren 4 plus trainers/coach: Hester, Dominique, Marieke, Frederike, Laurie, Felix, Jelle, Joan, Jochem, Matthias, Paul, Thomas, Tim en Wytse. Jullie hebben de weken sportiever en luchtiger gemaakt.

FAMILY

Lange Nieuwstraat has been a sort of second home in the NL. It would not be the same without Aisha, Alex, Anna, Anna, Carlo, Casper, Dhabia, Elena, Erik, João, Lisa, Magda, Maxence, Roberto, Sara, Saskia, Soraya, Susana, Tom and all the friends that they brought in the house. If in the struggle of a PhD life, I made it to the end, well, a big part of my gratitude goes to LNers and the unwritten rule of “sharing is caring” that can be felt after passing the doorstep of that house (maybe also outside the door, especially on a sunny summer day).

Teresa & Tonino, grazie per la vicinanza in tutti questi anni. Tonino, hai predetto un futuro come “direttore”, sono proprio curioso di vedere come andrà a finire la profezia. Teresa, le tue attenzioni sono state onnipresenti durante questi anni, grazie di cuore.

Dik & Marianne bedankt voor jullie gastvrijheid. Jullie duidelijke ondersteuning, samen met Roos, is enorm gewaardeerd. Oma Annie en opa Adrie, wat een inspirerende energie voor jullie leeftijd. Bedankt voor de attente vraag: “hoe gaat het met jouw studie?”. Een dikke “dankjewel” aan Iris en Pieter voor de constante interesse.

Un grosso “grazie” alla tribù di via Torre 7 (e limitrofi): è sempre bello tornare a casa ed incontrarvi e sapere che fate il tifo per qualunque cosa possa scegliere di fare. Dunque, grazie a (per distanza dalla casa in cui ho vissuto): Dario, Michi, Andrea, Enea, Matilde, zia Amabile, Claudia, Tito, Simona, Mauro, Giulia, Tommi, Sara & Lorenzo, Riccardo, Cristina, zia Betty & Maurizio, Giona, Marta & Pietro e, ultima per ossequioso rispetto alla saggezza maturata negli anni, la mitica nonna Enrica (il cui “fai il bravo” tuttora mi insegue benevolmente).

Enorme supporto, in tutti questi anni è di certo giunto da Elena & Francesca. Care sorelle, non è semplice vivere in un altro paese e sapere di non poter condividere le proprie vite nella quotidianità, ma avete sempre offerto un grande punto di appoggio per i miei vagabondaggi. Un grosso grazie anche a Massimiliano, Daniele & Luca; Adriano, Giovanni & Pietro, per la felicità che avete portato ad ogni incontro.

Cara Tessa, conto sul fatto che le lezioni di italiano stanno andando alla grande, anche se le nostre conversazioni sono esclusivamente in olandese. Grazie per l'enorme supporto in questo periodo finale. Hai salvaguardato la mia sanità mentale (o almeno ciò che ne resta dopo tutti questi anni di studi) nel periodo in cui mi sono dovuto concentrare totalmente sulla scrittura. Sono sicuro che non sia stato semplice. Grazie per la tua gentile presenza, cura e delicatezza. Sono proprio curioso di vedere come andrà questo nostro viaggio.

Mamma Luisa e papà Giulio, grazie di cuore per tutto il bene con cui mi accompagnate. Ad ogni passo siete sempre stati vicini, anche se di sicuro avete sofferto la distanza. Grazie per gli insegnamenti e la cura in tutti questi anni, spero di essere capace di portare il bagaglio di valori tramandatomi in tutte le esperienze passate e future.

Last but not least, I'd like to conclude this booklet from where I have begun. So, dear Reader, the last thank you goes to you! Thanks for indulging in these pages, the biggest gift you gave it to me by browsing them. Looking forward to seeing you in the next book...

Matteo

About the author

Matteo Maspero is a human being born in Como (Italy) a bit longer than 28 years ago (in May 1989, if you may prefer). After attending the “Liceo Scientifico E. Fermi” in Cantù (Italy), he studied Physics at the “Università degli Studi dell’Insubria” in Como (Italy) graduating - cum laude - in March 2014. During that years, he gained interest in experimental Physics, with a predilection for particle detectors. Following such an affair, he had the opportunity to develop (of course not all by himself) a detector for spectral measurements of neutrons produced by an in-hospital linear accelerator.

Feeling the need of broadening his horizons, he decided to step into the field of medical imaging, where, by chance, detectors are somehow involved. Since May 2014 he was enrolled as PhD candidate at the Radiotherapy Department of the Universitair Medisch Centrum Utrecht (The Netherlands).

This thesis is Matteo’s scientific contributions during his PhD project, where he had the luck to discover the beauty of magnetic resonance imaging in the practical realm of radiotherapy.

He is currently (March 9, 2018) deciding what will come next ...

